University of Naples Federico II

Faculty of Mathematical and Physical Sciences

Department of Physical Sciences

Galaxy evolution as a function of mass and environment: giant and dwarf galaxies in superclusters and in the field

Thesis submitted for the degree of

Doctor Philosophiae

Supervisors

Prof. M. Capaccioli
Dr. P. Merluzzi
Dr. C.P. Haines

Candidate

Adriana Gargiulo

Contents

Introduction

It has been known for decades that local galaxies can be broadly divided into two distinct populations (e.g. Hubble 1926, 1936; Morgan 1958; de Vaucouleurs 1961). The first population consists in red, passively-evolving, bulge-dominated galaxies mainly populated by old stars that, in the colour-magnitude diagram, makes up the "red sequence", while the second population makes up the "blue cloud" of young, star-forming, disk-dominated galaxies (e.g. Strateva et al. 2001; Kauffmann et al. 2003a,b; Blanton et al. 2003a; Baldry et al. 2004; Driver et al. 2006; Mateus et al. 2006).

It has also long been known that the environment in which a galaxy inhabits has a profound impact on its evolution in terms of defining both its structural properties and star-formation histories (e.g. Hubble & Humason 1931). In particular, passively-evolving spheroids dominate cluster cores, whereas in field regions galaxies are typically both star-forming and disk-dominated (Blanton et al. 2005a). These differences have been quantified through the classic morphology–density (Dressler 1980) and star-formation (SF)–density relations (Lewis et al. 2002; Gómez et al. 2003). However, despite much effort (e.g. Treu et al. 2003; Balogh et al. 2004a,b; Gray et al. 2004; Kauffmann et al. 2004; Tanaka et al. 2004; Christlein & Zabludoff 2005; Rines et al. 2005; Baldry et al. 2006; Blanton, Berlind & Hogg 2007; Boselli & Gavazzi 2006; Haines et al. 2006a; Mercurio et al. 2006; Sorrentino, Antonuccio-Delogo & Rifatto 2006a; Weinmann et al. 2006a,b; Mateus et al. 2007), it still remains unclear whether these environmental trends are: (i) the direct result of the initial conditions in which the galaxy forms, whereby massive galaxies are formed earlier preferentially in the highest overdensities in the primordial density field, and have a more active merger history, than galaxies that form in the smoother low-density regions; or (ii) produced later by the direct interaction of the galaxy with one or more aspects of its environment, whether that be other galaxies, the intracluster medium, or the underlying dark-matter distribution.

Several physical mechanisms have been proposed that could cause the transformation of galaxies through interactions with their environment such

as ram-pressure stripping (Gunn & Gott 1972), galaxy harassment (Moore et al. 1996), and suffocation (also known as starvation or strangulation), in which the diffuse gas in the outer galaxy halo is stripped preventing further accretion onto the galaxy before the remaining cold gas in the disk is slowly consumed through star-formation (Larson, Tinsley & Caldwell 1980).

The morphologies and star-formation histories of galaxies are also strongly dependent on their masses, with high-mass galaxies predominately passively-evolving spheroids, and low-mass galaxies generally star-forming disks. A sharp transition between these two populations is found about a characteristic stellar mass of $\sim 3 \times 10^{10}\,\mathrm{M}_{\odot}$, corresponding to $\sim \mathrm{M}^{\star} + 1$ (Kauffmann et al. 2003a,b). This bimodality implies fundamental differences in the formation and evolution of high- and low-mass galaxies. The primary mechanism behind this transition appears to be the increasing efficiency and rapidity with which gas is converted into stars for more massive galaxies according to the Kennicutt-Schmidt law (Kennicutt 1998; Schmidt 1959). This results in massive galaxies with their deep potential wells consuming their gas in a short burst ($< 2\,\mathrm{Gyr}$) of star-formation at $z > 2$ (Chiosi & Cararro 2002), while dwarf galaxies have much more extended star-formation histories and gas consumption time-scales longer than the Hubble time (van Zee 2001).

In the monolithic collapse model for the formation of elliptical galaxies this naturally produces the effect known as "cosmic downsizing" whereby the major epoch of star-formation occurs earlier and over a shorter period in the most massive galaxies and progressively later and over more extended time-scales towards lower mass galaxies. This has been confirmed observationally both in terms of the global decline of star-formation rates in galaxies since $z \sim 1$ (Noeske et al. 2007a,b) and the fossil records of low-redshift galaxy spectra (Heavens et al. 2004; Panter et al. 2007). Finally, in analyses of the absorption lines of local quiescent galaxies, the most massive galaxies are found to have higher mean stellar ages and abundance ratios than their lower mass counterparts, confirming that they formed stars earlier and over shorter time-scales (Thomas et al. 2005; Nelan et al. 2005). In this scenario, the mass-scale at which a galaxy becomes quiescent should decrease with time, with the most massive galaxies becoming quiescent earliest, resulting in the red sequence of passively-evolving galaxies being built up earliest at the bright end (Tanaka et al. 2005).

However, the standard paradigm for the growth of structure and the evolution of massive galaxies within a CDM universe is the hierarchical merging scenario (e.g. White & Rees 1978; Kauffmann, White & Guideroni 1993; Lacey & Cole 1993) in which massive elliptical galaxies are assembled through the merging of disk galaxies as first proposed by Toomre (1977) (see also Struck 2005). Although downsizing appears at first sight to be at odds with

the standard hierarchical model for the formation and evolution of galaxies, Merlin & Chiosi (2006) are able to reproduce the same downsizing as seen in the earlier "monolithic" models in a hierarchical cosmological context, resulting in what they describe as a revised monolithic scheme whereby the merging of substructures occurs early in the galaxy life ($z > 2$). Further contributions to cosmic downsizing and the observed bimodality in galaxy properties could come from the way gas from the halo cools and flows onto the galaxy (Dekel & Birnboim 2006; Kereš et al. 2005) and which affects its ability to maintain star-formation over many Gyrs, in conjunction with feedback effects from supernovae and AGN (e.g. Springel et al. 2005a; Croton et al. 2006). These mechanisms which can shut down star-formation in massive galaxies allow the hierarchical CDM model to reproduce very well the rapid early formation and quenching of stars in massive galaxies (e.g. Bower et al. 2006; Hopkins et al. 2006a; Birnboim, Dekel & Neistein 2007). In particular, the transition from cold to hot accretion modes of gas when galaxy halos reach a mass $\sim 10^{12} M_{\odot}$ (Dekel & Birnboim 2006) could be responsible for the observed sharp transition in galaxy properties with mass.

If the evolution of galaxies due to internal processes occurs earlier and more rapidly with increasing mass, then this would give less opportunity for external environmental processes to act on massive galaxies. Moreover, low-mass galaxies having shallower potential wells could be more susceptible to disruption and the loss of gas due to external processes such as ram-pressure stripping and tidal interactions. This suggests that the relative importance of internal and external factors on galaxy evolution and on the formation of the SF-, age- and morphology-density relations could be mass-dependent, in particular the relations should be stronger for lower mass galaxies. Such a trend has been observed by Smith et al. (2006) who find that radial age gradients (out to $1\,R_{vir}$) are more pronounced for lower mass ($\sigma < 175\,km\,s^{-1}$) cluster red sequence galaxies than their higher mass subsample.

With all this in mind, we undertook the work presented in this thesis studying galaxy evolution as a function of mass and environment (chapter 1). To this aim, we investigate the evolution of giant and dwarf galaxies in cluster environment (Part I) through the analysis of i) luminosity function and colour distribution (chapter 3), and ii) the fundamental plane of early-type galaxies (chapter 4). We extend, then, our analysis to a wide spread of environments, from the rarefied field to the high density regions, (Part II, chapters 6 and 7). This analysis allowed us to discriminate among the possible physical mechanisms which, driving the star-formation of giant and dwarf galaxies, are able to reproduce the observed bimodal galaxy distribution.

Technical aspects of the dataset used throughout the present analysis are presented in chapters 2 and 5.

Chapter 1

The Bimodality in Galaxy Properties

In this first chapter we present an overview of the astronomical field of galaxy evolution which is forms the basis of study for this thesis, describing the scientific background and pointing out the open issues.

1.1 Galaxy systems

Edwin Hubble, about 80 years ago, established the nature of galaxies as gigantic self-bound stellar systems. Galaxies are the places where stars form and evolve, in constant interaction with the interstellar medium (ISM), a complex mix of gas and plasma, dust particles, relativistically moving electrons, protons, other atomic nuclei, cosmic rays, and magnetic fields. These different components are tightly coupled together, thus for many purposes they may have to be studied as a single entity. The ISM is an important component in galaxy systems, accounting in some galaxies for more mass than stars, and with a fundamental role for star-formation. Most of the gas mass is contained in neutral unstable HI clouds ($10^2 < T < 10^4$ K) and in dense, cold molecular clouds ($T < 10^2$ K) where stars form, while a great part of the ISM volume is occupied by diffuse ($n \approx 0.1 \mathrm{cm}^{-3}$), warm/hot ($T \approx 10^4$-$10^5$ K) turbulent gas that confines clouds by pressure. The primary causes of star-formation in galaxies are though to be large-scale compression of the diffuse ISM driven by supernovae (SN), magneto-rotational or disk gravitational instabilities. At the centre of a significant fraction of galaxies is found a massive black hole (BH), which when fed by the surrounding material from an accretion disc, can experience a temporary AGN/quasar phase during which it releases, through powerful plasma jets and winds, the largest

amount of energy known among astronomical objects. This phenomenon of Active Galactic Nuclei (AGN) was much more frequent in the past (Avila-Reese 2006). Stars, gas, AGN, and all the luminous matter of galaxy constitute only a small (1-5%) fraction of the total mass. Under the assumption of Newtonian gravity, the observed kinematics of galaxies indicate the presence of enormous amounts of unseen mass, the dark matter (DM), whose presence can be inferred only indirectly from its gravitational influence. In their central regions galaxies are baryon-dominated and DM dominates only at large radii. Recently, from statistical analyses, it results that a typical galaxy with stellar mass M$\approx 6 \times 10^{10} M_{\odot}$ is surrounded by a DM halo of $\approx 2 \times 10^{12} M_{\odot}$ (Mandelbaum et al. 2006), and $\sim$200–250 kpc in extent. The baryonic mass is only $\simeq$3–5% of the DM mass in the halo. This fraction could be even lower for dwarf and very luminous galaxies.

Each galaxy is characterized by different percentages of these components: this mix determines the intrinsic features of the system making each galaxy different from the others.

Looking at the great variety of observable galaxies, the most evident differences are about:

- the morphology and light distribution;
- the ISM content and the spectral energy distribution;
- the dimension (and hence the mass);
- the distribution in space.

1.1.1 Morphological classification

In 1926 Edwin Hubble published *"The Realm of the Nebulae"* a catalogue of external galaxies with the first galaxy classification based on their overall appearance. He proposed that galaxies could be grouped into three primary categories: ellipticals, spirals and irregulars. This led to the morphological sequence known as the "Hubble sequence". Hubble arranged all morphological types into a diagram, shown in Fig. 1.1, with the form of a tuning-fork in which ellipticals occupy the single sequence on the left-hand end, while spiral galaxies were divided on the two branches on the right according to the presence or not of a central bar. Furthermore, at the junction of the ellipticals and spirals, in the middle of Hubble's tuning-fork diagram, there is a class of galaxies known as lenticulars. The tuning-fork diagram was interpreted by Hubble as an evolutionary sequence on which galaxies evolved from the

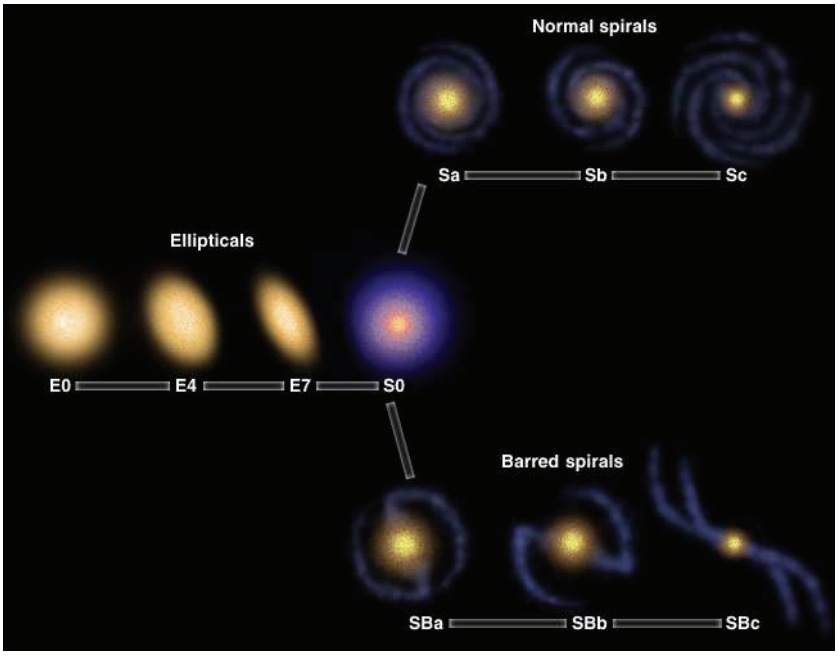

Figure 1.1: The tuning-fork diagram of Hubble.

left to the right: today this interpretation has been discredited even if it survives in the convention that elliptical and S0 galaxies are called "early-type" galaxies, while spirals are referred to as "late-type" galaxies.

The elliptical galaxies appear smooth (see Fig. 1.2), structureless, and are designated as En, where the index n, defined as n=10[1-(b/a)] with b/a being the apparent axial ratio, describes their elongated shape, and typically ranges between 0, for apparently round galaxies, and 7 for the most elongated galaxies. During the last thirty years, ellipticals have revealed themselves to be a complex class of objects rather different from the first models which represented them as simple oblate stellar systems flattened by rotation. Studies have shown, in fact, a probable triaxial structure, the presence of polar rings, dust lanes and multiple kinematically-decoupled components. Furthermore, elliptical galaxies show no or little rotation, suggesting the necessity for a formulation of more complex kinematical model in order to explain their shape. The lenticular galaxies are designated as S0 or SB0 according to whether they have a bar or not. The S0 galaxies are characterized by a central brightness condensation, which is similar to an elliptical and is called bulge or spheroidal component, surrounded by a disk, which has a different brightness profile with respect to the spheroidal component, being charac-

Figure 1.2: The elliptical galaxies M87 (E1) and M89 (E0).

terized by an intensity which decreases more rapidly (see next section) with radius. Typically the disk component of the lenticulars is characterized by the presence of a dust lane in such a way that the family of S0s is subdivided into three classes, $S0_1$, $S0_2$, $S0_3$, according to the growing strength of dust absorption. Also the barred lenticulars are divided into three classes: $SB0_1$, $SB0_2$ and $SB0_3$; but the division is made according to the prominence of the bar rather than to the dust strength.

Spiral galaxies (see Fig. 1.3) have a disk structure formed by a central bulge from which depart spiral arms. They are morphologically divided into normal spirals (S) and barred spirals (SB). Each of these classes can be separated into a finer classification: Sa, Sab, Sb, Sbc, Sc (and SBa, SBab, SBb, SBbc, SBc) according to i) the prominence of the central luminous bulge to the surrounding disk in producing the overall light distribution of the galaxy; ii) the tightness with which the spiral arms are wound; and iii) the distribution of stars in the arms. Sa and SBa have luminous bulges ($L_{bulge}/L_{disc} \sim 0.3$), and spiral arms tightly wound, and an uniform distribution of star towards the arms. Passing from a to c the bulge become less prominent ($L_{bulge}/L_{disc} \sim 0.05$), the spiral arms widen out and the stars are more clumpily distributed.

Irregular galaxies (I) are essentially low-mass disorganised and amorphous structures.

Figure 1.3: The spiral galaxies M81 (Sb).

1.1.2 Surface brightness distribution

The surface brightness is the energy emitted per unit of time, surface and solid angle. Although three dimensional in shape, we observe only their two dimensional projection on the sky. Several attempts have been made to find a suitable empirical law describing the light profiles of ellipticals galaxies and of the spheroidal components of lenticulars and spirals. In 1948, Gerard de Vaucouleurs described the brightness profile with the following law:

$$I(R) = I_e exp\{-k[(R/R_e)^{1/4} - 1]\}, \tag{1.1}$$

where R_e, called the effective radius, is the half-light radius, I_e, called the effective surface brightness, is the corresponding intensity and $k = 7.6692$ (Graham 2001) is a constant chosen so that half of the total flux from the galaxy is contained inside the radius R_e. More recently photometric data have shown, however, that, for a large fraction of elliptical galaxies and of bulges, the de Vaucouleurs' law is only an approximation of the radial brightness profile and, in particular, systematic deviations from this law have been observed. These deviations from the $r^{1/4}$-law have prompted a search for other representations of the brightness profile of early-type galaxies. A generalization of the de Vaucouleurs' law, was proposed by Sersic in 1968 that has been subsequently widely used. Sersic's law can be written as:

$$I(R) = I_e exp\{-b_n[(R/R_e)^{1/n} - 1]\}, \tag{1.2}$$

where I_e and R_e have the same meaning as the de Vaucouleurs law, while the exponent $1/4$ has been replaced by $1/n$, with n being the so-called Sersic

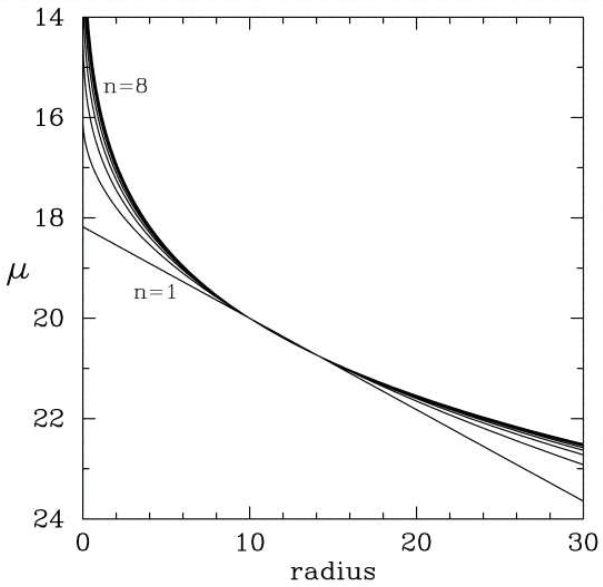

Figure 1.4: Different $R^{1/n}$ Sersic models normalized at $R_e = 10$" and $\mu_e = 20$ mag arcsec^{-2} (*Graham & Guzman* 2003).

index parameter, which determines the shape of the light profile (see Fig. 1.4). The figure shows that the profiles with higher values of the Sersic index are characterized by a distribution of light decreasing more rapidly with the distance from the centre, that those with lower Sersic index. The constant b_n is the analogous to k, but now is function of n. Sersic's law is often written in logarithm form:

$$\mu(R) = \mu_e + c_n[(R/R_e)^{1/n} - 1]. \tag{1.3}$$

If the shape parameter $n = 1$, the Sersic law assumes an exponential form which models well the brightness profile of the disk component present in the lenticular galaxies.

1.1.3 Spectral energy distribution

Galaxies, not only appear to have different shapes, but the same galaxy often look very different when viewed at different wavelengths of the electromagnetic spectrum. Indeed, each galaxy component (stars, gas, dust, etc.) emits over a different spectral range, and, hence, a complete picture of a galaxy requires multi-band observations which usually complement the

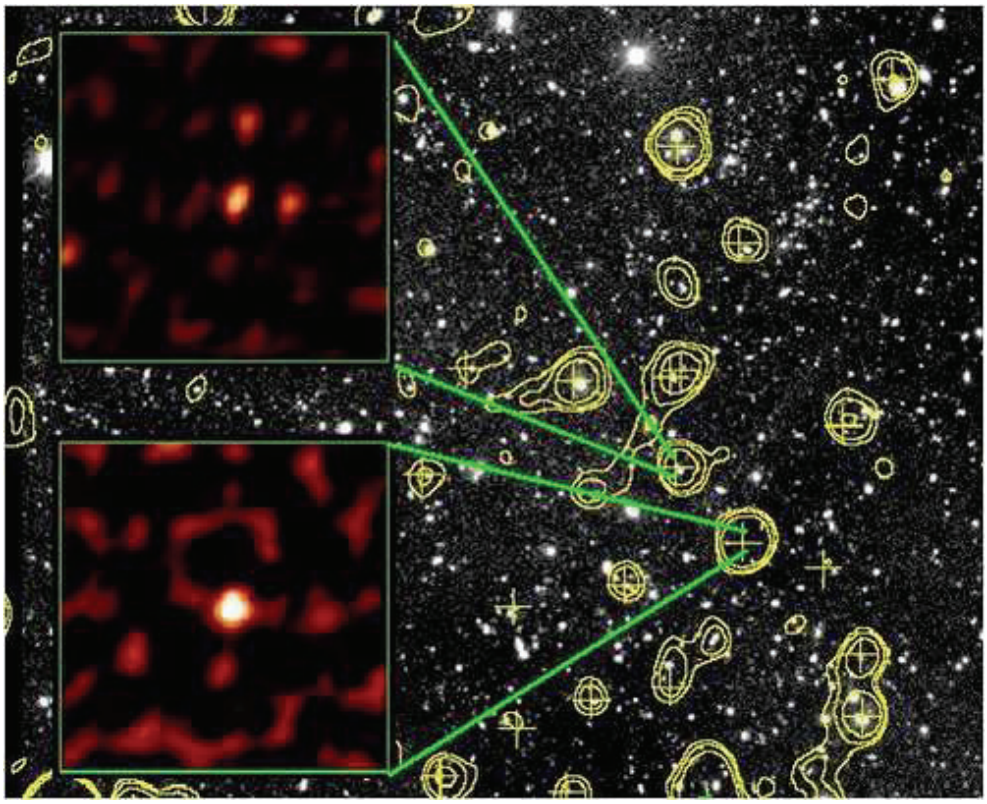

Figure 1.5: The combined optical (black and white) and radio wave (yellow contours) map: brightest radio wave emitting objects are not quite the same brightest objects in optical waveband.

traditional optical view dominated by the stellar component. Over the last thirty years, developments in instrumentation technology and a succession of space-based telescopes has opened up the full range of the electromagnetic spectrum to the astronomers, making multi-wavelength views of galaxies accessible, including: *XMM/Chandra* in X ray, *GALEX* in the far-ultraviolet (FUV), *Spitzer* in the infrared (IR),and SCUBA-2 in sub-mm.

Observing the Universe in radio waves allows us to obtain high resolution maps of very distant galaxies as well as very energetic sources of radiation such as quasars which simply cannot be detected at optical wavelengths (see Fig. 1.5). Looking at galaxies at a wavelength of 21cm (Hydrogen spectral line), we were able to determine the relative velocities of galactic arms and construct galactic rotation curves, which can be then used to derive the presence of DM in the galaxy.

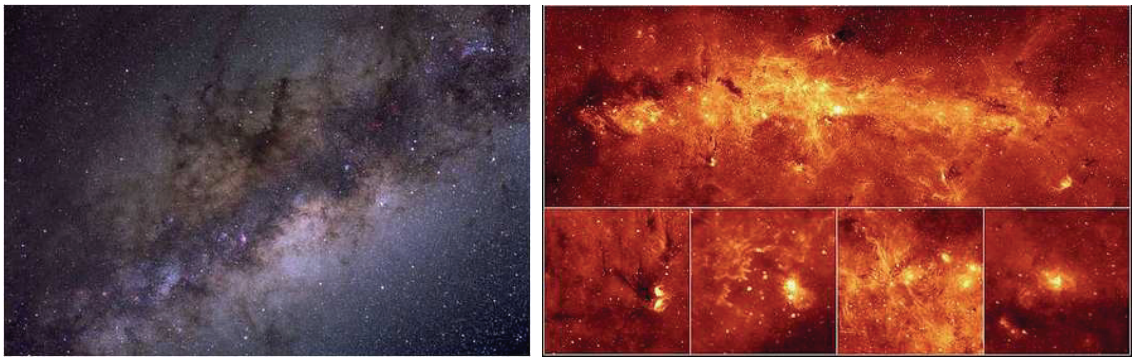

Figure 1.6: The centre of Milk Way as seen in the optical (*left panel*), and as seen in the MIR (*right panel*).

IR telescopes as *Spitzer* detect the interstellar dust emission heated by the radiation of the stars. In Fig. 1.6 (left panel) the centre of Milky Way, observed in the optical, is heavily observed by dust clouds, while the same region turns out to be very bright in the IR (right panel).

X-ray telescopes such as *Chandra* provide information on the structure of the Universe and the gas distribution detecting the intra-galactic and intra-cluster gas which maps the large-scale structure (see § 5.3). This gas is extremely hot (T $\sim 10^7$K) and emits through Bremsstrahlung emission, X-ray radiation (see Fig. 1.7).

Colour

Combining the IR, optical, X-ray and radio wavebands we can effectively show the contribution of the different components (Fig. 1.8) to galaxy systems. These different contributions are quantified by the so-called galaxy colour, derived observing the galaxies using different waveband filters, which allow us to select the flux emitted within different ranges of wavelength.

The ratio of the fluxes observed in two different filters A and B is known as the colour:

$$C = m_A - m_B = -2.5 \log \frac{f_A}{f_B}, \tag{1.4}$$

where f_A and f_B are the fluxes into the two bands, and m_A and m_B are the corresponding magnitudes (defined as m_A = -2.5log $L_A/4\pi d^2$ +k , where d is the distance of the objects expressed in pc, and L_A is total energy output of the galaxy in the waveband A, i.e. the luminosity). According to the definition, the colour index is larger for galaxies that emit more light at

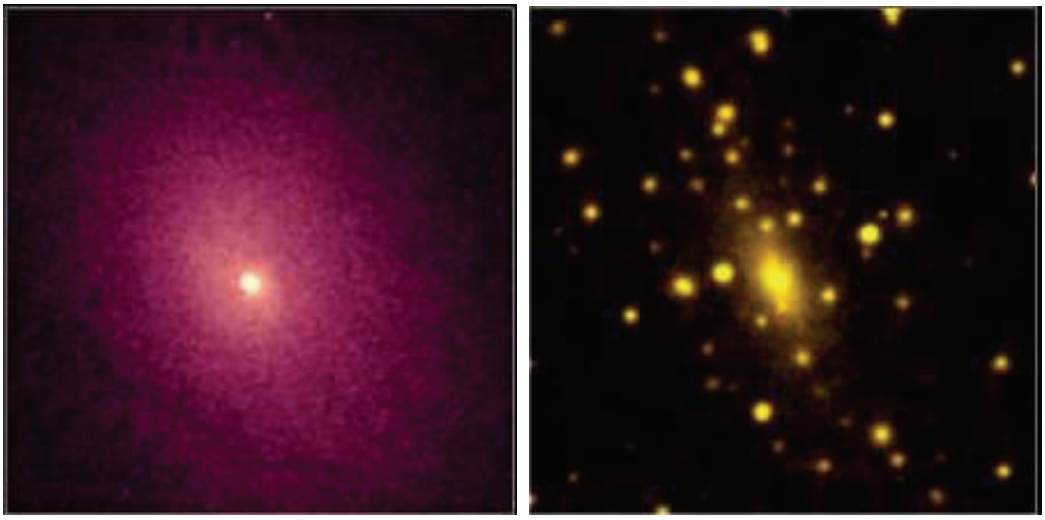

Figure 1.7: Galaxy cluster Abell 2029. In the optical waveband one can spot an extremely massive galaxy in the centre of the cluster (*right panel*). This galaxy strongly attracts the intracluster gas; the gas falling into the gravitational well emits huge amounts of the X-ray radiation due to the accretion (*left panel*).

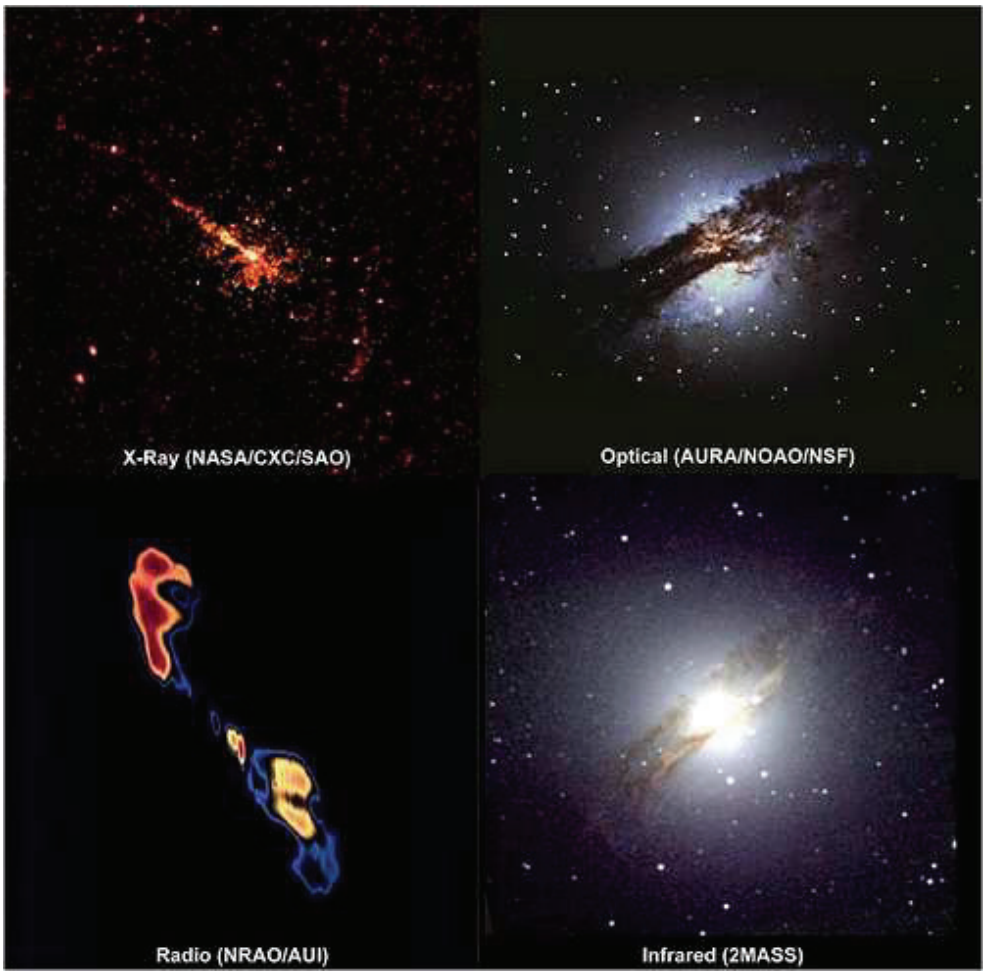

Figure 1.8: Centauri A radio galaxy, one of the most powerful sources of radio waves on the sky. In IR (*bottom right panel*) it is possible very clearly see through the dust hiding the centre of the galaxy at optical wavelengths (*top right panel*). X-ray (*top left panel*) and radio pictures (*bottom left panel*) show two jets of hot gas perpendicular to the galaxy's plane, not visible in the optical/IR/UV images.

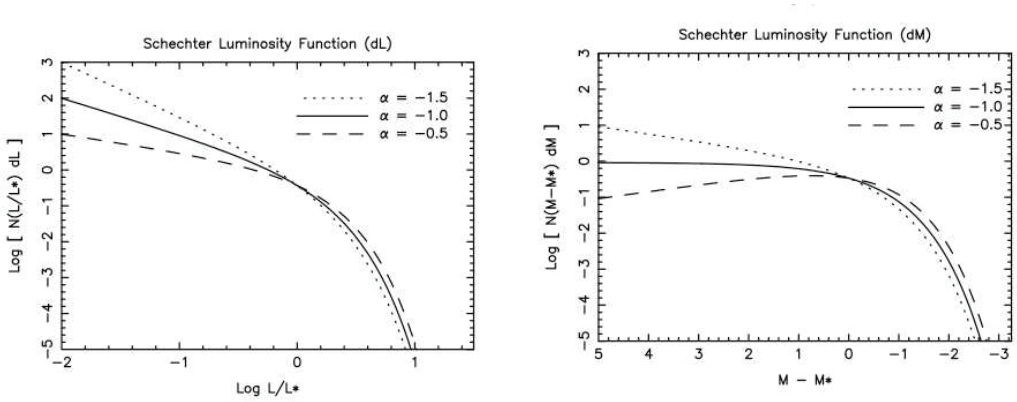

Figure 1.9: The luminosity function Φ expressed as function both of magnitude (right panel) and luminosity (left panel). In each panel are reported the Schechter function for three values of the parameter α: lower value of α corresponds to a steeper function.

longer wavelengths. Looking at galaxies we can see that some objects (see Fig. 1.2) look red, while other systems seem blue coloured (see Fig. 1.3). The colour index can give us a quantitative measure of this evidence.

Luminosity Function

Given a waveband, the luminosity function $\Phi(M)$ (LF, see Fig. 1.9), gives the number of galaxies per unit volume as a function of magnitude M. An efficient parametrisation of the LF was proposed by Schechter (1976) whereby:

$$\Phi(M) = (0.4 \ln 10)\Phi^* 10^{0.4(\alpha+1)(M^*-M)} \exp(-10^{0.4(M^*-M)}), \qquad (1.5)$$

but the formula assumes a simpler form if it is expressed as function of luminosity L:

$$\Phi(L) = (\Phi^*/L^*)(L/L^*)^\alpha \exp(-L/L^*). \qquad (1.6)$$

The function has two parts: a power law ($\Phi \propto \mathrm{L}^\alpha$) that dominates at low luminosities (L$\ll$L*) and an exponential cutoff ($\Phi \propto \mathrm{e}^{-L}$) that dominates at high luminosities (L>L*): L* is the luminosity value at which occurs the transition from the exponential growth and the power law. α is a parameter that determine the faint end slope (see Fig. 1.9) and Φ^* is a normalization factor.

1.1.4 Galaxy mass

Elliptical galaxies

Elliptical galaxies span a wide range of mass and luminosity from the gigantic cD galaxies, through normal and dwarf ellipticals, to the least massive galaxies in the Universe, the dwarf spheroidals.

- **cD ellipticals**
  cD galaxies are gigantic structures, with diameter up to $\sim$ 1Mpc, found at the centre of cluster of galaxies. They are characterized by a central component that resembles an elliptical galaxy with a surrounding diffuse halo made of stars whose surface brightness is lower than the central component. The magnitude of this objects can reach M_B = -25 and their mass $10^{14}M_\odot$.

- **Normal ellipticals**
  Normal ellipticals galaxies show strong stellar concentrations in the central regions, which can produce luminosities as high as M_B = -23. The mass of these systems can reach $10^{13}M_\odot$. Their light profiles are well described by Sersic law with n >2.

- **Dwarf ellipticals**
  Dwarf ellipticals are strongly different from the "normal" elliptical being much more compact and of lower luminosity. The surface brightness distribution can be described by a Sersic profile with n <2, indicating the presence of a shallow potential well. The total mass can reach $10^9M_\odot$ and the dimension does not exceed 10 kpc.

- **Dwarf spheroidals**
  Dwarf spheroidals are the lowest mass galaxies in the Universe, and while they may have extremely low luminosities (reaching $M_V \sim -3$) and surface brightnesses, they appear to have a minimum DM halo mass of $\sim 10^7M_\odot$.

Spiral galaxies

Differently from elliptical galaxies, spiral galaxies do not cover such a wide range of total mass, spanning from $10^9M_\odot$ to $10^{12}M_\odot$, against the seven orders of magnitude cover by ellipticals from $10^7M_\odot$ $10^{14}M_\odot$ but, on the contrary show strong differences in dimensions. In fact, the dimension of the disk can vary from 5 kpc of diameter to 100 kpc. However, for spiral galaxies it is necessary to distinguish between the bulge component and the disc. The

Figure 1.10: A small group of galaxies.

surface brightness distribution of the bulge follows a de Vaucouleurs' profile, while the disk is well described by an exponential law.

1.1.5 Galaxy environment

Galaxies are not distributed uniformly across the Universe, but belong to structures deeply different for density, shape, photometric and dynamic properties: from the enormous *voids* in which the number density of galaxies is greatly depleted, to the *field* where galaxies are relatively isolated, to rich and complex hierarchies of structures that includes: binary systems with two galaxies bound gravitationally each other; small groups of a few close galaxies (see Fig. 1.10), and clusters of galaxies (see Fig. 1.11), the densest regions of the universe, where 100–1000 galaxies are bound together by gravitational forces in a region of ∼3–6 Mpc in diameter. The differences between clusters and the field refers not only to the galaxy density, but also in how the galaxies are distributed. Indeed, in clusters, galaxies are distributed in a non homogeneous way being strongly concentrated towards the centre and with a number density decreasing toward the outer regions. Usually a cluster is defined an association of at least fifty objects whose luminosity lie

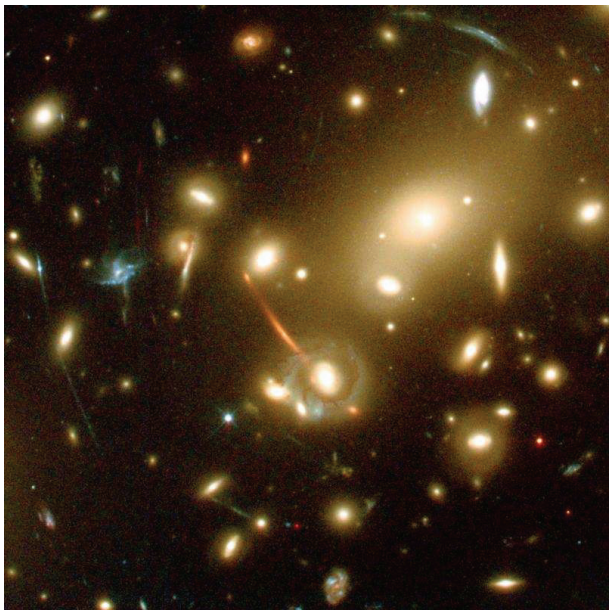

Figure 1.11: The cluster 2218.

within two magnitudes of the third brightest galaxy in the association.

Recent large surveys, such as the 2-degree Field Galaxy Redshift Survey (2dFGRS), the Sloan Digital Sky Survey (SDSS), and the Las Campanas Redshift Survey (LCRS) have shown, using statistically significant samples, that galaxies are distributed on filamentary-type structures (see Fig. 1.12; Bharadwaj et al. 2000) and superclusters (aggregation of clusters of galaxies), joined by filaments and walls of galaxies creating a foam-like structure of matter and gravitational potential. Voids within this foam can be as large as 50 Mpc across.

1.2 Mass and environmental dependence of galaxy properties

Despite the enormous differences observed within galaxy systems, in the last decade, many observations surprisingly have revealed that global properties of galaxies, such as colour, morphology, mean stellar age follow a bimodal distribution: less massive galaxies tend to be blue, star-forming discs and are commonly found in the field, while massive systems are mostly red spheroids with old stellar populations that dominate in cluster environments.

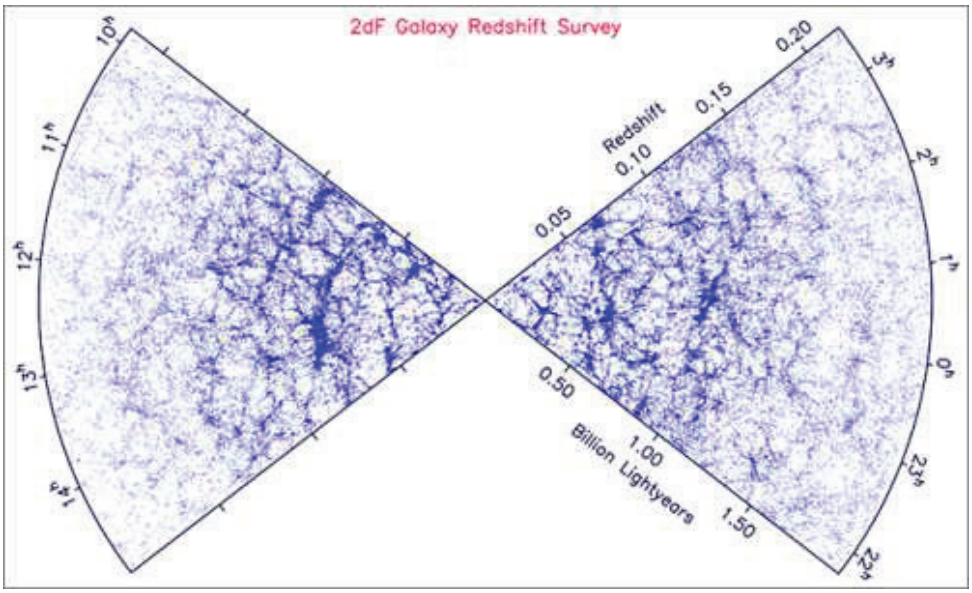

Figure 1.12: The large-scale structure as seen in the 2dFGRS.

1.2.1 Mass dependence

The characteristic mass scale which distinguishes the two families is $M_{crit} \simeq 3 \times 10^{10} M_{\odot}$ (Kauffmann et al. 2003b), which corresponds to a dark halo mass $M \leq 1 \times 10^{12} M_{\odot}$.

This bimodal behaviour of the galaxy population as function of mass is particularly evident in some relations such as the luminosity function, the scaling relations, and in particular features such as colour, morphologies, and the mean stellar age.

Luminosity function

Since the galaxy luminosity in optical and NIR bands is directly related to the stellar mass, the shape of the luminosity function provides direct information about the galaxy populations as function of mass. In particular the parametrization of the luminosity function, usually provided by the Schechter function, differs from different galaxy types and also environment.

Fig. 1.13 shows the LFs for galaxies in different environments, from rich clusters to the field, subdivided by morphological type. It seems that the LFs of the major galaxy types are different from each other, but are also relatively independent of environment: it is the variation in the relative proportions of

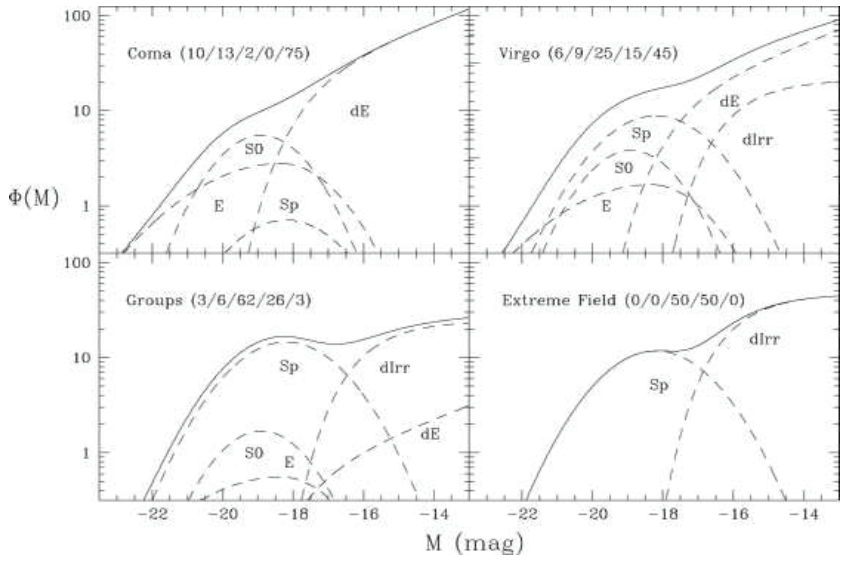

Figure 1.13: The luminosity function for different morphological types computed in different environments. The solid curves represent the total LF. The number in each panel represent the number of E, S0, Sp, dIrr, dE galaxies respectively from left to right.

each galaxy type between cluster and field regions that produces the peculiar characteristics of the total LFs for each environment.

The studies of the LF have shown that the bright end is mostly populated by red galaxies and, on the contrary, the faint end is principally dominated by blue systems: the luminosity value at which this sharp transition occurs is slightly below L^* which corresponds to a stellar mass $\sim 2M_{crit}$ (Dekel & Woo 2003).

Colour-Magnitude diagram

In the plane of observed colour and absolute magnitude, galaxies populate two distinct areas: the red sequence and the blue cloud, with an optimal colour separator of $u - r = 2.22$ (e.g. Strateva et al. 2001 in the SDSS, see Fig. 1.14). The red sequence is defined roughly by early-type galaxies (e.g Tully et al. 1982; Strateva et al. 2001). Along this red sequence, integrated colours of galaxies become progressively redder at bright magnitudes. Late-type galaxies, instead, populate the wider and more dispersed blue cloud. From the analysis of a low-redshift sample of galaxies from the SDSS covering an area 24 times wider than those studied by Strateva et

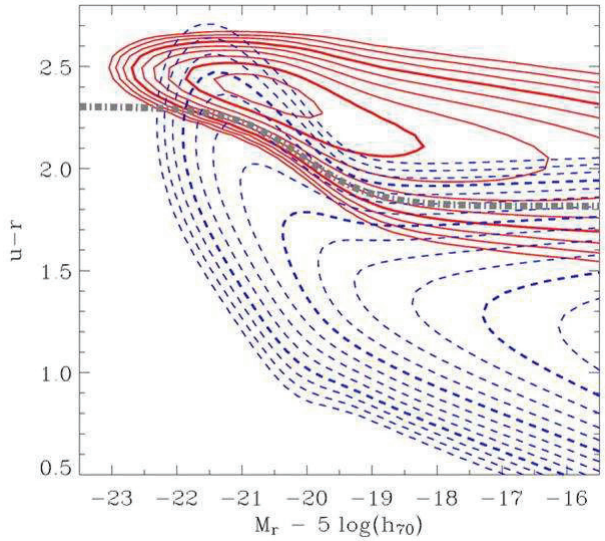

Figure 1.14: The colour-magnitude diagram. The solid contours represent the red distribution, while the dashed contours represent the blue distribution (*Baldry et al.* 2004).

al. (2001) (2400 deg^2, $0.004 < z < 0.08$, -23.5 $< M_r <$ -15.5), Baldry et al. (2004) confirmed that the colour distribution of galaxies (Fig. 1.15 and Fig. 1.16) can be approximated by a *bimodal* function made by the sum of two Gaussian functions. This trend is evident across seven magnitudes. Moreover they found that both red and blue sequences can be well fitted by a straight line plus a tanh function. By computing the stellar mass, they found that the point of transition from linear to tanh regime is around 2×10^{10} $M_\odot$. In addition, they found that the number density per magnitude of the red distribution overtakes the blue distribution at about 3×10^{10} $M_\odot$ in perfect agreement with the value found by Kauffmann et al. (2003b) using spectroscopic indicators.

Age and metallicity of stellar populations

Galaxy spectra constitute a mine of information about the properties of stellar populations, such as the age, metallicity, chemical composition and star-formation history. By comparing observed spectra and, in particular, the equivalent widths of absorption and emission lines to synthetic spectra from models of simple stellar populations (SSPs), it is possible to obtain information of these stellar population parameters.

For example, the strong absorption of Balmer lines (Hβ, Hδ) is char-

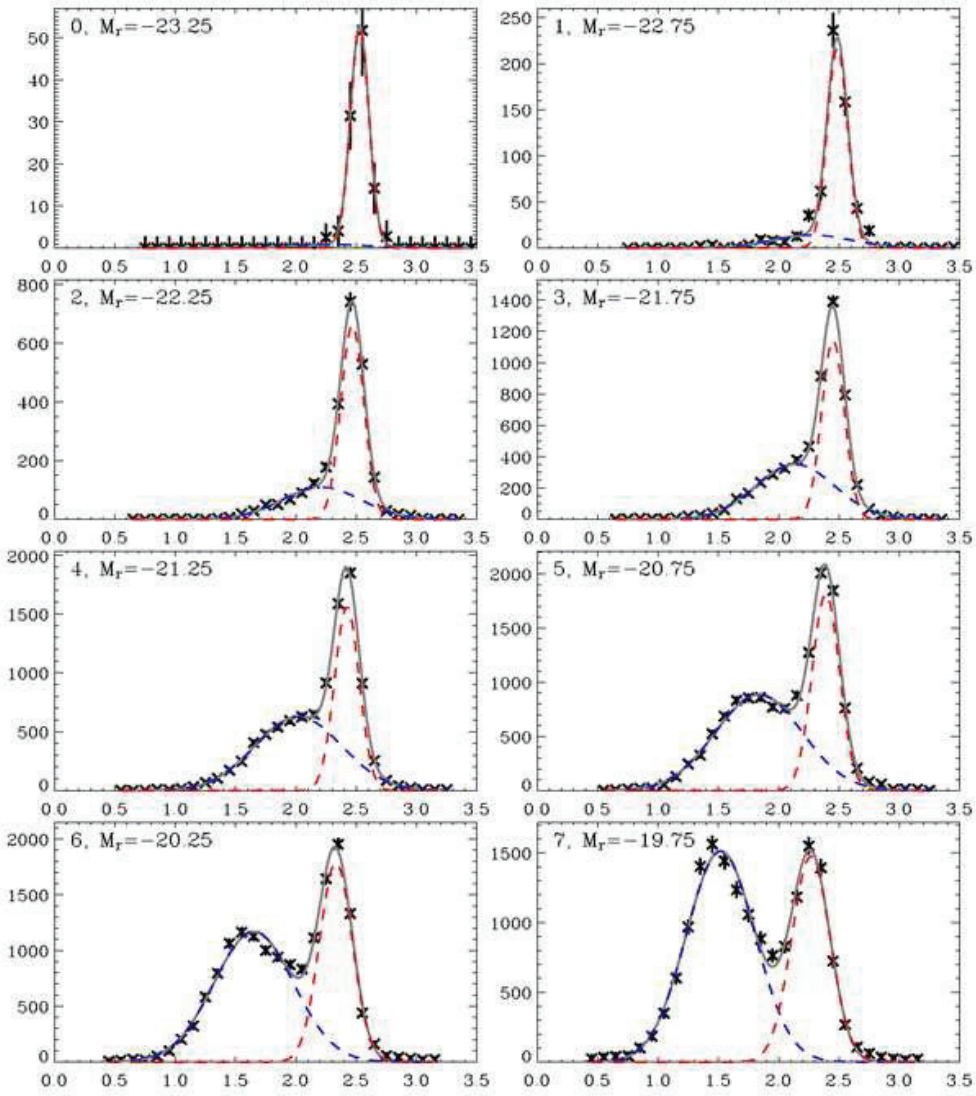

Figure 1.15: Colour distributions in absolute magnitude bins of width 0.5. Each plot shows galaxy number counts vs. rest-frame $u - r$ colour. The solid lines represent double-Gaussian fits, while the dashed lines represent the single Gaussians of the blue and red distributions (*Baldry et al.* 2004).

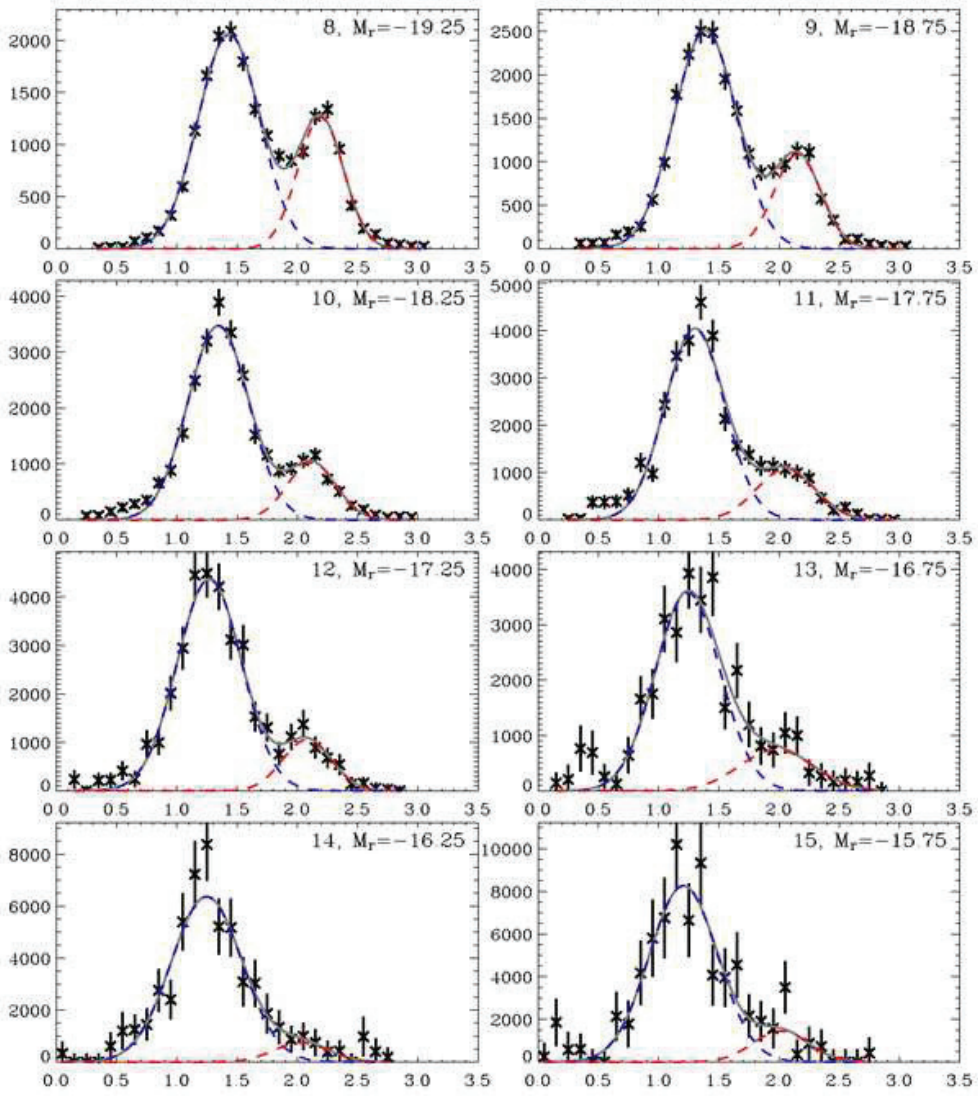

Figure 1.16: The same of Fig. 1.15 (*Baldry et al.* 2004).

acteristic of A-type stars, and stellar populations dominated by a burst of star-formation that ended $\sim$ 0.1-1 Gyr ago, i.e. at an age when A-type stars dominate the optical emission of SSPs. Hence high value of Hδ are indicative of recent star-formation while low values characterize galaxies with old stellar populations (Kauffmann et al. 2003b).

The index $D_n(4000)$ is the measure of the discontinuity observable at 4000Å in the spectrum. The break occurring at 4000Å is the strongest discontinuity in the optical spectrum due to the accumulation of many spectral lines in a narrow wavelength range. The principal contribution to the opacity of stellar photospheres comes from the ionized metals. In hot stars, due to their high temperatures, the elements are multiply ionized and the opacity decreases, so the 4000Å break will be small for young stellar populations and larger for old and metal-rich galaxies. The first definition of D(4000) was due to Bruzual (2003) and was defined as the ratio between the average flux density in the bands 4050–4250Å and 3750–3950Å, but in 1999 Balogh et al. proposed a new definition ($D_n(4000)$) using narrower band: 3850–3950Å and 4000–4100Å. The principal advantage to use $D_n(4000)$ instead of D(4000) is that the first is less sensitive to the effects of reddening.

The analysis of Kauffmann et al. (2003b) of $\sim$ 122000 galaxies from the Sloan Digital Sky Survey highlighted the bivariate distribution of mean stellar age as function of stellar mass (M_*). In Fig. 1.17 are reported the density distributions of $H\delta_A$[1] and $D_n(4000)$ as function of logarithm of stellar mass.

The grey-scale indicates the fraction of galaxies in a given logarithmic mass bin that fall into each age-indicator bin. The contours are separated by factors of two in population density. It shows the clear strong bimodality between stellar mass and mean stellar age: massive galaxies are characterized by older stellar population having typically lower values of $H\delta_A$ and higher values of $D_n(4000)$. At a mass value $\simeq M_{crit}$ a transition towards younger stellar populations beings to take effect.

Galaxy bimodality is observed also in the relation involving metallicity Z. As first observed by Lequeux et al. (1979), metallicity is strongly dependent on galaxy stellar mass, such that more massive galaxies are more metal rich. Using large datasets from optical surveys such as SDSS, more recent analyses have studied the luminosity-metallicity and mass-metallicity correlations (e.g Pilyugin & Ferrini 2000; Lee, McCall & Richer 2003; Tremonti et al. 2004; Shapley et al. 2005; Lee et al. 2006). Tremonti et al. (2004) for galaxies of $M_{crit} < M_* < 10^{12}$ $M_\odot$ found that $Z \propto {M_*}^{0.5}$, while for 10^8 $M_\odot < M_* <$ M_{crit} the correlation disappears being $Z \simeq$ constant in the entire low mass

[1]Following Worthey & Ottaviani (1997) the $H\delta_A$ index is defined using a central bandpass bracketed by two pseudo-continuum bandpasses.

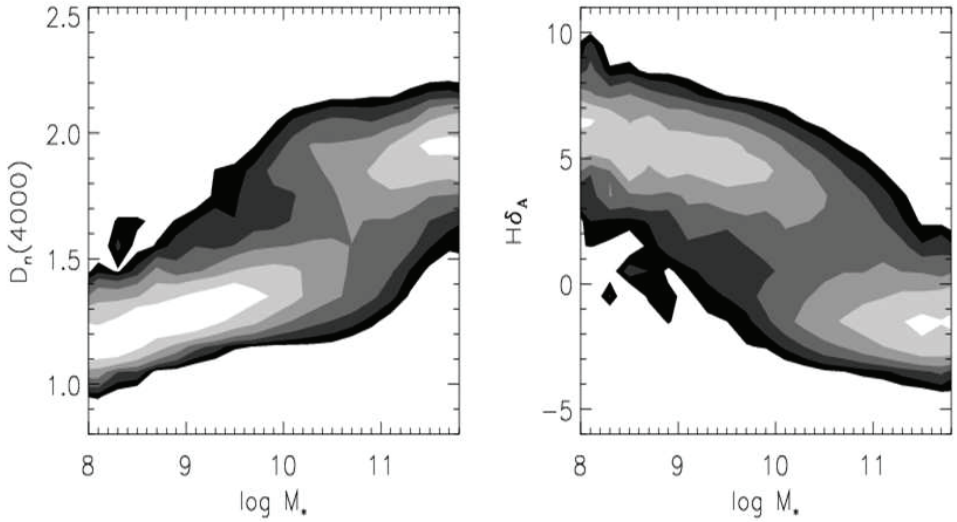

Figure 1.17: The density distribution showing trends in the stellar age indicators $D_n(4000)$ and $H\delta_A$ as functions of the logarithm of stellar masses (*Kauffmann et al.* 2003b).

range. The observed relation show a significant scatter, with only half of the spread due to measurement errors: Tremonti et al. (2004) analysing the correlations between the scatter and other galaxy properties point out a potential connection with stellar surface mass density, μ_*, such that galaxies with higher surface densities are more metal rich relative to galaxies of similar stellar mass.

Morphology

In the same work Kauffmann et al. (2003b) showed that also the distribution of galaxy luminosity "concentration" C as function of stellar mass is bimodal (see Fig. 1.18), and they interpreted this trend as a correlation between stellar mass and morphology. Following previous work (e.g. Blanton et al. 2001; Shimasaku et al. 2001) they defined the concentration index C as the ratio $R90/R50$, where $R90$ and $R50$ are the Petrosian radii containing 90% and 50% of Petrosian r-band light distribution. Strateva et al. (2001), using a by-eye morphological classification, showed that there is a strong correlation between C and galaxy type, whereby systems with C<2.6 are preferentially late-type, while galaxies with C>2.6 are mostly early-type. Fig. 1.18 shows that for galaxies with $M_* < M_{crit}$, C is nearly indepen-

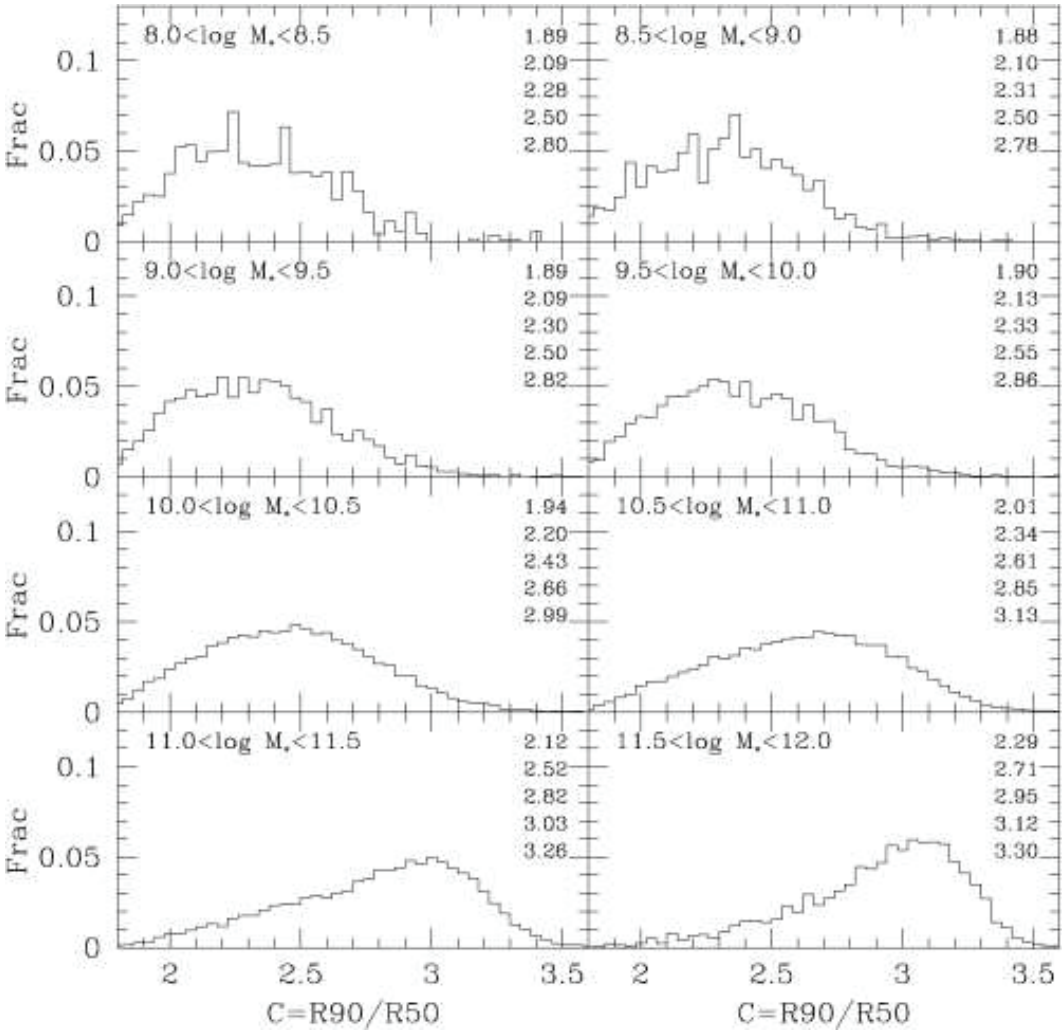

Figure 1.18: Histograms showing the distribution of galaxies as a function of C index for eight different ranges of stellar mass. The number in each panel list, from top to bottom, the fifth, 25th, 50th, 75th and 95th percentiles of the distribution (*Kauffmann et al.* 2003b).

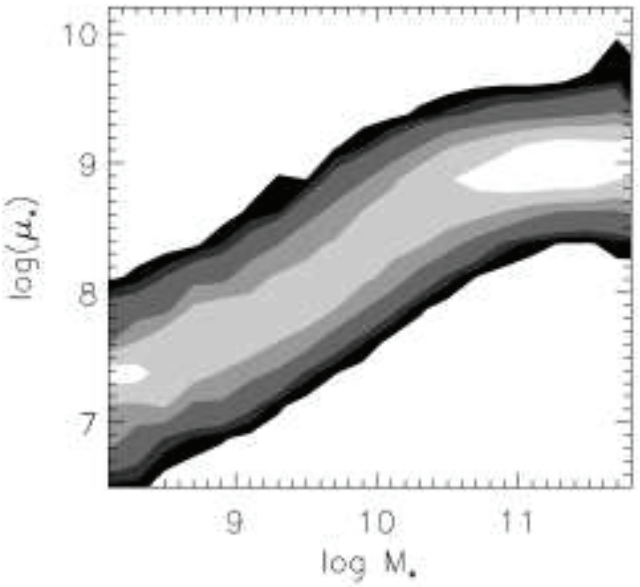

Figure 1.19: Density distribution showing trend between the structural parameter μ_* and stellar mass (*Kauffmann et al.* 2003b).

dent of mass with a median value of $\sim$ 2.3: only about 10% of low-mass galaxies have C>2.6. When higher mass bins are considered, the distribution shifts towards higher C values: in the most massive bin more than 90% of galaxies have C>2.6. This result implies that, in general, the bulge-to-disk ratio is observed to gradually decrease with decreasing M_*: galaxies in the blue cloud with $M \leq M_{crit}$ are disc-dominated, while massive galaxies in the red sequence are principally spheroids. On the contrary an increasing trend of gas-to-stellar ratio (e.g. Longmore et al. 1982, McGaugh & de Blok 1997) and a younger, bluer stellar population (e.g. de Blok, van der Hulst & Bothun 1995; McGaugh, Schombert & Bothun 1994; Sprayberry et al. 1995) are detected with decreasing M_*: at a given M_* the galaxies with lower bulge-to-disk ratios tend to have younger stellar ages.

Surface mass density

Strong differences in the behaviour of galaxies with masses above or below the critical value M_{crit} are also visible in the relation connecting the stellar mass to the surface mass density μ_*. Fig. 1.19 (Kauffmann et al. 2003b) shows the bivariate distribution of relatively bright galaxies in the plane of μ_* and stellar mass up to the completeness limit of r = -17 and μ_e = 23 mag

arcsec^{-2}. The surface mass density μ_* is defined as $0.5M_*/[\pi R50^2(z)]$, where $R50(z)$ is the Petrosian half-light radius in the z band. The bright galaxies in the mass range $M_{crit} < M_* < 10^{12}$ $M_\odot$ have surface mass densities scattered around the mean value $\mu \sim 10^9$ $M_\odot$ kpc^{-2}, with only a weak systematic trend of $\mu_* \propto {M_*}^{0.2}$. On the other end, the correlation in the range 10^8 $M_\odot$ $< M_* < M_{crit}$ is well represented by $\mu_* \propto {M_*}^{0.6}$. Woo, Courteau & Dekel (2008) analysing ∼40 dwarf galaxies in the Local Group, extend this tight correlation in the range $6\times10^5 < M_* < 10^{10}M_\odot$ finding $\mu_* \propto {M_*}^{0.55\pm0.03}$ in agreement with Kauffmann et al. (2003b). Similar relations were found also by Blanton et al. (2003a) for a sample of 144609 SDSS galaxies.

1.2.2 Environmental dependence

Global properties of galaxies are not only related to their mass, but also to the environment in which the galaxies inhabit. An impressive number of spectroscopic and photometric results reveal that properties such as the colours, morphologies and star-formation histories of galaxies in clusters are significantly different from those in field (e.g. Dressler et al. 1985; Couch et al. 1994; Balogh et al. 1997; Dressler et al. 1999; Poggianti et al. 2004)

The morphology-density relation

The first large scale study of morphological segregation was performed by Dressler (1980), who defined the morphological type of ∼ 6000 galaxies belonging to 55 clusters. The analysis of Dressler confirms the previous results of Oemler (1974) whereby the fraction of spiral galaxies, f(S), decreases toward the cluster centre (see Fig. 1.20).

Moreover, from Fig. 1.20, subtler effects are also visible: the fraction of S0s, f(S0) increases with R, passing from $30 \pm 5\%$ at 0.075 Mpc from the centre to $54 \pm 7\%$ at 0.25 Mpc from the centre (Whitmore & Gilmore 1991). Early-type galaxies are the dominant population of clusters and are mostly in the centre following overall density distribution, while late-type galaxies form less than 20% of the total cluster population and are principally found in the outer regions. From these results, Dressler inferred that the distribution of the different morphological galaxy types in clusters is strictly correlated to density: he pointed out that the main relation is not between morphology and radius, but between morphology and density.

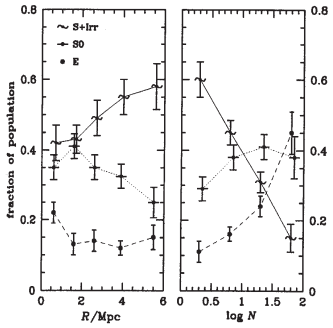

Figure 1.20: Fraction of galaxies for different morphological type as a function of distance from the centre R (left panel), and of density (right panel) (*Galactic Astronomy, Binney & Merrifield*).

The star-formation density relation

The star-formation properties of galaxies in rich clusters differ significantly from those of field galaxies (e.g. Osterbrock 1960; Dressler, Thompson & Shectman 1985; Balogh et al. 1997; Koopmann & Kenney 2004). In the field, the level of the star-formation in galaxies is several times higher than in systems of similar luminosity in the core of clusters. This is partly due to the morphology-density relation since elliptical and S0 galaxies, principally passive systems, are more abundant in clusters, but there is evidence that even later type galaxies in clusters form stars at lower rates than in the fields (Balogh, Navarro & Morris 2000). For example, Balogh et al. (1999) show that the [O II] equivalent widths, on average, are much larger for field galaxies then their counterparts in rich cluster with the same bulge-to-disk ratios and luminosities. One of the difficulties in inferring the star-formation rate from the [O II] emission is that it can be influenced by dust (Smail et al. 1999; Poggianti & Wu 2000). This limit can be overcome using the Hα index, which is less sensitive to dust effects (Kennicutt 1998). From the analysis of an Hα survey of galaxies in three clusters at $z \sim 0.3$, Couch et al. (2001) found that in one cluster the star-formation is strongly and uniformly suppressed, while, in general only 10% of galaxies show Hα emission, with an overall star-formation rate of ~ 4 $M_{\odot}yr^{-1}$. Similar results were found

by Balogh & Morris (2001) who found that only $\sim 12.5\%$ of galaxies in the cluster A2390 at $z = 0.23$ showed Hα emission.

The colour/luminosity-density relation

The distribution in colour depends strongly on the galaxy density on $\sim$1 Mpc scales (Dekel & Birnboim 2006): blue and red sequence galaxies tend to populate the low- and high-density environments respectively (Blanton et al. 2005a; Hogg et al. 2003; Balogh et al. 1997; Blanton et al. 2006; Kauffmann 2004).

Blanton et al. (2005) in the SDSS ($\sim$ 114000 galaxies) analysing (see Fig. 1.21) the distribution of g-r colour, mean surface brightness, Sersic index and luminosity found that galaxy colour is the most predictive property of local environment. Even if the dependence on luminosity appears more impressive, this dependence only affects a small fraction of the total number density of galaxies in this sample, and the dominant horizontal contours in the lower-right panel demonstrate that colour is in general more predictive than luminosity. For this reason, the pair colour and luminosity taken together can be considered the most predictive properties of local overdensities. At fixed colour and luminosity, density is not closely related to measures of galaxy structure – surface brightness of Sersic index, implying that the morphology-density relation is driven by the more fundamental colour-density relation.

Slightly different results were reached by Balogh et al. (2004) studing the $u - r$ and luminosity dependence on density for a sample of $\sim$ 25000 SDSS galaxies (see Fig. 1.22): at fixed luminosity, the mean colour of the blue/red distribution is roughly independent on environment; in contrast, at fixed luminosity the fraction of galaxies in red distribution as function of density changes drammatically passing from 10–30% in the low density regions up to $\sim 70\%$ in the high density regions.

Halo mass

The environment density is directly related to the mass of the underling DM halo. The halo occupation distribution (Yan, Madgwick & White 2003; Kravtsov et al. 2004; Abazajian et al. 2005) predicts that DM halos less massive than $\sim 10^{12}$ $M_\odot$ host one dominant galaxy, while more massive haloes tend to host groups or clusters of galaxies. The environment dependence hence implies a strong correlation with the mass of the host DM halo whose critical mass scale is $\sim 10^{12}$ $M_\odot$.

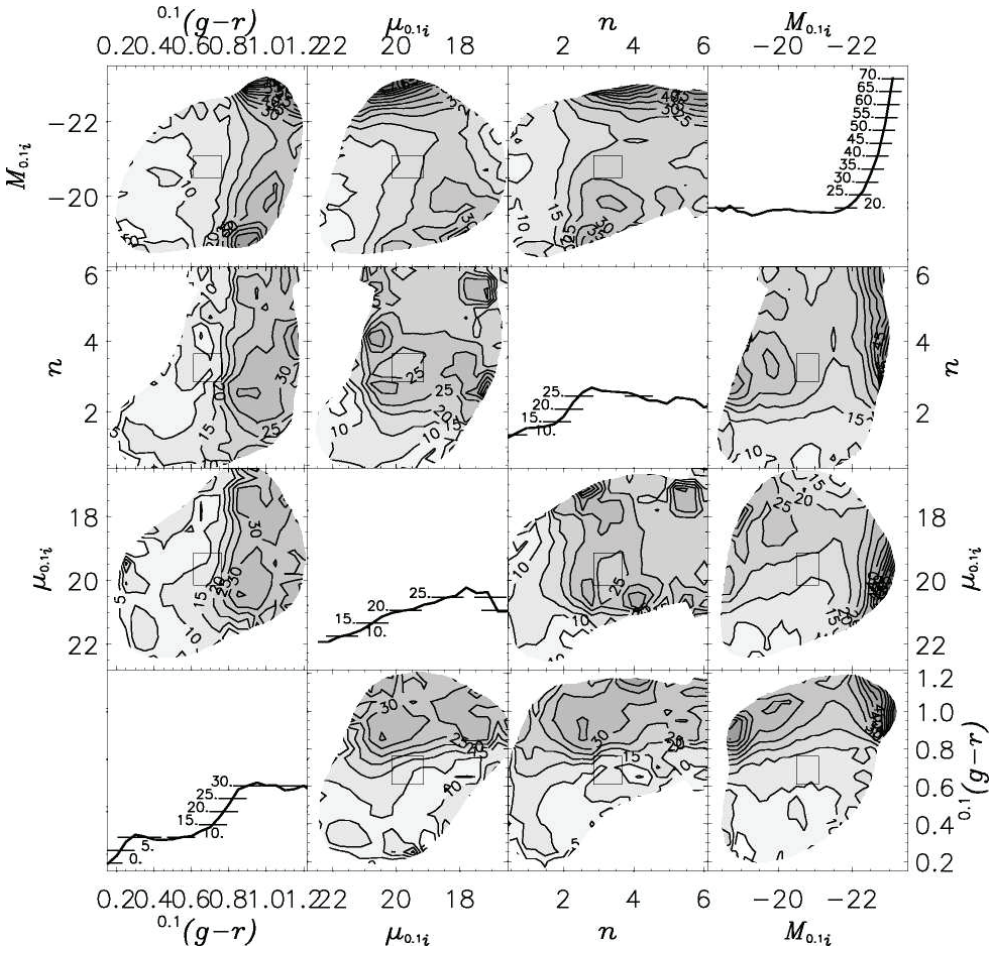

Figure 1.21: Mean local overdensity on 1 Mpc scales as a function of pairs of galaxy properties. Off-diagonals show the mean overdensity as a colour-coded contour plot in which darker areas indicate galaxies in denser environments. For example, in the lower-right corner, the blue, low-luminosity galaxies are on average in the least dense environments and the red, high-luminosity galaxies are on average in the most dense environments. Plots along the diagonal show the mean overdensity as a function of colour, surface brightness, Sersic index and magnitude on a linear scale. The mean is calculated in a sliding box with widths 0.15, 1.0, 0.8, and 0.6 in colour, surface brightness, Sersic index and absolute magnitude respectively (*Blanton et al.* 2005).

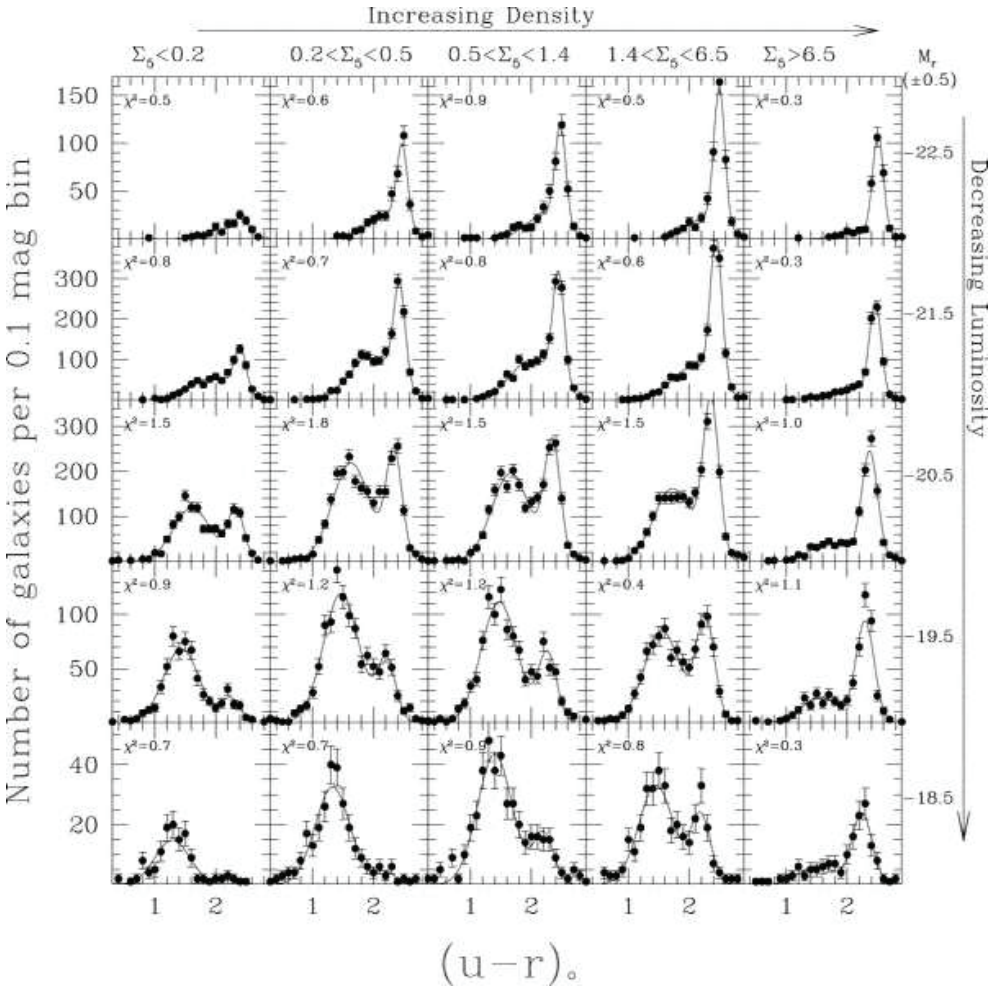

Figure 1.22: The solid points in each panel show the galaxy colour distribution for the indicated 1 mag range of luminosity (right axis) and the range of local projected density, in Mpc^{-2} (top axis). The solid line is the double Gaussian fit. The reduced χ^2 of the fit is reported in each panel (*Balogh et al.* 2004).

Considering both the galaxy properties (see § 1.1) and their bimodal distribution (see § 1.2), one of the most intriguing open questions of modern astrophysics is to know how do galaxies take shape and evolve: what is the origin of their diversity and scaling relations; why are they clustered in space following a sponge-like structure; and finally which are the physical processes that quench the star-formation and affect the structure of a galaxy, and are responsible of the sharp transition at M_{crit} between galaxies with $M_* > M_{crit}$ being preferentially red spheroids with old stellar population in cluster environments, and galaxies with $M_* \leq M_{crit}$ being mostly blue coloured discs, and in the field? To answer one or all of these questions is of fundamental importance to understanding the origin and evolution of galaxies.

1.3 Models of galaxy formation

The origin of cosmic structures, including galaxies of all types, is currently described through the dissipationless gravitational collapse in a Universe dominated by DM. Any model has to take as its initial conditions, the tiny fluctuations ($\sim$1 part in 10^5) in the cosmic microwave background, and grow via gravitational instability, firstly in the linear regime, and later non-linearly, forming by the present epoch the massive halos we see as galaxies and clusters, as well as the large-scale structure in which they are embedded. Within these DM halos, the baryonic component must also evolve to form the observed stars, galaxies and ICM.

The nature of DM is still a debated question. According to the composition of DM, the derived cosmologies are strongly different. In fact, the typical mass of density fluctuations is strictly dependent on the mass of DM particle: the smaller the particle is, the larger are the masses of the density fluctuations. This dependence has led cosmologists to classify hypothetical DM candidates into three broad categories (Bond et al. 1984): i) hot DM (HDM) made of low-mass particles like neutrinos (mass$\sim$10eV) in which massive ($M_{halo} \sim 10^{15} M_\odot$) halos collapse first, ii) warm DM (WDM) where the mass of a typical halo is $\sim 10^{11} M_\odot$ and, iii) cold DM (CDM) where the collisionless particles are so massive (10^2GeV) that fluctuations of all scales survive ($M_{halo} \sim 10^{-5} M_\odot$). From this picture it emerges that cosmology provides the theoretical framework for the initial and boundary conditions of the cosmic structure formation model and consequently for galaxy formation.

Starting from the preexisting DM model it is possible to construct a model for populating haloes of different mass with galaxies using simulations which take into account the dynamics of the DM and gas, star-formation, radiative cooling, and gas loss from galactic winds. Two main families of models may

be recognized:

- **the monolithic scenario** developed since the early work by Eggen et al. (1962) and Larson (1975), within which galaxies formed during a single event at very high redshift (z >3) through the gravitational collapse of proto-galactic gas clouds. For early-type galaxies, star formation ceases shortly after the collapse and the subsequent evolution of the galaxies is dominated by passive dimming of the stellar light. In this scenario, the massive galaxies are already in place very early, and hence are the oldest structures of the universe;

- **the hierarchical scenario** (White & Rees 1978) where massive galaxies have formed from smaller units through merging events. Less massive galaxies were the first objects to form at high redshift, while massive ellipticals and S0s have been slowly built up through many generations of mergers. This scenario predicts that the number of massive galaxies is larger at lower redshifts, as merging events form bigger and bigger objects.

The monolithic collapse hypothesis was able to produce the observed tightness of many scaling relations, such as the colour-magnitude relation and the fundamental plane, as well as the evolution of these relations with redshift (Kodama et al. 1998; van Dokkum & Stanford 2003). Moreover it well justifies the recent finding of galaxy objects at higher redshifts (z >2) with high star-formation rates (SFRs) such as Lyman break galaxies (LBG, star-bursting galaxies with SFRs of 10–1000 $M_\odot$/yr and masses of 10^9–10^{10} $M_\odot$), sub-millimeter (SCUBA) galaxies (strongly star-bursting galaxies with SFRs of ∼1000 $M_\odot$/yr obscured by dust), Lyman α emitters (galaxies with strong Lyman α lines which imply phases of rapid star-formation or strong cooling) and quasars (QSOs, visible up to z ∼6.5).

The monolithic collapse model for the formation of elliptical galaxies naturally produces the effect known as "cosmic downsizing" whereby the major epoch of star-formation occurs earlier and over a shorter period in the most massive galaxies and progressively later and over more extended time-scales towards lower mass galaxies. This has been confirmed observationally both in terms of the global decline of star-formation rates in galaxies since $z \sim 1$ (Noeske et al. 2007a,b) and in the fossil records of low-redshift galaxy spectra (Heavens et al. 2004; Panter et al. 2007).

Analysing the absorption lines of local quiescent galaxies, the most massive galaxies are found to have higher mean stellar ages and abundance ratios than their lower mass counterparts, indicating that they formed stars earlier and over shorter time-scales (Thomas et al. 2005; Nelan et al. 2005).

In this scenario, the mass-scale at which a galaxy becomes quiescent should decrease with time, with the most massive galaxies becoming quiescent earliest, resulting in the red sequence of passively-evolving galaxies being built up earliest at the bright end (Tanaka et al. 2005). It was previously thought that these effects could be considered the direct consequence of the deeper potential wells of giant galaxies, which accelerates the collapse of gas into stars.

However, in the last decades, some problems have arisen with this scenario: the ubiquitous presence of fine structure such shells, ripples, tidal plumes, nuclear light excesses, and kinematic subsystems in ellipticals (e.g. Schweizer & Seitzer 1992; Schweizer 1996) are interpreted as clear signatures of merger events. Moreover, considerable observational evidence indicates that the most massive starbursts, ultraluminous galaxies (ULIRGs), are always associated with mergers (e.g Sanders & Mirabel 1996), with dense gas in their centers providing material to feed black hole growth (Hopkins et al. (2008)); in the same way submillimeter galaxies and quasars are found to be triggered by merger events (for reviews see Barnes & Hernquist 1992; Schweizer 1998; Jogee 2006). However the strongest evidence in favour of the hierarchical scenario comes from the development of numerical simulations during the last 20 years.

Numerical simulations (e.g. di Matteo et al. 2005) have shown that major mergers of two gas-rich disk galaxies can produce elliptical galaxies (see §1.4.2): tidal torques developed during a merger, lead gas to fall into the centers of galaxies (Hernquist 1989; Barnes & Hernquist 1991, 1996) triggering sturbursts and feeding central black hole growth (Mihos & Hernquist 1994, 1996). Starbursts consume a great part of the gas in the galaxy and the remaining part is expelled through galactic winds and feedback from the black hole, producing red elliptical galaxies. However it is necessary to highlight some restrictions of this model: a major merger with masses ratio below $\sim$ 3:1 is required in order for the tidal torques to induce such a strong central inflow of gas that is able to modify the morphology. The great quantity of higher mass-ratio mergers (e.g. 10:1) show that gas inflows can be induced under some circumstances (e.g Hernquist 1989; Hernquist & Mihos 1995; Bournaud et al. 2005), but detailed studies indicate that this is limited to specific orbital geometries (Younger et al. 2008), and that the efficiency decreases with the increasing mass ratio. The results of these higher mass-ratio mergers could be a galaxy made by a central component like a spheroid surrounded by a surviving disk structure. However, it has to be emphasized that only mergers can reproduce the observed kinematic properties of elliptical galaxies and classical bulges (Hernquist 1989, 1992, 1993; Barnes 1988,

1992; Schweizer 1992; Naab & Burkert 2003; Bournaud et al. 2005; Naab et al. 2006a, 2006b; Naab & Trujillo 2006; Jesseit et al. 2007; Cox et al. 2006). Other processes such as harassment (see §1.4.3) may be able to produce spheroid component, but the analysis of these structures show that are characterized by different kinematics and properties from those observed for elliptical galaxies. An open debate in the merger scenario is the further disk formation around the elliptical through the subsequent accretion and cooling of gas as their host DM halos grow. Are elliptical galaxies able to quench their star-formation definitively by themselves or other external processes are needed to halt this mechanism?

The monolithic and hierarchical scenarios of formation of galaxies are well collocated into two "contradictory" cosmological models. The top-down monolithic scenario is consistent with a HDM model where massive haloes, in which elliptical galaxies form, develop first, while the hierarchical scenario is better reconciled with a CDM model where small objects would form first in the low-mass halos predicted in this cosmology, non-linearly interact, and merge to form larger halos which can then host massive galaxies (de Freitas Pacheco, Michard & Mohayaee 2003). The confrontation of the model predictions with astronomical observations have become the most powerful testbed for cosmology. In the last years, the CDM model plus a dark energy field (indicated by Λ), i.e. the well known ΛCDM model is the most accredited cosmological model since, among the others, nicely integrates i) cosmological theories (Big Bang and Inflation), ii) the cosmic microwave background, iii) the large-scale structure of the Universe (Springel et al. 2005c, see Fig. 1.23). The results of these simulations with observational evidence, seem to suggest the hierachical scenario as the most plausible for galaxy formation. In this scenario galaxy disks are envisioned to form as the result of gas accreted smoothly from the intergalactic medium (Katz & Gunn 1991), while the merger of disks is the process responsible for the formation, both of elliptical galaxies and the bulge components of spiral galaxies (Toomre 1977).

At first sight, one of the most major problems with the hierarchical scenario seems to be the observed downsizing. If massive galaxies are formed later, they should be also the youngest systems of the Universe. Chiosi & Carraro in 2002, by means of N-body-tree-SPH simulations incorporating cooling, star-formation, energy feedback and chemical evolution studied the SFR as a function of time for different masses as shown in Fig. 1.24. Massive galaxies are characterized by a single episode of star-formation very early in the past, while dwarf galaxies show irregular and intermittant star-formation which is prolonged over wide time intervals. Similar results were found by De Lucia et al. (2006), from the analysis of the Millennium simulation: they find

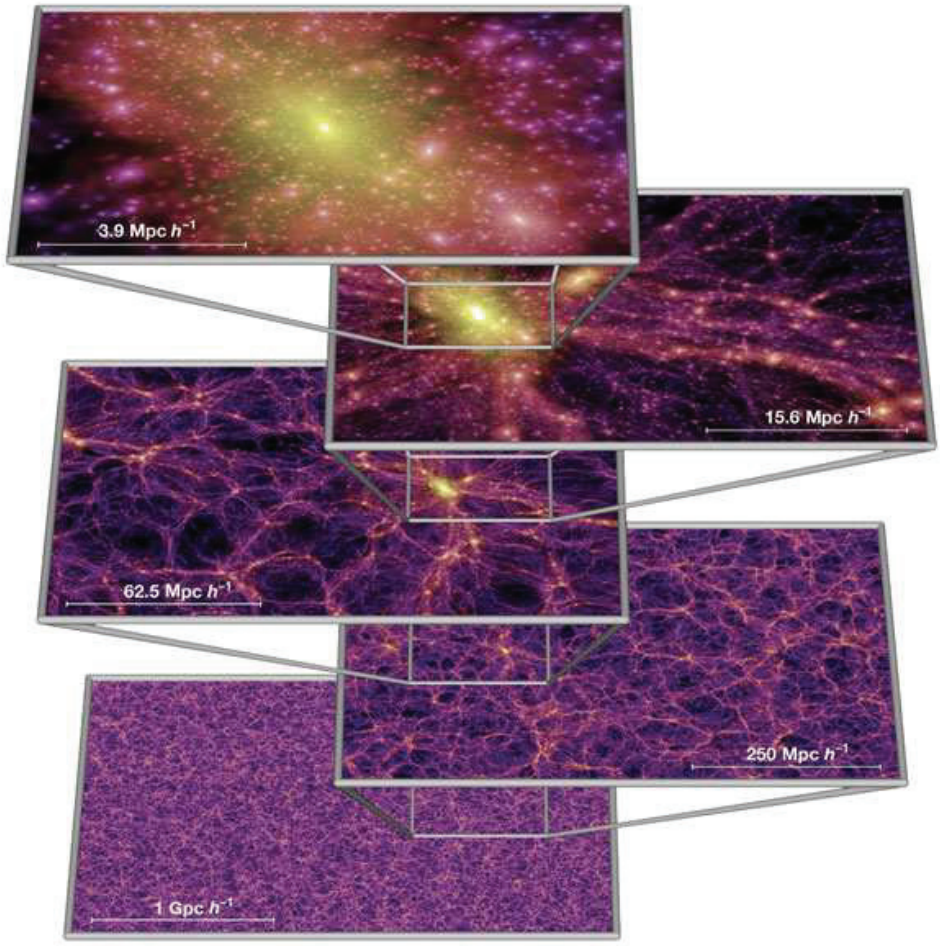

Figure 1.23: The DM density field on various scales from the Millennium simulation, the largest high-resolution simulation of cosmic structure growth ever carried out (2160^3 particles, analyzed from z=127 in a cube of 2230 billion light-years on a side, Springel et al. 2005c). Each individual image shows the projected DM density field in a slab of thickness $15h^{-1}$ Mpc, colour-coded by density of the DM distribution (*Springel et al.* 2005c).

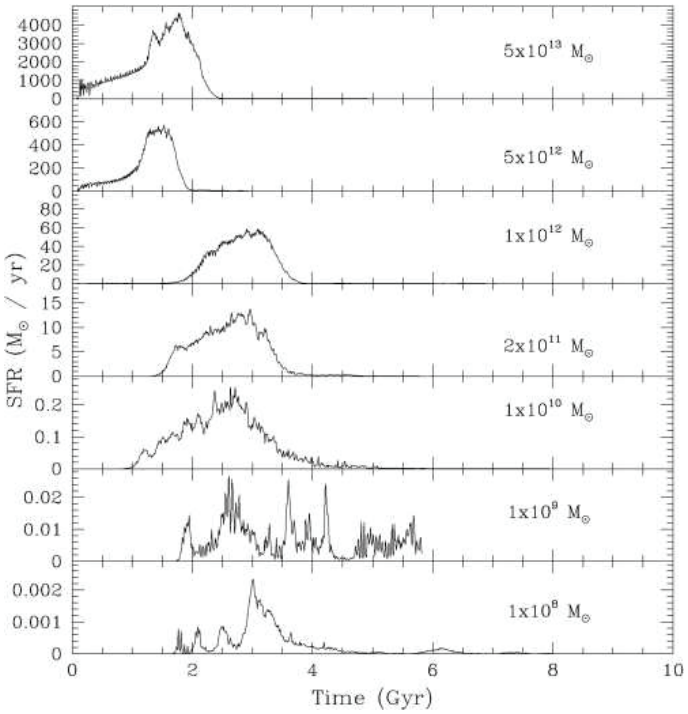

Figure 1.24: Star-formation histories for massive galaxies (top) down to dwarf galaxies (bottom) (*Chiosi* & *Carraro* 2002).

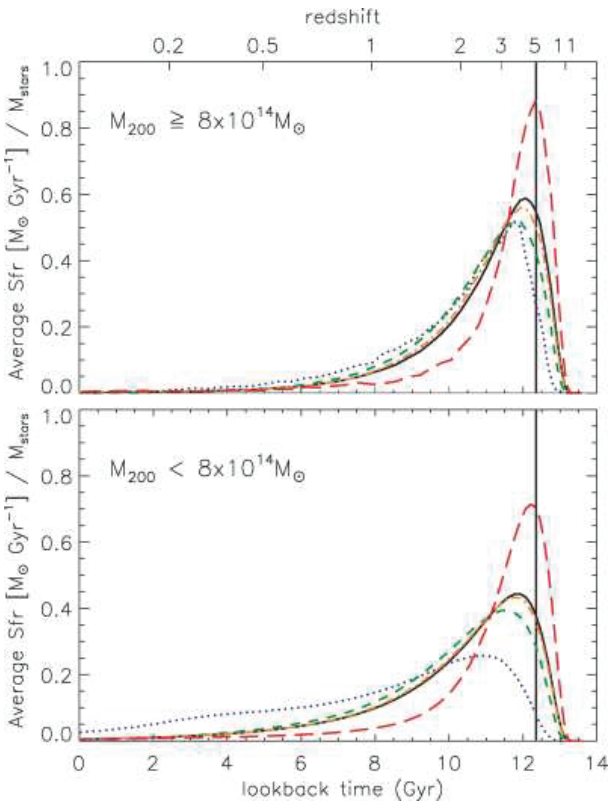

Figure 1.25: the average star-formation rate for elliptical galaxies in Millennium simulation both in "cluster" (top panel) and "field" environments (bottom panel). The different colours represent elliptical galaxies with different masses (red, yellow, green, and blue lines correspond to stellar masses of $\simeq 10^{12}$, 10^{11}, 10^{10} and $10^{9}M_{\odot}$ respectively) (*De Lucia et al.* 2006).

that massive galaxies are systematically older than less massive systems and convert gas into stars at higher level of efficiency. Fig. 1.25 shows the average star-formation rate for elliptical galaxies in the Millennium simulation both in "cluster" environment (top panel) and "field" environments (bottom panel). The different colours represent ellipticals galaxies with different masses (red, yellow, green, and blue lines correspond to stellar mass of $\simeq 10^{12}$, 10^{11}, 10^{10}, and $10^{9}M_{\odot}$). The most massive elliptical galaxies have star-formation rates that peak at higher redshift (z$\sim$5) and are characterized by higher levels of star-formation. The result is visible both in clusters and field, even if, due to the deeper potential wells, in clusters the star-formation rates are higher on average, and the time-scales over which the processes to form stars act, are shorter. Although downsizing appears at first sight to be at odds with

the standard hierarchical model for the formation and evolution of galaxies, Merlin & Chiosi (2006) are able to reproduce the same downsizing as seen in the earlier "monolithic" models in a hierarchical cosmological context, resulting in what they describe as a revised monolithic scheme whereby the merging of substructures occurs early in the galaxy life ($z > 2$). Conselice et al. (2006), using N-body simulations to study this early merging find that massive galaxies at $z \sim 3$ with $M > M^{10} M_{\odot}$ undergo $4.4^{+1.6}_{-0.9}$ major mergers at $z > 1$, while most of them undergo no mergers for $z < 1$.

To understand this apparent contradiction, it is important to distinguish between the epoch in which most of galaxy stars are formed, and the age in which galaxy spheroid acquired its dynamical properties through mergers. For the monolithic scenario these two epochs are coincident. Instead in the hierarchical scenario, a galaxy can be assembled recently, and so resulting in a young system when referred to its assembling history, yet the merging could involve galaxies with already old stars, and hence appearing old when referred to their stellar populations. De Lucia et al. (2006) show that for galaxies more massive than $10^{11} M_{\odot}$ the median redshift when half of the stars were formed is ~ 2.5, while for the same sample, the median redshift in which half of the stars were assembled in a single object is ~ 0.8.

Despite all of this observative evidence in favour of the hierarchical scenario, intriguing questions remain still open, such as the well known problem of the galaxy luminosity function (Benson et al. 2003). If no feedback processes are included in the formation and evolution of galaxies, the halo mass function deviates from the observed galaxy luminosity function at both ends (see Fig. 1.26). Why we do not find so many dwarf galaxies as predicted by the cosmology?, and why, on the other side, are there not massive galaxies greater than a certain mass? Different mechanisms have been proposed: at the faint-end the absence of dwarf galaxies is thought to be due to the energy injection from supernovae and stellar winds, and to the photoionization of pre-galactic gas at high redshifts, which make galaxy formation inefficient in small halos (Benson et al. 2003). However, this justification enlarges the problem at the massive end, since the heated gas that hasn't condensed onto dwarf galaxies can eventually cool onto massive haloes giving rise to an excess of bright galaxies that is not observed. In this case the proposed scenario can be summarized as the presence of a heating conduction at the center of massive halos and/or to superwinds. Unfortunately, no one of these scenarios is totally satisfactory since the heating source should have an implausibly high efficiency, while the supernovae explosions are not so powerful to prevent the cooling of gas. One of the recent scenario which receiving consent is the injection of energy from the central AGN. The underlying idea is based on the relation between M_{BH} and M_{bulge} whereby $M_{BH} \propto M_{bulge}$ (e.g. Ferrarese &

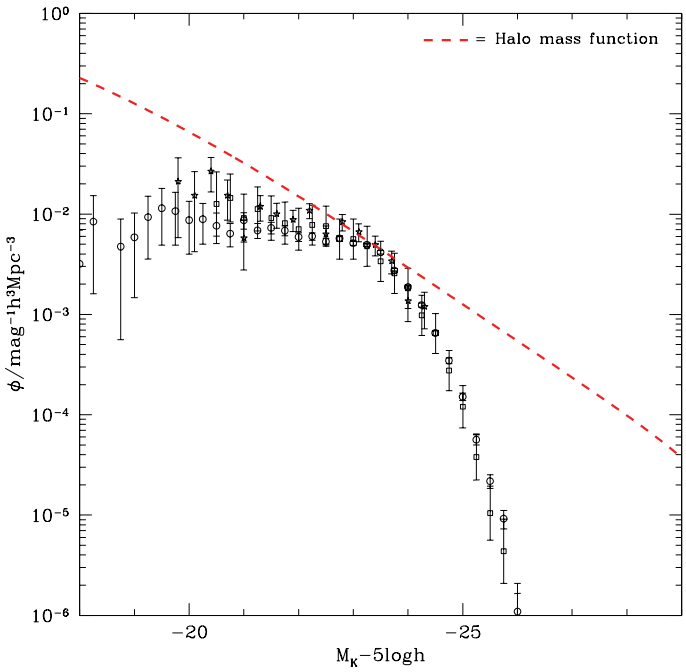

Figure 1.26: K-band luminosity function of galaxies. The points show the observational determinations of Cole et al. (2001; circles), Kochanek et al. (2001; squares), and Huang et al. (2003; z <1, stars). Lines show model results. Red dashed line shows the result of converting the DM halo mass function into a galaxy luminosity function by assuming a fixed mass-to-light ratio chosen to match the knee of the luminosity function (*Benson et al.* 2003).

Merritt 2000). The black hole mass is seen to grow until it reaches a limiting luminosity: the Eddington limit. At this luminosity, the accretion disk of the central black hole reaches a temperature of $\sim 10^{10}$ K: at this value the pressure of the disk photons is so high that they can escape from the disk forming a strong "wind" which, not only prevents further feeding of the central black hole, but also expels all the remaining gas in the galaxy, stopping the star-formation and the further accretion of mass onto the black hole.

The above picture, if on one side sheds light on the mechanisms that have led the formation of galaxies and their spatial distribution, on the other clearly shows that the existence of galaxies as they appear is a complex mix both of the initial cosmological conditions, but also of a great variety of processes that by quenching the star-formation and modifying the morphology are able to convert blue-disk galaxies in the field into red spheroidal galaxies in cluster.

1.4 Galaxy transformation mechanisms

In this section we present the different physical mechanisms that are likely to be important for determining the star-formation histories of galaxies both internal to the galaxy (e.g. gas consumption, AGN feedback and merging) and as the result of direct interactions between the galaxy and its local environment (e.g. ram-pressure stripping and galaxy harassment).

1.4.1 Star-formation, supernovae feedback, gas consumption and suffocation

Star-formation

Star-formation in disk galaxies is regulated by a variety of processes (neglecting here AGN feedback, bar instabilities, and galaxy interactions), gravitational instability and turbulence of the gas disk, supernovae feedback, and the inflow and cooling of gas from the halo. The most important parameter for determining the star-formation efficiency appears to be the local gas surface density Σ_{gas}: Schmidt (1959) showed that the observed surface densities of gas and star-formation in galaxies were related by a simple power law, $\Sigma_{\rm SFR} = A\,\Sigma_{gas}^{N}$, where $N = 1.4 \pm 0.15$ over several orders of magnitude in gas density (Kennicutt 1998). Moreover, there appears a critical gas density below which star-formation does not occur (Martin & Kenni-

cutt 2001). The empirical Kennicutt-Schmidt law is close to that predicted for a self-gravitating disk, where the star-formation rate scales as the ratio of the gas density to the free-fall time-scale ($\tau_{ff} \propto \Sigma_{gas}^{-0.5}$), and implies that star-formation efficiency (SFR/Σ_{gas}) increases with gas surface density, resulting in star-formation being most inefficient in low-surface brightness dwarf galaxies.

Supernovae feedback

Supernova feedback has also been proposed as a mechanism that could explain the inefficiency of star-formation in dwarf galaxies, as well as their tight correlations between their internal velocities, metallicities, surface brightnesses and stellar masses (e.g. Dekel & Woo 2003; Scannapieco et al. 2006), although Tassis, Kravtsov, & Gnedin (2008) argue that these scaling relations can be obtained without supernovae feedback, and are simply the result of the Kennicutt-Schmidt law with a critical density threshold. In these models, energy released by the supernovae triggers metal-enriched winds which can drive enriched gas from the disk into the halo and beyond, causing mass loss and self-regulating the star-formation activity, resulting in a quasi-periodic, bursty star-formation rate in low-mass galaxies. However, using hydrodynamic simulations, Mac Low & Ferrara (1999) and Marcolini et al. (2006) find instead that in quite low mass dwarfs with gas masses $M_{gas} \sim 10^7 M_\odot$ galactic winds due to supernovae do not form, even during quite large starbursts, despite the energy released by the supernovae being greater than the binding energy of the galaxy. Supernova feedback is likely to further reduce the star-formation efficiency in dwarf galaxies by reheating the surrounding cold gas clouds and blowing it out of the disk (if not from the galaxy entirely), at least for a while (Scannapieco et al. 2006), contributing to the gas depletion time-scales of the order ~ 20 Gyr observed for isolated dwarf irregular galaxies (van Zee 2001). The effects of supernova feedback are expected to reduce with increasing galaxy mass, as the deeper gravitational potential wells and larger gas masses make it more difficult for supernovae to drive outflows (Dekel & Silk 1986).

Gas consumption

In typical $\sim L^*$ spiral galaxies (including our Galaxy) star-formation occurs much more efficiently due to their much higher gas surface densities, resulting in gas consumption time-scales (calculated by comparing their star-formation rates and HI contents) of just ~ 3 Gyr. This implies that if no gas replenishment were to occur, most spiral galaxies would consume all their

gas in much less than a Hubble time, and this led Larson et al. (1980) to propose that their gas is continuously replenished from their extended halos, allowing them to continue forming stars to the present day.

Hydrodynamical simulations following this accretion and cooling of gas from the halo onto the disk have shown there are two processes by which this occurs, the relative importance of these modes depending strongly on galaxy mass (Kereš et al. 2005; Dekel & Birnboim 2006). In high-mass galaxies, the infalling gas follows the track expected in the conventional picture of galaxy formation, being shock-heated to roughly the virial temperature of the galaxy potential well ($T_{vir} \sim 10^6$ K), forming a stable diffuse atmosphere in quasi-hydrostatic equilibrium with the DM, before being accreted in a quasi-spherical manner through radiative cooling, condensing onto the disk and forming stars. In low-mass galaxies, or at high-redshifts, gas is accreted onto the disk along filamentary structures, and cools too rapidly for stable virial shocks to occur, allowing for a more rapid and efficient cooling, condensation and formation of stars. Although the approaches of Dekel & Birnboim (2006) and Kereš et al. (2005) are radically different, both obtain characteristic transition masses of $M_{vir} \sim 6 \times 10^{11} \mathrm{M}_{\odot}$ (corresponding to a stellar mass of $\sim 3 \times 10^{10} \mathrm{M}_{\odot}$) between the "hot" and"cold" accretion modes, which appear in good agreement with the observed characteristic stellar mass at which there is a sharp transition in the global properties of galaxies from low-mass, star-forming disks to high-mass, passively-evolving spheroids (Kauffmann et al. 2003a).

What would happen to galaxies if this accretion of fresh gas from the halo (through either hot or cold modes) were to be permanently shut off? Larson et al. (1980) proposed that when a galaxy enters a more massive halo, such as a group or cluster, its reservoir of halo gas is lost to that of its host halo, either through tidal effects or ram-pressure stripping. The remaining gas in the disk is slowly consumed by star-formation over a period of Gyr, leaving a passively-evolving galaxy. This physical process, described as "suffocation" (also starvation or strangulation), was proposed by Larson et al. (1980) as a mechanism that would strip away the halo gas reservoirs and exhaust the remaining gas of spiral galaxies, and transform them into passive S0s over a period of ~ 3 Gyr. They suggested that this could explain the Butcher-Oemler effect, where $z \sim 0.4$ clusters contain large numbers of star-forming spirals, while present day clusters are deficient in spirals, but contain many more S0s.

This model was elaborated by Balogh, Navarro & Morris (2000), who indicate that the gradual decline of star-formation on timescales predicted by suffocation could reproduce the Butcher-Oemler effect and the observed gradual star-formation density relations extending well beyond the cluster

virial radius (e.g. Lewis et al. 2002; Treu et al. 2003). They also indicate that a much more rapid truncation of star-formation would produce a large population of post-starburst galaxies which instead appear to be quite rare in low-redshift clusters. By simply assuming the Schmidt-Kennicutt law, Balogh et al. (2000) obtain a relation for the decline in star-formation where no further gas accretion is possible as,

$$\mathrm{SFR}(t) = \mathrm{SFR}(0)\left(1 + 0.33\frac{t}{t_e}\right)^{-3.5} \mathrm{M}_\odot\,\mathrm{yr}^{-1}, \tag{1.7}$$

where SFR(0) is the initial star-formation rate, and

$$t_e \approx 2.2\,[\mathrm{SFR}(0)/\mathrm{M}_\odot\,\mathrm{yr}^{-1}]^{-0.29}\,Gyr \tag{1.8}$$

is the characteristic gas consumption time-scale, including the effects of gas recycling. For a typical L^* spiral galaxy with SFR(0) $\sim 5\mathrm{M}_\odot\mathrm{yr}^{-1}$ we obtain $t_e \sim 1.4\,\mathrm{Gyr}$, resulting in the galaxy taking $\sim 4\,\mathrm{Gyr}$ to become passive (SFR(t)/SFR(0) ~ 0.1), a time-scale consistent with the cluster spiral population in $z \sim 0.4$ clusters becoming passive by $z = 0$.

The numerical and hydrodynamical simulations of Bekki et al. (2001, 2002) following the evolution of the extended halo gas of spiral galaxies in cluster or group environments show (see Fig. 1.27), that even if the spiral is orbiting the cluster ($\mathrm{M}_{cl} = 5\times10^{14}\mathrm{M}_\odot$) with pericentre distances of the order 500 kpc (i.e. well outside the cluster core), a combination of the hydrodynamic interaction with the ICM and the effects of the global tidal field of the cluster are able to effectively strip 80% or more of the halo gas within a few Gyr, and prevent further accretion of gas onto the galaxy. They found that in group environments ($\mathrm{M}_{grp} = 10^{13}\mathrm{M}_\odot$) halo gas stripping is only effective on orbits that pass through the core of the group.

Suffocation

Suffocation acts to *globally* remove gas from a galaxy, and hence the radial profiles of the remaining gas and star-formation should only be mildly affected (Boselli et al. 2006). The process should act to slowly dim the disk, without affecting its morphology or radial profile, and has been favoured as a mechanism to produce the anaemic spirals seen in present day clusters (van den Bergh 1976).

Applying Eq. 6.3 instead to a typical field dwarf galaxy with $M_r \sim -18$ and SFR(0) $\sim 0.2\,\mathrm{M}_\odot\mathrm{yr}^{-1}$ we obtain $t_e \sim 3.5\,\mathrm{Gyr}$, resulting in the galaxy taking $\sim 10\,\mathrm{Gyr}$ to become passive, consistent with the long observed gas depletion time-scales of dIrrs (van Zee 2001). Hence, even if deprived of further

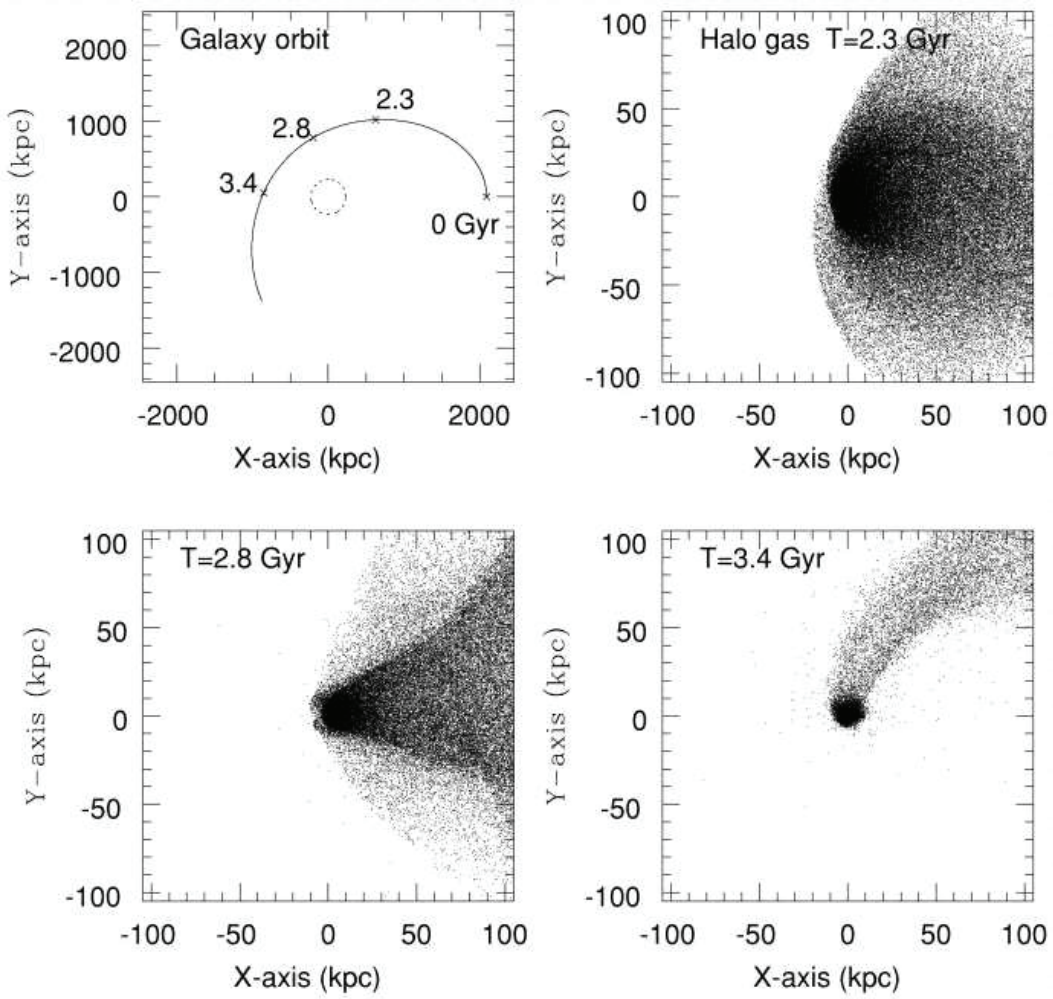

Figure 1.27: *Upper left panel*: Orbital evolution of a spiral in a cluster with $M_{cluster} = 5{\times}10^{14}M_{\odot}$, $R_{core} = 230$ kps, and $R_{virial} = 2.09$ Mpc. The orbit during 4.5 Gyr dynamical evolution of the spiral is given by the solid line. The cluster core radius is represented by a dotted circle. The time 0, 2.3, 2.8, 3.4 Gyr are represented by crosses along the orbit. In the other panels: time evolution of the halo gas distribution during the dynamical evolution of the spiral. (Results from numerical simulations of *Bekki*, *Couch* and *Shioya* 2002).

gas accretion through suffocation, star-formation in dwarf galaxies occurs at a sufficiently low rate that they are unlikely to have consumed all their gas by the present day.

1.4.2 Galaxy Merging

Toomre (1977) was the first to suggest that merging could have a profound impact on galaxy evolution, proposing that the elliptical galaxy population could result from the merging of disk galaxies. Subsequently the hierarchical merging scenario was developed to describe the growth of structure and the evolution of massive galaxies (e.g. White & Rees 1978; Kauffmann, White & Guideroni 1993; Lacey & Cole 1993).

Hydrodynamical simulations following the mergers of gas-rich disk galaxies showed that gas inflows induced by gravitational torques channel large amounts of gas onto the central nucleus, fuelling powerful star-bursts (often after the initial encounter, but before the galaxies coalesce) that use up significant fractions (65–85%) of the gas content from the original disk (Mihos & Hernquist 1996), leaving bulge-dominated remnants possessing the $r^{1/4}$ surface brightness profiles typical of early-type galaxies (Barnes & Hernquist 1992). More recent hydrodynamical simulations incorporating black hole growth (Springel et al. 2005a) show that the gas inflows fuel also rapid growth of the central supermassive black hole, which may become sufficiently massive to power quasar winds which entirely expel the remaining gas, effectively terminating star-formation in the merger remnant (di Matteo, Springel & Hernquist 2005).

Fig. 1.28 (taken from Hopkins et al. 2008) shows a schematic outline of current theoretical model for the main phases of the formation of a passive elliptical via a major merger of gas-rich disk galaxies. In panel (c) the two galaxies start to merge: the interaction has distorted the discs and a strong shock occurs in the impact region (Di Matteo, Springel & Hernquist 2005). Gas ha begun to fall into the central region accreting mass onto the central black hole, but no significant episode of star-formation occurs. In panel (d) the galaxies coalesce, and massive inflows of gas trigger starbursts (often heavily obscured by dust) with strengths similar to those inferred for ULIRGs and sub-mm galaxies, and a great part of the gas is converted into stars via central nuclear starbursts. The high gas densities feed rapid black hole growth, but thee black holes are obscured at optical wavelengths by gas and dust. Most of the nuclear gas is consumed by the starburst, and eventually feedback from supernovae and the black hole begins to disperse the gas (panel e). The remaining gas is then heated by the feedback energy provided by the accretion and is partly expelled in a powerful wind. During this short

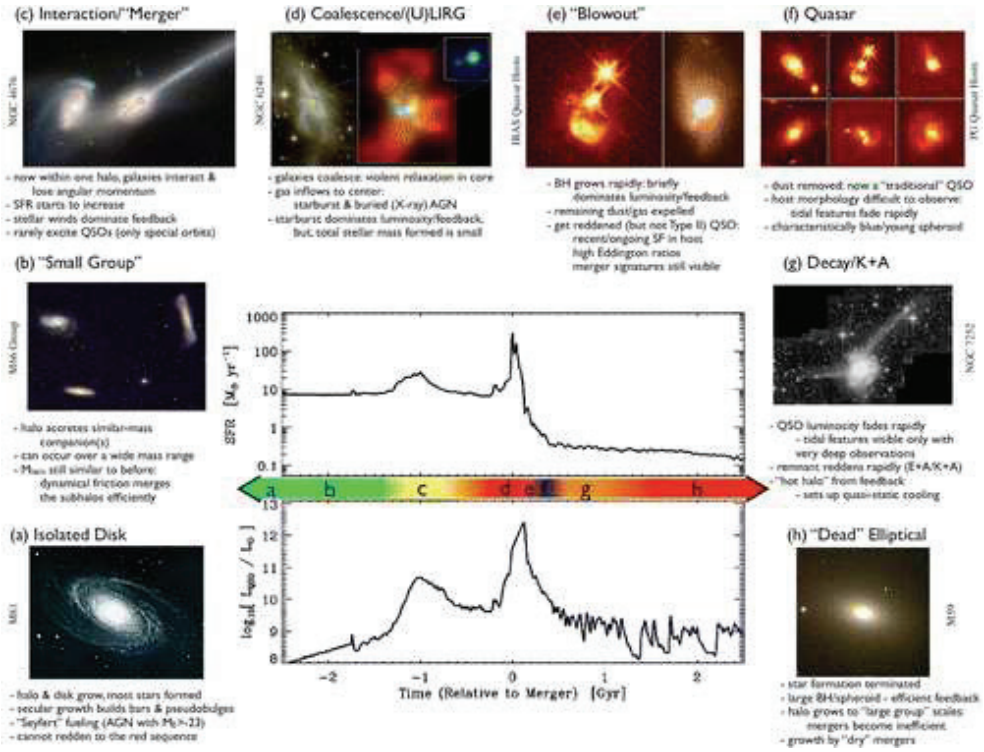

Figure 1.28: Schematic outline of the phases of growth in a typical galaxy undergoing a gas-rich major merger (*Hopkins et al.* 2008).

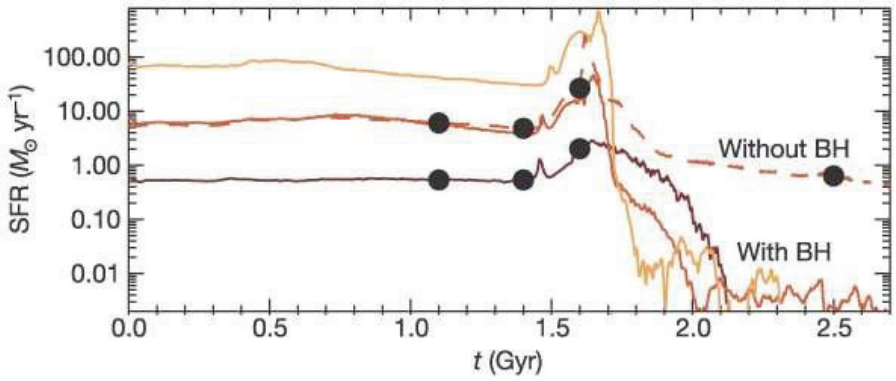

Figure 1.29: Star-formation rate as function of time during a galaxy-galaxy merger. The three solid lines (black, red and orange) correspond to galaxy-galaxy merger with black hole growth, with galaxies of virial velocity V_{vir} = 80 km s^{-1}, 160 km s^{-1}, 320 km s^{-1} respectively. The dashed line correspond to galaxies with V_{vir} = 160 km s^{-1} with no black hole growth.(*diMatteo, Springel & Hernquist* 2005).

phase the object could appear as a bright quasar (panel f). The expulsion of the gas by the wind imply a sudden quenching of the star-formation and of the accretion of the black hole itself, terminating the quasar phase (g), and leaving as a result a "dead" elliptical whose stellar population quickly evolves from blue to red. The central panel of Fig 1.28 shows the star-formation rate during the merger event: it shows the star-burst triggered during the coalescence/ULIRG phase (d) and the subsequent quenching of the star-formation as the gas is expelled from the galaxies by the quasar winds. Figure 1.29 reports the star-formation rate inferred by simulations of merger of two discs galaxies taking into account star-formation and supernovae feedback and in one case adding also the effect of central black hole growth (solid line) and in another case (dashed line) neglecting this effect (Di Matteo, Springel & Hernquist 2005). The three solid lines (black, red and orange) correspond to models with galaxies of virial velocity V_{vir} = 80 km s^{-1}, 160 km s^{-1}, 320 km s^{-1} respectively. The dashed line correspond to galaxies with V_{vir} = 160 km s^{-1}. The damping of star-formation is more abrupt in the more massive systems. Here, the total gas supply for accretion is larger, and the gravitational potential well is deeper, and so the black hole has to growth much more before its released energy is sufficient to expel gas in a quasar driven wind.

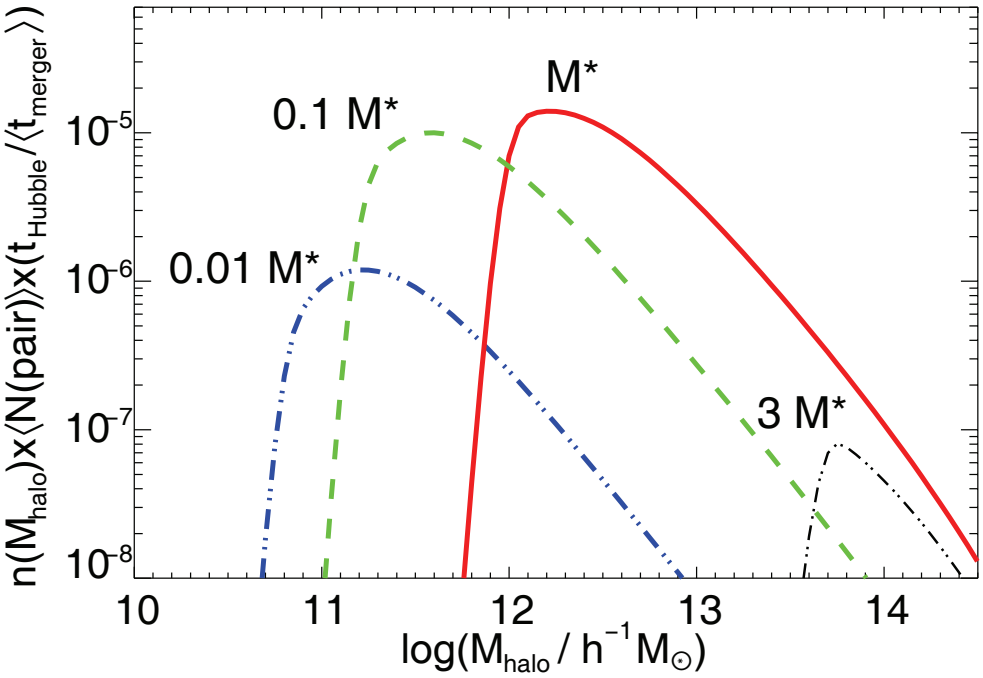

Figure 1.30: The relative number density of mergers of galaxies of a certain galaxy mass (0.01 M^* blue dot-dot-dashed curve; 0.1 M^* green dashed curve; M^* red solid curve; 3 M^* black dot-dashed curve) as a function of halo mass. (*Hopkins et al.* 2008).

On the contrary, in the simulations without black holes a certain quantity of cold dense gas persists after the merger, yielding prolonged star-formation at a steady rate.

Galaxy mergers at the present epoch are relatively rare, with just $\sim 0.5\%$ in close physical pairs (with real-space separations < 30 kpc de Propris et al. 2005; Bell et al. 2006). However, Alonso et al. (2006) find that high-mass galaxies in close pairs, that are presumably about to merge, are more likely to be undergoing strong star-formation or also appear very red, with respect to those systems without a close companion, observational evidence in favour of merging causing star-bursts, which may be heavily dust-obscured. For interacting galaxies to be able to merge their encounter velocity must be less than or comparable to their velocity dispersions (Aarseth & Fall 1980), and as a result mergers should be most frequent in poor groups which have high galaxy densities but low velocity dispersions (see Fig. 1.30). In contrast in rich clusters the encounter velocities are too high, meaning that while interactions are frequent, mergers are extremely rare (Ghigna et al. 1998).

While mergers may be rare now, in the much denser and active early universe they were much more frequent. Conselice (2006) shows that galaxies undergo a phase of rapid growth through merging at high redshifts $z>1$, but at later epochs the merger rate drops exponentially to a current rate that is only a hundredth of that at $1<z<3$. During this early and rapid merging, the stellar masses of an average galaxy increases by a factor 10–100, undergoing $\sim$4 major mergers at $z>1$. The epoch at which galaxies grow and merge is also dependent on environment. Halos that are in clusters at $z=0$ have built up their mass through mergers and accretion earlier than isolated halos of the same mass (Gottlöber et al. 2001; Maulbetsch et al. 2007). Additionally, during this epoch of rapid growth through mergers ($1<z<4$), progenitors of cluster and group halos have 3–5 times higher merger rates than isolated halos (Gottlöber et al. 2001).

1.4.3 Ram-pressure stripping, galaxy harassment and tidal interactions

There have been a number of physical processes proposed over the last decades to explain the observed SF-density and morphology-density relations through the interaction of cluster galaxies with the intra-cluster medium (ICM), other galaxies or the global cluster tidal field.

Ram-pressure stripping

Gunn & Gott (1972) first proposed that the ISM of cluster galaxies could be removed through ram-pressure stripping as they move at high velocities ($\sim 1\,000\,\mathrm{km\,s^{-1}}$) through the dense ($\sim 10^{-3}$ atom cm^{-3}), hot ($\sim 10^7$ K) ICM. As a galaxy orbits through the cluster, it experiences a wind because of its motion relative to the diffuse gaseous ICM. Although the ICM is tenuous, the rapid motion of the galaxy causes a large pressure front to build up to in front of the galaxy. Depending on the binding energy of the galaxy's own ISM, the ICM will either be forced to flow around the galaxy or will blow through the galaxy, removing some or all of the diffuse ISM. Gunn & Gott (1972) introduced a simple analytic condition to determine when ram-pressure stripping is effective:

$$\rho_{ICM} v_{gal}^2 > 2\pi \mathrm{G} \Sigma_\star \Sigma_{gas}, \tag{1.9}$$

where ρ_{ICM} is the density of the ICM, v_{gal} is the velocity of the galaxy through the ICM, and $\Sigma_\star, \Sigma_{gas}$ are the surface densities of stars and gas in the disk. The first term represents the ram-pressure, while the second term is the gravitational restoring force which keep bound the gas to the galaxy.

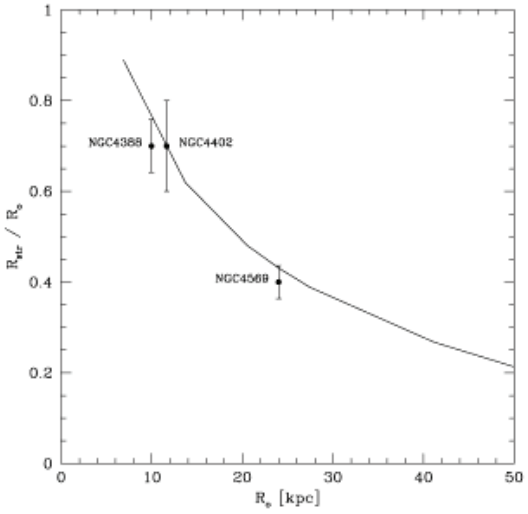

Figure 1.31: Dependence of the stripping radius, R_{str} as a function of the optical radius R_o, which scale linearly with the disk scale-length R_d such that for $R_d = 3.5$ Kpc, $R_o = 24$ kpc.(Results from three-dimensional SPH/N-body simulations of *Abadi* et al. 1999).

If ram-pressure is effective in removing gas from infalling galaxies into a cluster environment, then these objects should have truncated discs deficient in HI.

Hydrodynamic simulations of ram-pressure stripping confirm that gas should be stripped from cluster spirals from the outside in, and that the radius to which the gas is stripped is close to that predicted by the Gunn and Gott condition and hence that it depends (see Fig. 1.31) on the relation of the ram-pressure to the restoring force (e.g Marcolini et al. 2003; Abadi et al. 1999).

Before stripping a galaxy, ram-pressure compresses the gas ahead of the galaxy and in the case of edge-on interactions the central gas density may increase by a factor two, due to capture of the outer HII gas, resulting in a temporary ($\sim 10^8$ yr) increase in star-formation (Fujita & Nagashima 1999; Vollmer et al. 2001).

Equation 1.9 predicts that ram-pressure stripping should be more efficient for lower mass, low-surface-brightness galaxies, for those galaxies on radial orbits that take them through the densest parts of the ICM at the highest speeds, and for galaxies in the richest clusters. Using hydrodynamical simulations Roediger & Hensler (2005) find that the gas disks in massive spirals

are heavily truncated or even completely stripped in cluster cores, while even in lower density environments such as the cluster outskirts or in poor groups, they are partially stripped. In the same group environments Marcolini et al. (2003) find that dwarf galaxies can be completely stripped of their gas. The dense ICM is built-up over time (mainly at $z < 1$) through the gradual loss of gas from cluster galaxies through ram-pressure stripping, galaxy winds and interactions (Kapferer et al. 2007), and so ram-pressure stripping should be most effective at late epochs ($z < 0.5$). However, Kapferer et al. (2007) also show that gas loss from ram-pressure stripping is also important during the cluster formation epoch at $1 < z < 2$ when galaxies in sub-clusters enter the main cluster at high velocities. Such cluster-cluster mergers can create shocks in the ICM, triggering starburst in galaxies over large scales, before rapidly stripping them (Roettiger, Burns & Loken 1996).

Galaxy harassment

Moore et al. (1996) proposed that cluster spirals could be disrupted by "galaxy harassment", whereby repeated close ($<50\,\mathrm{kpc}$) high-velocity ($>1\,000\,\mathrm{km\,s^{-1}}$) encounters with massive galaxies and the cluster's tidal field cause impulsive gravitational shocks that damage the fragile disks of late-type disks, transforming them over a period of Gyr into spheroids. High-surface brightness L^* spirals are relatively stable to the effects of harassment, suffering little or no mass loss, although their disks may thicken and their spiral structure weaken (Moore et al. 1999). Low surface brightness dwarf spirals with their shallower potentials may suffer significant mass losses (up to 90%) of both their stellar and DM components during harassment. These low-mass galaxies undergo significant morphological transformations, even at the outskirts of the cluster, the remnants resembling dwarf ellipticals, although the disks are never completely destroyed (Mastropietro et al. 2005). Galaxy harassment may also cause starbursts, an example of which is NGC 4435 in the Virgo cluster, which $\sim$200 Myr ago underwent a high-velocity ($\sim 800\,\mathrm{km\,s^{-1}}$) with NGC 4438 $\sim$200 Myr ago, which triggered a highly obscured starburst which from *Spitzer* IR photometry and IRS spectra was coincident with the interaction with NGC 4438 (Panuzzo et al. 2007).

Tidal interactions

Dwarf spiral / irregular galaxies orbiting as satellites to massive galaxies may also be transformed into passively-evolving dEs through tidal interactions with the primary galaxy and ram-pressure stripping as they pass through its gaseous halo. Mayer et al. (2001) show that high-surface bright-

ness dwarf spirals orbiting a Milky Way type galaxy on eccentric orbits taking them within 50 kpc of the primary experience tidal shocks during their pericentre passages, that can cause significant mass loss (mostly of the outer gaseous halo and DM, but also of the stellar disk), formation of bar instabilities that channel gas inflows triggering nuclear star-bursts, and loss of angular momentum, resulting in their transformation over a period of ~ 5 Gyr into an early-type dwarf. Mayer et al. (2006) indicate that while tidal stirring of disky dwarf galaxies can transform them into remnants that resemble dEs after a few orbits, ram-pressure stripping is required to entirely remove their gas component. The tides may aid ram-pressure stripping by diminishing the overall potential of the dwarf, but the channelling of gas inwards to form a concentrated remnant makes subsequent stripping more difficult.

The mutual efficiency of these processes which act on different mass scales and environments could give rise to the sharp transition observed at M_{crit}.

From the picture described above it emerges that to deeply understand the scenarios regulating the galaxy formation and the mechanisms which could transform galaxy properties producing the observed variety, two complementary studies are necessary to follow the galaxy evolution as a function of *both* mass and environment.

To this aim, it is necessary to have: i) deep datasets which cover both the giant and dwarf regime allowing us to study and identify the different physical mechanisms acting on different mass scales; ii) extended datasets sampling both the field and clusters to study the effect of the surrounding media on galaxy evolution at each scale, i.e. not only the effects of the cluster environment on galaxy evolution, but also, on smaller scales, the effect of a single neighbour in otherwise isolated regions.

The availability of large field telescopes allow to performe extended surveys mapping large portions of the sky providing us with unprecedent databases such those used in this research project.

Part I

Galaxy evolution in the Shapley supercluster core

The Shapley supercluster

The Shapley supercluster (Shapley 1930) is the richest supercluster in the nearby universe ($z < 0.1$, Fig. 1.32), consisting of as many as 25 Abell clusters in the redshift range $0.035 < z < 0.055$. Extensive redshift surveys (Bardelli et al. 2000; Quintana, Carrasco & Reisenegger 2000; Drinkwater et al. 2004) indicate that these clusters are embedded in two sheets (Fig. 1.33) extending over a $\sim 10 \times 20\,\mathrm{deg}^2$ region of sky ($\sim 35{\times}70\ h_{70}^{-2}\,\mathrm{Mpc}^2$), and that as many as half the total galaxies in the supercluster are from the inter-cluster regions. The Shapley supercluster core (SSC, highlighted by the black ellipse in Fig. 1.34) is constituted by three Abell clusters: A 3558 ($z = 0.048$, Melnick & Quintana 1981; Metcalfe, Godwin & Spenser 1987; Abell richness R=4, Abell, Corwin & Olowin 1989), A 3562 ($z = 0.049$, Struble & Rood 1999, R=2, Abell et al. 1989) and A 3556 ($z = 0.0479$, Struble & Rood 1999, R=0, Abell et al. 1989) and two poor clusters SC 1327-312 and SC 1329-313. Dynamical analyses indicate that at least a region of radius $11\,h_{70}^{-1}\,\mathrm{Mpc}$ centred on the central cluster A 3558, and possibly the entire supercluster, is past turnaround and is collapsing (Reisenegger et al. 2000), while the core complex itself is in the final stages of collapse, with infall velocities reaching $\sim$2000 km s^{-1}.

A major study of the dynamical properties of the supercluster core was performed by Bardelli et al. (2001 and references therein). They showed that the supercluster core has a complex, highly elongated structure, and identified 21 significant 3-dimensional subclumps, including eight in the A 3558 cluster alone.

The X-ray observations show that the supercluster has a flattened and elongated morphology where clusters outside the dense core are preferentially located in hot gas filaments (Bardelli, Zucca, & Malizia 1996; Kull & Böhringer 1999; De Filippis, Schindler & Erben 2005). Moreover, Finoguenov et al. (2004) showed a strong interaction between the cluster A 3562 and the nearby group SC 1329-313 with an associated radio halo having a young age (Venturi et al. 2000, 2003). However, since this is one of the weakest radio halos found, Venturi et al. (2003) suggested that this halo is connected with the head-on radio galaxy of A 3562. Bardelli et al. (2001) suggested that the A 3558 complex is undergoing a strong dynamical evolution through major merging seen just after the first core-core encounter, and so the merging event has already been able to induce modifications in the galaxy properties. Very recently, Miller (2005), with a radio survey of a 7 deg^2 region covering the SSC, found a dramatic increase in the probability for galaxies in the vicinity of A 3562 and SC 1329-313 to be associated with radio emission. He interpreted this fact as young starbursts related to the recent merger of

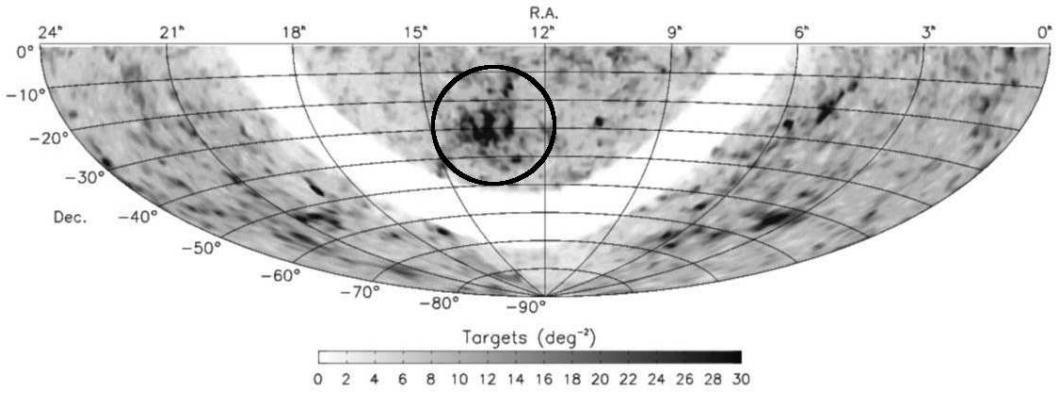

Figure 1.32: Density (per deg^2) of $K < 12.75$ galaxies selected as 6dFGS targets over the Southern sky (Jones et al., 2005). The black circles highlights the Shapley supercluster.

SC 1329-31 with A 3562.

These studies confirm the complex dynamical and structural picture of the supercluster core. The high infall and encounter velocities of galaxies ($>$ 1000 km/s), the presence of merging groups and clusters, and the observation that a significant fraction of galaxies are interacting for the first time with the hot (ICM) make the SSC the ideal target to study the impact of the environment on galaxy evolution, being the only system able to provide in such a limited region of the universe such a variety of different environments, in terms of both dynamics and density.

With this in mind we have undertaken a multi-band study of the Shapley Supercluster core. The first part of this thesis presents the photometric and spectroscopic optical study and discusses its main results .

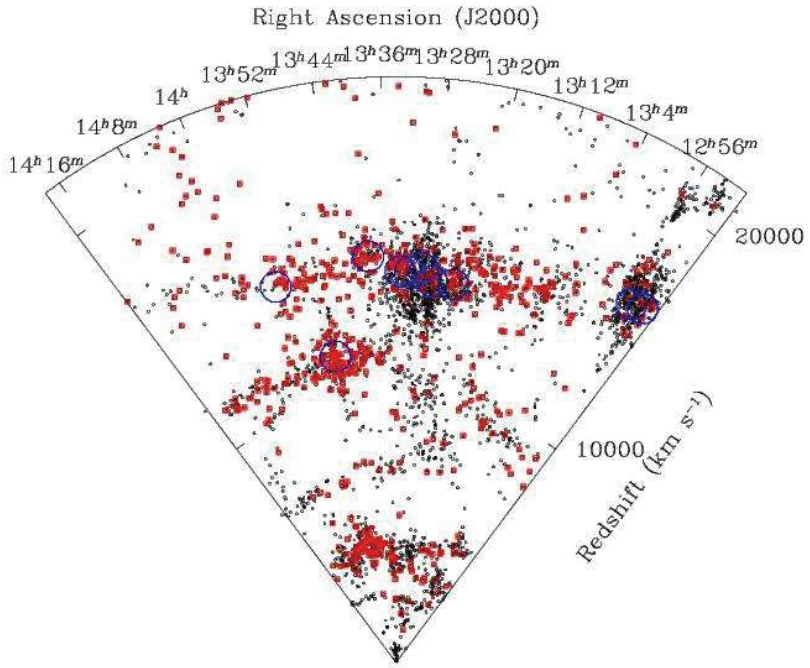

Figure 1.33: Cone velocity diagram in right ascension and declination. The richest galaxy clusters in the region are shown as large circles.

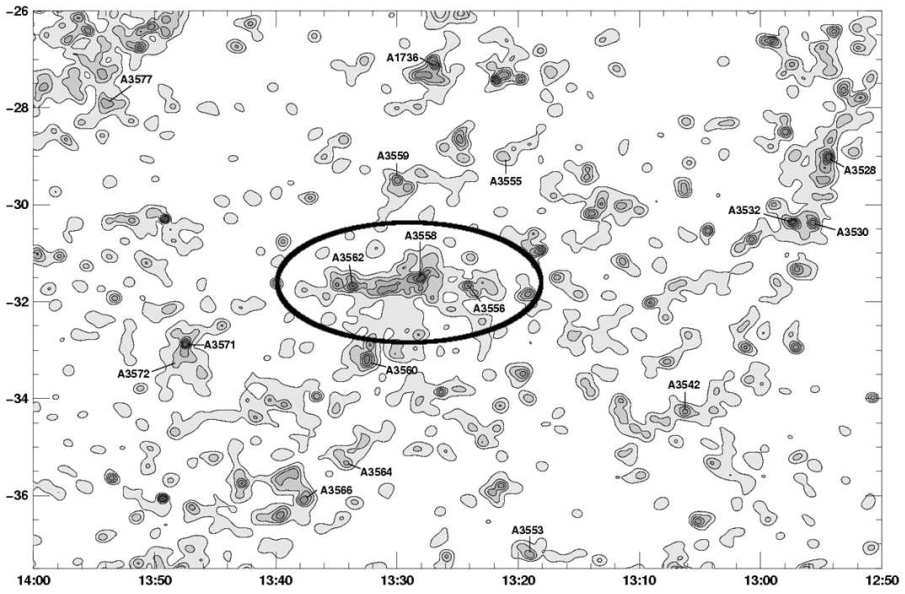

Figure 1.34: Surface density of $R < 18.5$ galaxies from the SuperCOSMOS survey *Hambly, MacGilivray & Read* 2001.

Chapter 2

Shapley Optical Survey: technical aspects

In this chapter we present the Shapley Optical Survey: the observations, the main steps of data reduction and photometric calibration. Moreover we describe the procedure designed *ad hoc* to obtain the photometric catalogues both in the B and R-bands. We then present the spectroscopic data and procedures used to perform the surface photometry of the galaxies used in the fundamental plane survey. Finally we present the algorithm used to define the environment through the measure of local galaxy density[1].

2.1 Photometric data: observations, data reduction and photometric calibration

The Shapley Optical Survey (SOS) is a photometric study of the central region of Shapley supercluster. The SOS data were obtained from the ESO Archive (68.A-0084, P.I. Slezak), and were acquired with the ESO/MPI 2.2-m telescope at La Silla. B- and R-band photometry were obtained for eight contiguous fields covering a 2 deg^2 region centred on the SSC, as shown in

[1]The contents of this chapter are published in the articles:

- Mercurio, A.; Merluzzi, P.; Haines, C. P.; Gargiulo, A.; Krusanova, N.; Busarello, G.; Barbera, F. La; Capaccioli, M.; Covone, G. "Shapley Optical Survey - I. Luminosity functions in the supercluster environment", 2006, MNRAS, 368, 109-120.

- Haines, C. P.; Merluzzi, P.; Mercurio, A.; Gargiulo, A.; Krusanova, N.; Busarello, G.; Barbera, F. La; Capaccioli, M.; "Shapley Optical Survey - II. The effect of environment on the colour-magnitude relation and galaxy colours", 2006, MNRAS, 371, 55-66.

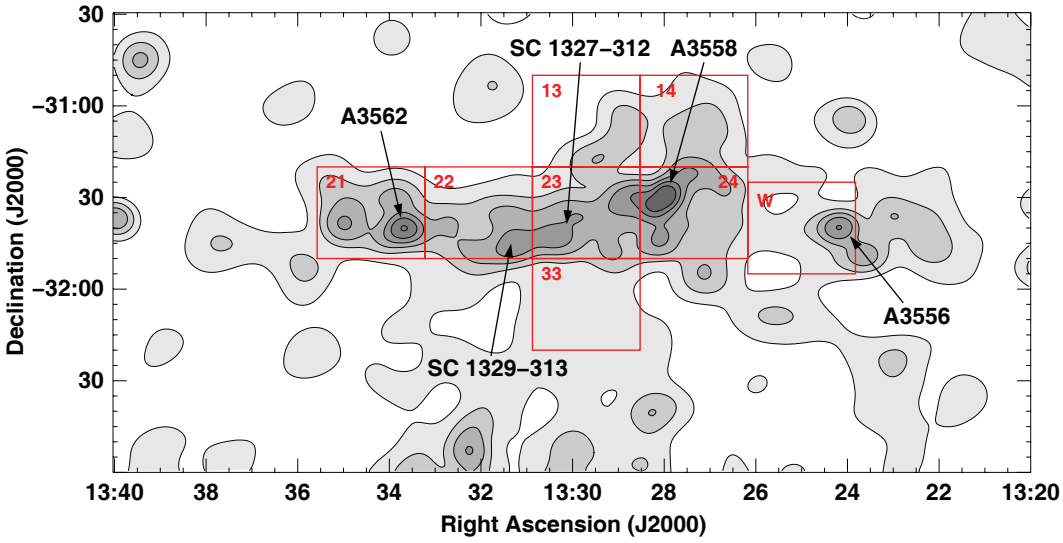

Figure 2.1: The surface density of R<18.5 galaxies of the the SSC core, obtained by using data of the SuperCosmos Sky Survey (*Hambly, MacGilivray & Read* 2001). Red rectangles indicate the 8 analysed fields of the SOS.

Fig. 2.1. The observations (see Table 2.1 for details) were carried out with the WFI camera, a mosaic of eight 2046 × 4098 pixels CCDs (see Fig. 2.2), mounted on the Cassegrain focus of the telescope. The camera has a field of view of $34' \times 33'$, corresponding to 2.0×1.9 h_{70}^{-2} Mpc^2 at the supercluster redshift, and a pixel scale of 0.238 arcsec. The central stripe were observed in good conditions on 18 March 2002 (*full width at half maximum*, FWHM, $\sim$ 0.7"), while the rest of the observations were taken in slightly poorer conditions. The total exposure times for each field are 1500 s (300 s × 5) in the B-band and 1200 s (240 s × 5) in the R-band, reaching R=25 (B=25.5) at 5σ. The single exposures are jittered to cover the gaps between the different CCDs of the camera. Landolt (1992) stars were observed in order to perform accurate photometric calibration.

The ALAMBIC pipeline (version 1.0, Vandame 2004) was used to reduce and combine the SOS images. The pipeline follows the standard procedures for bias subtraction and flat-field correction; the twilight sky exposures for each band were used to create the master flat.

The photometric calibration was performed into the Johnson-Kron-Cousins photometric system using the Landolt stars. With the IRAF tasks DAOPHOT and APPHOT the instrumental magnitudes of the stars were computed in a fixed aperture (10 arcsec diameter) in B and R-bands.

Table 2.1: The observations.

Field #	Band	Centre RA, Dec	Date	FWHM arcsec
21	B	13:34:24.1, -31:34:57.1	18 March 2002	0.95
	R	13:34:24.1, -31:34:57.0	”	0.87
22	B	13:32:03.2, -31:34:57.1	18 March 2002	0.79
	R	13:32:03.2, -31:34:57.1	”	0.70
23	B	13:29:42.4, -31:34:57.3	18 March 2002	0.76
	R	13:29:42.4, -31:34:57.5	”	0.71
24	B	13:27:21.5, -31:34:57.4	18 March 2002	0.77
	R	13:27:21.5, -31:34:57.1	”	0.73
W	B	13:25:00.6, -31:40:27.1	18 March 2002	0.83
	R	13:25:00.6, -31:40:26.6	”	0.73
13	B	13:29:42.5, -31:04:58.0	9 April 2003	0.98
	R	13:29:42.5, -31:04:59.3	9 June 2002	1.11
14	B	13:27:21.6, -31:04:57.6	19 March 2002	1.16
	R	13:27:21.5, -31:04:56.6	”	1.27
33	B	13:29:42.4, -32:04:57.5	9 April 2003	0.81
	R	13:29:42.3, -32:04:58.9	9 June 2002	1.43

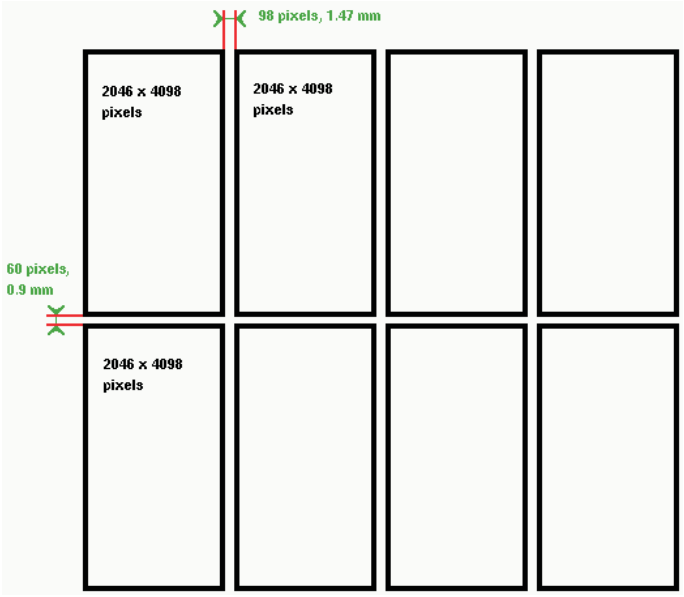

Figure 2.2: Displacement of CCDs in the *Wide Field Imager* camera.

Table 2.2: The results of the photometric fits for the B and R-bands.

Observing Night	Band	C	ZP	A	γ	rms
18 March 2002	B	B - R	-24.531 ± 0.024	0.189 ± 0.017	-0.131 ± 0.009	0.041
18 March 2002	R	V - R	-24.548 ± 0.038	0.147 ± 0.026	0.049 ± 0.035	0.036
9 April 2003	B	B - R	-24.562 ± 0.029	0.162 ± 0.019	-0.141 ± 0.017	0.034

For the R-band the flux was calibrated by adopting the following relation:

$$M' = M + \gamma C + AX + ZP, \tag{2.1}$$

where M is the magnitude of the star in the standard system, M' is the instrumental magnitude, γ is the coefficient of the colour term, C is the colour of the star in the standard system, A is the extinction coefficient, X is the airmass and ZP is the zero point. For the B-band the colour term (B-R) was also taken into account. The results are reported in Table 2.2.

Since photometric standards were not available for the nights of 9 June 2002 and 19 March 2002, relative calibrations were adopted for fields #13, #33 in R band and field #14 for both B and R-bands, by comparison of the

photometry of objects observed also by those fields with existing photometric calibrations. The photometric accuracy for the zero point was about 0.04 mag in both bands for all the fields.

2.2 The optical catalogues

The photometric catalogues from the SOS images were produced using SExtractor (Bertin & Arnouts, 1996) together with a set of software procedures developed *ad hoc* in order to increase the quality of final catalogues, removing spurious detections and misleading results (see Sect. 2.2.1).

The star/galaxy classification was based on both the parameter *class star* (CS) of SExtractor and the value of the FWHM. In Fig. 2.3 we plot FWHM as function of M_{kron}. Red and black points are objects classified by SExtractor as stars (CS<0.98) and galaxies (CS≥0.98), respectively. From visual checks on the images it was observed that objects with FWHM < 1 are mostly stars. This value was adopted to perform star/galaxy separation. Moreover, the presence of some objects with FWHM lower than the seeing of the images was noted (0.4 % of the total extracted sources). Once selected, these objects were visually checked on the images and rejected if they were spurious objects.

Stars were defined as those objects with CS≥ 0.98 or having FWHMs consistent with those of bright, non-saturated stellar sources in the image.

The completeness magnitudes were firstly estimated using the prescription of Garilli et al. (1999). Then the reliability and the completeness of the catalogues were checked by performing Monte Carlo simulations in which artificial stars and galaxies were added (see Sect. 2.2.2). The final catalogues consist of 16 588 and 28 008 galaxies in B and R band, respectively, and are more than 94% complete at magnitude limits B=22.5 and R=22.0.

Aperture and Kron (Kron 1980) magnitudes were measured in each band. To compare the colour of different clusters it is necessary to measure magnitudes in physically consistent apertures, since the physical region of galaxies have to be the same for the different clusters. For this reason, for aperture photometry, we referred to the aperture of 17 arcsec ($\sim$ 8 kpc) of diameter used by Bower, Lucey and Ellis (1992) for Coma. Converting this value from the redshift of Coma to that of Shapley we used an aperture of 8 arcsec of diameter. Colours were determined in matched apertures in B and R-bands by running SExtractor in dual-mode. Instead, for the estimate of the luminosity function it is necessary to adopt the magnitude which is the best estimate of the total flux. To this aim, we use the Kron magnitudes. Kron magnitudes (M_{Kron}) were computed in an adaptive aperture with diameter

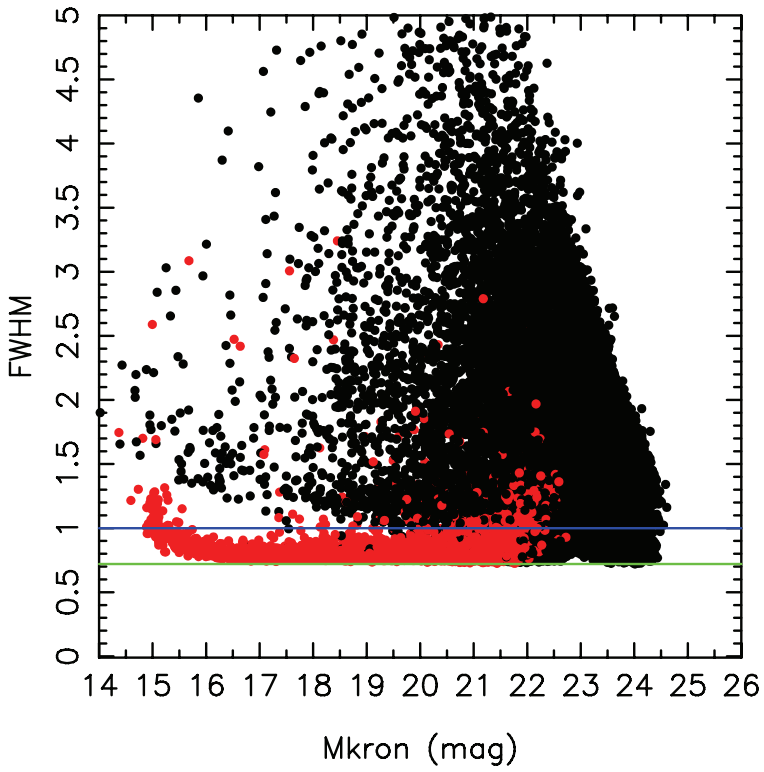

Figure 2.3: Distribution of the extracted objects in the plane FWHM vs M_{kron}. Red and black points are objects classified by SExtractor as stars and galaxies, respectively. The green line represents the FWHM limit imposed by the *seeing* of the images. The blue line represents the value adopted to separate stars and galaxies.

$a \cdot \mathrm{R}_{Kron}$, where R_{Kron} is the Kron radius and a is a constant. We chose a = 2.5, yielding $\sim$ 94% of the total source flux within the adaptive aperture (Bertin & Arnouts 1996). The uncertainties on the magnitudes were obtained by adding in quadrature both the uncertainties estimated by SExtractor and the uncertainties on the photometric calibrations. The measured magnitudes were corrected for galactic extinction (A_B=0.238 and A_R=0.149) following Schlegel et al. (1998).

2.2.1 Cleaning procedure

In order to obtain *clean* catalogues we used the following approach that takes into account both the performance of SExtractor and the characteristics of the analysed fields (crowdedness, background fluctuations, bright objects sizes and distribution).

The software SExtractor recognises as astronomical sources all the mosaic regions that have at least Y contiguous pixels which have registered more than X photons. The value of X and Y are set in the configuration file by the user.

The SOS mosaic images are obtained by stacking 5 single jittered exposures each of these formed of 8 CCDs separated by gaps. This peculiarity produces variable signal-to-noise ratios along the image, with the regions not covered by five exposures, such as the edges and the overlapping gap regions, having lower ratios than the bulk of the image. In these areas it is possible that SExtractor fails the identification classifying as astronomical sources peaks in the noise (see Fig. 2.4) To account for this, we run SExtractor with the weighted map: in this mode the software, for each pixel i, sets an optimal value of X (X_{opt}):

$$X_{opt} = X \times \sqrt{\sigma_i^2}, \tag{2.2}$$

where σ_i^2 is the noise level associated with the pixel i. Moreover, SExtractor can fail to accuratly identify sources in two particular cases: i) it recognises as a unique source two very close galaxies (see Fig. 2.5) and ii) it recognises as multiple sources single extended galaxies (see Fig. 2.6). This problem arises in crowded or deep fields where several sources whose pixels that lie above the detected threshold overlap, and hence are initially identified as a single object. SExtrator then attempts to separate such objects using a deblending method, whose efficiency can be varied using the deblending parameter.

We ran SExtractor with two different deblending parameters. We produced the bulk of the catalogue adopting a low deblending parameter (0.0001), which allows a suitable detection of close objects. However with this low deblending value, bright, extended galaxies (spirals in particular) are then

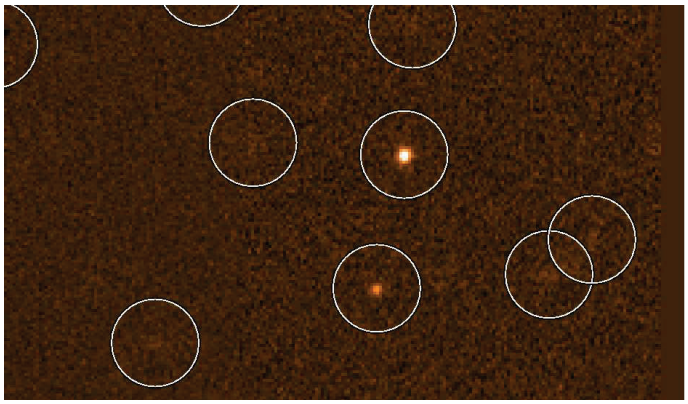

Figure 2.4: Examples of peaks in the noise identified by the software as astronomical sources.

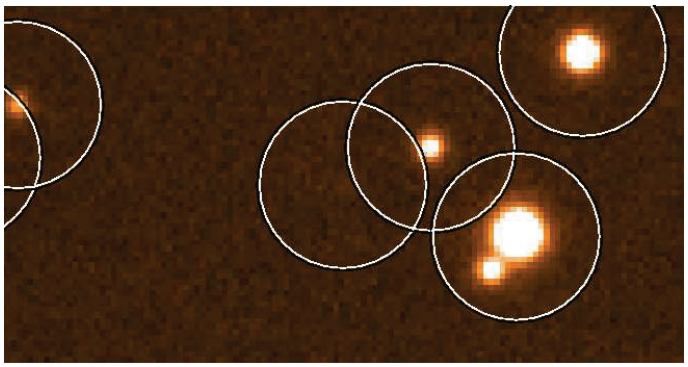

Figure 2.5: Examples of two sources identified by the software as a single astronomical source.

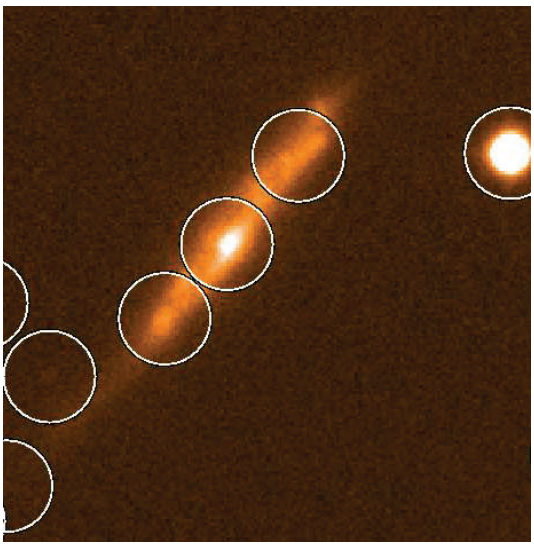

Figure 2.6: Examples of multiple detections of an extended object.

broken up by SExtractor into multiple sources. To correctly detect these objects, SExtrator was rerun using a high deblending parameter (>0.01) to ensure that SExtractor recognizes them as single entity.

The combined images show a significant number of bad and warm pixels, and cosmic ray residuals often detected by SExtractor as sources. These spurious detections were identified and then removed since either they are present only in a few exposures or they are particularly compact, comparing their M_{Kron} with the magnitude measured over the central pixel (see Fig. 2.7).

For faint sources, in the vicinity of bright galaxies with extended halos, SExtractor sometimes overestimates their R_{Kron} and M_{Kron}. To overcome this limit, we refer to plot of Fig. 2.2.1. From the direct visual check on the images, we tested that it is possible to select in this plot a region populated by objects with R_{Kron} much greater than the real extension of the sources. In these cases we substitute the M_{Kron} with an adaptive magnitude measured in a radius set according to the dimension of the source. These objects were identified and their M_{Kron} corrected.

Finally, spurious objects, ghosts or diffraction spikes around bright (R<15) stars were removed by defining circular avoidance regions (whose area is proportional to the stars flux level).

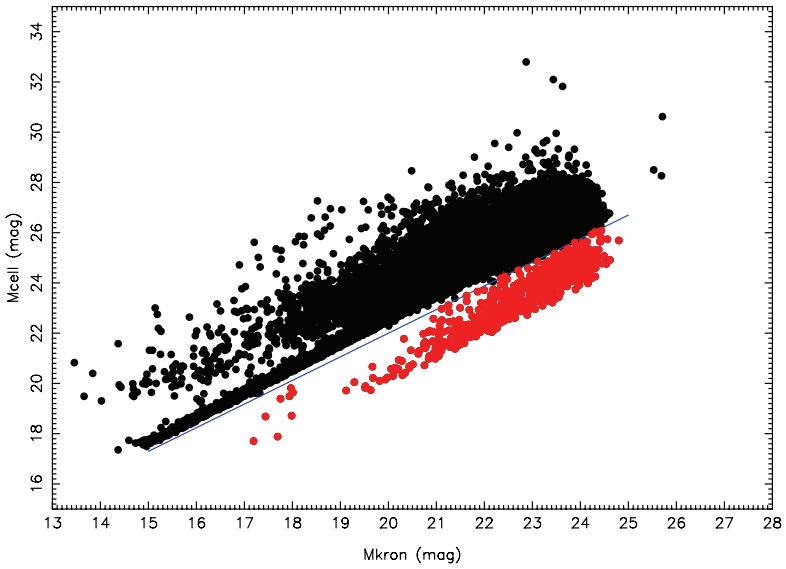

Figure 2.7: Magnitudes measured over the central pixel (M_{cell}) compared with the M_{Kron}. Red circles represent spurious objects. The blue line represents the cut imposed to reject these objects.

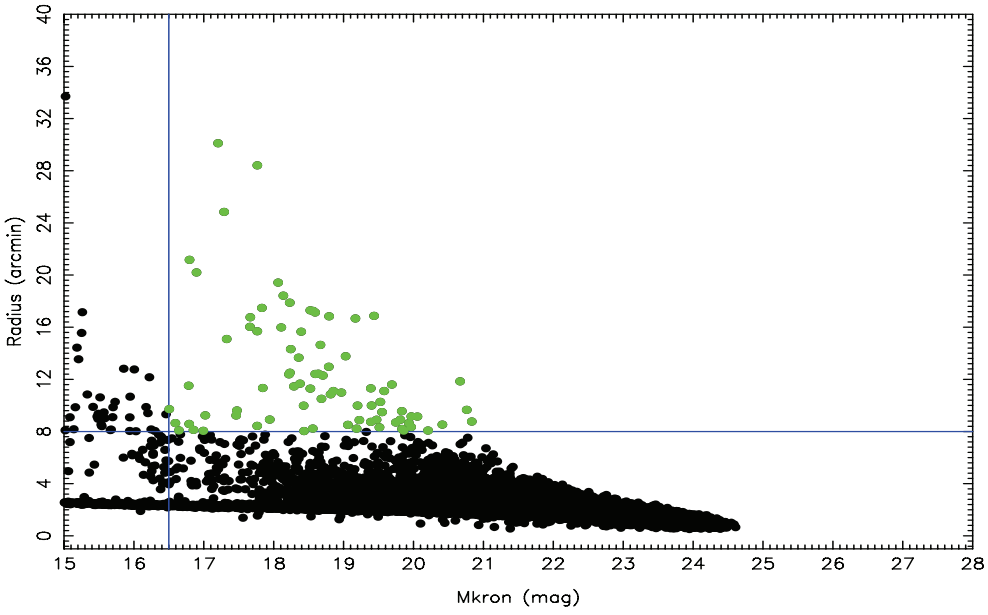

Figure 2.8: R_{Kron} vs M_{Kron}. In green are reported objects for which SExtractor fails the estimation of R_{Kron} and hence of M_{Kron}.

Table 2.3: Completeness and reliability of the SOS catalogues

R (mag)	completeness	% of stars misclassified
20.0–20.5	98.4	2.1
20.5–21.0	97.3	3.0
21.0–21.5	95.3	4.1
21.5–22.0	94.3	8.0
22.0–22.5	92.0	34.8
22.5–23.0	88.1	75.6

2.2.2 Completeness and reliability

The first estimates of the completeness magnitudes, derived using the prescription of Garilli et al. (1999), are 23.0 in the R-band, and 23.5 in the B-band. The reliability and completeness of the SOS catalogues were calculated for each 0.5 magnitude bin by adding 10 000 artificial stars and galaxies to the images, and computing the fraction of these sources detected and correctly classified by SExtractor. The artificial stars were created by taking a bright, non-saturated star (R $\sim$ 17) in the image and dimming it to the appropriate magnitude, while the galaxies were simulated by taking galaxies of differing Hubble types and the appropriate magnitude from the Hubble Ultra Deep Field (using photometry from the COMBO-17 Chandra Deep Field South catalogue; Wolf et al. 2004), resampling them to the resolution of the WFI, and convolving them with the image Point Spread Function (PSF).

At R = 22.0, 94.3% of the simulated galaxies were successfully detected and classified. In the SOS field the number of stars and galaxies become equal at R = 21.4. Beyond R = 22.0 the fraction of stars misclassified as galaxies increases dramatically mainly due to the blending of the sources. Moreover, further stellar contamination is due to the high number density of both stars and galaxies in this field (the Galactic latitude of the field is +30°) which increases the frequency of star-star and star-galaxy blends that can be misclassified as single galaxies. The estimates of completeness and reliability for the R-band are shown in Table 5.1.1. Analogous results were obtained for the *B*-band.

We adopted the conservative limits R = 22.0 and B = 22.5 as the magnitudes below which stellar contamination can be modelled and accounted for

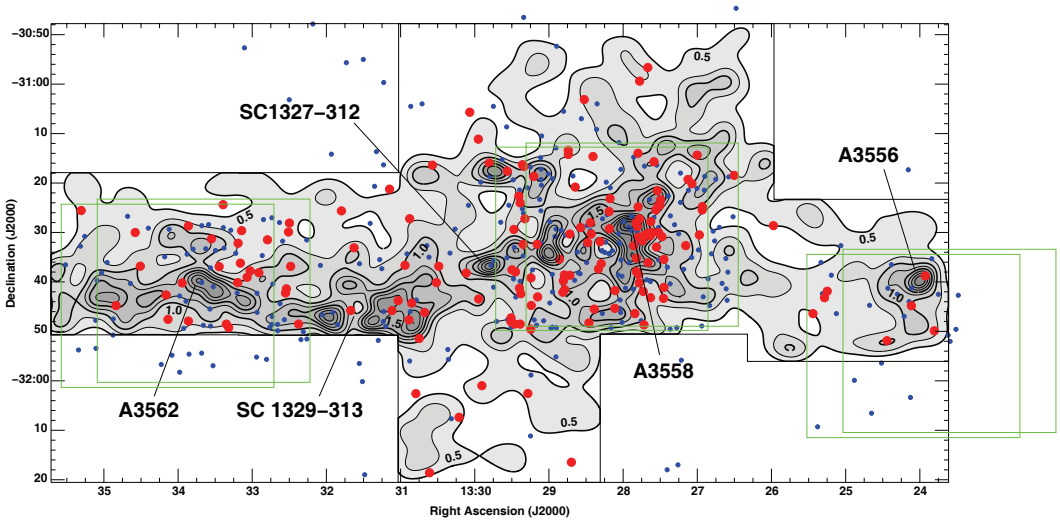

Figure 2.9: Density map of the SOS area (black lines) with supercluster galaxies observed spectroscopically but not included into the FP (blue points) and which enter the FP (red points) indicated. Green boxes are the regions covered by images of NFPS. The black contours are isodensity contours of R<21 galaxies (*Haines et al.* 2006a).

in the galaxy LF determination.

2.3 Complementary data

Spectra were obtained using the AAOmega fibre-fed spectrograph at the Anglo-Australian Telescope. The spectrograph consists of 400 fibres covering a field of view with diameter of 2 degrees. The fibre diameter of 2 arcsec corresponds to 1.9 kpc at Shapley redshift. The spectroscopic survey was carried by Dr. Russell J. Smith from Durham University, and a collaboration with his group has allowed us to have the full sample of 541 galaxies spectroscopically observed mainly in the Shapley supercluster core for the study of fundamental plane of this region (see chapter 4). The selection criteria set to choose the spectroscopic sample is simply R < 18 with no further regards for magnitude, colour or redshift. The bulk of target galaxies was drawn by the NOAO Fundamental Plane Survey (NFPS, Smith et al. 2004) BR-images centred on three clusters A3556, A3562, A3558 (green boxes in Fig. 2.9) and to fill vacant fibres brighter galaxies were selected from the 2MASS Extended Source Catalogue (R < 15.7). The total integration time

is about 8–9 hours. The blue arm of the spectrograph cover the main Lick indices (3700 Å $< \lambda <$ 5800 Å) with a resolution 3.5 Å FWHM sampled at 1.0 Å pixel^{-1}. Observations with the red arm (resolution equal to 1.9 Å at 0.6 Å pixel^{-1}) are also performed to obtain the H_α index. The spectral reduction was performed with the pipeline sc aao DRCONTROL plus a set of external procedures. Absorption-line heliocentric redshifts (z_{sp}) are measured with the IRAF package sc fxcor using the MILES (Medium resolution INT Library of Empirical Spectra) SSP models (Sánchez-Blázquez et al. 2006) with solar metallicity and ages 0.5, 1.0, 2.0, 4.0, 8.0 and 16.0 Gyr. Long integrations allow to obtain spectra of high signal-to-noise ratios, S/N∼45 per Å for σ<100 kms^{-1} and S/N∼90 per Å for σ>100 kms^{-1}. Velocity dispersions were measured with respect to the best-matching simple stellar population (SSP) templates. The errors were estimated from Monte Carlo simulations, and are ∼0.05 dex at σ<100 km s^{-1} and ∼0.01 dex for σ>100 km s^{-1}. The spectral resolution of 3.2 Å (82 km s^{-1} instrumental dispersion) allows recovery of velocity dispersions as low as ∼40 km s^{-1}. However, some galaxies in the sample remain kinematically unresolved, i.e. have velocity dispersions consistent with zero. The method used to obtain the velocity dispersions as well as the signal-to-noise levels of the spectra can produce systematic effects on the resultant values of σ, particularly for low-σ objects. Smith, Lucey & Hudson (2007, hereafter SLH) find that velocity dispersions obtained using single, old, solar-metallicity models instead of templates with different metallicities (as used in this paper) are underestimated by ∼6% for σ=75 km s^{-1} galaxies and by ∼18% for σ=50 km s^{-1}. When comparing the new velocity dispersion measurements with those previously obtained from the NFPS (having a factor ∼3 lower S/N), SLH find the new velocity dispersions of low-σ objects to be systematically lower by ∼0.10 dex, which they attribute to a combination of higher signal-to-noise, the use of templates over a range of metallicities, and Malmquist bias. Hence while our low-σ values are systematically lower than previous samples, an effect which could increase the FP tilt observed, we indicate that this is due to improvements in their measurements. Using the models of Thomas, Maraston & Bender (2003), the SLH absorption line data were used to estimate SSP-equivalent ages, metallicities and α-abundance ratios (Smith et al. in preparation). A full description of the survey is given by SLH.

The resulting scaling relations between the three stellar population parameters and velocity dispersion are:

$$\text{age} \propto \sigma^{0.426\pm0.053}, Z/H \propto \sigma^{0.320\pm0.045}, \alpha/\text{Fe} \propto \sigma^{0.204\pm0.026}. \qquad (2.3)$$

Typical errors for galaxies with σ in the range 50–100 km s^{-1} are 14% in age, 0.05 dex in [Z/H] and 0.04 dex in α/Fe, while they reduce to half these values

for galaxies with σ>150 km s^{-1}.

Starting from the sample of galaxies observed by SLH we selected those 396 galaxies belonging spectroscopically (0.039<z<0.056, shown as blue points in Fig. 2.9) to Shapley supercluster.

2.4 Structural parameters

SOS photometry is available for 378 supercluster galaxies observed by SLH, all of which are detected at signal-to-noise levels greater than 100 in each exposure, such that reliable structural parameters could be derived using the software 2DPHOT by La Barbera et al. (2008a). 2DPHOT is an automated tool to obtain both integrated and surface photometry of galaxies in an image and is furnished with several tasks to carry out reliable star-galaxy separation, PSF modelling, estimation of catalogue completeness and classification accuracy. The main steps of the 2DPHOT algorithm are: i) the creation of a clean catalogue of the input image with SExtractor; ii) estimation of the FWHM and the definition of "sure stars"; iii) the construction of an accurate PSF model taking in account both possible spatial variations as well as deviation of stellar isophotes from circularity; iv) the derivation of structural parameters (effective radius r_e, mean surface brightness $<\mu>_e$, Sersic index n, total magnitude m_{tot}, etc.) by fitting galaxy images with 2D PSF-convolved Sersic models.

The measurement of structural parameters is strictly dependent both on the PSF model and on the signal-to-noise ratio. Since the mosaic SOS images are obtained by stacking jittered images to cover the gap regions between CCDs, the signal-to-noise ratio is not constant along the images being lower in the overlapping gap regions. Moreover, the PSF is not well defined in the gap regions being strongly spatially varying. We removed the galaxies in these regions from our sample and performed the surface photometry only for galaxies in highest S/N regions (224 galaxies, Fig. 1 red dots), where the PSF is well defined. We corrected the mean surface brightnesses for cosmological dimming ($\sim$0.208), galactic extinction ($\sim$0.147) and k-correction ($\sim$0.05) and converted from mag arcsec^{-2} to $\log <I>_e$ expressed in physical units $L_{R\odot}$ pc^{-2} through $\log <I>_e = -0.4(<\mu>_e - M_{R\odot} - 5\log(206265\,\mathrm{pc}/10\,\mathrm{pc}))$ where $M_{R\odot}$ is the solar absolute magnitude set equal to 4.42.

2.4.1 Measuring the uncertainties in effective radius and mean surface brightness

To derive the errors, the structural parameters were measured also from the five single exposures (r_e^i, μ_e^i with i=1, 5), assuming the spread of values obtained to be caused by the effects of signal-to-noise uncertainties on the final mosaic value.

Due to the size of the sample (five exposures) only two scale estimators can be considered reliable (Beers et al. 1990): the classical standard deviation and the σ obtained by the gapper algorithm σ_{gap}. The gapper is a robust scale indicator (Wainer & Thissen 1976) based on the gaps between ordered statistics with an high level of efficiency for samples as small as five objects. If we have n measures of a quantity x ranked in increasing order (x_1,x_2,...x_{n-1},x_n), according to the gapper algorithm we can measure a robust scale indicator as:

$$\sigma_{gap} = \frac{\sqrt{\pi}}{n(n-1)} \sum_{i=1}^{n} w_i g_i, \tag{2.4}$$

where:

$$g_i = x_{i+1} - x_i, i = 1, ..., n-1 \text{ and } w_i = i(n-i). \tag{2.5}$$

To avoid an overestimation of the errors due to the presence of outliers, we first computed the σ_{gap} of the $\log r_e^i$ and $\log I_e^i$ distributions and rejected all values that deviated more than $3\sigma_{gap}$ from the median value, before subsequently computing the classical standard deviation as well as the covariance matrices of the clipped sample for both variables ($\delta_{\log r_e^i}$, $\delta_{\log I_e^i}$, cov[$\log r_e$; $\log I_e$]).

The errors on the mosaic value of $\log r_e$ and $\log I_e$ ($\delta_{\log r_e}$ and $\delta_{\log I_e}$ respectively) are given by $\delta_{\log r_e^i}/\sqrt{n}$ and $\delta_{\log I_e^i}/\sqrt{n}$, where n is the number of measures available. The typical errors on the logarithms of effective radius ($\log r_e$) and mean surface brightness ($\log I_e$) are 0.03 and 0.04 respectively. These errors explicitly include the effects of noise in the galaxy, but not the presence of neighbouring objects. The effect of the latter was measured by repeatedly placing copies of the galaxies one-by-one at random positions across the same CCD image (where the PSF should remain constant) and reapplying 2DPHOT, finding the variations in the structural parameters to be consistent with the previously obtained errors, albeit with a small number ($\sim$2%) of $>5\sigma$ outliers when the galaxy is placed very close to a bright star or galaxy.

2.5 The background control sample

Since the region covered by the SOS lies completely within the overdensity corresponding to the core complex, to perform a reliable statistical subtraction of field galaxies a suitable large control field is required, that has been observed with a similar filter set (B and R) to at least the depth of the SOS. The large area is necessary in order to minimize the effects of cosmic variance and small number statistics.

To this aim the Deep Lens Survey (DLS; Wittman et al. 2002) was chosen, which consists of deep BVRz imaging of seven $2^\circ \times 2^\circ$ degree fields. The observations have been made using the Mosaic-II cameras on the NOAO KPNO and CTIO 4-m telescopes, with exposure times of 12 000s in BVz' and 18 000 s in R, resulting in 5σ depths of B,V,R$\sim$ 27. The R-band images were obtained in good seeing conditions with a FWHM of $0.9''$, whereas the other bands have FWHM around $1.2''$. These characteristics allow accurate photometric measurements and star-galaxy classifications to be made to at least the depth of the SOS.

The catalogues were extracted following the same procedures as the SOS data. Thirteen $35' \times 35'$ Mosaic-II fields were chosen, covering a total area of ~ 4.44 square degrees (after removal of regions around bright stars) in two well separated regions of sky (fields 2 and 4 in the DLS). Given the depth of the DLS images, star-galaxy separation using the combined stellarity-FWHM classification method was found to be >99% efficient to R = 22.0. There are no nearby clusters in the regions covered. The rich cluster A 0781 at $z = 0.298$ is however located within field 2, and so the two affected fields closest to the centre of the cluster were not included among the thirteen.

2.6 Quantifying the Galaxy Environment

To study the effect of the cluster environment on galaxies in the SSC, the local density of galaxies, Σ, is determined across the SOS mosaic. This is achieved using an adaptive kernel estimator (Pisani 1993, 1996), in which each galaxy i is represented by a Gaussian kernel, $K(r_i) \propto \exp(-r^2/2\sigma_i^2)$, whose width, σ_i is proportional to $\Sigma_i^{-1/2}$ thus matching the resolution locally to the density of information available. For this study, the surface number density of $R < 21.0$ ($< \mathrm{M}^* + 6$) galaxies was considered, with an additional colour cut applied to reject those galaxies more than 0.2 mag redder in $B - R$ than the observed cluster red sequence (see § 3.3.2) to minimize background contamination, and to maximize the probability of considering only those galaxies belonging to SSC. As there are no known structures in

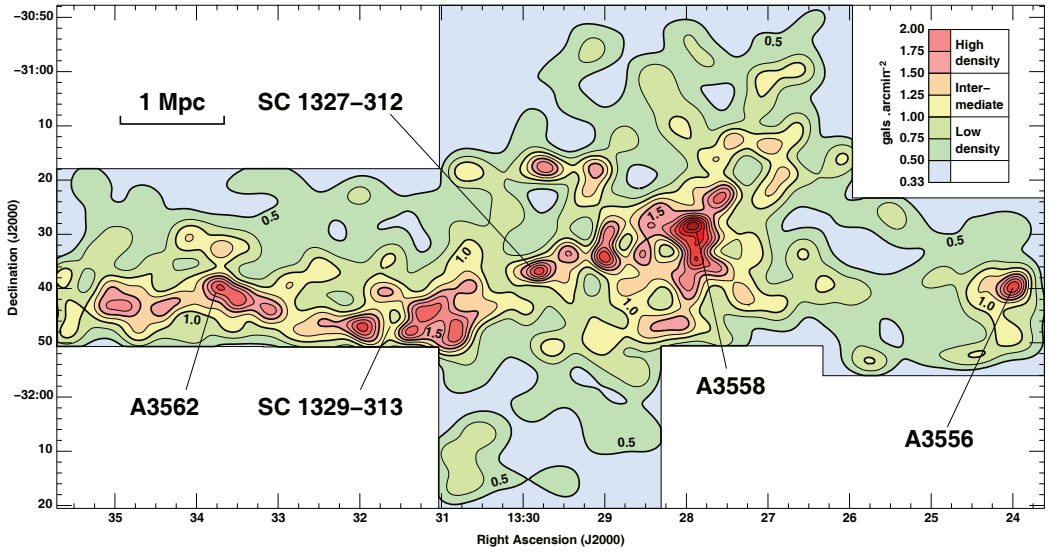

Figure 2.10: The surface density of $R < 21.0$ galaxies in the region of the Shapley Supercluster core complex. Isodensity contours are shown at intervals of $0.25\,\mathrm{gals\,arcmin^{-2}}$, with the thick contours corresponding to 0.5, 1.0 and $1.5\,\mathrm{gals\,arcmin^{-2}}$, the densities used to separate the three cluster environments. High-density regions ($\Sigma > 1.5$) are indicated by red colours, while intermediate- ($1.0 < \Sigma < 1.5$) and low-density ($0.5 < \Sigma < 1.0$) regions are indicated by yellow/orange and green colours respectively. The centres of X-ray emission for each of the clusters are indicated.

the foreground of the SSC (90% of $R < 16$ galaxies have redshifts confirming that they belong to the supercluster), any substructure identified in the density map is likely to be real and belonging to the supercluster. The local density is initially determined using a fixed Gaussian kernel of width 2 arcmin, and then iteratively recalculated using adaptive kernels. The resultant surface density map of the SSC is shown in Fig 5.1, with the three clusters and two groups indicated. Isodensity contours are shown at intervals of $0.25\,\mathrm{gals\,arcmin^{-2}}$, with the thick contours corresponding to 0.5, 1.0 and $1.5\,\mathrm{gals\,arcmin^{-2}}$, the densities used to separate the three cluster environments described below. The expected density of field galaxies is estimated through the analysis of the thirteen $35' \times 35'$ fields of DLS. Through applying the same colour-magnitude cuts, the density of field galaxies was estimated to be $0.335 \pm 0.019\,\mathrm{gals\,arcmin^{-2}}$, and hence the thick contours correspond to overdensity levels of ~ 50, 200 and $400\,\mathrm{gals}\,h_{70}^2\,\mathrm{Mpc}^{-2}$ respectively. The

entire region covered by the SOS can be seen to be overdense with respect to field galaxy counts.

For the following analyses on the effect of the cluster environment on its constituent galaxy population three regions are defined, selected according the local surface number density. Firstly we consider a high-density region with $\Sigma > 1.5\,\mathrm{gals\,arcmin^{-2}}$ which correspond to the cores of the clusters. Next we consider intermediate- ($1.0 < \Sigma < 1.5$) and low-density ($0.5 < \Sigma < 1.0$) regions which probe the filament connecting the clusters A3562 and A3558, as well as the wider envelope containing the whole supercluster core complex.

Chapter 3

Galaxy bimodality in the Shapley supercluster core: luminosity function and colour-magnitude relation

In this chapter we analyse the origin of galaxy bimodality in the complex region of the Shapley supercluster core, through the analysis of the luminosity function and colour magnitude relation as function of environment[1].

3.1 The scientific background

The luminosity function, which describes the number of galaxies per unit volume as function of luminosity, is a powerful tool to constrain galaxy evolution, since it is directly related to the galaxy mass function. Moreover, the effect of environment on the observed galaxy LF could provide a powerful discriminator among the proposed mechanisms for the transformations of galaxies. The effects of galaxy merging and suffocation on the cluster galaxy

[1]The results of this study are published in the articles:

- Mercurio, A.; Merluzzi, P.; Haines, C. P.; Gargiulo, A.; Krusanova, N.; Busarello, G.; Barbera, F. La; Capaccioli, M.; Covone, G. "Shapley Optical Survey - I. Luminosity functions in the supercluster environment", 2006, MNRAS, 368, 109-120.

- Haines, C. P.; Merluzzi, P.; Mercurio, A.; Gargiulo, A.; Krusanova, N.; Busarello, G.; Barbera, F. La; Capaccioli, M.; "Shapley Optical Survey - II. The effect of environment on the colour-magnitude relation and galaxy colours", 2006, MNRAS, 371, 55-66.

population have been studied through combining high-resolution N-body simulations with semi-analytic models for galaxy evolution (e.g., Springel et al. 2001; Kang et al. 2005). These show that while galaxy merging is important for producing the most luminous cluster galaxies, the resultant LF can always be well described by a Schechter (1976) function, although both M^* and the faint-end slope can show mild trends with environment. Galaxy mergers are also inhibited once the relative encounter velocities become much greater than the internal velocity dispersion of galaxies, and so are rare in rich clusters (Ghigna et al. 1998). In contrast, galaxy harassment and ram-pressure stripping may change the LF shape as galaxies lose mass in interactions with other galaxies, the cluster's tidal field, and the ICM. In particular Moore, Lake & Katz (1998) showed that harassment has virtually no effect on a system as dense as a giant elliptical galaxy or a spiral bulge and only purely disk galaxies can be turned into spheroidals, so these mechanisms produces a cutoff for Sd-Im galaxies. Since the luminosity function is strongly type specific, and those for Sc and Sd/Im galaxies can be described by narrow ($\sigma \sim 1$ mag) Gaussian distributions centred at $\sim M^*+1$ and $\sim M^* + 3$ (de Lapparent 2003), the effects of galaxy harassment could be characterized by a dip in the LF at these magnitudes.

Galaxy colours can be readily obtained to much fainter magnitudes than spectroscopic star-formation rates, and through the use of models can be directly related to star-formation histories with minimal assumptions (e.g. Bruzual & Charlot 2003). Recent large datasets have shown that the bimodality of galaxies is also manifested through their broadband photometry, in particular a separation can be made on the basis of colour into red and blue galaxy populations (Strateva et al. 2001; Blanton et al. 2003a), which correspond roughly to the two broad types previously known from their morphological and spectroscopical characteristics: passively-evolving early-type and star-forming late-type galaxies. This bimodality has been further quantified, resulting in colour-magnitude (C-M) relations and for both the red and blue galaxy populations (Baldry et al. 2004), and its evolution observed to $z \sim 1$ (Bell et al. 2004). Balogh et al. (2004a) show that the bimodal galaxy colour distribution is strongly dependent on environment, with the fraction of galaxies in the red distribution at a fixed luminosity increasing from 10–30% in the lowest density environments, to ∼70% at the highest densities.

In order to further investigate and to assess the relative importance of the processes that may be responsible for the structural galaxy transformations and that influence the star-formation history of galaxies, we have performed a photometric study of the SSC core, examining in particular the effect of the environment through the comparison of luminosity functions in regions with

different local densities and measuring the star-formation histories through galaxy colours.

The SSC was observed by Raychaudhury (1989) and the LF was firstly derived by Metcalfe, Godwin & Peach (1994; hereafter MGP94). By using photographic data, they investigate a region of 4.69 deg^2 around the cluster A 3558 considering a sample of 4599 galaxies complete and uncontaminated by stars (to 2% level) for $b < 19.5$. The derived LF for the central region of 1.35 deg^2 showed a broad peak in the number of galaxies at $b = 18$ which cannot be well fitted by a Schechter function. Moreover, MGP94 found a deficit of blue galaxies in the A 3558 core suggesting morphological segregation. However, their study is limited to bright magnitudes, preventing the determination of the faint-end slope while taking advantage of deeper photometry and larger sample of galaxies distributed in larger SSC area, we can provide clear evidence on the LF shape thus quantifying the environmental effect on the LF properties.

3.2 SOS Luminosity Functions

The LF in each band in the whole surveyed area was obtained up to the completeness magnitude limits, removing the interlopers by statistically subtracting the background contamination, as determined from thirteen control fields of the DLS, covering a total area of ~ 4.4 deg^2.

In order to investigate the effects of the environments we derived and compared the LFs, determined in the three different regions characterized by high-, intermediate- and low-densities of galaxies.

We fitted the observed galaxy counts with a single Schechter (S) function. However, since the LFs were generally poorly fitted by using such a model, the fits were also computed as the sum of Gaussian and Schechter (G+S) functions in order to describe bright and faint galaxy populations (e.g., de Lapparent et al. 2003; Molinari et al. 1998; Biviano et al. 1995). Moreover, we compared the LFs with the counts of the red sequence galaxies. We selected also galaxies bluer than the colour magnitude relation in order to derive the luminosity function of late-type galaxy populations.

Absolute magnitudes were determined using the k-corrections for early-type galaxies from models of Bruzual & Charlot (2003).

3.2.1 Background galaxy subtraction

We used data from the thirteen DLS control fields to estimate the background counts and the fluctuation amplitudes as in Bernstein et al. (1995).

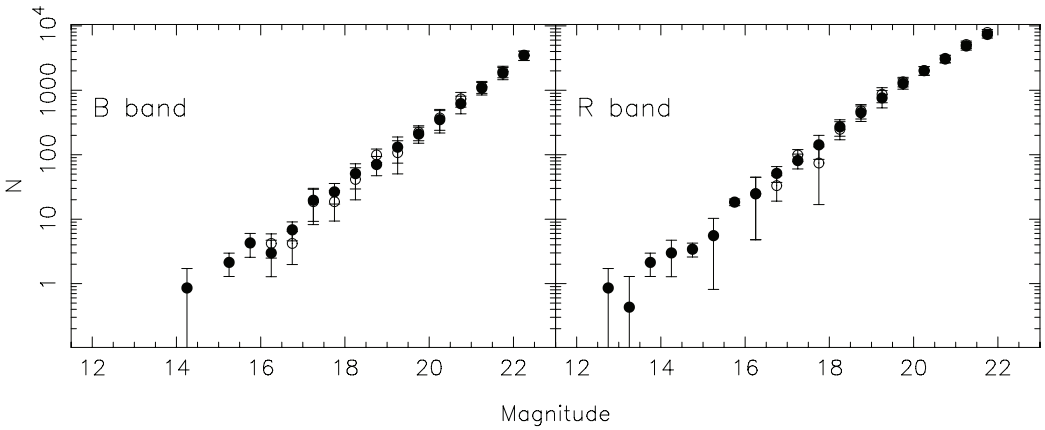

Figure 3.1: Comparison of galaxy counts obtained from the DLS (filled circles) and ESO-Sculptur Survey (open circles). The counts are normalized to the total area covered by the SOS data and are per half magnitude.

In this case the background counts were estimated as the mean of the control field counts (Eq. 1, Bernstein et al. 1995), and the fluctuations as the rms of the counts in each control field respect to the mean estimated in the all area (Eq. 2, Bernstein et al. 1995).

The galaxy number-magnitude counts obtained from the DLS data were found to be consistent with those from the literature (e.g., Arnouts et al. 1997) for the same passbands (see Fig. 3.1). An estimate for the total contribution from cosmic variance to the fluctuations of galaxy counts among the thirteen fields confirmed that, when combined, the obtained number magnitude counts are robust against cosmic variance.

The counts of SSC galaxies were defined as the difference between the counts detected in the supercluster fields and those estimated for the background (Eq. 3, Bernstein et al. 1995). By considering this definition, the uncertainties were measured as the sum in quadrature of fluctuations in the background and in the supercluster counts (Eq. 4, Bernstein et al. 1995).

In order to avoid the background counts taken from the DLS being too low, we make an additional comparison between SOS and DLS data. We selected galaxies 3 σ redder than the observed red sequence (Eqs. 3.12 and 3.2) in the SOS. Since galaxies redward of the sequence should be almost all background galaxies we compared these counts with those obtained for the DLS control fields applying the same colour cut. Figure 3.2 shows that these counts are consistent.

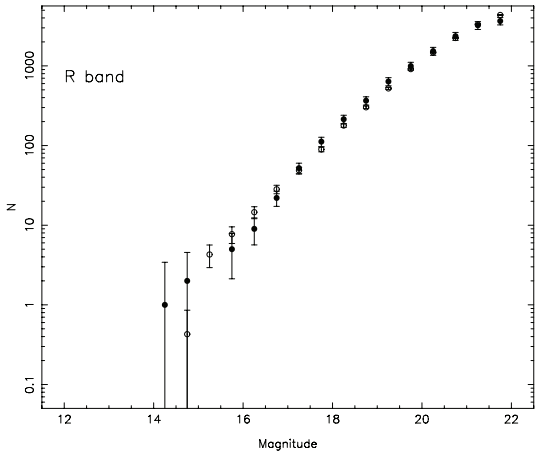

Figure 3.2: Comparison of R-band counts for galaxies redder than the red sequence (see text) obtained from the SSC (filled circles) and the DLS (open circles). The counts are normalized to the total area covered by the SOS data and are per half magnitude.

3.2.2 The total luminosity functions

Figure 3.3 shows the LFs in B and R bands for galaxies over the whole 2 deg^2 SOS area, covering the SSC core. The parameters of the fit are reported in Table 3.1. The weighted parametric fit of a Schechter function (dashed lines in Fig. 3.3) is unable to describe the observed changes in slope of the LF at faint magnitudes, in particular the dips apparent at B $\sim$ 17.5 ($M_B \sim$ - 19.3) and R $\sim$ 17.0 ($M_R \sim$ - 19.8) and the clear upturn in the counts for galaxies fainter than B and R $\sim$ 18 mag, apparent in Fig. 3.3. To successfully model these changes in slope requires a composite G+S LF (continuous line, Fig. 3.3), which represent the data distribution significantly better in both B ($P(\chi^2 > \chi^2_\nu)$=97% against $P(\chi^2 > \chi^2_\nu)$=0.08%) and R bands ($P(\chi^2 > \chi^2_\nu)$=95% against $P(\chi^2 > \chi^2_\nu)$=23%). The Schechter function fails most dramatically to describe the upturn in the galaxy counts at faint magnitudes, as demonstrated by the composite R-band faint-end slope being -1.62 as opposed to the Schechter slope of -1.26.

An upper limit to the background counts could be set by using the counts for galaxies in the SOS region with density less than 0.5, covering an area of $\sim$ 0.5 deg^2. The obtained LFs are consistent with those obtained by using DLS counts, but the error bars are too large to make any definitive conclusion on the faint-end part of the luminosity function.

Table 3.1: Fits to the LFs. Errors on the M* and α parameters can be obtained from the confidence contours shown in Figs. 3.3, 3.6 and 3.7. In the table S indicates the fit with a single Schechter and G+S those with Gaussian plus Schechter.

Region	Band	Function	m*	M*	α	μ		σ	χ^2_ν	$P(\chi^2 > \chi^2_\nu)$
all field	B	S	15.35	−21.42	−1.46				2.62	0.08%
all field	B	G + S	15.53	−21.24	−1.74	17.01	−19.76	1.32	0.36	97.1%
high density	B	S	14.64	−22.13	−1.46				0.95	50.3%
high density	B	G + S	16.47	−20.32	−1.51	17.00	−19.77	1.73	0.94	50.0%
int density	B	S	15.01	−21.76	−1.50				1.33	18.6%
int density	B	G + S	15.46	−21.31	−1.56	16.51	−20.26	0.85	0.50	89.1%
low density	B	S	15.57	−21.20	−1.49				2.22	0.69%
low density	B	G + S	16.11	−20.66	−1.66	16.96	−19.81	1.09	0.60	81.5%
all field	R	S	14.52	−22.26	−1.26				1.23	23.5%
all field	R	G + S	13.72	−23.06	−1.62	15.89	−20.89	1.23	0.46	94.7%
high density	R	S	14.29	−22.49	−1.30				0.86	61.7%
high density	R	G + S	14.15	−22.63	−1.30	20.92	−15.86	3.15	1.01	43.8%
int density	R	S	14.27	−22.51	−1.39				1.28	20.5%
int density	R	G + S	15.00	−21.78	−1.43	15.22	−21.49	0.98	0.74	71.3%
low density	R	S	13.75	−23.03	−1.50				3.33	0.002%
low density	R	G + S	15.28	−21.50	−1.80	16.37	−20.41	1.58	1.25	24.7%

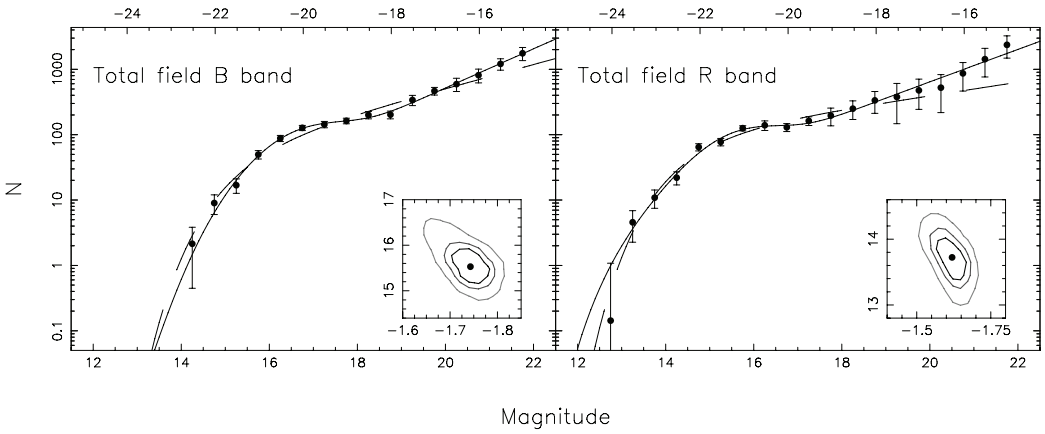

Figure 3.3: Luminosity function in the B and R bands over 2 deg^2 field covering the core of the SSC. Dashed and continuous lines are fits with the Schechter and with the Gaussian+Schechter (G+S) functions (see text), respectively. In the small panels the 1, 2 and 3σ confidence levels of the best–fit parameters for α and M* from the G+S fit, are shown. The counts are per half magnitudes.

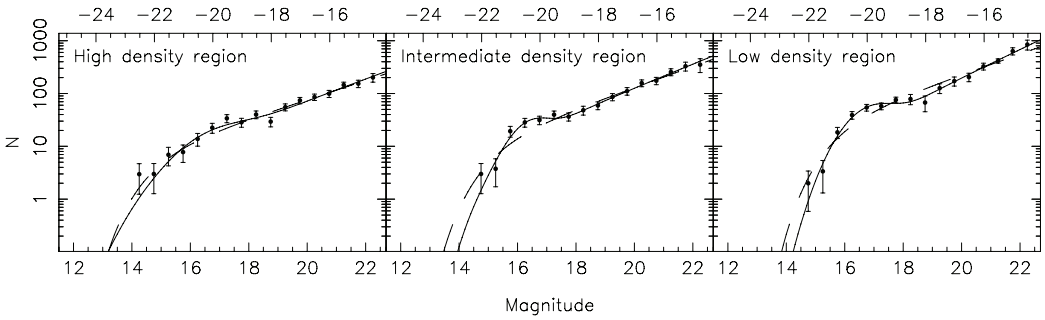

Figure 3.4: The B-band LFs of galaxies in the three cluster regions corresponding to high-, intermediate- and low-density environments. Dashed and continuous lines represent the fit with Schechter and Gaussian+Schechter functions respectively. The counts are per half magnitudes.

3.2.3 The effect of environment

Figures 3.4 and 3.5 show the B- and R-band galaxy LFs in the high-, intermediate- and low-density regions, covering areas of ~ 0.118, ~ 0.344, ~ 1.125 deg^2, respectively. Each LF was modelled by a weighted parametric fit to S (dashed lines) and to composite G+S functions (continuous lines). The best-fit values are listed in Table 3.1.

According to the χ^2 statistics in both bands the fit with a S function can be rejected in the low-density region, the LFs showing a bimodal behaviour due to the presence of a dip and an upturn for faint galaxies, that cannot be fitted by using a single function. In the intermediate-density region, although the Schechter function cannot be rejected, its fit gives a worse representation of the global distribution of data compared with a composite function ($P(\chi^2 > \chi^2_\nu) \sim 20\%$ against $P(\chi^2 > \chi^2_\nu) \sim$ 70-80%). On the other hand, in the high-density region the fit with a Schechter function is more suitable.

Figures 3.6 and 3.7 show the confidence contours of the best fitting functions for B and and R band, respectively, for the three density regions. The faint-end slope becomes significantly steeper from high- to low-density environments varying from -1.46 to -1.66 in B and from -1.30 to -1.80 in R band, being inconsistent at more than 3σ confidence level (c.l.) in both bands (right panel Figs. 3.6 and 3.7). Also the bright-end LF is inconsistent at more than 3σ c.l. in both bands, indicating that also the bright galaxy populations in the SSC depend on the environment. We note that the shape of the LFs vary dramatically from high- to low-density regions in both bands (see Fig. 3.8 for a direct comparison), demonstrating the strong effects of supercluster environment even in the low-density regions.

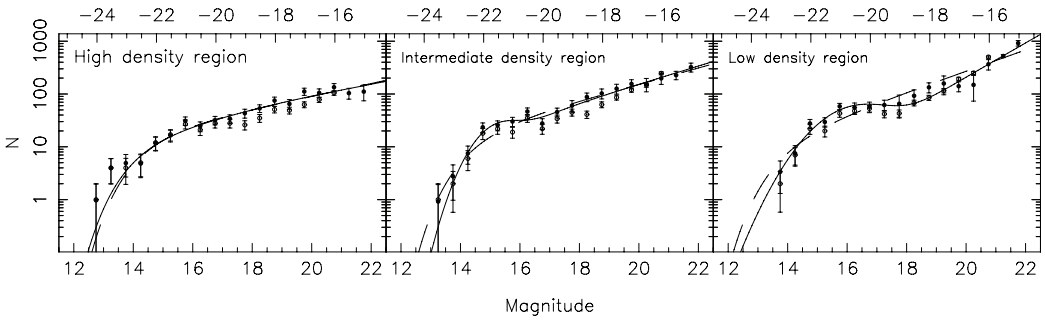

Figure 3.5: The R-band LFs of galaxies in the three regions corresponding to high-, intermediate- and low-density environments. Filled circles represent counts obtained from the photometric catalogue with a statistical background subtraction, open circles are the counts of galaxies with R<21 belonging to the red sequence of the CM relation (see Sect. 3.2.3). Dashed and continuous lines represent the fit with Schechter and Gaussian+Schechter functions respectively. The counts are per half magnitudes.

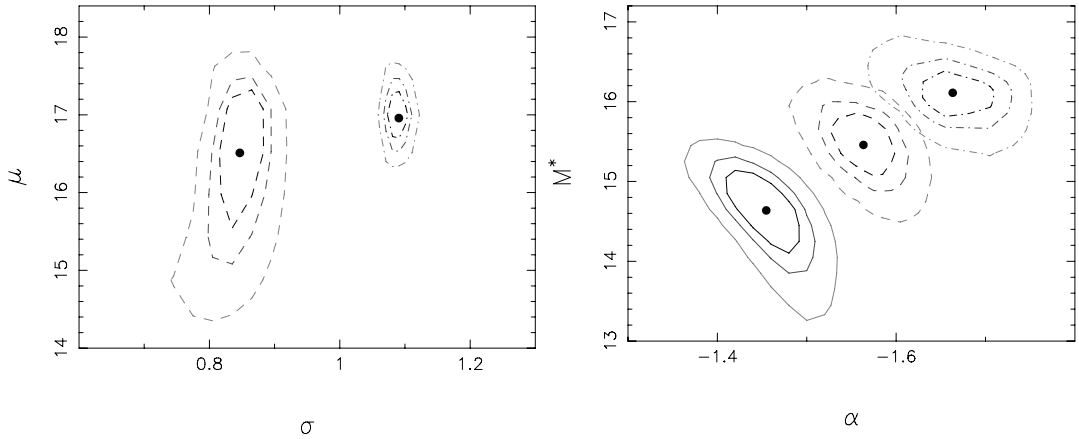

Figure 3.6: The 1, 2 and 3σ confidence levels for the B-band best-fitting Gaussian (left panel) and Schechter (right panel) parameters for the three cluster regions corresponding to high- (solid contours), intermediate- (dashed) and low-density (dot-dashed) environments. Contours in the high-density region are obtained by fitting data with a Schechter function.

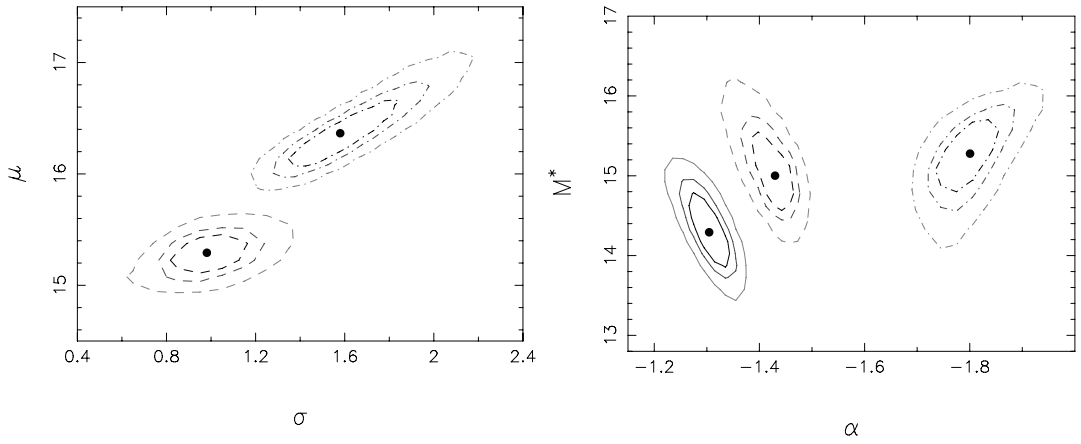

Figure 3.7: The 1, 2 and 3σ confidence levels for the R-band best-fitting Gaussian (left panel) and Schechter parameters (right panel) for the three cluster regions corresponding to high- (solid contours), intermediate- (dashed) and low-density (dot-dashed) environments. Contours in the high-density region are obtained by fitting data with a Schechter function.

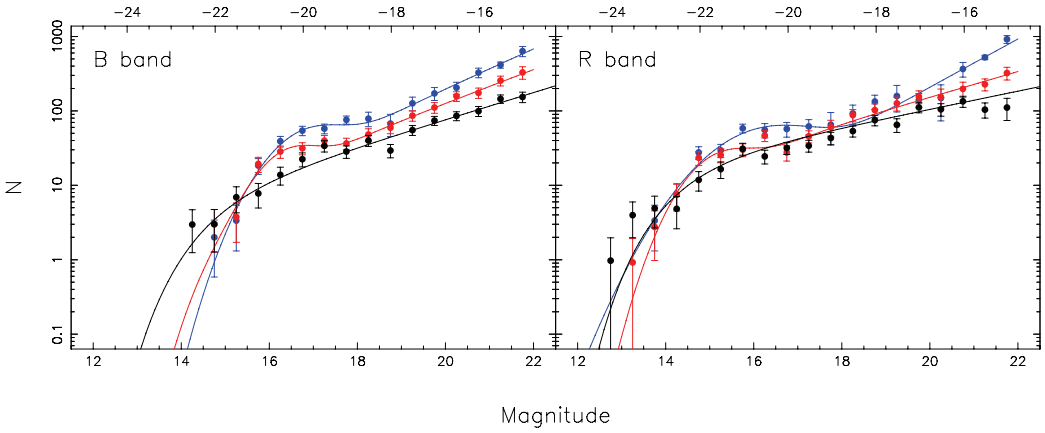

Figure 3.8: The B- (left panel) and R-band (right panel) LFs of galaxies in the three cluster regions corresponding to high- (black), intermediate- (red) and low-density (blue) environments. Continuous lines represent the best fit. The counts are per half magnitudes.

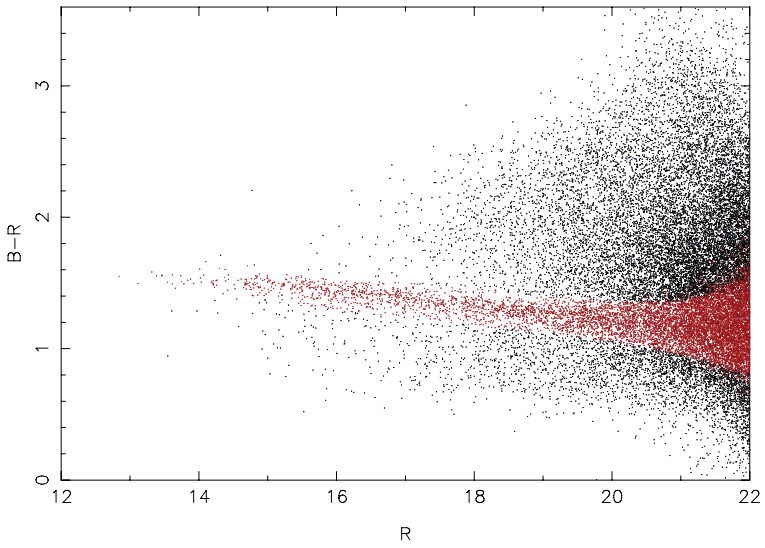

Figure 3.9: B-R vs R CM diagram for all the galaxies up to the completeness magnitude R=22.0 in the SOS field. Galaxies of the red sequence (see solid line) are plotted as red points.

3.2.4 LFs of red and blue galaxies

In order to further investigate the processes responsible for shaping the galaxy LF, we divided the galaxies into red and blue according to their location with respect to the colour magnitude relation (see par. 3.3.2 for determination):

$$(\mathrm{B}-\mathrm{R})_{\mathrm{CM}} = 2.3312 - 0.0563 \times \mathrm{R} \ . \tag{3.1}$$

We also evaluated the B-R colour dispersion around the red sequence as a function of the magnitude, $\sigma(\mathrm{R})$. The dispersion around the sequence is found to be consistent with the relation:

$$\sigma(\mathrm{R})^2 = \sigma^2_{\mathrm{int}} + \sigma^2_{(\mathrm{B-R})}(\mathrm{R}) \ , \tag{3.2}$$

where the intrinsic dispersion σ^2_{int} is equal to 0.0450 mag over the whole magnitude range covered (Haines et al. 2006a).

In Fig. 3.9 the red sequence galaxies are plotted as red points. We directly compare the counts of galaxies selected on the CM relation (open circles in Fig. 3.5) with those derived in Sect. 3.2.3 (filled circles in Fig. 3.5) in order to exclude projection effects due to background clusters. The counts for the sequence galaxies were obtained through a statistical background subtraction, applying the same colour cut of SOS galaxies to those in the

Table 3.2: Fits to the LFs of blue galaxies. Errors on the M* and α parameters are shown by the confidence contours shown in Fig. 3.11.

Region	m*	M*	α	χ^2_ν	P($\chi^2 > \chi^2_\nu$)
high density	16.59	−20.19	−1.39	0.78	66.1%
int density	14.66	−22.12	−1.56	0.96	48.9%
low density	14.70	−22.08	−1.52	1.05	40.0%

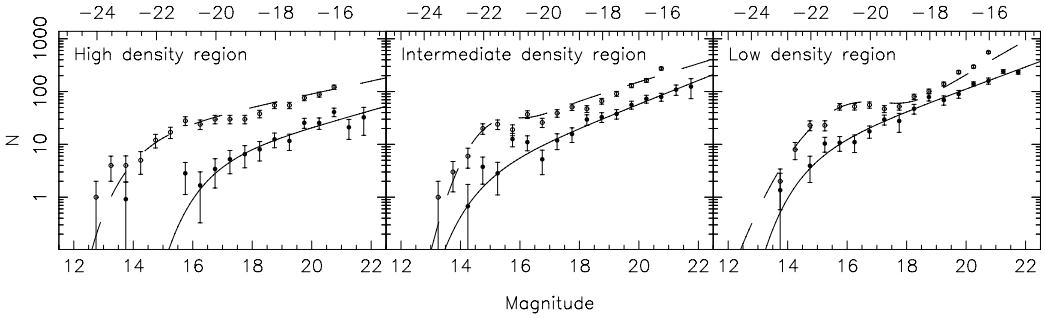

Figure 3.10: The R-band LFs of red (open circles) and blue galaxies (filled circles) in the three cluster regions corresponding to high-, intermediate- and low-density environments. Continuous and dashed lines represent the best fit for blue and supercluster galaxies respectively. The counts are per half magnitudes.

DLS control field. The distributions of red galaxies in the three different density regions are well described by the total LFs, since also in this case there is a dip at R$\sim$ 17.0 ($M_R \sim$ -19.8).

We also selected the blue supercluster galaxies considering the galaxies 3σ bluer than the CM relation. Figure 3.10 shows the LFs obtained for the red sequence and blue galaxy population in high-, intermediate- and low-density regions. The blue galaxy LFs were obtained through a statistical background subtraction, applying the same colour cut of the supercluster galaxies to those in the DLS control fields. In contrast to the red sequence galaxies, the blue galaxy LFs are well described by a Schechter function and do not vary with the density (see contours in Fig. 3.11). This indicates that the blue galaxies represent a population that have not yet interacted with the supercluster environment.

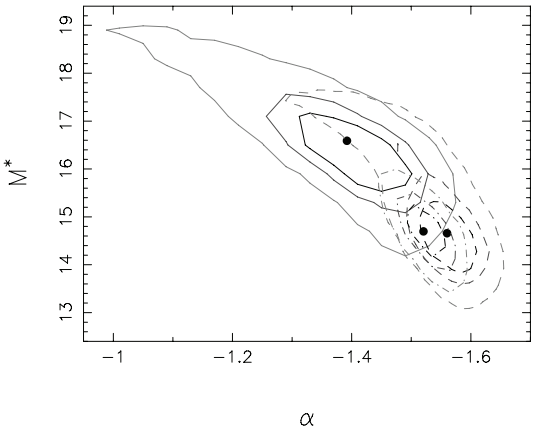

Figure 3.11: The 1, 2 and 3σ confidence levels for the R-band best-fitting Schechter parameters for the blue galaxies in the three cluster regions corresponding to high- (solid contours), intermediate- (dashed) and low-density (dot-dashed) environments.

3.2.5 SOS LF: summary and discussion

In this detailed analysis of the LFs for galaxies in the SSC core, all the luminosity functions were calculated through a weighted parametric fit of a single Schechter function and a composite function, given by the sum of a Gaussian for the bright-end and a Schechter for the faint-end of the LF. The main results of our analysis are the following.

- The LFs in the whole SOS area have a bimodal behaviour both in B and R band. The weighted parametric fit of a Schechter function is unable to describe the observed LF at faint magnitudes, in particular the dips apparent at B $\sim$ 17.5 ($M_B \sim$ - 19.3) and R $\sim$ 17.0 ($M_R \sim$ - 19.8) and the clear upturn for galaxies fainter than 18 mag. To successfully model these dip and changes in slope a composite Gaussian+Schechter LF is required.

- By deriving the LFs in regions with different local surface densities of R$<$ 21.0 galaxies we showed that, as observed in the LFs of the whole field, a dip is present at $M_R \sim$ -19.8 for LFs in intermediate- and low-density regions, while for the high-density region, the data are well represented by the Schechter function. Moreover the faint-end slope, α, shows a strong dependence on environment, becoming steeper at $> 3\sigma$ significance level from high- (α_B = -1.46, α_R = -1.30) to low-density environments (α_B = -1.66, α_R = -1.80) in both bands.

- We derived the LFs separately for red and blue galaxy populations according to their B-R colours. The LFs of these two populations show a very different behaviour. In fact differently from the red sequence galaxy counts that are very similar to those obtained with a statistical background subtraction, the blue galaxy LFs are well described by a S function and do not vary with the density.

These results confirm and extend those of MGP94 who found a peak in the number of galaxies at $b = 18$ and suggested that the Abell function is a better representation of the integral counts than the Schechter function. However, their optical LF is limited at galaxies three magnitudes brighter than those analysed in the present work, preventing the determination of the steepening of the LF faint-end and a more clear definition of the LF shape. On the other hand, MGP94 also noted that the CM red sequence galaxies show the broad peak at bright magnitudes in agreement with our findings.

The bimodality of the galaxy LF is commonly observed for rich clusters (e.g., Yagi et al. 2002; Mercurio et al. 2003), and using data from the RASS-SDSS galaxy cluster survey, Popesso et al. (2006) find a similar variation of the LF with environment to that observed here, but using cluster-centric radius rather than local density (e.g., Haines et al. 2004b) as a proxy for environment. This observed bimodality and its variation with environment can be best accommodated in a scenario where bright and faint galaxy populations have followed different evolution histories.

The SDSS and 2dFGRS surveys have indicated that the evolution of bright galaxies is strongly dependent on environment as measured by their local density, yet is independent of the richness of the structure to which the galaxy is bound, indicating that mechanisms such as merging or suffocation play a dominant role in transforming galaxies, rather than harassment or ram-pressure stripping (Gómez et al. 2003; Tanaka et al. 2004). However, it is difficult to reconcile the dramatic deviations from the S function observed for intermediate- and low-density regions with the transformation of field galaxies being due to just merging or suffocation, neither of which should alter the shape of LF, whilst they can be explained more easily by a scenario involving mass loss of low-luminosity galaxies.

One such mechanism is galaxy harassment (Moore et al. 1996, 1998), whereby repeated close ($<50\,\mathrm{kpc}$) high-velocity ($>1000\,\mathrm{km\,s^{-1}}$) encounters with bright galaxies and the cluster's tidal field cause impulsive gravitational shocks that damage the fragile disks of late-type spirals. The cumulative effect of these shocks is the transformation of late-type spirals to spheroidal galaxies over a period of several Gyr. An important aspect of galaxy harassment is that it has virtually no effect on systems as dense as giant elliptical

or spiral bulges, and hence only pure disk systems (Sc or later) are affected. While these galaxies make up the vast majority of the faint (M>M*+2) cluster galaxy population at z0.4, they become rarer exponentially at brighter magnitudes. The encounters can drive the bulk of the dark matter and 20–75% of the stars over the tidal radius of the harassed galaxy, whereas in contrast the bulk of the gas collapses inward, and is consumed in a nuclear starburst. The combined results of these effects is a dimming of the harassed galaxy by $\sim$ 2 magnitudes due to mass loss and passive ageing of the remaining stars. These remnants are apparent in present day clusters as dwarf spheroids which often show blue cores suggesting nuclear star-formation, as well as remnant disk and bar components (Graham, Jerjen & Guzman 2003), and signs of rotational support (de Rijcke et al. 2001).

In agreement with the recent work by Popesso et al. (2006) we suggest that the observed dip at $M_R \sim -19.8$ as well as the strong dependence on environment shown by the faint-end slope in the cluster galaxy luminosity can be explained naturally as the consequence of galaxy harassment.

Alternative mechanisms such as ram-pressure stripping by the ICM or tidal stripping can effect the galaxy population only in the cluster cores, which appears inconsistent with our observation that the dip is greatest in the low-density regions 1–2 Mpc from the nearest cluster. However, given the high infall velocities, any galaxy encountering the ICM is likely to be stripped rapidly of their gas, bringing star-formation to a swift halt. Given the high infall velocities, and the typical highly eccentric orbits of cluster galaxies, the low- and intermediate-density regions are likely to contain a significant fraction of galaxies that have already encountered the dense ICM. In high-density regions, high-velocity dispersions inhibit merging processes (e.g., Mihos 2004), hence it is unlikely that dwarf galaxies merge to produce bigger galaxies at the cluster centres. The most likely explanation for the lack of dwarf galaxies near the centre is tidal or collisional disruption of the dwarf galaxies.

This interpretation is also confirmed when analysing separately red sequence galaxies. In fact the red galaxy counts exhibit a behaviour similar to those of the LFs obtained with a statistical background subtraction, confirming the excess of dwarf early type galaxies. Moreover, differently from red sequence galaxies, the blue galaxy LFs are well described by a S function with a slope $\alpha \sim$ -1.50 and do not vary with density. This slope is consistent with those recently derived by Blanton et al. (2005b) and Madgwick et al. (2002) for field SDSS and 2dF galaxies respectively. This suggests that the observed blue galaxy population is characterized by infalling galaxies that have not yet interacted with the super cluster environment and transformed by the harassment mechanism.

3.3 SOS galaxy colours

The colour-magnitude relation (CMR) was estimated considering galaxies with local density $\Sigma > 1.0\,\mathrm{gal\,arcmin^{-2}}$ to avoid a priori field contamination. For this sample a statistical field galaxy subtraction is performed, on the basis of spectroscopic data of Bardelli et al. (1998)
We study the dependence of CMR on environment measuring the overall distribution of B-R colours with respect to the observed CM. Moreover, as galaxy colour can be directly related to galaxy star-formation histories, through the analysis of the spatial distribution of red and blue galaxies we gain information on influence of environment on star-formation.

3.3.1 Statistical Field Galaxy Subtraction

To accurately measure the global photometric properties of the galaxy population in the SSC requires the foreground / background contamination to be estimated efficiently and corrected for. There exists already a wealth of spectroscopic data in the region, comprising 607 published galaxy redshifts (Bardelli et al. 1998) corresponding to 90% of $R < 16$ galaxies, dropping to 50% for $R < 17.7$. For those galaxies without redshifts, particularly at fainter magnitudes, we estimate the probability that they are supercluster members. This probability is dependent on the spatial position, the R-band magnitude and $B - R$ colour. The dependence on its spatial position, through its local number density, is clear as galaxies towards one of the density peaks will be more likely to be members than those in regions where the surface density is closer to that expected for the field. The dependence on the galaxies colour and magnitude is complex, with galaxies located on the cluster red sequence most likely to be members, while those galaxies much redder than the sequence most likely to belong to the background population. It is important that all three parameters are considered simultaneously, as the relationship between the broad-band properties of galaxies and their environment has been shown to be complex (Blanton et al. 2003a).

We account for this by considering separately the three cluster environments described previously when estimating the probability that galaxies are supercluster members through their R-band magnitude and $B-R$ colour using the methods described in Kodama & Bower (2001). For each of these three cluster environments and the Deep Lens Survey field comparison, two-dimensional histograms are built with bins of width 0.4 mag in R and 0.2 mag in $B - R$ to properly map the galaxy C-M distribution. The histogram of field galaxies is normalised to match the area within each cluster region, and for each galaxy, the probability that galaxy i belongs to the supercluster is

then defined as:

$$P^i_{SC} = \frac{\Sigma_{SC}(R, B-R)_i - \Sigma_{field}(R, B-R)_i}{\Sigma_{SC}(R, B-R)_i}, \tag{3.3}$$

where $\Sigma_{SC}(R, B-R)_i$ and $\Sigma_{field}(R, B-R)_i$ are the number densities of galaxies in the supercluster and field environments belonging to the corresponding bin in R and $B-R$. In low-density environments it is possible that $\Sigma_{SC}(R, B-R)_i < \Sigma_{field}(R, B-R)_i$ for a particular bin, and so in these cases the excess number of field galaxies are redistributed to neighbouring bins with equal weight until $\Sigma_{SC}(R, B-R)_i \geq \Sigma_{field}(R, B-R)_i$ for all bins. For those galaxies with redshifts P^i_{SC} is set to 1 for $0.035 < z < 0.056$ (the redshift range of known supercluster members in the SOS field) or 0 otherwise. Hence for each $R < 21$ galaxy in the region covered by the SOS, we estimate the likelihood of its belonging to the Shapley supercluster based upon its R-band magnitude, $B-R$ colour and local density.

3.3.2 The Colour-Magnitude relation

To estimate the location of the colour-magnitude relation for galaxies in the supercluster, we consider those galaxies with local densities $\Sigma > 1.0$, i.e. both intermediate- and high-density environments, in order to avoid *a priori* field contamination effects when measuring the C-M slope. Figure 3.12 shows the resulting C-M diagram for a Monte Carlo realisation of the galaxy population in these regions, in which those galaxies predicted to belong to the supercluster indicated by the larger symbols, and those belonging to the field indicated by the small points. A clear red sequence is apparent for $13 < R < 20$. However at $R < 15$ it becomes notably flatter, while at $R > 19$ it becomes increasingly difficult to separate it from the remainder of the cluster population. This flattening at the brightest magnitudes has been noted previously for this region (Metcalfe, Godwin & Peach 1994), and has been observed for a large sample of galaxies from the Sloan Digital Sky Survey (Baldry et al. 2004), indicating this is a universal phenomenon. The slope in the C-M relation has been considered due to a progressive increase in metallicity with mass due to the greater ability of more massive galaxies to retain metals dispersed by supernova during their formation, and so the observed flattening of the C-M slope probably represents the same flattening of the mass-metallicity seen for galaxies with $M_* 10^{10.5}\,M_\odot$ (Tremonti et al. 2004), which in turn may reflect the observation that the brightest galaxies are built up through "dry mergers" of $\sim M^*$ galaxies (e.g. Faber et al. 2007), and hence would have the same metallicities and colours as their progenitors.

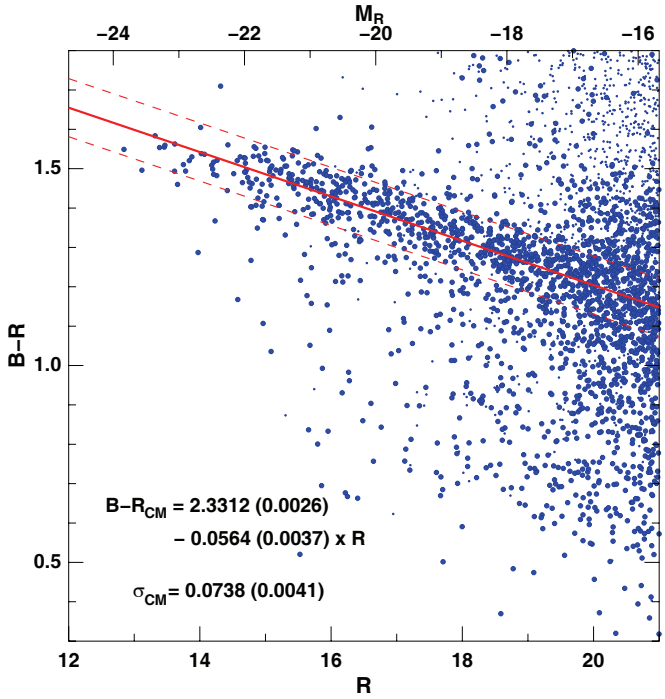

Figure 3.12: The $B - R/R$ colour-magnitude diagram of galaxies in the regions corresponding to intermediate- and high-densities ($\Sigma > 1.0\,\mathrm{gal\,arcmin^{-2}}$). The larger points represent a Monte Carlo realisation of the supercluster galaxy population, while the remaining (and hence field) galaxies are shown by the small points. The best-fitting C-M relation is indicated by the solid red line, with the parallel dashed lines indicating the 1σ dispersion levels.

We perform a fit to the C-M relation over the range $14.5 < R < 19.0$, where the red sequence relation appears linear and can be separated from the rest of the cluster population. Although the red sequence appears visually quite distinct, obtaining a robust fit to it is not trivial, particularly given the presence of outliers which are heavily skewed bluewards of the relation, and so simple least-squares methods are unsuitable. We apply the same method as López-Cruz et al. (2004), which produced the most robust results by iteratively applying the biweight algorithm (Beers, Flynn & Gebhardt 1990) with 3σ clipping to counteract the heavily skewed distribution. A range of slope values were searched to determine the best-fitting value that minimizes the biweight scale of the deviations from the median value.

The uncertainties in the slope and intercept are derived using the non-parametric bootstrap method. The number of cluster galaxies, n, is estimated as $n = \sum_{i=1}^{N} P_{SC}^{i}$ for the N galaxies with $14.5 < R < 19$, and each bootstrap performed by sampling n galaxies with replacement according to the probabilities P_{SC}^{i} calculated using Eq. 3.3. Babu & Singh (1983) have analytically estimated that $\sim n \log^2 n$ bootstrap resamplings give a good approximation to the underlying density population. The resultant best-fitting C-M relation is found to be:

$$(B-R)_{CM} = 2.3312 \pm 0.0026 - 0.0564 \pm 0.0037 \times R, \qquad (3.4)$$

where the quoted uncertainty in the intercept assumes a fixed value of slope. The obtained dispersion about the relation as given by the biweight scale of the deviations is 0.0738 ± 0.0041 mag.

As a robust test of the results obtained using the biweight algorithm, we plot a histogram of the distribution of $\Delta(B-R)_{CM}$, the $B-R$ galaxy colour offset from the C-M relation, and model the distribution as a sum of two Gaussian functions, one to represent the red sequence, and another to represent the "blue cloud" population. Fig 3.13 shows that a bimodal Gaussian distribution describes well the distribution of $\Delta(B-R)_{CM}$ ($\chi^2/\nu \approx 1$), but with a mean offset of 0.0069 ± 0.0027 mag with respect to the biweight median, and a dispersion of 0.0453 ± 0.0019 mag that is significantly smaller than predicted by the biweight scale estimator, and comparable to the 0.054 mag dispersion observed for the Coma cluster in the same passbands (López-Cruz et al. 2004). Hence despite iteratively clipping galaxies $> 3\sigma$ from the median value of the relation, both the intercept and dispersion of the relation obtained using the biweight algorithm have been affected by outliers and the heavily skewed distribution.

We do not expect that photometric uncertainties are a major contributor to the observed dispersion as: firstly the mean $B-R$ uncertainty for galaxies

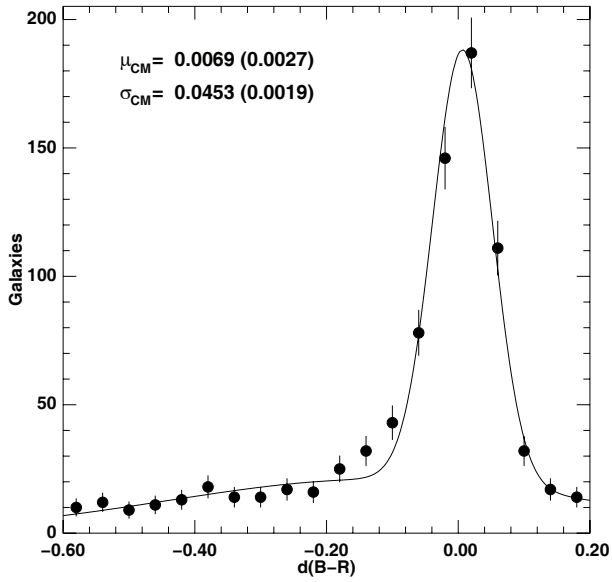

Figure 3.13: The distribution of $B-R$ galaxy colours offsets from the C-M relation predicted by the biweight algorithm for $R < 19$ galaxies with local densities greater than $1.0\,\mathrm{gal\,arcmin^{-2}}$.

in the red sequence is found to be 0.012 mag, only reaching 0.025 mag by $R = 19.0$; and secondly the observed dispersion does not vary significantly as a function of magnitude over $14.5 < R < 19$.

It is remarkable that such a small dispersion is obtained, given the large number of galaxies involved (~ 600) over two orders of magnitude in luminosity, and spread across three rich clusters and $\sim 9\,h_{70}\,\mathrm{Mpc}$. The wide spread of redshifts within the supercluster complex ($0.035 < z < 0.056$) could introduce a significant component to the observed dispersion through the spread of k-corrections required for the red sequence galaxies, as the predicted change in the $B-R$ k-correction of an elliptical galaxy from 0.035 to 0.056 is ~ 0.08 mag (Poggianti et al. 2004), as is the observed increase in $B-R$ colour of red sequence galaxies (López-Cruz et al. 2004).

To measure the possible effect of k-corrections on the obtained colour dispersion of red sequence galaxies, we consider those red sequence galaxies with known redshifts. Although the redshift data is less than 50% complete beyond $R = 17.7$, the $B-R$ colour dispersion of the red sequence galaxies with redshifts is consistent with that for the whole $R < 19$ sample. After applying suitable k-corrections to each of the galaxies with known redshifts, and the colour dispersion about the red sequence is recalculated, found to be still consistent with that before the k-correction has been applied. Hence

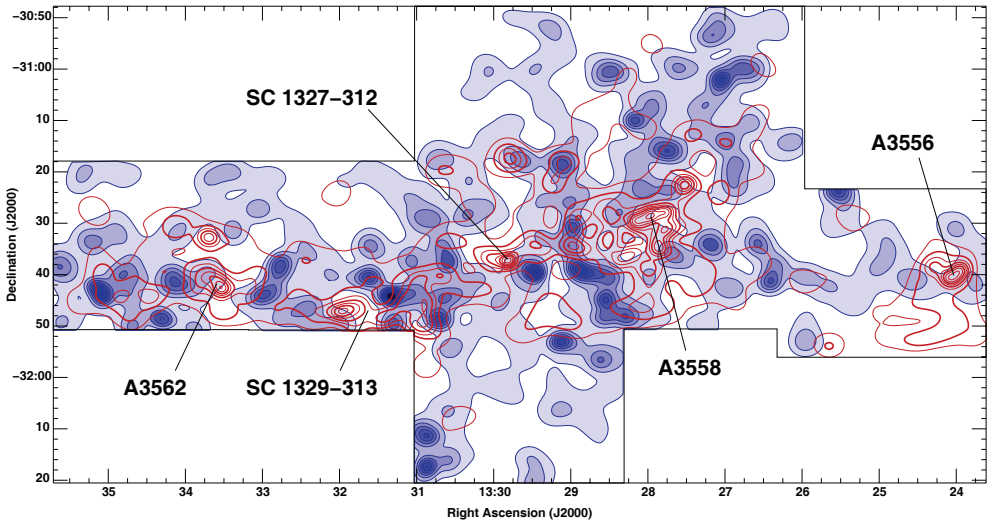

Figure 3.14: The surface density of $R < 21$ galaxies $> 3\sigma$ bluer than the cluster red sequence (blue filled contours) and those within 3σ of the cluster red sequence (red contours) over the supercluster core complex. The isodensity contours for the blue galaxies are shown at intervals of $0.125\,\mathrm{gals\,arcmin^{-2}}$, while the red contours are at intervals of $0.25\,\mathrm{gals\,arcmin^{-2}}$. The centres of X-ray emission for each of the clusters are indicated.

the observed internal dispersion of galaxy colours around the red sequence is not primarily the effect of different k-corrections over the redshift range of the supercluster. This can be explained by considering that the redshift distribution has a standard deviation of 0.0036 ($\sim 1\,100\,\mathrm{km\,s^{-1}}$), corresponding to an rms σ of ~ 0.014 mag in $B-R$, significantly smaller than the observed σ_{CM}.

To examine the effect of environment on the colour of the C-M relation we fit bimodal Gaussian distributions to the $\Delta(B-R)_{CM}$ distribution in the three environments as parametrised by the local $R < 21$ galaxy density. The slope and zero-point are maintained fixed at the values indicated in Eq., in order to measure the shifts in the overall $B-R$ colour of the red sequence with environment. We do not make any attempt to determine the slope and intercept in the differing environments using the biweight algorithm, as the effect of the heavily skewed distribution on the determination of these values will be dependent on environment, due to the increasing blue galaxy fraction from high- to low-density regions. Hence the resulting fits would be biased by the changing blue galaxy population, and mask any inherent changes in the red sequence population with environment.

The results of the Gaussian fits to the red sequence population are shown

Table 3.3: Gaussian fits to the $B-R$ colour distribution around the C-M relation for $R<19$ galaxies in the different density environments

$R<21$ gals arcmin^{-2}	μ_{CM}	σ_{CM}	χ^2/ν
$\Sigma>1.0$	$+0.0069\pm0.0027$	0.0453 ± 0.0019	0.99
$\Sigma>2.0$	$+0.0191\pm0.0064$	0.0460 ± 0.0044	0.24
$\Sigma>1.5$	$+0.0142\pm0.0043$	0.0486 ± 0.0031	0.47
$1.0<\Sigma<1.5$	-0.0004 ± 0.0035	0.0442 ± 0.0024	1.40
$0.5<\Sigma<1.0$	-0.0012 ± 0.0042	0.0540 ± 0.0031	1.04

in Table 3.3. In each case the galaxy colour distribution is well described by a double Gaussian function. The zero-points of the red sequence are consistent for the low- and intermediate-density regions, but the red sequence is found to be 0.0147 mag redder in the high-density region, a result significant at the 2.6σ level. The redward shift of the red sequence continues if the density threshold is increased further, reaching 0.0195 mag for $\Sigma>2.0$. The $B-R$ colour dispersion of the red sequence remains constant at $\sim$0.045, for each of the environments, suggesting that the observed reddening indicates an overall *shift* in the red galaxy population, rather than a *broadening* of the distribution due to increased numbers of bluer galaxies.

3.3.3 The Spatial Distribution of Red and Blue Galaxies

To examine where star-formation has been triggered or inhibited by the supercluster environment, we split the galaxy population into two according to colour. We identify red galaxies as those within 3σ (after including photometric uncertainties) of the cluster red sequence, and blue galaxies as those $>3\sigma$ bluer than the red sequence. Hence these blue galaxies are all those *not* belonging to the red sequence, due to being either currently having some star-formation, or having had some in the previous $\sim$2 Gyr.

Figure 3.14 shows the spatial distribution of both red and blue galaxies over the supercluster complex, after correcting for the expected background contribution of 0.147 and 0.071 gals arcmin^{-2} for the red and blue galaxy subsets respectively, as estimated from the 13 DLS fields. The blue isodensity contours for the blue galaxies are shown at intervals of 0.125 gals arcmin^{-2}, which are filled with increasingly intense blue colours with density. Overlaid are the red isodensity contours at intervals of 0.25 gals arcmin^{-2} to represent

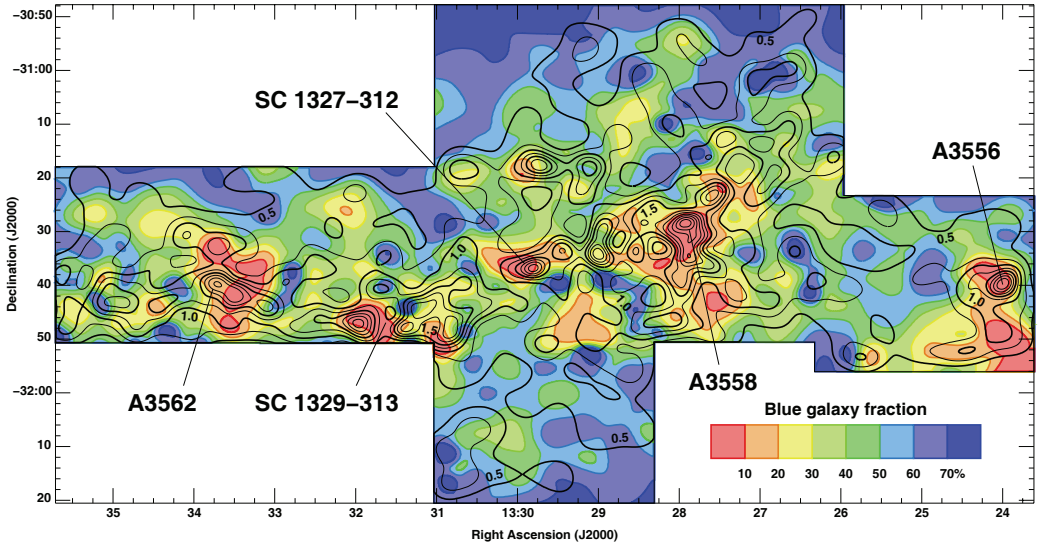

Figure 3.15: The fraction of $R < 21$ galaxies $> 3\sigma$ bluer than the cluster red sequence as a function of spatial position (see text).

the local density of the red galaxy population. Note that all the contours indicate overdensities in comparison to the field, and that the spacing of the contours for the red galaxy population is twice that of the those for their blue counterparts. The centres of the X-ray emission from each of the clusters in the region are indicated.

The spatial distribution of the red and blue galaxy populations differ significantly. Whereas the blue galaxies appear reasonably evenly spread across the whole field, the red galaxies are highly concentrated towards the cluster centres and the filamentary structure connecting A3562 and A3558. In contrast, none of the three Abell or two poor clusters show particular overdensities in the blue galaxy distribution towards their cores, in fact they appear underdense in comparison to their immediate surroundings, as noted by Metcalfe, Godwin & Peach (1994) in the case of A3558. However, several localised overdensities of blue galaxies are apparent along the filamentary structure connecting A3562 and A3558, indicative of regions of enhanced star-formation within the supercluster core complex. What is particularly interesting is their distribution within the filamentary structure with respect to the clusters. The most overdense regions are located *between* each of the clusters A3562, A3558 and the two poor clusters. The two most notable overdensities of blue galaxies appear to be the western flank of the poor cluster SC 1329-313, and a linear structure bisecting the clusters A3558 and

SC 1327-312. Both these overdensities contain numerous blue galaxies which are spectroscopically confirmed as belonging to the supercluster. The region where these overdensities of blue galaxies are located is where the two clusters A3562 and A3558 are both experiencing merging events, which may suggest that this merging has recently triggered star-formation in these blue galaxies, possibly through shock fronts produced when the ICMs of merging clusters collide. Alternatively these overdensities could reflect infall regions along the filament connecting the clusters A3558 and A3562.

Further insights into the effect of the supercluster on star-formation in its member galaxies are possible through the complementary information provided by the *fraction* of supercluster galaxies that are classed as blue. Figure 3.15 shows the fraction of $R < 21$ galaxies $> 3\sigma$ bluer than the cluster red sequence as a function of spatial position, as obtained by dividing the local surface density of blue galaxies by that for all $R < 21$ galaxies after correcting both for background contamination. The blue galaxy fraction is represented by the coloured contours, with red indicating low blue galaxy fractions ($< 10\%$) and blue indicating high blue galaxy fractions ($> 50\%$). For comparison the isodensity contours of the overall $R < 21$ galaxy density of Fig. 5.1 are overlaid.

Whereas the local blue galaxy density shows little correlation with that of the overall local galaxy density (see Fig. 3.14), the blue galaxy *fraction* appears strongly anti-correlated with the overall local galaxy density. Each of the three Abell clusters, and the two poor clusters, are marked by regions of low ($< 10\%$) blue galaxy fractions, while the filamentary structure connecting the clusters A3562 and A3558 has typically $\sim$20–50% blue galaxies, which rises still further for the regions furthest from the clusters. It is however this avoidance of the cluster cores by the blue galaxies that is the most notable feature of Fig. 3.15, with $> 90\%$ of galaxies in these regions located within the narrow locus of the cluster red sequence to $R = 21$ or $M^* + 6$. It is clear that in the central regions ($r < 300\,\mathrm{kpc}$) of all the clusters in this region star-formation has been severely truncated in *almost all if not all* galaxies.

A crucial insight into what physical process is resulting in this termination of star-formation can be obtained through comparison with complementary XMM X-ray imaging of the region around A3562 and SC 1329-313 as reported in Finoguenov et al. (2004). A comparison of their Fig. 1 shows that while the centre of the X-ray emission from A3562 is coincident with that obtained from our galaxy surface density, there is an extension to the north-east, where we also find the blue galaxy fraction to be lowest as shown in Fig. 3.15.

Figure 3.16 shows how the blue galaxy fraction varies with spatial position in the vicinity of SC 1329-313, and whereas in Fig. 3.15 the overlaid black isodensity contours show the local galaxy density distribution, here they

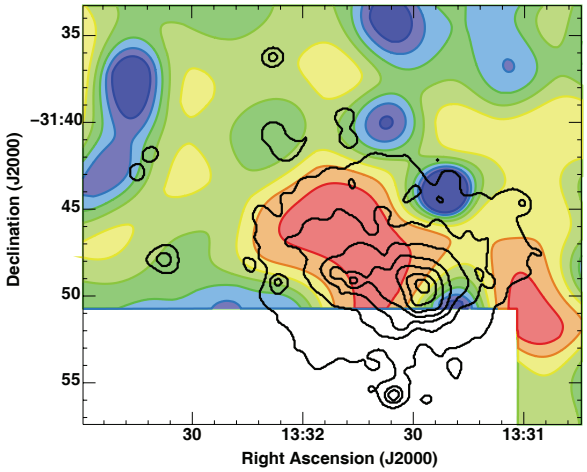

Figure 3.16: The relation between the fraction of blue galaxies (coloured filled contours as in Fig. 3.15) and X-ray emission (black contours) in the vicinity of the cluster SC 1329-313.

represent the X-ray emission from the ICM of SC 1329-313, taken from the XMM science archive (OID 10526, P.I. Aschenbach).

The centre of X-ray emission (as indicated by the arrow in Fig. 5.1) does not coincide well with either of the two peaks in the local galaxy density distribution, but appears to lie in between them. This displacement between the ICM and the galaxy distribution may be a dynamical effect from the merger, the result of the collisional gas lagging behind the collisionless DM and galaxies. A comparison of Figs. 3.14 and 3.16 suggests that while the region where the blue galaxy fraction is lowest does not coincide with either of the two peaks in the local galaxy distribution, it covers approximately the same region as the observed X-ray emission from the cluster. For both the clusters A3562 and SC 1329-313, regions where the blue galaxy fractions are lowest ($< 20\%$) appear more strongly coincident with the centres and extensions of the X-ray emission, than the corresponding centres and extensions of the clusters as measured by the overall galaxy number density. The regions of low blue galaxy fractions appear coincident with the peaks in the galaxy surface density for the remaining clusters A3558, A3556 and SC 1327-312, and so it is not possible to separate the effects of galaxy density with those of the ICM for these regions.

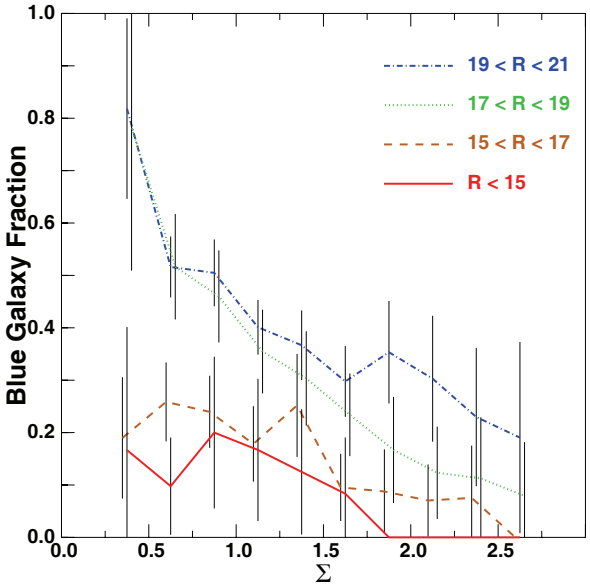

Figure 3.17: The blue galaxy fraction as a function of local density. Four lines are shown corresponding to four different R-band magnitude ranges as indicated.

3.3.4 The Relations Between Colour, Luminosity and Environment

As galaxy colours can be directly related to star-formation histories, by examining the environmental dependencies of galaxy colours it is possible to gain insight into where and how star-formation is affected by the supercluster environment. Figure 3.17 shows the overall blue galaxy fraction as a function of local density for four different R-band magnitude ranges, quantifying the global anti-correlation with local density. The highest-density regions (Σ>1.5) are dominated by red sequence galaxies over the entire magnitude range studied. There are two clear trends: the blue galaxy fraction decreases with increasing density; and in all environments the blue galaxy fraction increases monotonically with magnitude. The strength of this second trend appears greatest at $R \sim 17$: whereas at bright magnitudes ($R < 17$ or $M_R < M^* + 2$) the fraction of blue galaxies only increases marginally with decreasing local density, reaching only $\sim 20\%$ at the lowest densities studied; at fainter magnitudes ($R > 17$) the blue galaxy fraction increases rapidly to $\sim 80\%$ in the lowest density bin.

The most luminous members of the supercluster are predominantly red sequence galaxies, and so would be expected to be strongly clustered in the

high-density regions. To examine whether luminosity segregation contributes to the observed trends in galaxy colour with density, we plot in Fig. 3.18 the average environment as a function of both galaxy colour and magnitude. The grey-scale and contours indicate mean local density as a function of both the $B-R$ colour offset and R-band magnitude, smoothed on scales of 0.05 mag in $B-R$ and 0.4 mag in R. The global trends are very similar to those observed for galaxies in the SDSS (Blanton et al. 2006, 2005a), with the predominantly horizontal contours indicating that for all but the brightest galaxies, where environment is strongly luminosity-dependent, local density is a strong function of galaxy colour, while remaining almost independent of luminosity. Red galaxies are typically found in high-density regions, while blue galaxies are on average located in low-density regions, the two populations separated at a density $\sim$1.0–1.1 gals arcmin^{-2}, or $\sim$200–250 gals h_{70}^2 Mpc^{-2}. This separation reflects the trend shown in Fig. 3.17 for the blue galaxy fraction to increase with decreasing local density.

In a comparable study of the A901/902 supercluster at $z = 0.16$, Gray et al. (2004) use the 17-band COMBO-17 survey data to precisely isolate supercluster members within a thin photometric redshift slice ($0.15 < z_{phot} < 0.18$). They find a strong segregation of faint quiescent and star-forming galaxies around a local surface density of $\sim 200\,h_{70}^2$ Mpc^{-2} to a limit of M$^*+6$, in excellent agreement with our value. While Gray et al. (2004) find a sharp transition in the galaxy properties at this density, our observed trends in mean galaxy colour and blue galaxy fractions with environment appear more gradual. This we put down to the fact that whereas Gray et al. (2004) use the 17-band photometry to accurately isolate the supercluster galaxies, we perform a statistical background subtraction based on just the R-band magnitude, $B-R$ colour and local density, and hence any trends will be blurred out somewhat by interlopers.

We find that the brightest galaxies ($R < 14$) are the most clustered, which could appear contrary to the results of Metcalfe, Godwin & Peach (1994) who found that $b < 17$ galaxies within 1.1 Mpc of A3558 were significantly less clustered than those with $b > 17$ both in projection and redshift space. However their limit of $b = 17$ corresponds to $R \sim 15.5$, which is more than a magnitude fainter than the point at which we find luminosity segregation to become important.

Blanton et al. (2006) also reported that, as well the environments becoming denser with increasing luminosity for red galaxies at the brightest magnitudes, the environments of low-luminosity red galaxies become denser with increasing absolute magnitude down to $M_R = -17.7$, the limit of their survey. A similar phenomenon is apparent in our data, and although our survey extends two magnitudes fainter, we find that the trend for low-luminosity

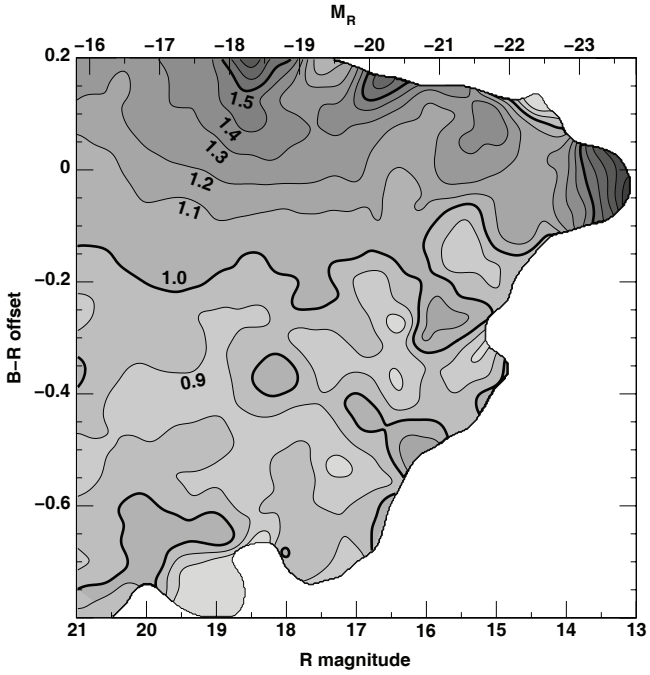

Figure 3.18: The mean local density as a function of the $B-R$ colour offset from the red sequence and R-band magnitude.

red galaxies to be found in dense environments is limited to those with $M_R \sim -18$. However it should be remembered that the uncertainties from the statistical background subtraction we have applied to measure the global supercluster galaxy populations become increasingly large at faint magnitudes.

3.3.5 SOS CMR: summary and discussion

We have examined the effect of the Shapley supercluster environment, as measured in terms of the local surface density of $R < 21.0$ galaxies, on the star-formation histories of galaxies through their colours.

The Colour-Magnitude Relation

To examine the effect of environment on the *global* properties of red sequence galaxies, we measure the *overall* distribution of $B-R$ colours with respect to the observed C-M relation using a double Gaussian fit to describe the global bimodal galaxy distribution. The use of this approach to measure environmental trends is vital, as the usual method of obtaining the best-

fitting C-M relation and measuring the effect of environment on these fits are biased by the strongly skewed distribution and changing contribution of the blue galaxy population. We show that the *location* of the C-M relation is dependent on environment, with the relation 0.0147 ± 0.0055 redder in $B-R$ in the high-density regions corresponding to the cluster core ($r<0.3h_{70}$ Mpc), than the low- and intermediate-density regions which represent the cluster periphery ($0.3<r<1.5\,h_{70}$ Mpc). This is a similar result to that obtained for the rich cluster A209 at $z = 0.21$ where the red sequence was observed to be 0.022 ± 0.014 mag redder in $B - R$ in the cluster core than the periphery (Haines et al. 2004b). By considering a model red sequence galaxy as a 10 Gyr old (at $z = 0$), $\tau = 0.01$ Gyr, solar-metallicity stellar population (Bruzual & Charlot 2003), the observed reddening of the C-M relation in the high-density region of A209 was interpreted as these galaxies being on average 500 Myr older or 20% more metal-rich than their counterparts in lower density environments. The observed reddening in the high-density regions of the Shapley supercluster is also consistent with the red sequence galaxies being ∼500 Myr older in the high-density regions than those in lower density environments, the resultant reddening of the $B - R$ colour being 33% lower than for A209 as the galaxies should be on average 2 Gyr younger in A209 than in the Shapley supercluster.

These results are consistent with analysis of the spectra of 22 000 luminous, red, bulge-dominated galaxies from the SDSS, which were found to be marginally older and more metal-rich in high-density regions than their low-density counterparts (Eisenstein et al. 2003), although they were unable to quantify these differences due to their models being unable to vary α–Fe abundance ratios. By considering the effects of age, metallicity and α–Fe ratios simultaneously on the spectra of 124 local early-type galaxies, Thomas et al. (2005) show that those in high-density environments are ∼2 Gyr older and slightly (10–25%) more metal-rich than their counterparts in field regions. We should expect much smaller differences in the predicted average ages of red sequence galaxies as even our low-density environments are typically within 1 cluster radii, while gradients in the star-formation histories of cluster galaxy populations have been shown to extend out to 3–4 virial radii before reaching field values.

These results are understandable in the framework of cosmological structure formation models, in which galaxies form earliest in the highest-density regions corresponding to the cluster cores, and have their star-formation terminated earliest as the cores become filled with shock-heated virialised gas which does not easily cool or collapse, suppressing further formation of stars and galaxies (Blanton et al. 2000). Age-gradients remain in clusters to this epoch, as mixing of the galaxy population is incomplete, and the position

of the galaxies within the cluster are correlated with the epoch at which they were accreted, and the point at which star-formation within them is suppressed (Diaferio et al. 2001).

Galaxy Colours

We identify two predominant trends relating galaxy colours, luminosities and their local environment: the anti-correlation between blue galaxy fraction and local density; and the monotonic increase in the blue galaxy fraction with R-band magnitude in all environments studied. These trends mirror those obtained by Balogh et al. (2004a) relating the red galaxy fraction (selected by $u-r$ colour), M_r and local density for galaxies taken from the SDSS first data release, although they indicate that the strength of the trend with environment is independent of luminosity, whereas we find that the effect of environment on the blue galaxy fraction is much greater at fainter magnitudes ($17 < R < 21$) than at brighter magnitudes ($R < 17$) where red galaxies dominate in all environments. As all the environments studied here lie within $\sim 1\,\mathrm{R}_{vir}$ of one of the clusters, this suggests that processes directly related to the supercluster environment are much more important for the evolution of faint galaxies ($\mathrm{M}^* + 2$) than their brighter counterparts. However, it is also possible that these differences primarily reflect differences in the field galaxy populations at bright and faint magnitudes. Unfortunately, as our data does not extend into field regions where galaxies are unlikely to have been affected by the supercluster environment, it is not possible to confidently distinguish between these two effects. However, as the blue galaxy fraction at faint magnitudes has already risen from 10% in the cluster cores to 80% by the virial radius, in conjunction with the observation that the faint red galaxies are strongly concentrated towards the cluster cores and the filamentary structure connecting them (Fig. 3.14), it appears that the formation of these faint, red galaxies is primarily due to mechanisms directly related to the supercluster environment. Equally, the studies of Gray et al. (2004) and Tanaka et al. (2004), which follow the environmental dependence of galaxy colours out to field regions, find that for faint galaxies a clear break is seen at densities corresponding to $\sim 1\,\mathrm{R}_{vir}$, while the colour-density relation of bright galaxies ($< \mathrm{M}^* + 1$) shows no such break.

We find that the $B-R$ colour of a galaxy is dependent its environment, whereas its luminosity is independent of local density, except at the very brightest magnitudes ($\mathrm{M}_R < -22$). Red galaxies located on average in regions with a mean local density greater than 1.0–1.1 gals arcmin^{-2} ($\sim$200–250 $h_{70}^2\,\mathrm{Mpc}^{-2}$), while blue galaxies are on average found in less dense regions.

We find evidence for an increase in clustering of low-luminosity red galax-

ies as also observed in the SDSS (Blanton et al. 2006; Zehavi et al. 2005). The effect appears to be greatest at M_R∼-18, with fainter red galaxies found in less dense environments. This is most likely to be related to the dramatic effects of environment on the luminosity function of faint galaxies observed for this region, in which dips are apparent at $-18 < M_R < -20$, which becomes deeper with decreasing local density. The observed dips are due to a relative lack of red sequence galaxies at these magnitudes in the lower density regions in comparison to the cluster core, and so it is manifested here as an enhanced clustering of red galaxies at $M_R \sim -18$. These observed changes in the galaxy luminosity function with environment were explained in terms of the galaxy harassment scenario, in which infalling Sc–Sd spiral galaxies are transformed by repeated high-velocity encounters over a period of several Gyr, and in the process become 1–2 mag dimmer due to both mass loss and as a result of their star-formation being terminated (Moore, Lake & Katz 1998). These galaxies which predominate in $z \sim 0.4$ clusters at $M_R \sim -20$ are thus shifted to fainter magnitudes, producing the observed dip, and hence the red galaxies at $M_R \sim -18$ are found preferentially in the highest-density environments as they are produced as a direct result of harassment by the supercluster environment. At fainter magnitudes the harassment becomes too great, and in fact the dwarf galaxies are completely disrupted by tidal forces in the cluster centre (Moore, Lake & Katz 1998) and their stars cannibalised by the cD galaxy.

Galaxy colours and the ICM

The cores of each of the clusters are completely dominated by red sequence galaxies, as indicated by regions containing very low fractions ($< 10\%$) of blue galaxies, and red mean galaxy colours. In the cases of A3562 and SC 1329-313 these regions, which coincide with both the centres of X-ray emission and the location of the brightest cluster galaxy (BCG), are displaced from the peaks in the $R < 21$ galaxy surface density, particularly for SC 1329-313. The displacement, at least between the X-ray emission/BCG and the peaks in the galaxy surface density are likely to be related to the dynamics of the system, that is an ongoing cluster merger, which has been proposed from an analysis of the X-ray emission (Finoguenov et al. 2004) and the finding of a young radio halo at the centre of A3562 (Venturi et al. 2000). The strong correlation between the regions devoid of blue galaxies and the X-ray emission, as opposed to the density peaks, may be evidence in support of ram-pressure stripping having an important role in terminating any remnant star-formation in galaxies that encounter the cluster cores, although equally it could be a consequence of the dynamics of the system displacing the faint

galaxy population.

The A3562–SC 1329-313 system appears the most active in terms of star-formation, with the highest densities of blue galaxies across the supercluster survey region found here, in particular the north-western flank of SC 1329-313, but also between the two clusters. These are also the regions where in a $7\,\mathrm{deg}^2$ VLA radio survey of the whole supercluster core complex Miller et al. (2003) found dramatic increases in the fraction of $\sim \mathrm{M}^* + 1$ galaxies belonging to the supercluster (i.e. with redshifts) which have associated radio emission. From a visual inspection of their morphology, these radio emitters are found to be spirals/irregulars, and this region marks the greatest concentration of bright $R < 16$ spiral galaxies across the supercluster complex. Miller et al. (2003) interpreted these as young starburst galaxies related to the cluster merger event, and taking this in addition to our results which are sensitive to the dwarf galaxy population, we can say this star-formation activity extends to $\mathrm{M}^* + 6$.

Are these galaxies which are undergoing starbursts triggered by the effects of the cluster merger, for example by encountering shocks in the ICM (Roettiger, Burns & Loken 1996), or are they are a group of normal star-forming galaxies which have just entered the supercluster?

Through an analysis of the X-ray emission from A3562 and SC 1329-313, Finoguenov et al. (2004) argued that SC 1329-313 had recently passed westwards through the northern outskirts of A3562 and then been deflected south. This would appear to contradict the idea that SC 1329-313 is a remnant from the ongoing A3562-A3558 merger, and instead suggests it represents a recent arrival in the supercluster core complex. However the regions containing the largest concentrations of faint blue galaxies are located *between* clusters, in particular along the filament connecting the clusters A3558 and A3562, which would support the hypothesis that shocks in the ICM produced by cluster mergers is triggering starbursts in these galaxies.

3.4 Conclusions

The area covered by the SOS dataset lies mostly within one virial radius (1–1.5 h_{70} Mpc) of one of the clusters. The results presented here show that the global properties of faint galaxies change significantly from the cluster cores to the virial radius, both in terms of the luminosity function, and the mean galaxy colours, which indicates that these galaxies are being transformed by processes directly related to the supercluster environment. As galaxy mergers should be infrequent in any of the environments covered by the SOS, the finding of such large changes in the mean galaxy colour or frac-

tion of faint blue galaxies within the SOS, indicates that some process other than merging must be responsible. The analysis of the LF suggests that galaxy harassment is important for shaping the galaxy luminosity function at magnitudes fainter than $\sim M^* + 1$, and additional evidence in favour of faint galaxies being transformed by ram-pressure stripping and undergoing starbursts triggered by shocks in the ICM produced by cluster mergers are found studying the colour distribution.

These results indicate that the effect of environment on faint $(M^* + 1)$ galaxies is quite different from that observed for bright galaxies (Gómez et al. 2003; Lewis et al. 2002). While bright galaxies appear to be transformed by processes that can take place well outside the virial radius, that is galaxy merging or suffocation, we find in this analysis that many faint galaxies are affected directly by their interaction with the supercluster environment, although we cannot rule out that the faint galaxies are also transformed outside the virial radius, beyond the limits of our survey. It is also possible that the observed environmental trends are partly due to a population of primordial, early-type galaxies that formed preferentially in the high-density regions that later became clusters (e.g. Poggianti 2006). The differences in the environmental trends of bright and faint galaxies are likely to be related to the observed global bimodality in galaxy properties (e.g. Kauffmann et al. 2003b) about a stellar characteristic stellar mass of $\sim 3 \times 10^{10}\,\mathrm{M}_{\odot}$. A possible explanation could lie within the context of the hot and cold flow model of galaxy evolution (Dekel & Birnboim 2006; Kereš et al. 2005). At low masses, galaxies are able to merge and still retain their gas supply, and hence mergers would have little effect on star-formation or galaxy colours. In contrast, once galaxies merge to become more massive than a characteristic mass, shocks in the halo become stable, and preventing further cooling of gas from the halo, bringing about a transformation in the galaxy star-forming properties.

Chapter 4

The fundamental plane of early-type galaxies in the Shapley supercluster

In this chapter we present the study of the fundamental plane (FP) for a sample of 141 early-type galaxies in the Shapley supercluster core, taking advantage of the high-quality AAOmega spectroscopy available (§ 2.3) to robustly quantify the contribution of the stellar population parameters such as age, metallicity and [α/Fe] to the tilt and scatter of the FP. The main result is the strong correlation between the FP residuals and the enrichment of α elements, a strong confirmation of the merger hypothesis for the formation of elliptical galaxies, and implying a fundamental connection between the build-up of the structure and stellar populations of early-type galaxies[1].

4.1 The fundamental plane of early-type galaxies

Early-type galaxies are observed to obey a set of scaling relations that connect their photometric and kinematic properties (e.g. Kormendy relation, Kormendy 1977, Faber-Jackson relation, Faber & Jackson 1976), the most notable, due to its surprisingly small scatter ($\sim$0.1 dex), being the relation between effective radius r_e, velocity dispersion σ_0, and mean surface brightness $< I >_e$ (Djorgovski & Davis 1987; Dressler et al. 1985). In the 3D-logarithmic space ($\log r_e$, $\log \sigma_0$, $\log <I>_e$) elliptical galaxies populate a tight plane known as the fundamental plane (FP) which is usually expressed

[1]The results of this work are presented in an article submitted to MNRAS.

in the form:

$$\log r_e = \alpha \log \sigma_0 + \beta \log <I>_e + \gamma. \quad (4.1)$$

If elliptical galaxies were perfectly homologous systems, i.e. systems with density, luminosity and kinematical structures equal over the entire early-type sequence and with constant mass-to-light ratios, then the virial theorem predicts a relation with α=2, β=−1. However, observations show that the plane is somewhat "tilted" with respect to virial expectations, with best-fit scalings $\alpha\sim$1.3, $\beta\sim-$0.8 (e.g. Jørgensen et al. 1996).

The origin of this tilt has been much debated and can be interpreted as the breakdown of either of the two assumptions in the virial expectation. A systematic variation in the mass-to-light ratio along the FP could be due to variations in the stellar content (age, metallicity or IMF) or the amount of dark matter among ellipticals. Performing detailed dynamical analyses of 25 galaxies with SAURON integral-field stellar kinematics to r_e, Cappellari et al. (2006) find the "tilt" almost exclusively due to real M/L variations of the form $(M/L)\propto M^{0.27\pm0.03}$, while structural and dynamical non-homologies have negligible effects. They also find the variation of the dynamical M/L ratio to correlate with the H_β line-strength, and ascribe most of the tilt to stellar population (age) effects. In contrast Trujillo et al. (2004) show that stellar populations account for only a small fraction of the tilt, and indicate that the bulk of the tilt is driven by structural non-homology, resulting from the observed systematic increasingly concentrated profiles (as measured by the Sersic index n) of more massive ellipticals (e.g. Graham & Guzmán 2003). La Barbera et al. (2008b) compared the fundamental planes derived for a sample of 1430 early-type galaxies in the optical (r-band) and near-infrared (K-band), to assess the dependence of the FP on the waveband (but see also Bernardi et al. 2003). Since the effects of stellar populations on galaxy luminosity are expected to be wavelength dependent, the observed finding that the FP is essentially wavelength independent, indicates that the tilt is not primarily driven by stellar populations, but instead results from other effects, such as non-homology.

The existence of the fundamental plane, its small observed scatter and its tilt have presented a long standing challenge to theoretical models explaining the origin of early-type galaxies. While, in the monolithic scenario (see §1.3),tight relations like FP are populate by uniformly old systems, for which the star-formation stopped at the early epoch z>2, in the hierarchical scenario ellipticals are believed to form from the merging of disk galaxies (Toomre & Toomre 1972; Toomre 1977). One of the most challenging debates is to understand if and how the properties such as the tilt and the scatter of the fundamental plane can be produced within this scenario.

In the merging context, broadly supported by simulations and observations, significant new insights have been made through large-scale SPH simulations of galaxy mergers (Robertson et al. 2006), indicating that for lower mass galaxies, dissipation becomes increasingly important, driving nuclear starbursts that contribute larger mass fractions, and producing systematic trends with mass in both the structures and stellar populations of the remnant ellipticals (Hopkins et al. 2003). The FP tilt then arises as a direct consequence of the systematic trends with mass of the importance of dissipation during mergers.

Jørgensen et al. (1996) claimed that even if small, a significant fraction of the scatter of the FP is due to an intrinsic scatter related to the properties of the elliptical galaxies, and not just to measurement uncertainties. They found also that the introduction of other parameters into fitting the relation such as ellipticity or isophotal shape of the galaxies, were not able to reduce this intrinsic component. In the merger scenario, the origin of the intrinsic scatter in the FP arises as a combination of the scatter in the total baryon-to-dark matter content of the progenitor galaxies, and variations in the dissipational fractions at fixed stellar mass. This latter factor should be observable as correlations between the residuals in the FP and the stellar population parameters, and represents a critical test of the merger scenario (Hopkins et al. 2003), through the predicted coevolution of the stellar populations and structures of elliptical galaxies. Indeed variations in stellar populations along the sequence of early-type galaxies are found to be partially responsible of the intrinsic scatter (e.g. Gregg 1992). Prugniel and Simien (1996) studying the correlation between the residuals to the FP and the residuals to the colour and Mg_2 line-strength vs. luminosity relations found that blue and low-metallicity elliptical galaxies deviate systematically from the value predicted by the FP. Following this evidence Forbes et al. (1998), studying a sample of non-cluster galaxies, found that the residuals of the FP correlate with the ages of the galaxies, i.e. that the scatter of the FP is mainly due to variation in galaxy age at a given mass, and in particular to variations in the time of the last starburst. On the contrary, they found that the effect of changes in metallicity is negligible. Similar results were obtained by Reda et al. (2005) analysing a sample of 23 isolated galaxies: some objects deviate from the FP relation having lower M/L ratio and this was interpreted as due to their younger stellar populations, probably induced by a recent gaseous merger. The same conclusions were reached by Wuyts et al. (2003) for two high-redshift clusters. Performing an analysis on a sample of 22 and 26 galaxies they claimed that the observed scatter is not related to environmental effects, instead finding that the residuals of the FP correlate with the residuals of the H_β - σ relation. This confirms the role played by

stellar populations in determining the appearance of the FP with relations appearing more dispersed for samples of galaxies that are more dispersed in age.

The increasing importance of dissipation in the formation of low-mass galaxies and the different mechanisms that drive the evolution and the star-formations for low- and high-mass galaxies (Haines et al. 2007) should reflect in variations with mass of the structural and kinematical properties and hence in variations both in the shape and orientation of the FP for these two families of galaxies.

To date no large homogeneous sample of galaxies covering both the giant and dwarf regime exists. Even if many FP datasets for systems as different as BCGs, normal Es, dEs, dSphs have been analysed and compared to look for changes in α (Zaritsky et al. 2006), these studies suffer from the non-homogeneity of the samples both in terms of differences in measuring the quantities entering the FP (for example different fits to derive structural parameters, different apertures to measure the velocity dispersion) as well as the selection of the galaxies themselves, and the results obtained can be strongly influenced by all of these factors.

We now present a fundamental plane analysis of 141 R<18 early-type galaxies from the Shapley supercluster (z∼0.048, red points in Fig. 2.9) distributed over the entire Shapley Optical Survey (SOS) area with both new R-band surface photometry measurements (§ 2.4) and published velocity dispersion measurements from Smith et al. (2007). The sample is randomly selected down to $M_R^* + 3$ and represents the largest homogeneous sample of low-mass early-type galaxies with reliable velocity dispersions down to $\sim 50\,\mathrm{km\,s^{-1}}$ (see § 2.3).

4.2 Morphological classification

In the SOS images, we have morphologically classified by eye, with the help of the residual maps provided by 2DPHOT, the 224 galaxies with available surface photometry: early type galaxies being those with no signature of spiral structure, and late-type the remainder with no regards for spirals or irregulars. The resolution of SOS images does not allow any finer classification, for example into elliptical and lenticular galaxies, since the presence of a residual disk can be seen only in particular cases, i.e. when it is very bright, widespread and edge-on. Figure 4.1 shows some examples of galaxies classified as early- and late-types covering the full range of magnitudes we studied. We have checked this classification by comparing our results with those of Thomas & Katgert (2006) for a subsample of 54 galaxies belonging

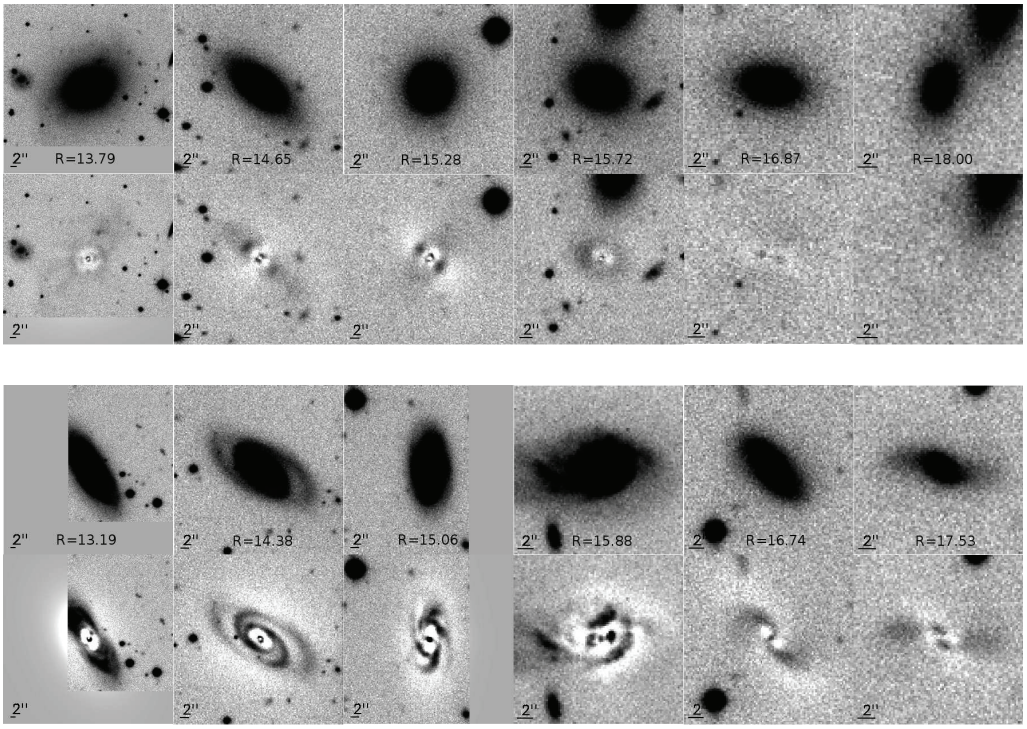

Figure 4.1: *Upper panels:* Images of six early-type galaxies covering the whole range of magnitudes of our sample with their corresponding residual maps beneath. *Lower panels:* As upper panel for late-type galaxies. In the third case it is possible to note how the residual map, showing the presence of clear spiral structures, helps us to classify as late-type an object looking like an elliptical. Observing the examples reported we can see the efficiency of 2DPHOT in fitting the galaxy profile even when the object is near either the edge of the image or bright objects.

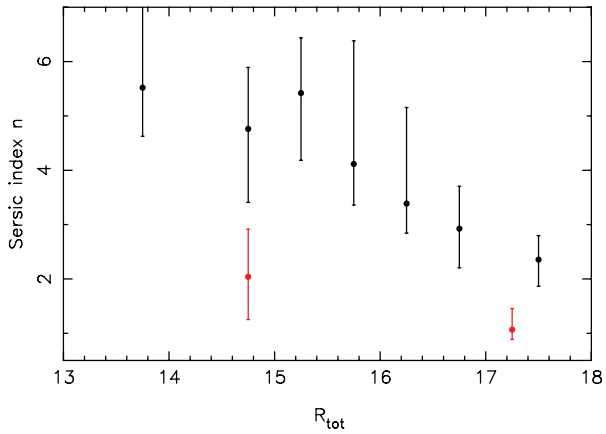

Figure 4.2: Distribution of Sersic index as function of morphological type and magnitude. The black point indicate the median value of n for early-type galaxies in each magnitude bin (chosen to contain the same number of galaxies), while the error bars indicate the inter-quartile values. The red points correspond instead to late-type galaxies.

to A3558 and A3562, finding perfect agreement. In their classification galaxies were subdivided into E and S0: our early-type sample include only E and S0 galaxies according to their classification.

The strong correlation between the Sersic index n and luminosity (Young & Currie 1994; Caon et al. 1993) prevents any morphological classification based on Sersic index alone. Graham & Guzmán (2003) show that the values of Sersic index n of dE, ordinary E/S0 galaxies and BCGs follow a *continuous* trend from $n<0.5$ to $n\sim10$, whereby brighter galaxies have larger values of n.

Figure 4.2 shows the Sersic index distribution as a function of morphological type and magnitude. The median value of n for early-type (black points) and late-type (red points) galaxies are shown for each magnitude bin (chosen to contain the same number of galaxies), while the error bars indicate the inter-quartile values. As pointed out by Graham & Guzmán (2003) the distribution of n for early-type galaxies is shifted towards higher values with increasing luminosity. Late-type galaxies have lower values of n at all magnitudes, but there is not a clean separation between the two morphological classes.

The morphological classification results in a sample of 141 early-type galaxies and 41 late-type or irregular galaxies, while 31 galaxies are removed from the sample since they are not kinematically resolved, and 8 are removed as having significant H-alpha emission (EW(Hα)>3Å). We summarize the

Table 4.1: Spectroscopic sample

Galaxies with spectra	565
Cluster members ($0.039<z<0.055$)	396
Cluster members in SOS region	378
Cluster members in SOS region with surface photometry	224
early-type	141
late-type	44
unresolved kinematically	31
with EW(Hα)>3$\mathring{A}$	8

characteristics of the sample in Table 4.1, while in Table 4.2. We report the value of structural and kinematical parameters with the correspondent errors for a subsample of galaxies.

4.3 The fundamental plane of R<18 Shapley galaxies

For the FP we use the representation of Eq 4.1 where r_e is the effective radius measured in kpc, σ_0 is the central velocity dispersion in $\mathrm{km\,s^{-1}}$ and $<I>_e$ is the mean surface brightness within r_e expressed in $L_\odot\,\mathrm{pc}^{-2}$. We have corrected the velocity dispersions (σ_{ap}) acquired with fibres of $1''$ radius (r_{ap}, corresponding to $0.658\,h^{-1}\,\mathrm{kpc}$ at z=0.048) to the apertures of $\mathrm{r}_e/8$ (Jørgensen et al. 1995):

$$\log \frac{\sigma_{ap}}{\sigma_{re/8}} = -0.04 \log \frac{r_{ap}}{r_e/8}. \tag{4.2}$$

To derive the value of α, β and γ the orthogonal fit was adopted, which minimizes the quantity χ:

$$\chi = \sum_{i=1}^{N} \frac{|\log r_e^i - (\alpha \log \sigma_0^i + \beta \log <I>_e^i + \gamma)|}{\sqrt{1+\alpha^2+\beta^2}}, \tag{4.3}$$

i.e. the sum of the absolute residuals perpendicular to the plane. This is less sensitive to outliers than the classic least-squares method (JFK96). The

Table 4.2: Structural and kinematical parameters for a sample of galaxies. *Col 1*: ID number; *Col 2*: RA(J2000); *Col 3*: DEC(J2000); *Col 4*: total R-band magnitude; *Col 5*: log σ_0 referred to an aperture of $r_e/8$ radius; *Col 6*: log σ_0 error; *Col 7*: log r_e; *Col 8*: log r_e error; *Col 9*: log $<I>_e$; *Col 10*: log $<I>_e$ error; *Col 11*: n

ID	RA(J2000)	Dec(J2000)	M_{tot}	$\log\sigma_0$ (km/s)	$\delta_{\log\sigma_0}$	$\log r_e$ (kpc)	$\delta_{\log r_e}$	$\log <I>_e$ $L_\odot\,\mathrm{pc}^{-2}$	$\delta_{\log I_e}$	n
1	13:27:46.60	-30:59:24.10	15.165	2.200	0.010	0.907	0.042	1.767	0.070	10.708
2	13:28:28.60	-31:32:4.52	15.404	2.135	0.012	0.311	0.002	2.861	0.003	1.589
3	13:27:38.00	-31:30:41.10	16.548	2.078	0.016	0.042	0.004	2.944	0.008	2.282
4	13:34:8.10	-31:47:34.42	16.083	1.765	0.097	0.686	0.044	1.843	0.058	3.518
5	13:29:54.20	-32:00:59.44	15.228	2.169	0.010	0.478	0.005	2.597	0.007	4.616
6	13:26:56.00	-31:25:27.38	14.813	2.035	0.007	0.800	0.007	2.119	0.010	5.451
7	13:29:48.30	-31:15:58.49	14.074	2.292	0.004	0.987	0.023	2.044	0.035	6.944
8	13:28:10.50	-31:23:9.70	13.919	2.258	0.004	1.111	0.043	1.876	0.067	7.795
9	13:24:26.50	-31:51:53.18	14.856	2.317	0.006	0.510	0.036	2.685	0.051	8.414
10	13:29:23.20	-31:48:32.03	15.059	1.715	0.062	0.975	0.046	1.674	0.073	9.544

resulting FP for the whole sample is:

$$\log r_e = 1.03\pm0.06\log\sigma_0 - 0.82\pm0.02\log <I>_e + 0.33, \tag{4.4}$$

with a scatter of 0.106 dex in the log r_e direction. The errors on coefficients are computed via bootstrap procedure.

One of the most challenging debates in FP studies is to understand the origin of the observed scatter. JFK96 pointed out that the dispersion around the FP relation is not completely due to the measurement errors but has an intrinsic scatter whose nature is not yet understood. Many galaxies have very small uncertainties ($\sim$0.01 dex for each variable, see Fig. 4.4), and subtracting these measurement uncertainties in quadrature from the rms scatter, we find the intrinsic scatter σ_{int} be equal to 0.079. In the estimation of σ_{int} also the errors on distance estimated through the standard deviation of the redshift distribution are taken into account. To take into account the different uncertainties on σ_0, r_e, $<I>_e$ along the plane, following Cappellari et al. (2006) a weighted fit is adopted, adding in quadrature to the measurement errors the intrinsic scatter orthogonal to the FP, $\delta_{int\perp}$, in order to have a reduced chi-squared value of one. The fitting function to be minimized is:

$$\chi = \sum_{i=1}^{N} w_i |\log r_e^i - \alpha\log\sigma_0^i - \beta\log <I>_e^i - \gamma|, \tag{4.5}$$

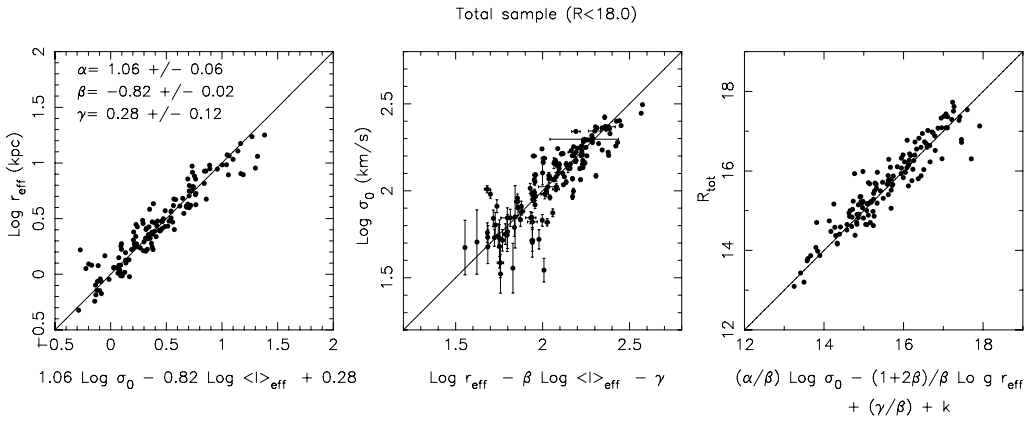

Figure 4.3: *Left,* and *central panels:* The edge-on views of the Shapley R<18 FP. *Right*: The edge-on view of the FP as it appears along the direction of luminosity. Black lines are the best-fit line. α, β and γ values are reported in the left panel.

where the sum is extended over the all galaxies sample and where

$$w_i = \frac{1}{\sqrt{\delta^2_{int\perp} + \delta^2_{\log r_e} + (\alpha\delta_{\log\sigma_0})^2 + (\beta\delta_{\log I_e})^2 - 2\beta \mathrm{cov}[\log r_e; \log < I >_e]}}. \quad (4.6)$$

The resulting equation for the FP is:

$$\log r_e = 1.06 \pm 0.06 \log\sigma_0 - 0.82 \pm 0.02 \log <I>_e + 0.28. \quad (4.7)$$

The orthogonal and weighted fits are consistent, demonstrating that the results are robust to the effects of the large σ_0 uncertainties (0.01 dex for $\sigma_0 > 100$ km s^{-1} and 0.05 for $\sigma_0 < 100$ km s^{-1}) for the lowest mass galaxies. Also the scatter in the log r_e direction is the same of unweighted fit. Figure 4.3 shows the two edge-on FP views (left and central panels) and its trend along the direction of luminosity (right panel). The value of the α coefficient obtained for the total sample, is significantly lower than the typical values found in literature ($\sim$1.2–1.3) even if most of the published works do not extend to the low values of σ_0 of our sample. Considering those galaxies with velocity dispersions greater than 100 km s^{-1} (high-σ_0 sample) we obtain the FP:

$$\log r_e = 1.35 \pm 0.11 \log\sigma_0 - 0.81 \pm 0.03 \log <I>_e - 0.40, \quad (4.8)$$

with the overall scatter in $\log r_e$ reduced to 0.092. In Figure 4.4 we plot the FP for the high-σ_0 sample (black points). Galaxies with σ_0<100 km s^{-1}

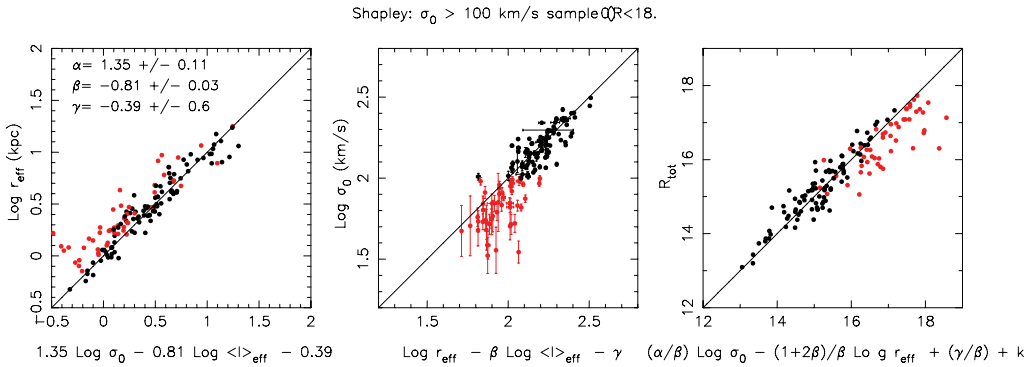

Figure 4.4: *left,* and *central panels:* The edge-on views of the Shapley R<18 σ_0>100 km s^{-1} (black dots) FP. *right panel:* The edge-on view of the FP as it appears along the direction of luminosity. Black lines are the best-fit line of the high σ sample. Galaxies with σ_0<100 (red dots) are reported for comparison. α, β and γ values are reported in the left panel.

are also reported for comparison (red dots). The fit values of the high-σ_0 sample are now closer to those of other authors. The lower α value we find for the total sample, is probably due to the extension of our sample to very low mass galaxies, down to σ_0 ∼40km s^{-1}. In this extreme range the estimates of velocity dispersions can be affected by many factors which lead to underestimate these quantities (see § 2.3). However, the high S/N of the spectra and the improved method used to derive the velocity dispersion make these data reliable.

The determination of the three FP coefficients is strictly dependent on different factors such as the selection criteria of the sample, the fit algorithm, the procedure used to derive structural and kinematical parameters (Kelson et al. 2000). Bearing this in mind we compare our FP with the extensive work by Jørgensen, Franx & Kjægaard (1996, hereafter JFK96), it being the largest dataset to study cluster FP in the local universe. The sample used by JFK96 consists of 81 early-type galaxies down to Gunn r<15.3 in the central region of Coma cluster. We have corrected our velocity dispersions to the standard aperture of 0.595 h^{-1} kpc of radius used by JFK96. To analyse the consistency of the two samples, in Fig. 4.5 we plot the spectroscopic completeness functions (CFs) of the Coma (red circles) and Shapley (black circles) FP samples as a function of magnitude. The magnitudes of the Shapley galaxies are converted from R to the Gunn-r photometric system according to the relation: $r-R$=0.35 obtained for elliptical galaxies (Fukugita et al. 1995). The Coma CF is computed using the JFK96 FP sample and the complete

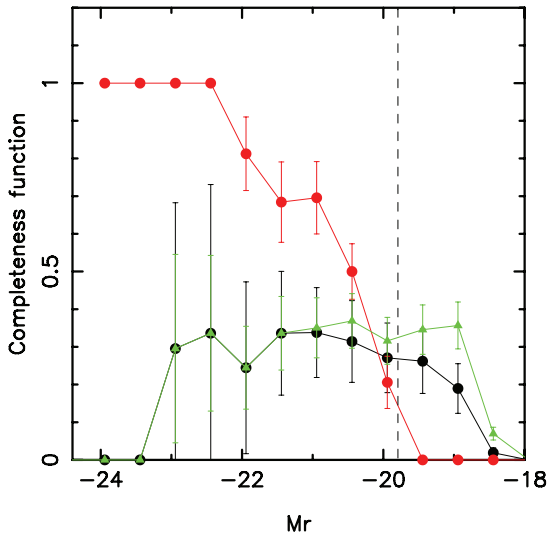

Figure 4.5: The spectroscopic completeness function both for Coma (red points) and for Shapley (black points) sample. Green points represent the CF of Shapley galaxies observed spectroscopically with no regards on successful velocity dispersion measurement.

photometric catalogue of early-type Coma galaxies published by Jørgensen & Franx (1994). The limiting magnitude of the Coma sample is M_r=−19.79 (dashed line). The Coma sample is complete at bright magnitudes, but the completeness declines rapidly towards zero at the faint magnitude limit. Differently, about 30% of Shapley galaxies are spectroscopically observed and have available velocity dispersion measurements independent of magnitude down to M_r=−19.79. In the faintest magnitude bins (M_r>−19.0) the Shapley CF drops down drastically. This is mainly due to the increasing number of galaxies observed spectroscopically but with surface brightnesses too low to be able to measure their velocity dispersions. Green triangles represent the CF of Shapley galaxies observed spectroscopically with no regards to successful velocity dispersion measurements: the decline at faintest magnitude has now disappeared except for the faintest bin (M_r>−18.5). The distribution reflects well the random selection criteria of our spectroscopic survey for R<18 galaxies. To compare the FPs of the two samples we have selected for the Shapley only early-type galaxies with M_r<−19.79 and σ_0>100 km s^{-1} (hereafter Shapley-Coma sample) corresponding roughly to the limits of the Coma FP sample. This new sample consists of 88 galaxies. The FP of the Shapley-Coma sample is:

$$\log r_e = 1.21\pm0.08 \log \sigma_0 - 0.75\pm0.02 \log <I>_e - 0.19, \qquad (4.9)$$

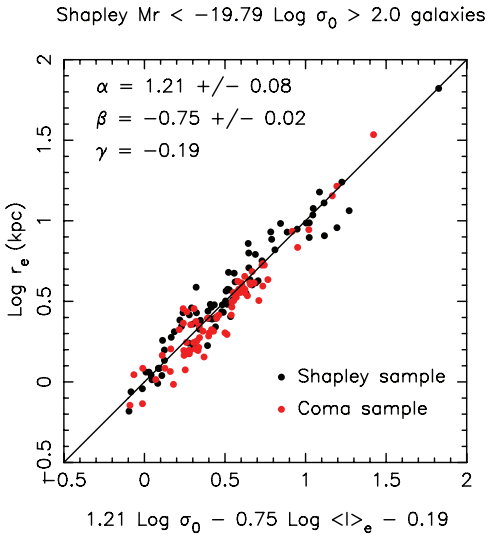

Figure 4.6: Edge on view of FP of Shapley $M_r<-19.79$ $\sigma>100\,\mathrm{km\,s^{-1}}$ galaxies (black points). The solid line represents the Shapley FP fit. For comparison are reported also Coma galaxies (red points).

with a scatter equal to 0.08 dex in log r_e direction. In Fig. 4.6 we plot the edge-on view of the FP for the Shapley-Coma sample (black points). Coma galaxies (red points) are reported for comparison. Since in JFK96 the value of H_0 is set equal to $50\,\mathrm{km\,s^{-1}\,Mpc^{-1}}$, the effective radii of Coma galaxies are shifted by a factor -0.146. Both the distributions and the dispersions of the two samples are consistent, in fact the FP for Coma sample, as found by JFK96 is:

$$\log r_e = 1.31\pm0.07 \log \sigma_0 - 0.84\pm0.02 \log <I>_e - 0.082\pm0.3. \qquad (4.10)$$

Two possible reasons for the slight differences between the two FPs could be the different sampling at the brightest magnitudes of the two datasets, and the different procedures used to obtain the structural parameters, as JFK96 fit their early-type galaxies with de Vaucouleurs profiles. However, a repeat analysis of the Coma sample using PSF-convolved Sersic profiles obtains a fundamental plane that is unchanged from that of JFK96 (John Lucey, private communication).

4.3.1 A curved surface or a selection effect?

Observing the high-σ fit (see Fig. 4.4) it is notable that all galaxies with velocity dispersions less than $100\,\mathrm{km\,s^{-1}}$ are systematically displaced above

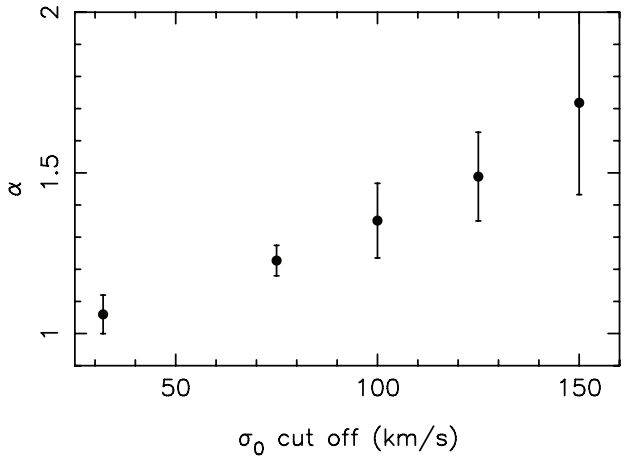

Figure 4.7: α values for sample of galaxies with increasing low velocity dispersion cuts. The point with σ_0<50 km s^{-1} represents the coefficient for the whole sample.

(left panel) or below (central panel) the best-fit plane as defined by the high-σ sample. In particular, in the log σ_0 edge-on view it seems evident that faint galaxies do not follow the same relation as bright galaxies, being characterised by lower values of σ_0 than those predicted by the FP relation, and indeed the FP appears curved, as suggested also by JFK96 and Zaritsky et al. (2006). Studying a sample of 69 faint early-type galaxies in the core of Coma cluster, Matković & Guzmán (2005) find a similar behaviour for the $L-\sigma$ relation with dwarf galaxies following a trend ($L\propto\sigma^{2.01\pm0.36}$) shallower than that observed by elliptical giant systems ($L\propto\sigma^4$) .

In Fig. 4.7, we investigate this possible curvature analysing the dependence of α as a function of σ_0 range. We cut the galaxy sample at various values of σ_0 and estimate the FP coefficients through the same weighted orthogonal fit procedure. One can see that α increases systematically as the σ_0 cut moves to higher values, removing more galaxies from the sample. The difference in α between that for the whole sample (α=1.03±0.06) and those for the highest-σ_0 cuts (α=1.72±0.28) are significant at >2σ, indicating a possible curvature of FP. To investigate if these observed variations of α with the sample selection are due to a real curvature of the FP, or induced by selection effects, a set of simulations were performed. We construct 1000 mock catalogues using the observed values of $\log <I>_e$ and $\log\sigma_0$ and the value of $\log r_e$ derived through the observed relation:

$$\log r_e = \alpha \log\sigma_0 + \beta \log <I>_e + \gamma + \delta, \qquad (4.11)$$

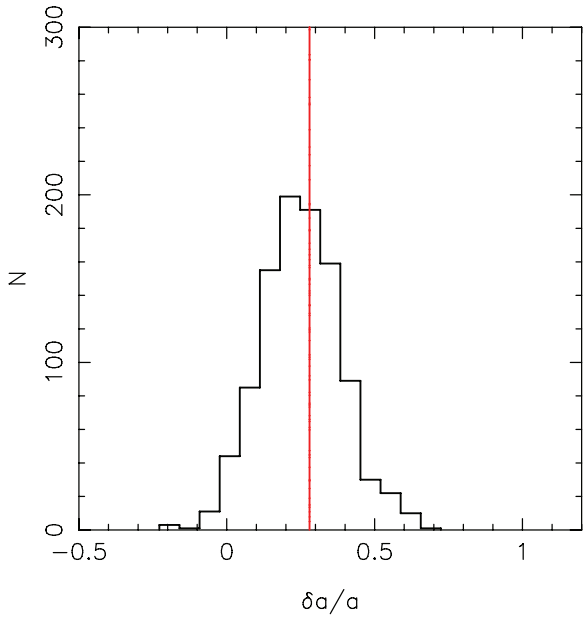

Figure 4.8: The distribution of the relative variation of α coefficient after applying the $\sigma_0 > 100\,\mathrm{km\,s^{-1}}$ cut for the simulated sample. The red line marks the variation of α when applying the σ cut to the Shapley data.

where α = 0.92, β = -0.78, and γ = 0.496 are the coefficients derived from the best fitting FP to the overall sample with log r_e as the dependent variable, and δ = 0.099 is the observed scatter in the log r_e direction. For each catalogue we evaluate the relative change in α ($\delta\alpha/\alpha$) between the othogonally-weighted fits obtained for the whole sample and after applying a cut at $\sigma_0 = 100\,\mathrm{km\,s^{-1}}$. The resulting histogram of $\delta\alpha/\alpha$ values is shown in Fig. 4.8, where the red line indicates the $\delta\alpha/\alpha$ computed directly for the Shapley sample. This shows that the observed change in α is fully consistent with that expected for a linear relation. Moreover, in Fig. 4.9 we compare the FP edge-on projection (Eq. 11) for the observed high-σ_0 sample (solid symbols) and a simulated sample obeying the overall Shapley FP relation (open symbols). The two samples show similar behaviour, with the same apparent curvature such that galaxies with low velocity dispersions are placed systematically below the FP relation. Given that the simulated sample is defined to follow a linear relation, this suggests that the apparent curvature in Fig. 4.4 can be explained solely by selection biases. Hence, in spite of the wide-range in velocity dispersions covered by our sample, this is not sufficient to distinguish between either a linear or curved FP relation.

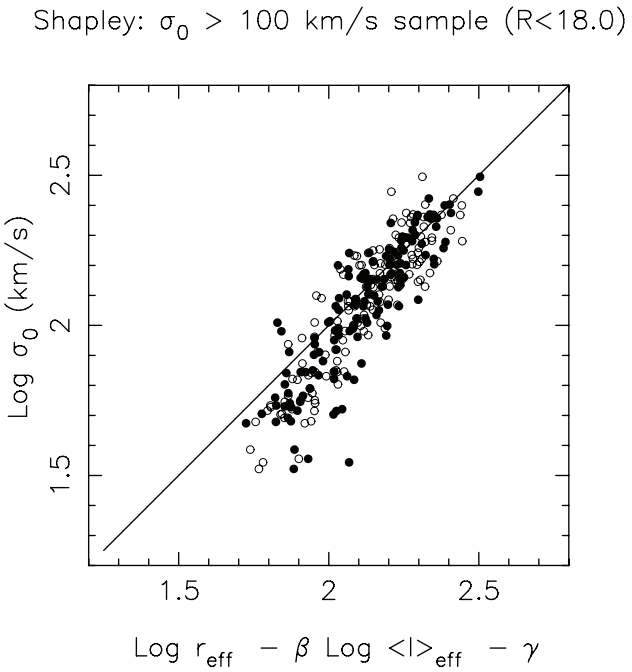

Figure 4.9: The edge-on projection of the FP for the Shapley high σ_0 sample (black dots) and for one of the simulated catalogue (open circle). The line represent the best fit relation.

4.4 Correlations between the FP residuals and stellar population parameters

JFK96 pointed out that the dispersion around the FP relation is not completely due to the measurement errors but has an intrinsic scatter whose nature is not yet understood. The existence of this intrinsic scatter was interpreted as due to the existence of another "fundamental" parameter characterising the family of the early-type galaxies. In many of the previous works on the FP (see § 4.1) a strong effort has been made to find correlations between the FP residuals and different line-indices known to be representative of a particular stellar population parameter (for example H_β for age, Mg_2 for metallicity, etc.).

Taking advantage of the wide variety of indices derived by SLH we investigate the possible origin of the scatter of the FP looking for correlations between spectral indices whose relation to the main stellar population parameters is best understood like Mgb, Fe5015, F4383, Hβ, HgF and HdF and the residuals of the FP. These indices show a correlation with σ_0, either strong or weak, which, if not corrected for, could produce spurious correlations with the FP residuals. To avoid this problem, rather than use the spectral indices themselves, we consider their residuals with respect to the index-log σ_0 relation. For each index, we fitted first the index-sigma relation, using a simple least squares estimator and then get the residuals with respect to that relation (see right panels of Figs. 4.10 and 4.11). In Figs. 4.10 and 4.11 (right panels) the red lines represent the best fit relation between residuals and logσ_0: notice that no kind of correlation persists.

The left and central panels show the index-σ_0 residuals versus the residual of the FP in the log r_e (left panel) and log $< I >_e$ (central panel) directions. We do not show the corresponding correlations with the FP residuals along the $\log \sigma_0$ direction as they are completely defined by residuals along the other two axes, but with the correlations acting in the opposite directions (i.e. positive correlation with the residuals in log r_e and log $< I >_e$ direction become anti-correlation in σ_0 direction). For each panel, the correlation between the FP residuals and spectral index ones is quantified through the correlation factor r and the bisector least-squares fit, assuming that the distributions are both Gaussian. Uncertainties in r and the fit are estimated through 10000 Monte Carlo realisations, taking into account the errors on each value. There are positive correlations between the Z/H dependent indices Fe4383 and Fe5015 and the FP residuals, while Mgb shows a weak negative correlation (Fig. 4.10). Each of the Balmer indices weakly correlate with the FP residuals suggesting a positive correlation for age (Fig. 4.11).

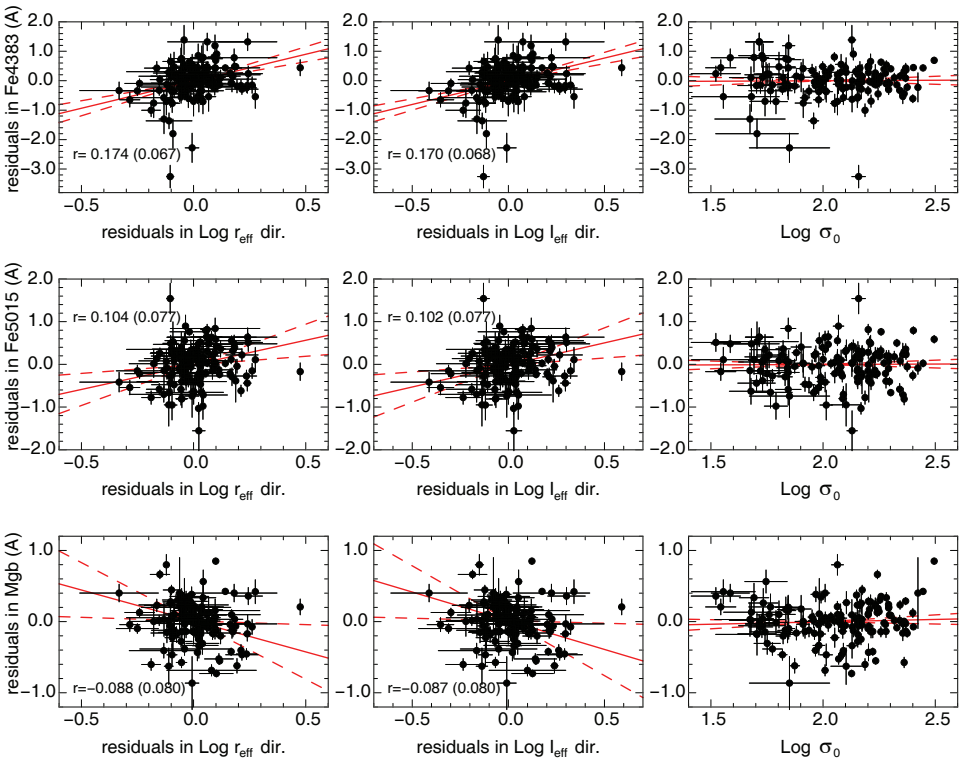

Figure 4.10: Correlations between the residuals of the spectral indices Fe4383 (top panels), Fe5015 (middle panels), Mgb (bottom panels) with respect to the logσ_0 relations and the residuals with respect to the best-fitting fundamental plane. The left, and middle panels indicate the correlations with residuals along the r_e and $<I>_e$ projections respectively. The right panels show spectral index residuals plotted against σ. The solid (dashed) red lines indicate the mean (and 1σ confidence limits) bisector least-squared fits to each set of points after 10000 Monte Carlo realizations. The corresponding correlation coefficient r (and uncertainty) is indicated in each panel.

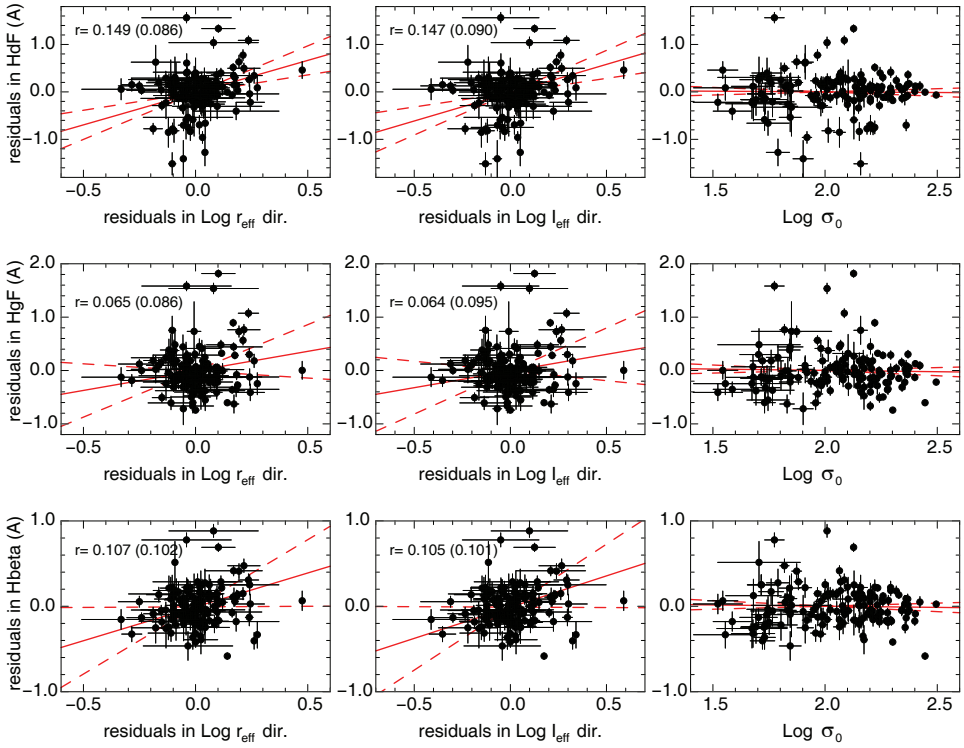

Figure 4.11: The same of Fig. 4.10 for the spectral indices HdF (top panels), HgF (middle panels) and Hβ (bottom panels)

Using a single spectra index index it is not possible to disentangle between the effects of age and metallicity. To have a deeper insight into the picture we performed the same analysis using the estimates of age, metallicity and α enhancement (α/Fe) obtained with a multi-index procedure which provide more physically meaningful information. In particular, for what concerns α/Fe, it has long been realised (Tinsley 1980) that in the study of galaxy formation and evolution, a major role can be played by the analysis of the abundance ratios, due to them being relatively model independent and primarily affected by stellar nucleosynthesis and the initial mass function (Matteucci 1996). In particular, the ratio between the so called α elements (O, Ne, Mg, Si, Ca, Ti) and iron is widely accepted to be affected by both galaxy age and duration of star-formation, the α elements and iron having different production timescales through supernovae explosion (Greggio & Renzini 1983). In fact, the α elements are produced on short periods with respect to the galaxy lifetime by type II SNe, while Fe is mainly ejected throughout the galaxy by explosion of type Ia SNe: this process requires more than 0.5 Gyr. Hence, according to the simplest and widely accepted scenario, a galaxy with high value of α/Fe has experienced many type II SNe events, but almost no SNe of type Ia during the major epoch of star-formation: this constrains the timescale for this epoch of stellar formation to be shorter than $3{\times}10^8$ years.

Here we investigate possible correlations between the three stellar population parameters age, metallicity and α/Fe and the residuals of the FP along the $\log r_e$ and $\log < I >_e$ axes directions. As for the case of single spectral index, all three stellar population parameters correlate strongly with σ_0 through the scaling relations of Eq. 2.3, therefore we first compute the residuals of stellar population parameters with respect to their index-σ_0 relations. Figure 4.12 shows the resultant correlations between the age, metallicity and α/Fe residuals (top, middle and bottom panels respectively) and the FP residuals along the $\log r_e$ (left panels) and $\log <I>_e$ (middle panels) projections. The right panels show the stellar population residuals against $\log \sigma_0$ to demonstrate the lack of correlations between the residuals and $\log \sigma_0$ itself.

Both age and α/Fe are seen to be strongly anti-correlated (at 2 and 3σ respectively) with the residuals computed in the $\log r_e$ and $\log < I >_e$ directions, while metallicity shows a *positive* correlation with the FP residuals along the same axes. In table 4.3 we report also the percentage that two quantities with correlation factor r are not correlated.

Given that age and α/Fe are known to correlate strongly for galaxies of a given mass, while age and metallicity anti-correlate (e.g. Proctor & Sansom 2002; Smith et al. 2007), it is not clear which of the three parameters drive the correlations. For example, if one starts with an intrinsic correlation of

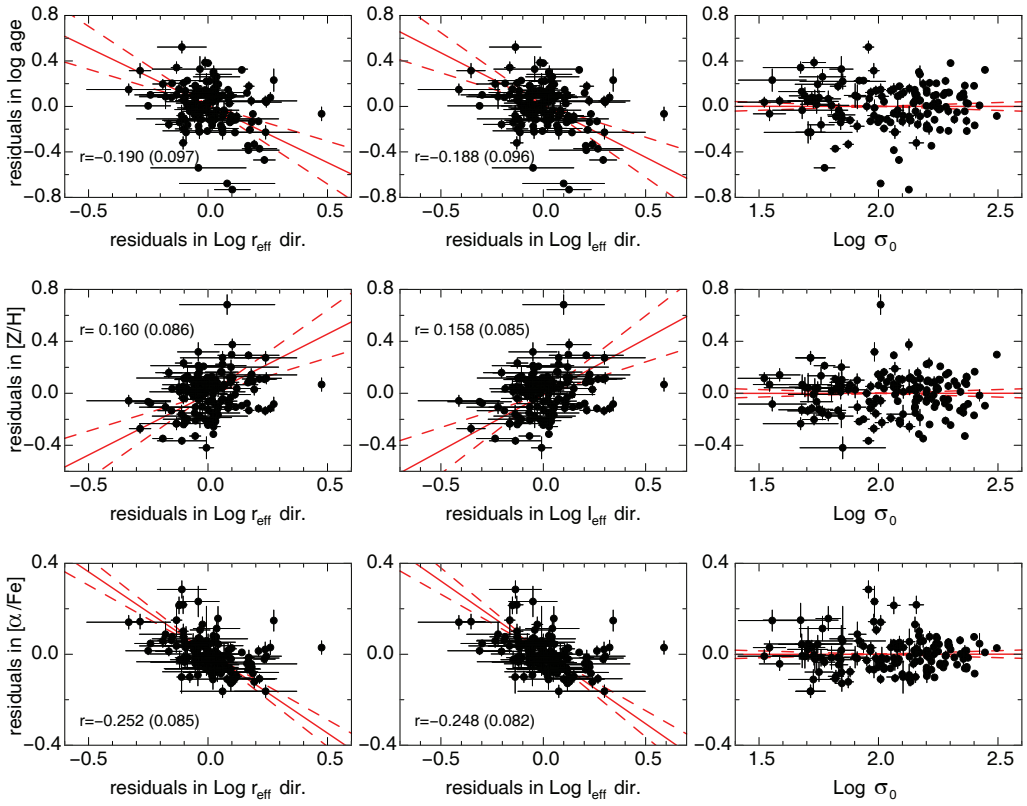

Figure 4.12: Correlations between the residuals of the stellar population parameters (age, metallicity and abundances) with respect to their corresponding scaling relations (Eq. 1) and the residuals with respect to the best-fitting fundamental plane. The top, middle and bottom panels correspond to correlations with the age, metallicity and [α/Fe] residuals respectively. The left, and middle panels indicate the correlations with residuals along the r_e and $<I>_e$ projections respectively. The right panels show the age, metallicity and α/Fe residuals plotted against log σ_0. The solid (dashed) red lines indicate the mean (and $1\sigma_0$ confidence limits) bisector least-squared fits to each set of points after 10000 Monte Carlo realisations. The corresponding correlation coefficient r (and uncertainty) is indicated in each panel.

Table 4.3: Percentage that two quantities with correlation factor r are not correlated.

	Mgb	Fe5015	Fe4383	Hbeta	HgF	HdF	Log age	Z/H	α/Fe
Log r_e dir.	29.4%	21.5%	3.7%	20.1%	43.89%	7.4%	2.25%	5.54%	0.23%
Log $< I >_e$	29.9%	22.3%	4.16%	21.0%	44.6%	7.8%	2.4%	5.85%	0.27%

α/Fe with the FP residuals, the known age-α/Fe and age-metallicity correlations could induce the part of the observed correlations between age and metallicity with the FP residuals.

It should be remembered that the stellar population parameters presented here are derived through fixed apertures covering only the galaxy center. Therefore, if galaxies have significant population gradients, the observed trend could be due to the sampling at different radii of the central stellar population. In the case of metallicity, this may be a factor, as early-type galaxies are observed to have negative metallicity gradients (Kuntschner et al. 2006; Rawle et al. 2008) of the order -0.20 ± 0.05 dex in [Z/H]. However, spatially-resolved spectroscopy of early-type galaxies show that they generally have flat radial trends in age and [α/Fe] (Sánchez-Blázquez et al. 2007; Rawle et al. 2008), indicating that the anti-correlation of age and abundance ratios with the FP residuals in the log r_e and log $< I >_e$ directions is robust. The finding of this trend between age and [α/Fe], can be used to set strong constraints on the scenario of galaxy evolution.

The strong relations found between the stellar population parameters, principally the α/Fe, and the residuals of the FP suggest that its scatter is in part due to variations in the stellar populations at fixed galaxy mass. To this aim we fit the modified FP relation:

$$\log r_e = \alpha \log \sigma_0 + \beta \log <I>_e + \delta spp_i + \gamma, \tag{4.12}$$

where spp_i is, in turn, α enhancement, age and metallicity of the galaxies and observe the variation induced in the scatter by keeping α and β fixed as in Eq. 4.11 and allowing δ to vary in order to minimize the FP scatter. It is necessary to keep α and β fixed as each of the SSP parameters correlate strongly with σ_0, and hence would introduce spurious variations in α. The results obtained are listed in table 4.4, where the second column indicates the estimated strength of the SSP term δ, the following two columns indicate the overall scatter in the FP residuals in the log r_e direction after the addition of the SSP term, and the intrinsic scatter after subtracting in quadrature the

Table 4.4: The impact on the overall and intrinsic FP scatter of adding a further term (ssp) term to the orthogonal fit of the fundamental plane. The δ value is that which minimizes the overall FP scatter along the log r_e direction to Eq. 4.12,the next two columns indicate the resultant overall and intrinsic scatters, while the last column indicates the rms contribution of the SSP term in the log r_e direction.

spp	δ	rms log r_e dir.	intrinsic rms	rms contribution
-		0.106	0.079	
α/Fe	$+0.618 \pm 0.166$	0.093	0.059	0.050
Log Age	$+0.194 \pm 0.082$	0.100	0.069	0.033
Z/H	-0.188 ± 0.088	0.102	0.074	0.027

measurement uncertainties in log r_e, and the final column represents the rms contribution of the SSP term to the scatter in log r_e. From the analysis of table 4.4 two main results emerge. The only fit with the δ coefficient significant at more than 3σ (3.7σ) is the fit with the [α/Fe] as fourth parameter. In the case of age and metallicity, the new coefficient is non-zero at just the 2σ level, indicating the lesser impact of these parameters on the fundamental relation.

While it seems that none of the additional SSP terms reduce the overall scatter significantly, the relative impact of the three SSP terms becomes clearer when considering the intrinsic scatter (i.e. after accounting for the measurement uncertainties): both age and metallicity have an intrinsic scatter of $\sim$0.07, only marginally lower than the value without the SSP term, while in the case of [α/Fe] the value drops down to 0.059, comparable to the rms contribution from the [α/Fe] term (0.050), indicating that the distribution of galaxies around the FP are tightly related to the enrichment, and hence to the timescale of star-formation.

4.5 Origin of the FP tilt

Under the assumption of a constant total mass-to-light ratio and that early-type galaxies form a homologous class of objects, the virial theorem predicts the existence of a FP in the form r_e=$K(M/L)^{-1}\sigma^2 I_e^{-1}$ where K is dependent on density, luminosity and kinematical structure. To match the

observational results r_e=$K_{obs}\sigma_0^\alpha I_e^\beta$ it is necessary that the quantity

$$K(M/L)^{-1} \propto \sigma^{\alpha-2} I_e^{\beta+1} \tag{4.13}$$

(i.e. the structural constants and the M/L ratio) varies in a systematic way in order to reproduce the FP tilt.

4.5.1 Galaxies as homologous systems

If we assume galaxies to be homologous systems, then following Eq. 4.13 the FP tilt can be expressed as:

$$(M/L) \propto L^{(2-\alpha)/2\alpha} I_e^{-1/2-2\beta/\alpha-1/\alpha}. \tag{4.14}$$

Since for typical values of β the exponent of the I_e term is negligible we have:

$$(M/L) \propto L^{(2-\alpha)/2\alpha} \propto L^\gamma = L^{0.44\pm0.06}. \tag{4.15}$$

In other words, we can say that under the assumption that early-type galaxies obey the virial theorem and are homologous systems, then the M/L ratio has to vary according Eq. 4.15. If we write the total mass-to-light ratio as

$$\frac{M}{L_R} = \frac{M_\star}{L_R}\frac{M}{M_\star}, \tag{4.16}$$

the tilt can be explained as due to either a variation of $M_\star/L_R$ or a variation in the total amount of dark matter, i.e. in the fraction $M/M_\star$. We take advantage of the robust SSP age and metallicity measures obtained for each galaxy by SLH to investigate the relative contribution of trends in the stellar populations with mass to the tilt in the fundamental plane. We estimate the stellar mass-to-light ratio of each galaxy as

$$\log(M_\star/L_R) = -0.287 + 0.809 \times \log \mathrm{age(Gyr)} + 0.209 \times [Z/H], \tag{4.17}$$

based on comparison with the SSP models of Maraston (2005) over the age range 1.5–15 Gyr and metallicity range 0.01–0.1 with a Kroupa (2001) IMF. Within these models a scatter of 0.06 dex is obtained, which is added in quadrature to the uncertainties in age and metallicity. The results are shown in the top-left panel of Fig. 4.13, the red line indicating the weighted best-fit relation. We obtain a relation between the $M_\star/L_R$ and luminosity as

$$M_\star/L_R \propto L_R^{0.17\pm0.02}. \tag{4.18}$$

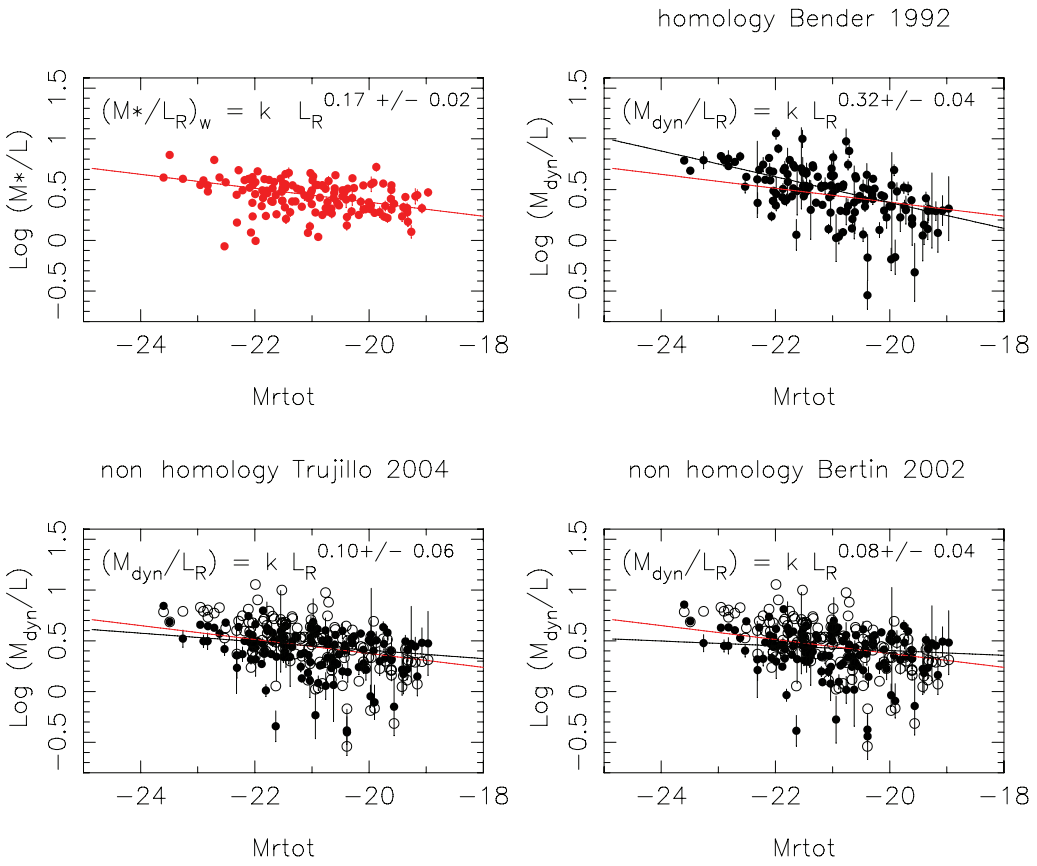

Figure 4.13: *Top-left panel*: the stellar mass-to-light ratio as function of absolute R magnitude. In each panel the solid red line is the weighted best-fit line of the stellar mass-to-light ratio vs luminosity relation. *Top-right panel*: the total dynamical mass-to-light ratio as function of absolute R magnitude. The mass is estimated assuming galaxies to be a structural-homologous class with structure constant c_2 equal to 5. The solid black line, as well as in the subsequent panels, is the corresponding fit line. The dashed line is the best fit relation for velocity dispersions corrected to the physical constant aperture of $0.595\,h^{-1}$ kpc following JFK96. *Bottom-left panel*: the total dynamical mass-to-light ratio as function of absolute R magnitude. The mass is estimated assuming galaxies *not* to be a structural-homologous class with structure constant c_2 a well-defined function of Sersic index n $c_2(n)$ following Trujillo et al. (2004). *Bottom-right panel*: The same as the previous panel but using the prescription of *Bertin et al.* bertin01 for $c_2(n)$.

To estimate the dynamical mass-to-light ratio we adopt

$$L_R = 2\pi I_e r_e^2 \tag{4.19}$$

and

$$M = c_2 G \sigma_0^2 r_e, \tag{4.20}$$

where c_2 is the structure constant and G is the gravitational constant. Following Bender et al. (1992) we set the structure constant c_2 equal to 5 (consistent with the results of Cappellari et al. 2006). The trend of dynamical mass-to-light with absolute magnitude for this case is shown in the top-right panel of Fig. 4.13. Using velocity dispersions corrected to an aperture of $r_e/8$ we find the relation (black solid line):

$$M/L_R \propto L_R^{0.32\pm0.04}. \tag{4.21}$$

Looking at equations 4.15 and 4.21 we see that the dependence of M/L ratio from L predicted by virial theorem (γ=0.44) is 0.12 ($\Delta\gamma$=0.12) greater than that obtained with homology assumption (γ=0.32). This evidence implies that the tilt of the FP cannot only be due to a variation of M/L ratio along the sequence of elliptical galaxies, but that other factors are responsible of the deviation of early-type galaxies from the virial theorem. Moreover, the assumption of homology leads to having dynamical mass-to-light ratios lower than stellar ones at faint magnitudes based on comparing the two corresponding best-fit relations. However, the stellar mass-to-light ratio is uncertain up to a constant factor depending on the choice of IMF (e.g. Conroy, Gunn & White 2008). If in the estimates of stellar M/L ratio an IMF with fewer low-mass stars than Kroupa was set, all the ratios would be shifted down and consequently they could result lower than the dynamic mass-to-light ratio. One caveat in this argument, is related to the discussion of curvature earlier, in that the two estimates of the tilt are based on fits along rather different axes. Just as estimates of α based on orthogonal fits, or fits along the r_e, σ_0 axes are markedly different, we should not be so surprised to see the estimates of γ based on the orthogonally-weighted FP fit, and weighted fits along the M_r axis to be so different.

4.5.2 Galaxies as non-homologous systems

Having observed inconsistencies in the results for the homology assumption, we investigate the hypothesis that the tilt is partially due to the variation in the density structures (K in Eq. 4.13) of early-type galaxies. We assume instead that galaxies have as the structure constant a well-defined

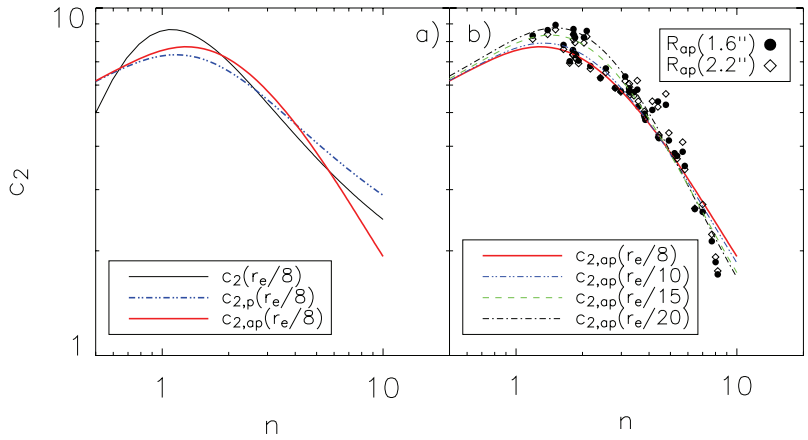

Figure 4.14: *Left panel:* Estimated virial coefficient $c_2(n)$ for a Sérsic model based on an aperture radius $r_e/8$; $c_2(n)$ is obtained by using the velocity radial profile $\sigma_r(r)$ (black curve), the projected radial profile $\sigma_p(R)$ (blue dot-dashed curve) and the projected aperture radial profile $\sigma_{ap}(R_{ap})$ (red curve). *Right panel:* Estimated values of $c_2(n)$ for two different fixed angular apertures (1.″6 and 2.″2). Overplotted are the expected $c_2(n)$-values for different apertures. Taken from *Trujillo et al.* (2004).

function of Sersic index n, $c_2(n)$, according to Trujillo et al. (2004) (red curve in Fig. 4.14). The relation we find in this case

$$M/L_R \propto L_R^{0.10\pm0.06} \tag{4.22}$$

is reported in the bottom-left panel of Figure 4.13. In this panel, dynamical mass-to-light ratios obtained under the assumption of homology (black open dots) are reported for comparison. The main effect to using different values of the constant is, as expected, to flatten the relation since fainter galaxies have systematically lower values of n, and consequently according to Trujillo et al. (2004), values of c_2 greater than in the case of homology. By comparing the Bender and Trujillo expectations of total mass-to-light ratios, we can see that the effect of non-homology accounts for a $\Delta\gamma$=0.22 (∼68%) of the FP tilt. From these results we can see that taking into account the effects of stellar population variations with luminosity (γ=0.17, see Eq. 4.18) and the effects of non-homology ($\Delta\gamma$=0.22), we can already explain all of the observed tilt (γ=0.39). These results agree well with the work of Trujillo et al. (2004). In the bottom-left panel, for comparison, we test the hypothesis of non-homology assuming the correlation between c_2 and n presented in Bertin

et al. (2002). The fit obtained is

$$M/L_R \propto L_R^{0.08\pm0.04}. \quad (4.23)$$

The two non-homology cases are statistically comparable. Taking into account the non-homology we find the total mass-to-light ratios to be consistent with those predicted for the stellar populations over the whole range of luminosity. This agreement implies that early-type galaxies of all masses are systems with very low dark matter fractions within r_e. Hopkins et al. (2008) studying the remnants of mergers involving lots of dissipation, suggest that dark matter accounts only for ∼15% of the total mass within r_e. Similary, Gerhard et al. (2001) and Thomas et al. (2005) find that early-type galaxies are not dark matter dominated systems obtaining DM fractions ∼20% within r_e.

4.6 Summary and Conclusions

We have derived the FP of a sample of 141 early-type R<18 galaxies in the Shapley supercluster at z=0.048. For velocity dispersions and stellar population parameters 1 refer to the published SLH values, while R-band photometry is from the SOS (Mercurio et al. 2006). The final sample extends down to M_R^*+3 in magnitude and 50 km s^{-1} in σ_0. Using the software 2DPHOT we derived for each galaxy the structural parameters r_e, $<\mu>_e$, n, and m_{tot} by fitting a 2D PSF-convolved Sersic model. Errors on structural parameters are evaluated using the estimates of r_e and $<\mu>_e$ measured on the 5 single exposures. The morphological classification is performed by eye and checked with those of Thomas & Katgert (2006) for a subsample of 54 galaxies finding complete agreement.

Adopting a weighted fit (see Eq. 4.5) we derived the FP: $r_e \propto \sigma^{1.06} I_e^{-0.82}$, while considering the subsample of $\sigma_0 > 100$ km s^{-1} FP turns out to follow the relation $r_e \propto \sigma^{1.35} I_e^{-0.81}$ which is consistent with the Coma FP by JFK96. The low value of α can be related to the extension of our sample towards very low values of velocity dispersion and on the higher uncertainties of σ_0 at low end. Observing the consistent change in the α value between the total and the high-σ samples, we investigate the possible curvature of the FP. Applying the same cuts to a simulated sample following a linear FP relation, we ascertain that the observed curvature can be explained by selection effects, rather than an intrinsic curvature. Departure from a linear trend of the FP relation has been claimed by D'Onofrio et al. (2008), but see also Desroches et al. (2001), who find that "*the faint-end luminosity cut influences the coefficient α of the FP*", in agreement with Nigoche-Netro (2008). Similar results was found by

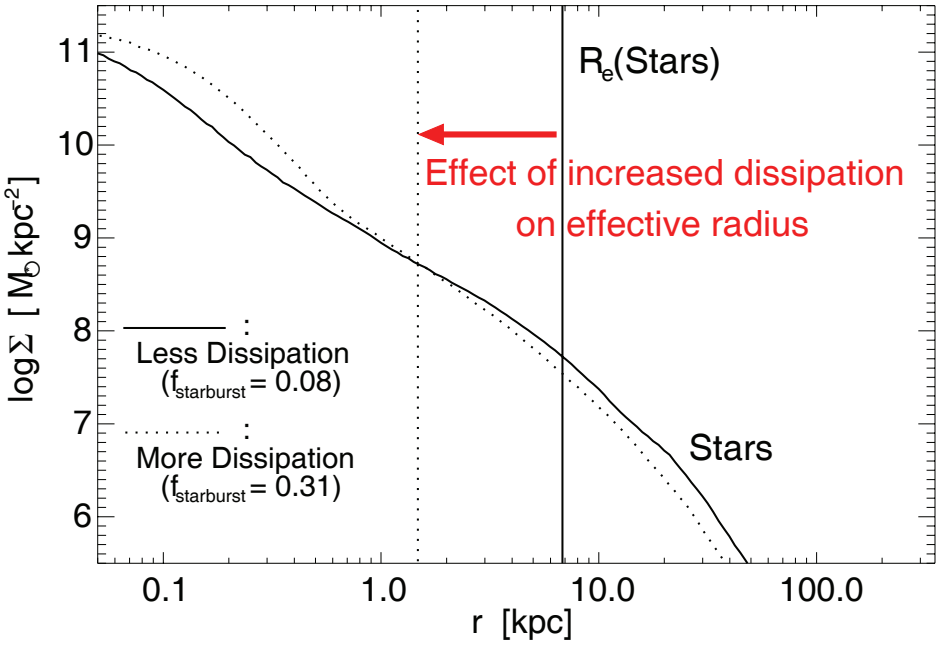

Figure 4.15: The effect of varying levels of dissipation on the radial light profiles of merger remnants. The solid line shows a case with a moderate degree of dissipation — a mass fraction in the final centrally concentrated and dissipational merger-induced starburst $f_{sb} = 0.08$. The dotted line shows the remnant of a very gas-rich merger, with $f_{sb} = 0.31$. The profile shapes are similar, although the gas-rich merger remnant shows an excess of light in the core regions due resulting from the star-burst. The effective radii of the stellar distributions (as shown by the vertical lines) are quite different, owing to the dense central concentration of mass from the starburst in the latter case. Taken from *Hopkins et al.* 2003.

Hyde & Bernardi (2008) studying the FP residuals along the plane. However, these works pointed out that conclusive evidences of the FP curvature needs either a more robust statistics or higher accuracy in the velocity dispersion estimates for low mass systems.

We confirm, in agreement with previous work, that a simple homology origin to the FP tilt is inconsistent with our data. We then investigate the contribution of M/L variations and non-homology to the tilt of the FP (γ=0.44): we found that ∼89% ($\Delta\gamma$=0.39) of the tilt can be explained assuming non-homology (50%, $\Delta\gamma$=0.22) and stellar population variations along the sequence of elliptical galaxies (39%, $\Delta\gamma$=0.17). With the assumption of non-homology we found total mass-to-light ratio to be consistent with those

predicted for the stellar populations over the whole range of magnitudes, implying that early-type galaxies are systems with negligible fractions of DM within r_e.

We investigate the correlations between the FP residuals in the three axis directions and the stellar population parameters age, metallicity and α/Fe. The main results of this work are the observed clear trend between the FP residuals and age and α/Fe, with those galaxies with effective radii smaller than predicted by the FP to have stellar populations systematically older and with higher abundances than average, fully consistent with the predictions of Hopkins et al. (2003). Hopkins et al. (2003) make specific predictions for the effects of varying the dissipational fraction on the remnant spheroids of a given mass, resulting in correlations between the structural and stellar population parameters. By considering identical progenitor disks (at $t = 0$) with initial gas fractions $f_{gas} = 1$ following an exponential star-formation history with time-scale τ, we have the gas fraction at the time of the merger t_m(and hence dissipational fraction in the merger-induced starburst) will scale as $f_{gas} = \exp(-t_m/\tau)$. If the remaining gas is then consumed in the central star-burst, producing a passively-evolving spheroid remnant, then the dissipational fraction will increase for earlier mergers, and hence mean stellar age. Hopkins et al. (2003) also show that ellipticals formed through mergers with higher dissipation fractions should be more α-enriched. As merger remnants involving more dissipation are expected to be more compact (as shown in Figure 4.15, we should expect both mean stellar age and [α/Fe] to anti-correlate with the residuals in the r_e direction, as we find. These observed significant anti-correlations strongly supports the merger hypothesis for the formation of elliptical galaxies, and imply a fundamental connection between the structures and stellar populations of early-type galaxies.

Part II

Probing galaxy bimodality with the Sloan Digital Sky Survey

The Sloan Digital Sky Survey

The Sloan Digital Sky Survey (SDSS) is the largest astronomical survey ever undertaken having started in 2000, with the aim to cover more than half of the North Galactic hemisphere with both multi-filter imaging and spectroscopy observing around 200 million objects and measuring spectra for more than 700000 galaxies, 95000 quasars and 185000 stars. The survey uses a dedicated 2.5-m wide-angle optical telescope at Apache Point Observatory in New Mexico provided by two instruments designed *ad hoc* for the purpose of the survey: a large-format mosaic CCD camera to image the sky and two digital spectrographs (York et al., 2000). The imaging camera consists of a CCD array made up of 30 2048 $\times$ 2048 Tektronix CCDs distributed in five rows and six columns able to cover 1.5 square degrees of sky at each exposure. Each row observes the sky through a different filter, in a temporal sequence r', i', u', z', and g' with effective wavelengths of 6230, 7260, 3550, 9130, and 4770 Å, respectively. The effective integration time per filter is 54.1 s. The imaging survey reaches up to a depth of $g' \sim 23$ mag and is 95% complete for point sources at r$\sim$22.2. The photometric calibration is accurate to about 3% in r (Hogg et al. 2001; Smith et al. 2002). Objects detected in the imaging survey are classified as point sources or extended. From the catalogue of the extended objects, galaxies with $r \leq 17.77$ and $\mu_{50} \leq$24.5 mag arcsec^{-2} are selected to be observed spectroscopically. The magnitude limit is set in order to target a mean of 90 galaxies per square degree, which corresponds to a depth at which the variations of galaxy numbers due to the large-scale structure are quite substantial on degree scales. The magnitude limit $r \leq 17.77$ yields 92 galaxies per square degree. Briefly the surface brightness limit is set since observations of objects with μ_{50} >24.5 mag arcsec^{-2} are unlikely to produce a redshift. Spectra were acquired with two fiber-fed double spectrographs covering the wavelength range 3800-9200 Å over 4098 pixels. The resolution $\lambda/\Delta\lambda$ varies between 1850 and 2200. The two spectrographs together are fed by 640 optical fibers (diameter equal to 3"). The finite diameter of the fiber prevents fibers to be placed closer than 55". As the survey progressed, photometrically and astrometrically calibrated imaging catalogues and spectroscopic catalogues are released to the scientific community and to the general public in annual release. In Figure 4.16 and 4.17 are reported the coverage of imaging and spectroscopic survey respectively, for the six published releases from 2000 to nowadays. When we start our investigation the last version published was the fourth data release.

The great area covered, the extension of the catalogue down to $r = 17.77$, and the spectroscopic information, including indices and derived products such as stellar masses and star-formation rates, makes the SDSS the ideal

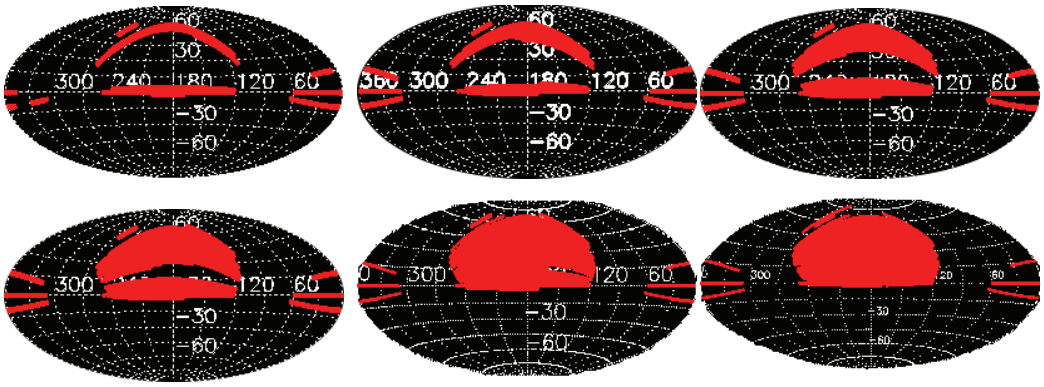

Figure 4.16: The sky coverage of the six published imaging SDSS data releases (DR). From top-left to bottom-right from DR1 to DR6.

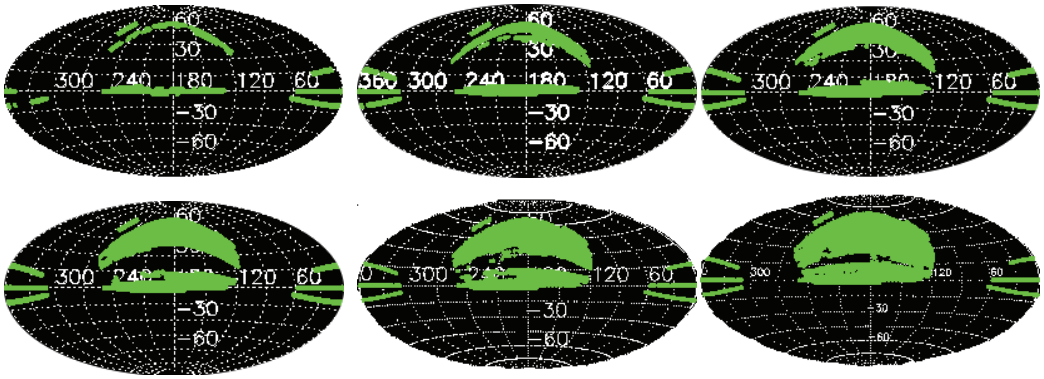

Figure 4.17: The same of figure 4.16 for spectroscopic coverage.

survey to study the dependence of star-formation on function both of environment and mass. The spectroscopic information provided by the survey allow a robust determination of the different structures, and hence of the environment with no contamination due to background or foreground galaxies. Moreover, thanks to the wide extension of the survey we are able to i) extend the study performed on the SOS to the field regions where the effects of the environment on galaxy evolution is negligible, and ii) to strengthen our SOS results on a statistical basis thanks to the large variety of environments provided by the SDSS. To this aim we select from the DR4 a volume limited sample of $\sim$28000 galaxies in the redshift range $0.005 < z < 0.037$ to analyse the different physical mechanisms that drive the star-formation on giant and dwarf galaxies, both in superclusters and the field.

Chapter 5

Technical aspects

In this chapter we present the volume-limited sample of local SDSS galaxies used in this work, discussing its completeness limit and the bias introduced by using the spectroscopical information derived with a 3 arcsec diameter aperture, rather than over the full extent of the galaxy. We present also the near-ultraviolet (NUV), and far-ultraviolet (FUV) catalogues and the algorithms used to define the environment over the entire extension of Data Release 4 (DR4)[1].

5.1 The Data

To study the star-formation and nuclear activity in galaxies as function both of luminosity and environment, we refer to a volume-limited sample of galaxies taken from the SDSS DR4. Moreover, we combine this catalogue with Galaxy Evolution Explorer GALEX near-ultraviolet photometry to examine the composition and the environmental dependencies of the optical and ultraviolet-optical colour-magnitude (CM) diagrams.

[1]The contents of this chapter are published in the articles:

- Haines, C. P.; Gargiulo, A.; La Barbera, F.; Mercurio, A.; Merluzzi, P.; Busarello, G., "The different physical mechanisms that drive the star formation histories of giant and dwarf galaxies", 2007, MNRAS, 381, 7-32.
- Haines, C. P.; Gargiulo, A.; Merluzzi, P., "The SDSS-GALEX viewpoint of the truncated red sequence in field environments at z 0", 2008, MNRAS, 385, 1201-1210.

5.1.1 The SDSS DR4 sample

The sample of galaxies used in this work is taken from the fourth data release of the Sloan Digital Sky Survey (SDSS DR4, Adelman-McCarthy et al. 2006) The area covered by the imaging survey has a total extension of 6670 square degrees, from which *ugriz* broad band imaging data have been acquired for 180 million objects.

Instead of the spectroscopic catalogue obtained with the SDSS reduction and calibration procedures, we refer to the low redshift catalogue (LRC) taken from the New York University Value Added Galaxy Catalogue (NYU-VAGC) of Blanton et al. (2005c). The LRC is a catalogue of SDSS galaxies with $0.0033 < z < 0.05$, $r_{Petro} < 18$ and with $\mu_{50} \leq 24.5\,\mathrm{mag\,arcsec^{-2}}$ in the r-band (where μ_{50} is the surface brightness within a circular aperture containing half of Petrosian flux). Blanton et al. (2005c) also perform some further quality control checks on the catalogues, including: *i*) a procedure for dealing with large, complex galaxies that were incorrectly deblended by the SDSS pipeline, and correctly associating spectra from fibres that were offset from the actual centres of the objects; *ii*) bringing into the LRC a number of galaxies with redshifts but morphologically classified as stars; and finally *iii*) performing a number of visual checks on objects in the catalogue. In addition, Blanton et al. (2005c) computed the K-correction for each object of the NYU-VAGC using the version 3.2 of the software K-CORRECT (Blanton et al. 2003c) providing in this way, the absolute magnitudes of the objects.

The region covered by the SDSS survey in this release (see Fig. 4.17, first globe, second line) includes two wide contiguous regions in the North Galactic Cap, one centred roughly on the Celestial Equator and the other around $\delta = +40°$, both with $120° < \alpha < 240°$, and three narrower stripes, one centred on the Celestial Equator again, and two at $\delta = +15°$ and $\delta = -10°$ with $-60° < \alpha < 60°$. Since we are interested to define the local environment through the local galaxy density, we have excluded the LRC galaxies belonging to the three stripes as the computation of local galaxy density could be biased due to the narrow dimension of these regions (no point is more than 3.4 Mpc from the boundary).

In this analysis we focus our attention particularly on the environmental impact on the dwarf galaxy population. Hence we have only selected from the LRC the galaxies with $0.005 < z < 0.037$ in order to obtain a catalogue which is $> 90\%$ complete to $M_r < -18$ ($M_r < M^\star + 3$) yielding a final catalogue of 27 753 objects. The lower limit in redshift at $z = 0.005$ is due both to the peculiar velocities which can seriously influence the distance estimates and to the great problems arising from the deblending of the large and resolved objects.

As dwarf galaxies tend to have low surface brightnesses, it is important to consider whether significant numbers of dwarf galaxies are missing from the SDSS spectroscopic catalogue (and hence ours) due to surface brightness selection effects, which are three-fold: *i*) photometric incompleteness; *ii*) galaxies not being targetted due to being shredded by the deblending algorithm; *iii*) targetted galaxies which did not yield reliable redshifts. Blanton et al. (2005b) analysed the surface brightness completeness of the LRC up to $\mu_{50} < 24.5$ and found that for $M_r < -18.0$ the LRC does not suffer from significant ($> 10\%$) incompleteness due to surface brightness effects. At fainter magnitudes they find that although low-surface brightness dwarf galaxies are clearly detectable in the SDSS images, the photometric pipeline tended to mistakenly deblend them or overestimate the background sky levels.

Spectral indices of the galaxies

The stellar indices used are taken from MPA/JHU SDSS DR4 catalogues (Kauffmann et al. 2003a, hereafter K03), in which a continuum fitting code was adopted that was optimized to work with SDSS data in order to recover also the weak features of the spectra and to account for the Balmer absorption (Tremonti et al. 2004). The library of spectra templates are composed of single stellar population models following the assumption that the star-formation history of a galaxy is made up of a set of discrete bursts. The models are based on the new population synthesis code of Bruzual & Charlot (2003) which incorporates a spectral library covering the 3200-9300Å range and with high resolution (3Å) matching the SDSS data. The templates span a wide set of ages and metallicities. After a Gaussian convolution of the templates in order to match the stellar velocity dispersion of each galaxy, the best fitting model is constructed by performing a non-negative least-squares fit with the dust extinction values A_z of K03 and the $\lambda^{-0.7}$ attenuation law of Charlot & Fall (2000). K03 use the amplitude of the 4000Å break (as defined in Balogh et al. 1999) and the strength of the $H\delta_A$ absorption line as diagnostics of the stellar populations of the galaxies, from which maximum-likelihood estimates of the z-band mass-to-light ratios are made. These in conjunction with the z-band absolute magnitude and the dust attenuation A_z yield the stellar mass of each galaxy.

The stellar mass estimates of K03 are only available for galaxies in the range $14.5 < r < 17.77$. For the remainder of the galaxies we use the same technique as Baldry et al. (2006) who estimate the stellar mass-to-light ratio of each galaxy from its $u - r$ colour, using the analysis of Bell & de Jong (2001) who show that for models of star-forming disk galaxies with reasonable metallicities and star-formation histories, the stellar mass-to-light ratios cor-

relate strongly with the colours of the integrated stellar populations. Briefly, for each 0.05 mag bin in $u-r$ we determine the median value of $(\mathcal{M}/L_r)$ for those galaxies with stellar mass estimates by K03, and linearly interpolating between bins, create a relation between the $u-r$ colour and its stellar mass-to-light ratio. This relation is then used to estimate stellar masses for the remaining galaxies from their r-band luminosity and $u-r$ colour. Additionally, using the spectral line indices, we identify AGN with the [N II]λ6584 / Hα versus [O III]λ5007 / Hβ diagnostics BPT diagrams of Baldwin, Phillips, & Terlevich (1981) (see Fig.5.1) as those galaxies lying above the 1σ lower limit of the models defined by Kewley et al. (2001). When either the [O III]λ5007 or Hβ lines are unavailable (S/N<3), the two-line method of Miller et al. (2003) is used, with AGN identified as having $\log([\text{N II}]\lambda6584\,/\,\text{H}\beta) > -0.2$.

The completeness of the catalogue

The completeness (i.e. the fraction of galaxies brighter than the SDSS spectroscopic magnitude limit of $r = 17.77$ that have been spectroscopically observed resulting in good redshifts) of our catalogue is strictly influenced by three factors:
i) The dimension of the fibres which prevents two objects closer than $55''$ from being observed. Roughly 6% of the objects are not spectroscopically observed for this reason (Blanton et al. 2003b).
ii) The blending of bright galaxies with saturated stars. Bright galaxies which overlap saturated stars are flagged themselves as SATURATED and hence will not be targeted spectroscopically. As one goes to fainter magnitudes the blending goes down as the area covered by the galaxy decreases. The fraction of galaxies not targeted for spectroscopy for this reason rises from 1% overall to 5% at the bright end of galaxy sample ($r<15$) (Strauss et al. 2002).
iii) The selection criteria set by LRC are broader than those of the selection algorithm used to target galaxies for the spectroscopic SDSS survey (Strauss et al. 2002).

The pronounced incompleteness of the spectroscopic catalogue at the bright end may bias the detection and characterization of low-z groups of galaxies, since the most luminous objects of these structures are not included. To cope with this deficiency, we have matched the photometric catalogue of SDSS with the NASA/IPAC Extragalactic Database (NED). For all the objects with a positive match we have associated the SDSS *ugriz* photometry with the corresponding redshift from NED and calculated the absolute magnitudes. There are a total of 803 galaxies added this way to our catalogue with $0.005<z<0.037$ and $r<17.77$. Their contribution is largest at bright magntitudes where the 202 $r<14.5$ galaxies from NED make up $\sim$8% of the

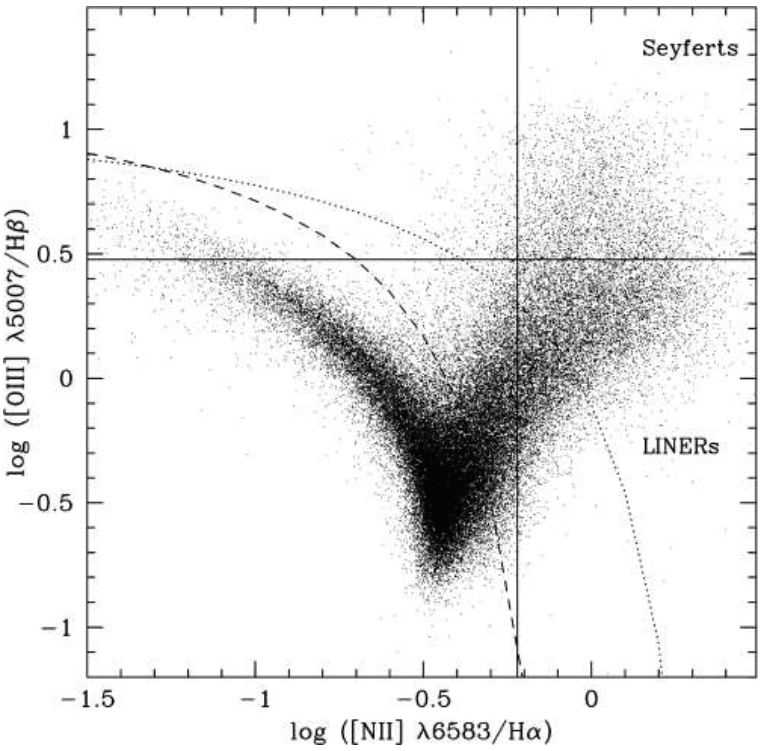

Figure 5.1: An example of a BPT diagram taken from *Kauffmann et al.* 2003. The emission-line flux ratio [OIII]/Hβ versus the ratio [NII]/Hα are reported for all the galaxies in the sample analyzed by $Kauffmann\ et\ al.$ (55 757 objects). All four spectral lines are detected with S/N $>$ 3. The dotted curve shows the demarcation between starburst galaxies and AGN defined by Kewley et al. (2001). The dashed curve shows the revised demarcation of Kauffmann et al. (their equation 1). Seyfert galaxies are often defined to have [OIII]/H$\beta > 3$ and [NII]/H$\alpha > 0.6$, and LINERs to have [OIII]/H$\beta <$ 3 and [NII]/H$\alpha > 0.6$.

catalogue. We do not have the spectral indices for the galaxies taken from NED, and so they are only used here in defining the local environment of the LRC galaxies.

Despite the contribution from NED, our improved spectroscopic catalogue is still incomplete. To compute the completeness, assuming that in the catalogue all the objects with spectra are correctly classified, it is firstly necessary to check the classification of the objects without spectra. From a first visual check on the limited sample of bright galaxies ($r < 14.5$) with no spectra we found many objects such as saturated stars and satellite tracks classified as galaxies. To remove these objects from our photometric catalogue in the most automatic way, we have compared their flags with those of known galaxies (i.e. with redshifts) looking for some peculiar differences. From this comparison we have noticed that, differently from galaxies, all the saturated stars have the flags SATURATED, SATUR_CENTER and the great part of those due to satellite tracks have the flag EDGE (Stoughton et al. 2002). After removing the objects with these flags, we have performed a visual inspection of a subsample of galaxies in the range $14.5 < r < 17.7$ which were not targetted for spectroscopy. In this subsample we found that the photometric pipeline sometimes fails the detection, recognizing inexisting objects. Real $r < 17.7$ galaxies should be clearly detected also in at least the g, i and z images, whereas this should not be the case for inexistent objects, and hence to exclude these objects we have only selected galaxies as having $g, i, z < 21$ and $r < 17.77$ the last limit due to the selection criteria of the SDSS spectroscopic survey. Finally, in the photometric catalogue we also found a small percentage ($\sim 1\%$) of stars classified as galaxies and of badly deblended objects. Since no particular flag characterizes them and it being impossible to reject these by hand we have left these objects in the catalogue their influence on determining the completeness being negligible.

To compute the completeness of this *cleaned* catalogue we have followed the prescription of Blanton et al. (2003b) based on the algorithm used by SDSS to locate the plates and to assign the fibres. This procedure places on the area covered by the survey a set of $1^\circ 49'$ radius circles (defined tiles) such to maximize the number of available fibres. The intersection between the tiles and the survey region defines a set of spherical polygons. The union of all the polygons that could have been observed by a unique set of tiles is called "sector". These sectors are the regions over which we have computed the completeness, $\mathcal{C}$, as the fraction of galaxies in the cleaned photometric catalogue that have good redshifts.

5.1.2 The NUV sample

The launch of the *Galaxy Evolution Explorer* (GALEX; Martin et al. (2005)) has allowed UV photometry to be obtained for a large sample of galaxies from the SDSS, and for this analysis we use both FUV (λ_{eff} = 1539Å, $\Delta\lambda$ = 268Å) and NUV (λ_{eff} = 2316Å, $\Delta\lambda$ = 732Å) imaging from the third GALEX data release (GR3). Passively evolving galaxies at $z\sim0$ have FUV-$r \sim 7$ and NUV-$r \sim 5.4$-6 (Yi et al. 2005), requiring $m_{FUV} > 24.5$ and $m_{NUV} > 23.5$ imaging to detect all galaxies from our $0.005 < z < 0.037$ SDSS spectroscopic sample. Hence for the NUV, we consider those GALEX GR3 images from the Medium Imaging Survey (MIS), Nearby Galaxy Survey (NGS) and the publicly available Guest Investigator images which have exposure times ~ 1 ksec and 5σ depths of $m_{NUV} \sim 23$. We also use images from the Deep Imaging Survey (DIS) and two fields from Guest Investigator Program 35 (PI G. Williger) which have exposure times ~ 30 ksec and 5σ depths of m_{FUV}, $m_{NUV} \sim 24.5$ (Martin et al. 2005). In total 528 GALEX GR3 NUV images from these surveys overlap with the SDSS DR4 footprint, for a total area of 490.1 deg^2.

For each galaxy in our $0.005 < z < 0.037$ catalogue that is covered by deep GALEX imaging, we take the *best* (this is defined by SDSS archive as the image with the best available reduction and which may not have been that used to select the spectroscopic target) SDSS r-band "corrected frame" 2048×1489 pix^2 ($13.5' \times 9.8'$) image from the SDSS Data Archive Server (DAS). If there is more than one image, we take the one where the galaxy is furthest from the image boundaries. We then register the associated GALEX image with the SDSS r-band image with the IRAF tool SREGISTER. This takes as input the pipeline astrometric calibrations for each image, the relative astrometric precision between the two images being 0.49 arcsec (Morrissey et al. 2005). We obtain the integrated galaxy NUV-r and FUV-r colours, by running SExtractor in dual-image mode, determining the colour over the Kron aperture determined from the r image. This step is necessary as the light distribution from galaxies can be quite different between the UV and r bands: the dominant source of UV flux is star-forming regions in the discs, while the r-band flux comes more from the old stellar population in the bulge. In the late-type spirals, in particular, the UV flux distribution may be shredded by SExtractor into separate star-forming regions. Hence simply matching the nearest GALEX NUV/FUV detection with the SDSS r-band detection can result in artificially red colours as the UV aperture does not cover the whole galaxy. We use the SDSS and GALEX photometric calibrations (Stoughton et al. 2002; Morrissey et al. 2005) which have zero-point uncertainties of 0.01 and 0.03 m_{AB} in the r and NUV bands, respectively

(Morrissey et al. 2007). We make no correction for the different point-spread functions (PSFs) of the UV and r-band iamges, the typical full width at half maximums (FWHMs) being 4.9 and 1.0-1.5 arcsec, respectively. This can result in a loss of flux due to the extended PSF in the UV bands, but for the typical-sized Kron apertures in our sample the effects should be less than 0.10 mag (Morrissey et al. 2007). We correct for Galactic extinction using $\mathrm{A(FUV)} = 8.28\,\mathrm{E}(B-V)$, $\mathrm{A(NUV)} = 8.18\,\mathrm{E}(B-V)$, $\mathrm{A}(r) = 2.751\,\mathrm{E}(B-V)$ and the dust extinction maps of Schlegel et al. (1998). In total, 4065 galaxies from our $0.005 < z < 0.037$ sample were covered by the GALEX NUV imaging, of which just two were not detected, both of which were passively evolving dwarf galaxies ($\mathrm{M}_r = -18.0$) in high-density regions ($\rho > 1$, see §5.3 for definition of ρ)

5.2 Aperture biases in the SDSS spectroscopic sample

To understand the origin of bimodality we analysed the current SF and the nuclear activity as function both of the luminosity and environment. To quantify the current production of stars and the presence of AGN in the galaxies of our sample, we refer to their spectral indices, in particular their Hα emission. One possible cause of bias in estimating the star-formation rate of galaxies in our sample is due to the galaxy spectrum being obtained through a 3 arcsec diameter aperture rather than over the full extent of the galaxy. Significant radial star-formation gradients are possible within galaxies, particularly those undergoing nuclear star-bursts or spiral galaxies with a prominent passively-evolving bulge, that can result in the "global" star-formation rate being significantly over or underestimated based upon spectra containing flux dominated by the galaxy nucleus. Kewley, Jansen & Geller (2005) indicate that star-formation rates based on spectra obtained through apertures covering less than $\sim$20% of the integrated galaxy flux can be over or underestimated by a factor $\sim$2, and to ensure the SDSS fibres sample more than this 20% require galaxies to be at $z > 0.04$. Clearly in order to use the SDSS dataset to study star-formation in $\mathrm{M}_r \sim -18$ galaxies this is not possible, as at $z = 0.04$ they are already too faint to be included in the SDSS spectroscopic sample. Brinchmann et al. (2004) quantify the effects of aperture bias on their estimates of star-formation rates in SDSS galaxies, and find that indeed in the case of galaxies with $\mathcal{M} > 10^{10.5}\mathrm{M}_\odot$ strong trends are apparent when plotting SFR/$\mathcal{M}$ as a function of redshift (their Fig. 13), the star-formation rate being systematically underestimated for galaxies at

the lowest redshifts by as much as a factor three. However they also find that for lower-mass galaxies, which cover the same redshift range as our dataset, the aperture biases are considerably smaller (20%) and a simple scaling of the fiber SFR by the r-band flux, as done by Hopkins et al. (2003), is perfectly acceptable.

Since we are primarily interested in the simple classification of galaxies into passive and star-forming, the main issue is the number of early-type spiral galaxies which may appear passive from spectra that sample only their bulge, but have also a normal star-forming discs. The integrated NUV-r colours gives a robust separation of passive and star-forming galaxies (Salim et al. 2005; Kauffmann et al. 2007; Martin et al. 2007). Hence, we can quantify the level of aperture bias as the fraction of galaxies that are calssified as 'passive' from their spectra by having EW(Hα) < 2Å, yet have global UV-optical colours indicative of star-forming galaxies, defined as those with NUV-$r < 4$ (Wyder et al. 2007). In Fig.5.2 we show the r-band (panel a) and NUV-band (panel b) images of a typical misclassified galaxy from our sample ($z = 0.0323$, $M_r = -21.71$), with the apertures used to obtained the SDSS spectra indicated by the red circles. The galaxy is a face-on early-type spiral, whose r-band flux is dominated by a bulge, but also with apparent spiral arms. In the NUV-band image however, this bulge disappears almost completely, while the extended UV-flux from star formation in the disk and spiral arms is now dominant. The reason for the misclassification is clear, the SDSS aperture covers only the central bulge which is passively evolving as apparent from the "hole" in the UV-emission in the nuclear regions, yet misses entirely the extended star-forming regions from the outer disk and spiral arms.

In panel (c), we show the fraction of galaxies misclassified due to aperture effects as a function of absolute magnitude. We find that the level of misclassification due to aperture effects is strongly luminosity dependent, dropping from 8 per cent at $M_r < -21.0$ (20 out of 246) to zero for $M_r > -19.5$ galaxies. We indicate that the aperture biases are significant for $M_r < -20$ galaxies, where $\sim$7 per cent are spectroscopically classified as passive (EW[Hα] $<$ 2Å), yet whose blue-integrated NUV-r colours (NUV $- r < 4$) are indicative of recent star-formation. As expected, many of these galaxies appear as face-on spiral galaxies with prominant bulges, whose predominately old and passive stellar populations dominate the flux within the SDSS spectral apertures. In contrast, we find that none of 1375 ($M_r > -19.5$) galaxies in the SDSS sample covered by GALEX NUV photometry are misclassified, indicating that the classification of such low-luminosity galaxies based on their Hα emission as measured through the SDSS fibres is robust against the aperture biases. Note that here we are only discussing bias in terms of classifying galaxies as

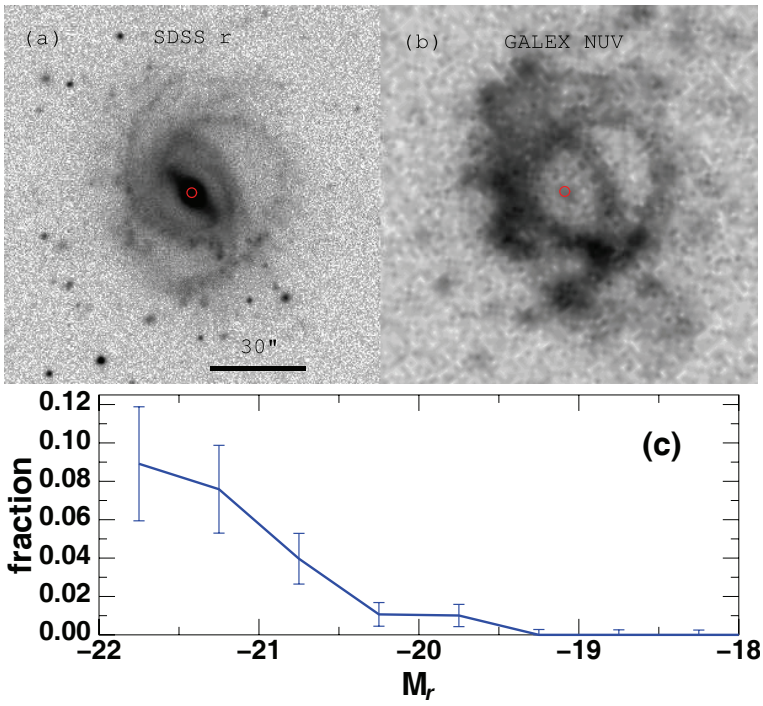

Figure 5.2: r-band (a) and NUV-band (b) images of a bright face-on early type spiral from our sample, highlighting the effects of the fibre apertures on classifying galaxies as passive from their SDSS spectra. The red circles indicate the size of the 3″ diameter apertures of the SDSS spectroscopic fibres. (c) The fraction of galaxies as a function of absolute magnitude that are classified as passive from their SDSS spectra (EW[Hα]<2Å) and also have blue UV-optical integrated colours (NUV$-r$<4) indicative of recent star-formation.

star-forming or passive, and the fibre-based SFR estimates of dwarf galaxies may well have significant uncertainties, in particular, for dIrrs which have rather patchy star-formation.

We can understand this luminosity dependence for the level of aperture bias as the combination of two effects: i) more luminous galaxies at the same distance will have larger apparent sizes, and so the fraction of flux covered by the SDSS fibres will be reduced and ii) low-luminosity galaxies tend to be either late-type spirals or dwarf ellipticals and hence do not have such significant radial gradients in their SFRs. The luminosity function of early-type spirals (Sa+b) for which aperture biases are by far the most important has a Gaussian distribution centred at $M_r \sim -21.7$ and width $\sigma \sim 0.9$ mag (de Lapparent 2003), and hence are rare at $M_r > -20$.

5.3 Definition of Environment

To study how the evolution of galaxies is related to their local environment, we firstly need to define the environment by means of the local number density of $M_r < -18$ galaxies.

To compute the local number density $\rho(\mathbf{x}, z)$ we use a variant of the adaptive kernel estimator (Silverman 1986; Pisani 1993, 1996) where each galaxy i with $M_r < -18$ is represented with an adaptive Gaussian kernel $\kappa_i(\mathbf{x}, z)$ in redshift space. Differently from Silverman (1986) and its previous applications to astronomical data (e.g. Haines et al. 2004a,b, 2006a) in which the kernel width σ_i is iteratively set to be proportional to $\rho_i^{-1/2}$, we fix the radial width to $500\,\mathrm{km\,s^{-1}}$ and the transverse width σ_i to $(8/3)^{1/2}\,D_3$, where D_3 is the distance of the third nearest neighbour within $500\,\mathrm{km\,s^{-1}}$, a limit which includes $\sim 99\%$ of physical neighbours (as determined from the Millenium simulation considering the three nearest galaxies in real-space) and minimizes the contamination of background galaxies. The choice of D_3 was made to maximize the sensitivity of the density estimator to poor groups containing as few as four galaxies, while the $(8/3)^{1/2}$ smoothing factor was added to reduce the noise of the estimator, so that in "field" regions $\sigma_i \approx D_8$ which, as shown in paragraph 5.3.1 and Table 5.1, appears the optimal value for the smoothing length-scale.

The choice both of the method and of the kernel dimensions is designed to resolve the galaxy's environment on the scale of its host dark matter halo, as it is the mass of its host halo and whether the galaxy is the central or a satellite galaxy, that is believed to be the dominant factor in defining its global properties such as star-formation history or morphology (e.g. Lemson & Kauffmann 1999; Kauffmann et al. 2004; Yang et al. 2005; Blanton et al.

2007). In the case of galaxies within groups or clusters, the local environment is measured on the scale of their host halo (0.1–1 Mpc), while for galaxies in field regions the local density is estimated by smoothing over its 5–10 nearest neighbours or scales of 1–5 Mpc.

For each galaxy i the local galaxy density is defined as

$$\rho_i(\mathbf{x}, z) \propto \sum_j \eta_j \exp\left[-\frac{1}{2}\left\{\left(\frac{D_{ij}}{\sigma_j}\right)^2 + \left(\frac{\nu_i - \nu_j}{500\,\mathrm{km\,s^{-1}}}\right)^2\right\}\right], \qquad (5.1)$$

where $\eta_j = \mathcal{C}_j^{-1}(2\pi)^{-3/2}\sigma_j^{-2}$ is the normalization factor, D_{ij} is the projected distance between the galaxies i and j, ν_i is the recession velocity of galaxy i, and the sum is over all galaxies with $\mathrm{M}_r < -18$. Note that we also calculate the local galaxy density for galaxies fainter than $\mathrm{M}_r = -18$.

We have performed a number of tests of the efficiency of this density estimator, in particular with regard to identifying group and isolated field galaxies, by applying the estimator to the public galaxy catalogues from the Millennium simulation (Springel et al. 2005c), and comparing it to other estimators based on the nearest-neighbour algorithm as applied by Balogh et al. (2004b, hereafter BB04) and Baldry et al. (2006, hereafter BB06). These tests are described in detail in the paragraph 5.3.1, and confirm that the estimator is at least as efficient as any variant of the nearest-neighbour algorithm for the same dataset. In particular the estimator is very sensitive to the presence of even poor groups containing as few as four galaxies, the result being that selecting galaxies with $\rho < 0.5\,\mathrm{Mpc}^{-2}(500\,\mathrm{km\,s^{-1}})^{-1}$ a pure field sample is produced, with *no* contamination from group members. In contrast 90% of $\rho > 4$ galaxies lie within the virial radius of a galaxy group or cluster, while those galaxies in the transition regions between groups and field environments ($r \sim \mathrm{R}_{vir}$) have densities in the range $1 < \rho < 4$.

Figure 1 shows the resultant r-band luminosity-weighted density map for galaxies with $\mathrm{M}_r < -18$ over the redshift range $0.023 < z < 0.037$ for the whole SDSS DR4 North Galactic Cap region. The adaptive kernel estimator used has the advantage of being able to be used as a group-finder (e.g. Bardelli et al. 1998; Haines et al. 2004a), by identifying groups and clusters as local maxima in the galaxy density function $\rho(\mathbf{x}, z)$, and as demonstrated in the paragraph 5.3.1 all groups and clusters having four or more $\mathrm{M}_r < -18$ galaxies in the SDSS DR4 catalogue will be marked by local maxima in the density map of Figure 1. To put this in perspective, we are sensitive to environments comparable to the Local Group (which contains four $\mathrm{M}_r < -18$ galaxies: Milky Way, LMC, M 31 and M 33) and the other nearby groups (the M81, Cen A/M 83 and Maffeigroups; Karachentsev 2005). Such poor groups represent the preferential major-merger mass scale ($\mathrm{M}_{\mathrm{halo}} \sim 10^{12}\mathrm{M}_\odot$

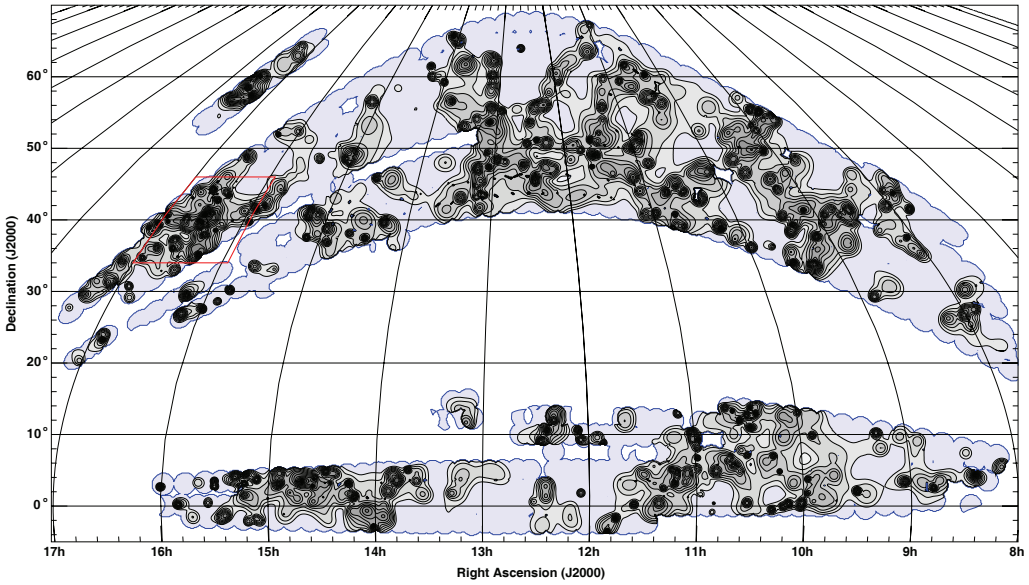

Figure 5.1: Luminosity-weighted density map of $M_r < -18$ galaxies over the redshift range $0.023 < z < 0.037$ over the entire SDSS DR4 North Galactic Cap region. The isodensity contours are logarithmically spaced, the spacing between each contours indicating a factor $\sqrt{2}$ increase in the r-band luminosity-weighted local density. The red box indicates the $12^\circ \times 12^\circ$ region containing the $z = 0.03$ A2199 supercluster analysed in Haines et al. (2006b) (see par.6.1).

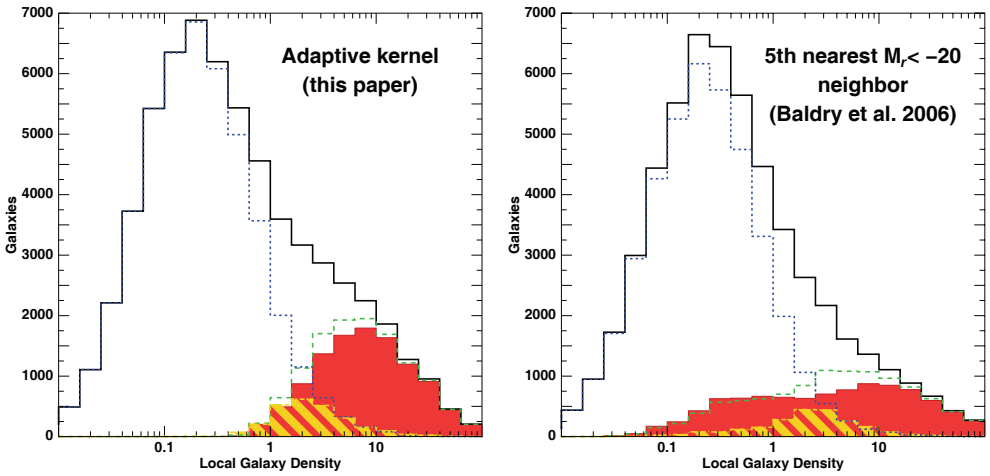

Figure 5.2: Distribution of "observed" local galaxy densities from Millennium simulation as calculated using the adaptive kernel algorithm (left) and based on the distance of the 5^{th} nearest neighbour with $M_r < -20$ (Balogh et al. 2004a; Baldry et al. 2006). The histograms show the local density distributions of all $M_r < -18$ galaxies (black solid lines), those galaxies within groups containing 4 or more members (red filled histogram), those galaxies within $1\,R_{vir}$ (green dashed lines), $0.8 < (r/R_{vir}) < 1.2$ (yellow hatched histogram with dot-dashed lines), and more than $2\,R_{vir}$ (blue short-dashed lines) from the nearest group or cluster.

for galaxies of stellar mass $\sim 10^{10}$–$10^{11}\,M_\odot$ (Hopkins et al. 2008).

5.3.1 Reliability of the density estimator

We test the efficiency of this density estimation algorithm, by applying it to the public galaxy catalogues from the Millennium simulation (Springel et al. 2005c; Croton et al. 2006). These simulations cover a $(500\,h^{-1}\mathrm{Mpc})^3$ volume producing a galaxy catalogue complete to $M_r = -17.4$ containing some 9 million galaxies, for which positions, peculiar velocities, absolute magnitudes in each of the SDSS filters, stellar masses are all provided. From this, we consider 61 981 $M_r < -18$ galaxies from a subregion of volume $200 \times 200 \times 100\,\mathrm{Mpc}^3$. We estimate the local density of each galaxy in physical space, $\rho(3D)$, by applying the adaptive kernel method, representing each galaxy by a spherically-symmetric Gaussian kernel whose width is equal to the distance to its 5^{th} nearest neighbour. Galaxy groups and clusters are identified through a percolation analysis using a friends-of-friends algorithm with a linking length equal to 0.2 times the mean interparticle separation.

For each group containing four or more members, the velocity dispersion (σ_ν) and virial radius (R_{vir}) are calculated following Girardi et al. (1998).For each galaxy we combine the position and peculiar velocity in the z-direction to create a redshift, producing a volume-limited redshift catalogue, to which we apply exactly the same adaptive kernel method as for the SDSS data, representing each galaxy by a Gaussian kernel of transverse width defined by the distance to its 3^{rd} nearest neighbour within $500\,\mathrm{km\,s^{-1}}$ and of width $500\,\mathrm{km\,s^{-1}}$ in the radial/redshift direction. The resultant distribution of local galaxy densities, ρ, is shown in the left panel Fig.5.2 by the solid black lines. It shows a peak at ~ 0.2, which is close to the global mean $M_r < -18$ galaxy density of $0.11\,\mathrm{Mpc^{-2}}\,(500\,\mathrm{km\,s^{-1}})^{-1}$, and a long tail extending to high densities.

To examine the efficiency of this density estimator in identifying galaxies within groups the red filled histogram shows the density distribution of galaxies that were identified by the percolation analysis to belong to a group containing four or more members. Alternatively, the green-dashed histogram shows the density distribution of those galaxies within the virial radius of a group containing four or more galaxies. In both cases, the observed local galaxy density of group galaxies are strongly biased to high densities with $\rho > 1$, while *no* group galaxy has $\rho < 0.5$. The yellow hatched histogram shows the density distribution of those galaxies in the transition regions between group and field environments having $0.8 < (r/R_{vir}) < 1.2$. Galaxies in these transition regions have local densities in the range $1 < \rho < 4$. Finally, the blue short-dashed histogram shows those galaxies in isolated field regions more than two virial radii from the nearest group, and hence are unlikely to have encountered the group environment during their evolution or be affected by group/cluster-related physical processes. As expected, they are observed to have low local densities with $\rho < 1$.

The left panel of Fig. 5.2 demonstrates the efficiency of this density estimator in identifying group and isolated field galaxies, in particular the latter. By selecting galaxies with $\rho < 0.5$ we can be sure of obtaining a sample of field galaxies, the vast majority ($> 97\%$) at $> 2\,R_{vir}$, and with no contamination from any galaxies belonging to groups or clusters, even those containing as few as four galaxies. Considering instead those galaxies with $\rho < 1.0$, $> 95\%$ still have $> 2\,R_{vir}$, while only 0.7% lie within the virial radius of a group. In contrast, $\sim 60\%$ of $\rho > 1.0$ and $\sim 90\%$ of $\rho > 4$ galaxies are at $< 1\,R_{vir}$.

For comparison the right panel of Fig. 5.2 shows the same density distributions of field and group galaxies brighter than $M_r = -18$ using the nearest neighbour algorithm as applied by BB04 and BB06 who estimate the local density on the basis of the projected distance to the 5^{th} nearest neighbour that is brighter than $M_r = -20$ and has a radial velocity within $1\,000\,\mathrm{km\,s^{-1}}$

of each galaxy. The overall density distributions are quite similar, as although there are three times fewer $M_r < -20$ galaxies than $M_r < -18$ galaxies, the recession velocity range over which the projected density is estimated is quadruple that used for the adaptive kernel estimator ($2\,000\,\mathrm{km\,s^{-1}}$ instead of $500\,\mathrm{km\,s^{-1}}$). The most important difference between the two estimators is the much broader density distribution of group galaxies (red filled histogram) for the nearest neighbour algorithm, which extends to much lower "observed" densities than our approach. Even at the lowest densities studied by BB04 and BB06, corresponding to $\Sigma_5 \simeq 0.1$, $\sim 5\%$ of the galaxies are group members, and hence could have been affected by group-related environmental processes. Equally, Σ_5 does not appear very sensitive to the position of a galaxy within a halo, as is apparent by the densities of those galaxies at and around the virial radius of groups being covering a wide range of values of Σ_5 and peaking at a mid-range value for galaxies within groups, rather than that obtained from the adaptive kernel approach where galaxies near the virial radius have generally the lowest densities of those galaxies in groups. The value of Σ_5 is instead most sensitive to the *mass* of the nearest massive halo, rather than whether a galaxy is inside or outside that halo.

To fairly compare the efficiency of the adaptive kernel estimator against nearest neighbour approaches, we retested the nearest neighbour algorithm using the same $M_r < -18$ datasets, varying the number of neighbours used over the range 3–10, and the velocity range used to select neighbours from 400 to $1000\,\mathrm{km\,s^{-1}}$. We define the efficiency of the density estimators in two ways: firstly in terms of the rank correlation between the observed projected density and the actual physical 3-dimensional galaxy density $\rho(3D)$; and secondly its sensitivity to the position of the galaxy within a halo, as measured by the correlation with the distance r do the nearest massive halo (containing four or more galaxies) scaled by the virial radius R_{vir}. We measure the strengths of these correlations through the Spearman rank correlation test as presented in Table 5.1. Firstly, varying the numbers of neighbours used to estimate the local density, we find that Σ_5 is the most sensitive to the actual physical local density $\rho(3D)$, while Σ_{10} is the most sensitive to the position of the galaxy within the halo (for neighbours within $500\,\mathrm{km\,s^{-1}}$. Secondly, varying the velocity range over which neighbours are selected, we find that a range of $400\,\mathrm{km\,s^{-1}}$ is most sensitive to the physical density, while a range of $600\,\mathrm{km\,s^{-1}}$ is the most sensitive to the position of the galaxy within the halo. These confirm that using a range of $500\,\mathrm{km\,s^{-1}}$ is the optimal general purpose value for estimating the local density of galaxies (at least for samples extending to $M_r \sim -18$, while the commonly used value of $1\,000\,\mathrm{km\,s^{-1}}$ is much less efficient due to contamination of projected background galaxies. Comparing our adaptive kernel estimator to the nearest neighbour algorithm,

Table 5.1: Comparison of efficiencies of density estimators

Method used	No. of neighbours	Magnitude limit	Velocity range ($\mathrm{km\,s^{-1}}$)	Spearman rank correlation ρ(3D)	$r/R_{\rm vir}$
AK	3	$M_r < -18$	500	**0.891**	**-0.800**
NN	3	$M_r < -18$	500	0.849	-0.744
NN	5	$M_r < -18$	500	**0.896**	-0.774
NN	8	$M_r < -18$	500	0.890	-0.786
NN	10	$M_r < -18$	500	0.877	**-0.789**
NN	5	$M_r < -18$	1000	0.856	-0.766
NN	5	$M_r < -18$	800	0.872	-0.772
NN	5	$M_r < -18$	600	0.889	**-0.775**
NN	5	$M_r < -18$	500	0.896	-0.774
NN	5	$M_r < -18$	400	**0.898**	-0.766
NN	5	$M_r < -20$	1000	0.785	-0.741

we find that it is always more sensitive to the position of the galaxy within a halo, and is only marginally less efficient than the optimal choice of parameters for the nearest neighbour algorithm (Σ_5). The adaptive kernel estimator we have adopted is at least as efficient as any comparable nearest neighbour algorithms, and is particularly sensitive to the position of a galaxy within a halo, which is likely to be the most important aspect of the environment in terms of affecting its evolution (Lemson & Kauffmann 1999).

In comparison we note that the particular algorithm used by BB04, BB06 is significantly less sensitive to both the $\rho(3D)$ and the position of the galaxy within the host halo (last row of Table 5.1). These differences reflect the practical issue of the density of information used to characterize the environment of a galaxy. By measuring the local environment using just $M_r < -20$ galaxies, the density of information is much sparser, making it that much less sensitive to effects on the scales of poor groups, which may contain three or less $M_r < -20$ galaxies. However, a volume of the universe can be covered that is a factor ten larger than is possible using our approach which is limited by the necessity of being complete to $M_r = -18$, and indeed for galaxies brighter than $\sim M^\star$ our analysis of their environmental trends are strongly limited by the small sample size. In addition, in the volume covered by our analysis, the only rich structures (with $\sigma_\nu > 500\,\mathrm{km\,s^{-1}}$) are the supercluster

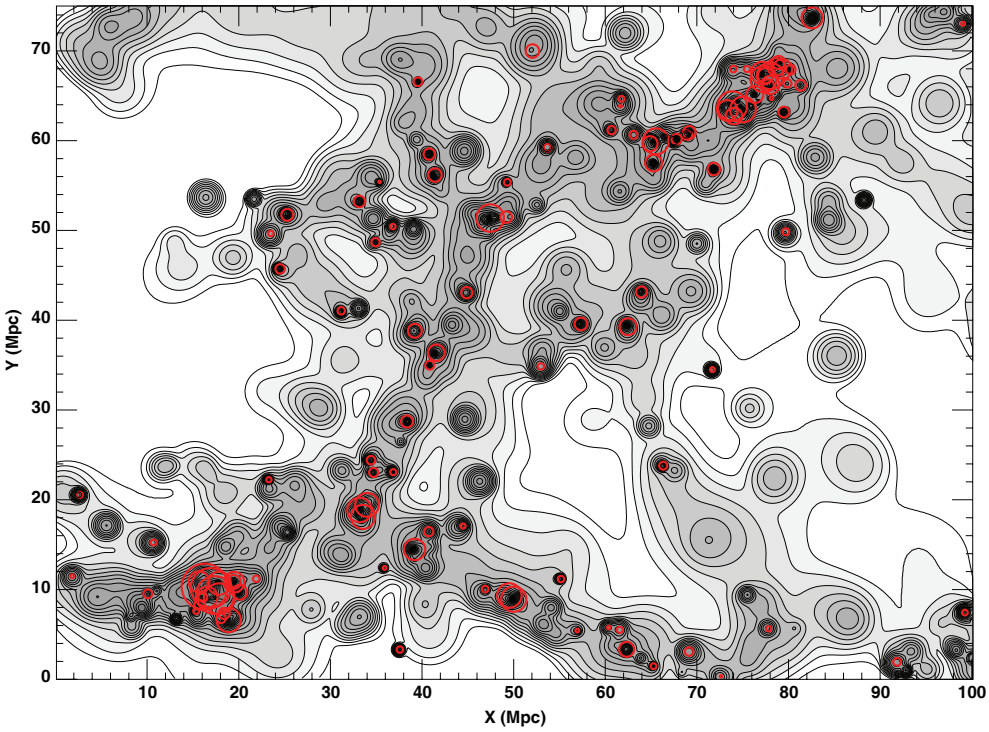

Figure 5.3: The resultant density map when applying the adaptive kernel estimator to a $75 \times 100\,\mathrm{Mpc}^2$ region in the Millennium simulation. The iso-density contours indicate the projected r-band luminosity weighted density of $\mathrm{M}_r < -18$ galaxies over a depth of 25 Mpc. The red circles indicate the virial radii of galaxy groups and clusters containing at four or more members identified within the same volume through a percolation analysis.

associated with the rich cluster Abell 2199 studied in Haines et al. (2006b), and Abell 1314, limiting our ability to follow the environmental trends to the highest densities.

The adaptive kernel method has the added advantage of being able to be used as a group-finder (e.g. Bardelli et al. 1998; Haines et al. 2004a), by identifying groups and clusters as local maxima in the galaxy density function $\rho(\mathbf{x}, z)$. A comparison of the groups identified in the Millennium simulation (see Fig.5.3) from a percolation analysis, finds that all such groups containing four or more members are marked as clear local maxima in the luminosity-weighted density maps. Unlike group finding algorithms based on a percolation analysis, the adaptive kernel approach is also able to efficiently define substructures that are the natural consequence of the hierarchical merging of galaxy groups and clusters.

Chapter 6

The different physical mechanisms driving the star-formation histories of giant and dwarf galaxies

In this chapter we address the question of galaxy bimodality through a comprehensive analysis of star-formation and nuclear activity in galaxies as a function both of luminosity and environment. Using the sample of 27753 local galaxies taken from SDSS DR4, we investigate the physical mechanisms responsible of the quenching of the star-formation in giant and dwarf galaxies, as function of environment[1].

6.1 Previous studies

Haines et al. (2006b) in their work investigated the possible mass-dependency of the age-density and SF-density relations by comparing the global trends with environment for giant ($M_r < -20$) and dwarf ($-19 < M_r < -17.8$) galaxies in the vicinity of the $z = 0.03$ supercluster centred on the rich cluster A 2199, the richest low-redshift ($z < 0.05$) structure covered by the SDSS DR4 spectroscopic dataset (see red box in Fig.5.1).

[1]The results of this study are published in the article:

- Haines, C. P.; Gargiulo, A.; La Barbera, F.; Mercurio, A.; Merluzzi, P.; Busarello, G., "The different physical mechanisms that drive the star formation histories of giant and dwarf galaxies", 2007, MNRAS, 381, 7-32.

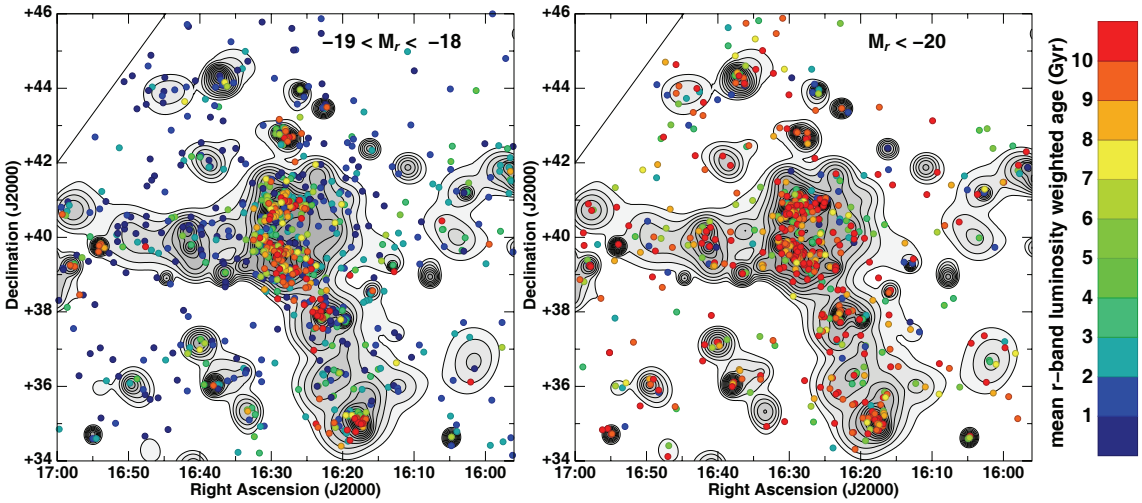

Figure 6.1: The mean r-band luminosity weighted stellar age (solid coloured circles) as a function of spatial position in the A2199 supercluster environment, for dwarf ($-19 < M_r < -18$; left) and gaint ($M_r < -20$; right) galaxies. The black contours represent the local luminosity-weighted surface density of galaxies with redshifts within $2\,000\,\mathrm{km\,s^{-1}}$ of A2199, and are logarithmically spaced with every second countour indicating a factor 2 change in density. The different colours of the symbols indicate the mean stellar age from young (< 2Gyr, blue) to old (> 7Gyr, red) (*Haines et al.*, 2006b).

A strong bimodality was seen in the mean stellar age-M_r distribution about a mean stellar age of 7 Gyr, with a population of bright (L^*) galaxies $\sim$10 Gyr old, and a second population of fainter galaxies dominated by young ($<$3 Gyr) stars, while a clear age-density distribution was identified for both giant and dwarf subsamples (see Fig.6.1).

They confirmed the findings of Smith et al. (2006) that the age-density relation is stronger for dwarf galaxies, while the critical density at which the ages increase markedly is higher for dwarf galaxies, occurring at values typical of the cluster virial radius. In the highest-density regions they found that $>$80% of both giant and dwarf subsamples were old ($>$7 Gyr). However, whereas the fraction of old giant galaxies declines gradually with decreasing density to the global field value of $\sim$50%, that of dwarf galaxies drops rapidly, tending to *zero* for the lowest density bins. Identical trends with density were independently observed when passive galaxies were identified from their lack of Hα emission.

Looking directly at the spatial distribution of galaxies in the vicinity of

the supercluster, in field regions the giant population shows a completely interspersed mixture of both young and old populations, indicating that their evolution is driven primarily by their merger history rather than direct interactions with their environment. In contrast, the mean stellar ages of dwarf galaxies were strongly correlated with their immediate environment: those passively-evolving or old dwarf galaxies found outside of the rich clusters were always found within poor groups or as a satellite to an old, giant ($>L^*$) galaxy. No isolated old or passively-evolving dwarf galaxies were found.

In this analysis, with the volume-limited sample of $\sim$ 28 000 galaxies with $0.005<z<0.037$, complete $>90\%$ to $M_r=-18$ ($M^*+3.2$), we extend the study of Haines et al. (2006b) covering the entire SDSS DR4 footprint. We reexamine the arguments of Haines et al. (2006b) taking advantage of this much larger dataset to provide quantitative measures of the environmental dependencies on star-formation in galaxies and in particular how these vary with the galaxy mass/luminosity. We attempt to disentangle the different contributions to the SF-density relation caused by physical mechanisms internal to the galaxy (e.g. AGN feedback) and those caused by the direct interaction of the galaxy with its surroundings (for a review of how the diverse mechanisms leave different imprints on the environmental trends see e.g. Treu et al. 2003).

Throughout we assume a concordance ΛCDM cosmology with $\Omega_M=0.3$, $\Omega_\Lambda=0.7$ and $H_0=70\,\mathrm{km\,s^{-1}Mpc^{-1}}$.

6.2 Dependence of star-formation on luminosity and environment

One of the best understood and calibrated indicators of the star-formation rate (SFR) in galaxies is the Hα nebular emission-line, whose luminosity is directly proportional to the ionizing radiation from massive ($>10\,M_\odot$) short-lived (<20 Myr) stars, and hence the Hα emission provides a near-instantaneous measure of the current star-formation rate (Kennicutt 1998). Figure 6.2 shows the EW(Hα) distribution of $M_r<-18.0$ galaxies in the redshift range $0.005<z<0.037$ from the SDSS DR4 spectroscopic dataset. The x-axis is scaled as $\sinh^{-1}$ EW(Hα): this results in the scale being linear at EW(Hα)$\approx$0Å where measurement errors dominate, and logarithmic for EW(Hα)$>$10Å allowing the lognormal distribution of equivalent widths for star-forming galaxies to be conveniently displayed.

We exclude galaxies showing an AGN signature, as their Hα emission may be dominated by emission from the AGN rather than star-formation. AGN

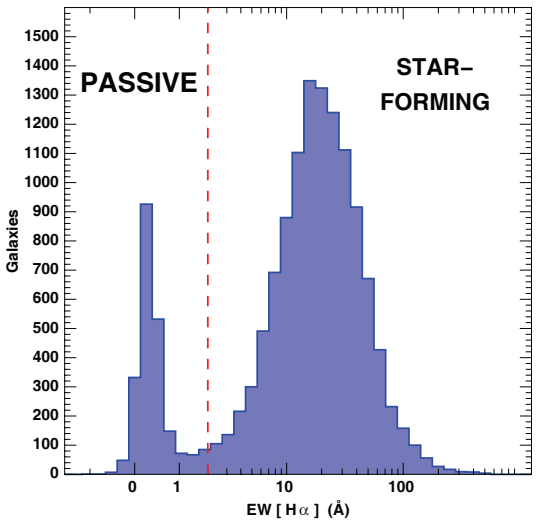

Figure 6.2: The EW(Hα) distribution of $M_r < -18.0$ galaxies (AGN excluded) in the redshift range $0.005 < z < 0.037$ from the SDSS DR4 spectroscopic dataset.

are defined using the [N II]λ6584 / Hα versus [O III]λ5007 / Hβ diagnostics of Baldwin, Phillips, & Terlevich (1981) as lying above the 1σ lower limit of the models defined by Kewley et al. (2001). When either the [O III]λ5007 or Hβ lines are unavailable (S/N<3), the two-line method of Miller et al. (2003) is used, with AGN identified as having $\log(\text{[N II]}\lambda6584 \,/\, \text{H}\beta) > -0.2$. We also exclude those galaxies without an Hα measurement.

The distribution is clearly bimodal, with two approximately Gaussian distributions: one that is narrow and centred at EW(Hα)$\sim$0.2Å, corresponding to passively-evolving galaxies with little or no ongoing star-formation; and another that is wider and centred at EW(Hα)$\sim$20Å, corresponding to galaxies currently actively star-forming. Midway between these two distributions there are relatively-speaking very few galaxies, and we identify the dividing line between passive and star-forming galaxies as being EW(Hα) = 2Å, that corresponds approximately to the minimum in the distribution between the two peaks. Note that this value is different to that used in the studies of Balogh et al. (2004a, hereafter B04) and Tanaka et al. (2004, hereafter T04) who use EW(Hα) = 4Å to separate passive and star-forming galaxies, but is the same as used by Rines et al. (2005, hereafter R05). The lower value however appears justified empirically from Fig. 6.2, and is sufficiently large that even for the faintest galaxies ($r \sim 17.77$) the limit still represents a 4σ detection in Hα, the median uncertainty in EW(Hα) only reaching 0.5Å by $r = 17.77$. The inclusion of galaxies with optical AGN signatures would tend

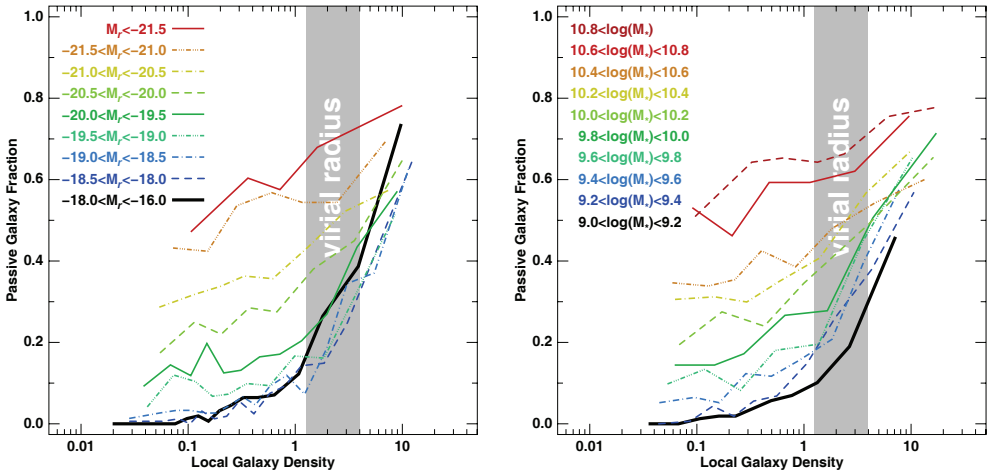

Figure 6.3: The fraction of passively-evolving galaxies (EW[Hα] < 2 Å) as a function of both local density and luminosity (left panel) or stellar mass (right panel). Each coloured curve corresponds to a different luminosity / stellar mass bin as indicated. Each density bin contains 150 galaxies. The grey shaded region indicates the typical densities found for galaxies near the virial radius ($0.8 < (r/\mathrm{R}_{vir}) < 1.2$) of groups or clusters in the Millennium simulation (see Fig. 5.2).

to fill in the gap in the bimodal distribution, their Hα equivalent widths typically in the range 0.5–10Å (median=1.56Å).

The left panel of Fig. 6.3 shows how the bimodality in EW(Hα), and hence the ongoing star-formation rate of galaxies, depends on both luminosity and environment. Each coloured curve shows the fraction of passively-evolving galaxies (EW[Hα]$<$2Å) as a function of local density for a particular luminosity range as indicated. The lowest luminosity bin ($-18 < \mathrm{M}_r < -16$) is far from complete, and is biased heavily towards galaxies close to the bright magnitude limit, but the environmental trends should be representative of those galaxies slightly fainter than $\mathrm{M}_r = -18$. Galaxies that lie very close to the edge of the SDSS DR4 footprint are likely to have biased density estimates, and so we exlude those galaxies that are within 2 Mpc or σ_i Mpc, whichever is smaller, of the survey boundary are excluded from all further analyses. This results in a final sample of 22 113 galaxies.

At the highest densities ($\rho > 5$), corresponding to the centres of galaxy clusters or groups, passive galaxies dominate for the entire luminosity range studied, with $\sim$70% of galaxies being passive independent of luminosity. At lower densities in contrast the fraction of passive galaxies depends strongly on luminosity. Even at densities comparable to those seen at the virial radius

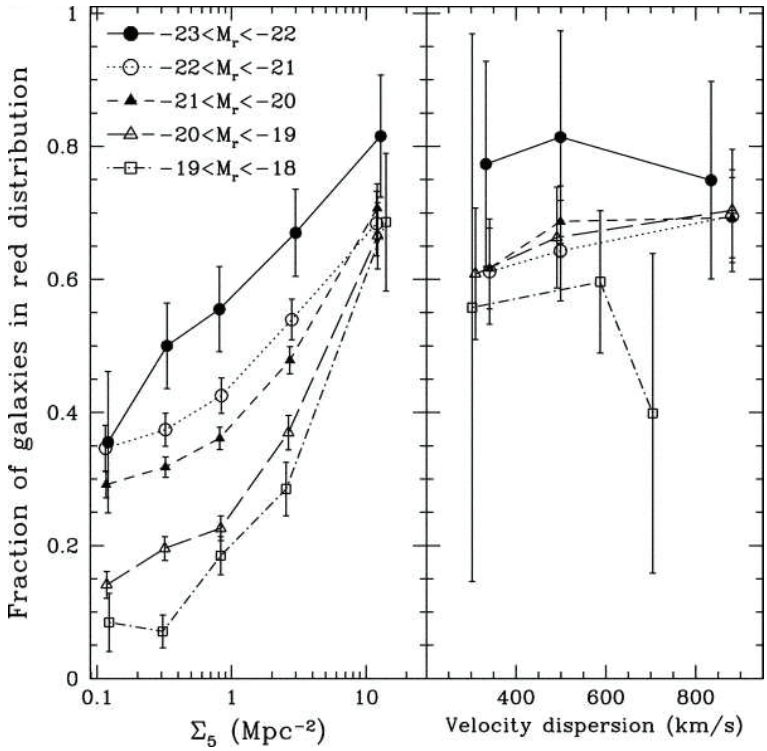

Figure 6.4: Fraction of galaxies in the red distribution, in bins of local density (left panel) or cluster velocity dispersion (right panel). Five lines are shown, corresponding to five different luminosity ranges, as indicated. Points are shown with 1 s error bars at the median density or velocity dispersion of each bin. Each point represents the fraction of red galaxies only among galaxies with that luminosity and environment and, therefore, they do not need to add to 100% *Balogh et al.* 2004a.

of groups/clusters, the fraction of $M_r > -20$ galaxies that are passive has dropped to $\sim$20% or lower, while that of brighter galaxies has dropped only slightly. The luminosity dependence is greatest for the lowest density regions corresponding to field environments well beyond the environmental influence of galaxy clusters or groups. Here the fraction of passive galaxies drops from $\sim$50% for $M_r < -21$ galaxies to $\sim$0% for $M_r > -19$ In the lowest luminosity bin ($-18 < M_r < -16$) the passive galaxy fraction has dropped to precisely zero in the lowest density regions. In fact, there are no passive galaxies in the lowest density quartile, corresponding to $\simeq 600$ galaxies in total.

These results can be compared with the analysis of BB04 who show in their Fig. 2 (see Fig.6.4) the fraction of red sequence galaxies as a function

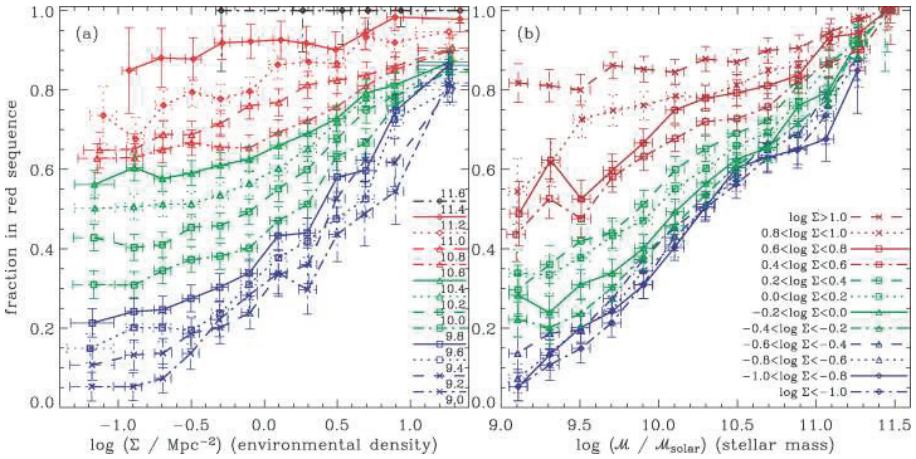

Figure 6.5: Fraction of red-sequence galaxies versus environment and versus stellar mass. In panel (a), the symbols and lines represent different stellar masses as shown in the legend (from 9.0 to 11.6). In panel (b), the lines represent different environmental densities. Systematic errors of 0.03 were added in quadrature to the Poisson errors. *Baldry et al.* 2006.

of both environment and r-band luminosity using data from SDSS DR1. As here, BB04 find that $\sim$70% of galaxies in their highest density bin belong to the red sequence. However, in their lowest density bin, the luminosity dependence is somewhat less than presented here, dropping from $\sim$35% for $-22 < \mathrm{M}_r < -21$ to $\sim$8% for $-19 < \mathrm{M}_r < -18$.

The right panel of Fig. 6.3 repeats the analysis using stellar mass ($\mathcal{M}$) instead of r-band luminosity. Essentially the same results are obtained, with passive galaxies dominating in high-density regions independent of stellar mass, while in low-density regions the fraction of passively-evolving galaxies depends strongly on stellar mass, dropping from $\sim$50% at $\mathcal{M} \sim 10^{10.8}\,\mathrm{M}_\odot$ to zero by $\mathcal{M} \sim 10^{9.2}\,\mathrm{M}_\odot$. We note that for stellar masses below $10^{9.2}\,\mathrm{M}_\odot$ we are no longer volume-limited introducing a selection bias, whereby passively-evolving galaxies are more likely to be missed by the $r = 17.77$ magnitude limit than star-forming galaxies of the same mass and at the same distance.

BB06 have performed a very similar analysis of the same SDSS DR4 dataset, examining how the fraction of *red sequence* galaxies varies as a function of both environment and stellar mass (see Fig.6.5, their Fig. 11a). They consider a much larger volume than our analysis, resulting in a significantly larger sample, particularly at the high-mass end, allowing them to follow the environmental trends for stellar mass bins to $\log \mathcal{M} = 11.6$. BB06 use a different approach to K03 to calculate the mass-to-light ratios of the galaxies

based on the $u-r$ colour only, but they use the same IMF, and as shown in Fig. 5 of BB06 obtain stellar masses that on average are within 0.1 dex of one another. The global trends are qualitatively the same, with red sequence galaxies dominating in high-density environments independently of stellar mass, while in the lowest density environments the fraction of red sequence galaxies is a strong function of stellar mass. This latter trend extends to the higher stellar masses studied by BB06, falling from $\sim 100\%$ at $\log \mathcal{M} \sim 11.6$ to 5% by $\log \mathcal{M} \sim 9.0$. However for the same stellar mass bin, the red sequence fractions of BB06 in low-density regions are systematically $\sim 10\%$ higher than the passive galaxy fraction from our analysis.

Although the trends shown here in Fig. 6.3 are similar to those of BB04 and BB06, as discussed above there are some important differences. In particular, we find that for $M_r > -18.0$ or $\mathcal{M} < 10^{9.2} M_\odot$ there are no passively-evolving galaxies in the lowest-density bins, whereas for the same stellar mass/luminosity ranges both BB04 and BB06 find that 5–10% of the galaxies belong to the red sequence in their lowest density bin. This difference has important consequences for the conclusions that can be drawn from the data (see § 7.4). What is the cause of this remnant population of faint red galaxies in low-density environments, that disappears in our analysis? Firstly, as discussed previously, the local density estimator used in BB04 and BB06 is not completely able to separate group and field galaxies, so that even for the lowest density bin considered $\sim 5\%$ of the galaxies are group members, the majority of which lie on the red sequence at all luminosities. Secondly, not all red sequence galaxies are passively-evolving: a significant fraction are known to be star-forming, and appear red due to high levels of dust extinction. In an analysis of the SDSS main sample galaxies covered by infrared imaging from the SWIRE survey, Davoodi et al. (2006) find that 17% of red sequence galaxies are dusty star-forming galaxies (identified by their high 24μm to 3.6μm flux ratios and Hα emission), while Wolf et al. (2005) find that dusty star-forming galaxies constitute more than one-third of the red sequence population in the A901/2 supercluster region.

Conversely, due to the SDSS spectra being obtained through $3''$ diameter fibres, the region covered may only cover the central bulge region of nearby large galaxies, resulting in galaxies appearing passive despite having normal star-forming disks. As discussed earlier (§ 5.2) based on a comparison of the SDSS and *GALEX* NUV photometry of $\sim 15\%$ (4065 galaxies) of our low-redshift sample we find that $\sim 8\%$ (20 out of 246) of bright ($M_r < -21$) galaxies are classified as passive yet have blue UV-optical colours ($\mathrm{NUV} - r < 4$) indicative of normal star-forming galaxies (cap. 7). This fraction drops steadily with magnitude (being 2.5% for $-21 < M_r < -20$ galaxies), falling to zero (0 out of 1375) for galaxies at $M_r > -19.5$. We find no significant varia-

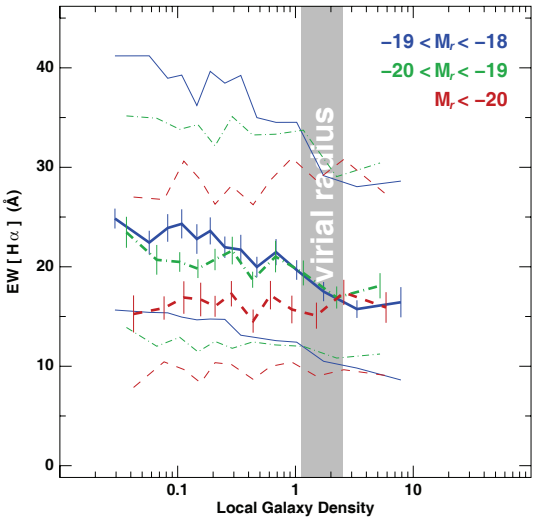

Figure 6.6: The dependence of EW(Hα) on local density for galaxies with EW(Hα) $>$ 2Å. The red dashed lines represent giant galaxies ($M_r < -20$), the green dot-dashed lines represent galaxies with $-20 < M_r < -19$, while the blue solid lines represent dwarf galaxies ($M_r > -19$). The thick and thin lines show respectively the median and interquartile values of the distribution. The median lines are accompanied by 1σ error limits estimated by bootstrap resampling including the measured error in EW(Hα). Each bin contains 300 galaxies.

tion of these fractions with environment. We thus indicate that the passive galaxy fractions obtained for the higher luminosity/mass bins are overestimated due to aperture effects, but that those for the lower luminosity galaxies ($M_r > -20$) are robust against aperture biases.

6.3 Star-forming Galaxies

If star-forming galaxies at the present day are affected by environmental mechanisms when they move from low- to high-density regions, we should see a signature of this transformation which depends on the relevant time-scale. In particular, if the dominant environmental mechanism produces a gradual (>1 Gyr) decline in star-formation when galaxies become bound to groups or clusters (e.g. suffocation), then star-forming galaxies in dense regions should show systematically lower star-formation rates or EW(Hα). On the other hand, if the dominant environmental mechanism suppresses star-formation in galaxies on a very short timescale, then we should not expect any sig-

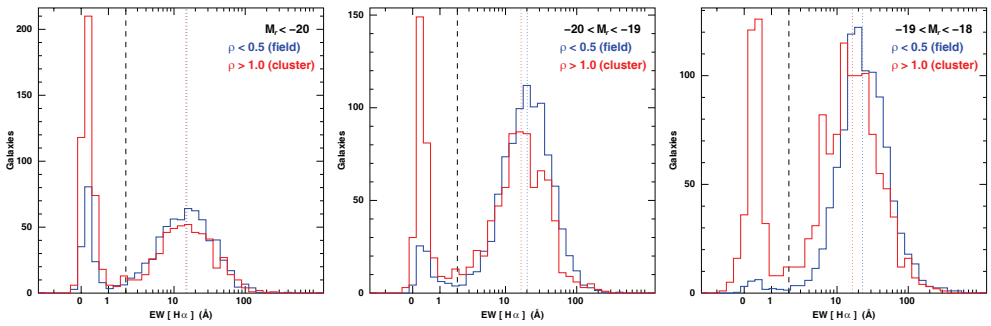

Figure 6.7: A comparison of the EW(Hα) distributions for galaxies in high- ($\rho > 1.0$; red histogram) and low-density ($\rho < 0.5$; blue dashed histogram) regions for three luminosity ranges, corresponding to $M_r < -20$ (left panel), $-20 < M_r < -19$ (middle) and $-19 < M_r < -18$ (right). The vertical scale corresponds to the number of galaxies per bin in the high-density histogram, while the low-density histogram has been scaled to allow comparison of the distribution of star-forming galaxies. The red and blue dotted lines indicate the median values of star-forming galaxies (H$\alpha > 2$ Å) in the high- (red) and low-density (blue) regions.

nificant changes in the EW(Hα) distribution of star-forming galaxies, since the galaxies will quickly become classed as passive and hence not contribute to the EW(Hα) distribution. In the previous studies of B04 and T04 the distributions of EW(Hα) of giant ($M_r < M^\star + 1$) star-forming (EW[Hα]$>$4Å) galaxies show no dependence on local density, while R05 found no difference in the EW(Hα) distributions of star-forming galaxies inside the virial radius, in infall regions ($1 < (r/R_{200}) < 5$) or in field regions. From these results they imply that few giant galaxies can be currently undergoing a gradual decline in star-formation due to environmental processes. However, when considering fainter galaxies with $M^\star + 1 < M < M^\star + 2$ T04 found the EW(Hα) of star-forming galaxies to be slightly smaller in dense regions, a result taken to be a signature of the slow truncation of star-formation in faint galaxies.

6.3.1 Hα-density relation for star-forming galaxies

Following B04 and T04 we show in Fig. 6.6 the EW(Hα) distribution of star-forming galaxies as a function of local density for three luminosity ranges: $M_r < -20$ (red dashed lines) which can be compared with the results of B04 ($M_B < -20.2$; $M_r < -21.3$) or the bright sample of T04 ($M_r < -20.3$); $-19 < M_r < -20$ (green dot-dashed lines) which is comparable to the faint sample of T04; and $-18 < M_r < -19$ (blue solid lines). In each case, star-

forming galaxies are defined as having EW(Hα) $>$ 2Å as throughout this article. Note that both B04 and T04 use EW(Hα) $>$ 4Å, but using this value instead makes no noticeable difference to the results. We also exclude here those galaxies classified as AGN. As observed in previous studies, there is no apparent dependence on density for the EW(Hα) distribution for galaxies with $M_r < -20$. In contrast, the trends for lower luminosity galaxies show a significant drop in EW(Hα) with increasing density, most of the drop occuring within the range $0.5 < \rho < 2$ which represents the transition between galaxies inside and outside bound structures. The significance of the trends are measured using the Spearman rank correlation test and reported in Table 6.1. Whereas the EW(Hα) distribution of $M_r < -20$ star-forming galaxies shows no correlation with local density ρ, significant anti-correlations are found for the $-20 < M_r < -19$ and $-19 < M_r < -18$ star-forming galaxy populations at the 5σ and 10σ level respectively.

We do not expect aperture biases to have any significant effects on the environmental trends presented here, as we observe no dependencies on local galaxy density for the distribution of SDSS fiber aperture covering fractions in any of the luminosity ranges. Similarly, we find no environmental trends for the fraction of the early-type spiral galaxies classified as passive from their SDSS spectra yet having blue NUV$-r$ colours. The only possible effect could be a systematic underestimation of the Hα emission in the $M_r < -20$ luminosity bin, but our results for this bin are fully consistent with the comparable trends obtained by T04 and B04 based upon galaxy samples at $0.03 < z < 0.065$ and $0.05 < z < 0.095$ respectively, where aperture effects should not be important (Kewley et al. 2005).

To see exactly how the distribution of EW(Hα) changes with environment, Fig. 6.7 shows the EW(Hα) distribution of galaxies in high ($\rho > 1.0$; red histogram) and low ($\rho < 0.5$; blue dashed histogram) density envrironments for three luminosity ranges, corresponding to $M_r < -20$ (left panel), $-20 < M_r < -19$ (middle) and $-19 < M_r < -18$ (right). The vertical red and blue dotted lines indicate the median values of star-forming galaxies (EW[Hα] $>$ 2Å).

The bimodal character of the EW(Hα) distribution is apparent in both the high- and low-density environments for each of the luminosity ranges studied. The two environmental dependencies described in Figs. 6.3 and 6.6 can both be seen when comparing the EW(Hα) distributions for the high- and low-density environments.

Firstly, a global shift in the relative fractions of star-forming and passively-evolving galaxies is apparent. The two histograms have been normalized so that distributions of the star-forming galaxies appear to have approximately the same height. As a result, the relative increase in the fraction of

Table 6.1: Comparison of the EW(Hα) distributions in high-($\rho > 1.0$) and low ($\rho < 0.5$) density environments.

Magnitude range	Median EW[Hα](Å) $\rho < 0.5$	$\rho > 1.0$	Probability (Kolmogorov-Smirnov)	U test (σ)	Spearman rank correlation ρ
$M_r < -20$	15.19	14.66	0.464	0.07	0.0102±0.0242
$-20 < M_r < -19$	20.23	16.58	2×10^{-6}	5.26	-0.0753±0.0179
$-19 < M_r < -18$	22.85	16.48	6×10^{-25}	11.27	-0.1580±0.0156

passively-evolving galaxies from low- to high-density environments is clear. This relative increase is strongly dependent on luminosity, rising from about a factor 2.5–3 for luminous ($M_r < -20$) galaxies to a factor ~ 20 for the dwarf ($-19 < M_r < -18$) galaxy population.

The second effect can be seen as a global shift in the EW(Hα) distribution of the star-forming galaxies from high- to low-density environments. In each environment and luminosity range, the EW(Hα) distribution of the star-forming galaxies can be well described as being log-normal (and hence appearing as a Gaussian distribution in the figure). However, whereas there is no apparent difference in the high- and low-density distributions for luminous ($M_r < -20$) star-forming galaxies, at lower luminosities, the high-density EW(Hα) distributions are *systematically* shifted to lower valaues than their low-density counterparts. The level of this shift is quantified by comparison of the median values of the distribution, while the significance of the differences between the two distributions are estimated through application of the non-parametric Kolmogorov-Smirnov and Wilcoxon-Mann-Whitney U tests, the results of which are shown in Table 6.1. These results confirm that while the EW(Hα) distribution of the high- and low-density $M_r < -20$ galaxy populations are fully consistent with one another, for the lower luminosity samples the null hypothesis that the high- and low-density star-forming populations have the same EW(Hα) distribution is rejected at very high significance levels. For the $-19 < M_r < -18$ sample, the Hα emission from star-forming galaxies in high-density environments is systematically lower by $\sim 30\%$ with respect to their low-density counterparts.

The Hα emission (and hence star-formation) must be suppressed in a significant fraction of galaxies when they fall into a cluster or group for the first time. However, for these galaxies to remain classed as star-forming, this suppression must act over a long period of time, to allow a significant fraction of galaxies to be seen in the process of transformation into passively-evolving galaxies. If we assume that the Hα emission of galaxies declines

exponentially with time as they are being transformed, and that the rate at which galaxies are transformed remains constant, the EW(Hα) of galaxies which are *currently* in the process of being transformed but are still classed as star-forming, will drop from ~ 20Å to 2Å, with an average of ~ 8Å. Hence star-forming galaxies in the process of transformation will have *on average* $\sim 40\%$ of their emission prior to their being transformed. To produce a global systematic reduction of $\sim 30\%$ in the Hα emission would then require $\sim 50\%$ of the dwarf star-forming galaxies in high-density regions to be in the process of being transformed into passive galaxies. Given that, as discussed previously, as many as 30–40% of galaxies in the high-density do not lie within the virialized regions of a cluster or group, this suggests that the vast majority of dwarf star-forming galaxies in groups or clusters are *currently* in the process of being transformed into passive galaxies.

6.3.2 SFR-density relation for star-forming galaxies

The current star-formation rate of a galaxy can be estimated from its Hα flux through the calibration given by Kennicutt (1998):

$$\mathrm{SFR}\left(\mathrm{M}_{\odot}\mathrm{yr}^{-1}\right) = \frac{L(\mathrm{H}\alpha)}{1.27 \times 10^{34}\mathrm{W}}. \tag{6.1}$$

Before applying this calibration, it is necessary to correct for the effects of dust obscuration and account for the effects of emission lost by virtue of the spectra being obtained through a fibre whose aperture may be significantly smaller than the galaxy. The obscuration correction is measured by the Balmer decrement, estimated by measuring the ratio of the stellar absorption-corrected Hα and Hβ line fluxes, and assuming case B recombination and the obscuration curve of Cardelli, Clayton & Mathis (1989). The aperture correction is quantified as the ratio of the observed r-band Petrosian flux and the continuum flux at the wavelength of Hα within the fibre aperture. A full discussion of these corrections and the use of Hα line emission as a SFR indicator in SDSS data is given in Hopkins et al. (2003) where the explicit calculation used is given as equation

$$\mathrm{SFR}\left(\mathrm{M}_{\odot}\mathrm{yr}^{-1}\right) = \frac{L(\mathrm{H}\alpha)}{1.27 \times 10^{34}\mathrm{W}}. \tag{6.2}$$

Moustakas, Kennicutt & Tremonti (2006) compare the integrated SFRs estimated from the Hα flux using the above procedure with those estimated from IRAS infra-red data and find the two estimates consistent with a precision of $\pm 70\%$ and no systematic offset, confirming that the extinction-corrected

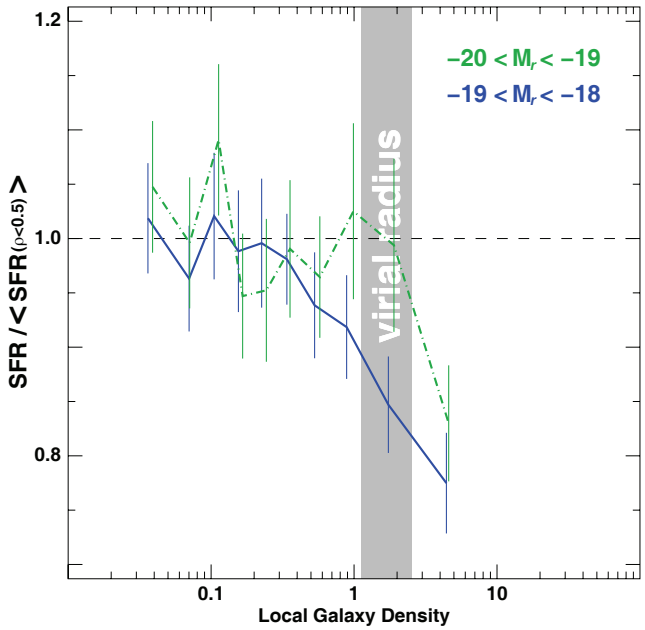

Figure 6.8: The dependence of the median star-formation rate on local density for star-forming galaxies with EW(Hα) > 2Å. The green dot-dashed lines represent galaxies with $-20 < M_r < -19$, while the blue solid lines represent dwarf galaxies ($M_r > -19$). The lines are accompanied by 1σ error limits estimated by bootstrap resampling and include the measured error in EW(Hα) and uncertainties in the level of dust obscuration. Each bin contains 300 galaxies.

Table 6.2: Comparison of the SFRs of star-forming galaxies in high- ($\rho > 1.0$) and low ($\rho < 0.5$) density environments.

Magnitude range of galaxies	Median SFR ($M_\odot yr^{-1}$) $\rho < 0.5$	$\rho > 1.0$	P(K-S)	U test (σ)
$-20 < M_r < -19$	0.496	0.443	0.0079	2.30
$-19 < M_r < -18$	0.191	0.157	7×10^{-9}	6.52

Hα luminosity can be used as a reliable SFR tracer, even for the most dust-obscured systems.

Using the above calibration and corrections, we plot in Fig. 6.8 the median SFR of star-forming galaxies as a function of local density for galaxies in the luminosity range $-20 < M_r < -19$ (green dot-dashed line) and $-19 < M_r < -18$ (blue solid line). As discussed in §5.2 aperture effects will strongly bias the estimates of star-formation rates made using the method of Hopkins et al. (2003) for the most massive galaxies in our sample and so we do not plot the results for $M_r < -20$ galaxies. To allow the effect of high-density environments on star-formation to be measured, each curve is normalized to the median SFR of "field" ($\rho < 0.5$) star-forming galaxies in the same luminosity range.

The environmental trends in SFR broadly match those shown earlier in Fig. 6.6 for the EW(Hα) distribution of star-forming galaxies, confirming that those trends do indeed reflect changes in the global SFR with environment, and are not due to variations in dust obscuration or aperture biases. These trends are quantified in Table 6.2 which compares the median SFRs of star-forming galaxies in high- and low-density environments for both luminosity ranges, as well as estimates the significance of any differences. The most significant result ($\sim 6\sigma$) is the observed systematic drop of $\sim 20\%$ in the median SFR of dwarf ($-19 < M_r < -18$) star-forming galaxies in high-density regions with respect to field galaxies. In both luminosity bins there appears a systematic drop in SFR for densities greater than $1\,\mathrm{Mpc}^{-2}$, which suggests that star-formation is suppressed in a significant fraction of galaxies when they infall for the first time into a cluster or group.

As discussed earlier we do not expect aperture biases to be important for galaxies in these luminosity bins. Moreover we find no dependencies on local galaxy density for the fraction of galaxy flux covered by the SDSS fiber apertures in either luminosity bin.

As a final check to confirm that aperture effects are not behind the observed environmental trends in EW(Hα) and star-formation rates, we repeat the analyses using galaxy $u - r$ colours as a measure of their current/recent star-formation. The $u - r$ colours are determined over apertures defined by the Petrosian radius, and hence represent an integrated measure of a galaxy's star-formation history. The resultant trends in the median $u - r$ colour with local density for each of the luminosity ranges are presented in Fig. 6.9.

For each of the three luminosity ranges star-forming galaxies become increasingly redder with density. The strength of the trend increases with decreasing luminosity from 0.07 mag for $-21 < M_r < -20$ galaxies to ~ 0.2 mag for $M_r > -20$ galaxies. Almost identical trends were observed by Balogh et al. (2004b) for galaxies selected as star-forming by their $u - r$ colour. In the

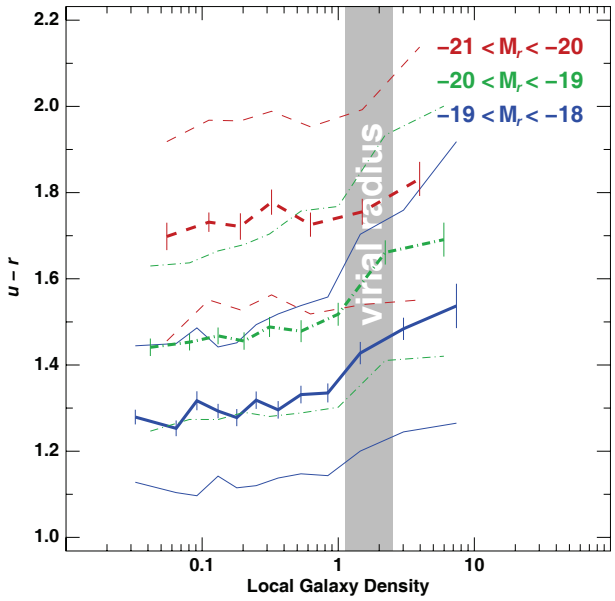

Figure 6.9: The dependence of the $u-r$ galaxy colour on local density for star-forming galaxies with EW(Hα) $>$ 2Å. The red dashed lines represent giant galaxies ($M_r < -20$), the green dot-dashed lines represent galaxies with $-20 < M_r < -19$, while the blue solid lines represent dwarf galaxies ($M_r > -19$). The thick and thin lines show respectively the median and interquartile values of the distribution. The median lines are accompanied by 1σ error limits estimated by bootstrap resampling and include the measured errors in $u-r$. Each bin contains 300 galaxies.

case of the two lower luminosity ranges ($M_r > -20$) the bulk of the change in $u - r$ colour with density occurs at $\rho > 1$, as seen for the trend in SFR of Fig. 6.8. These trends are fully consistent with those seen in the Hα emission and SFR, confirming that the previous trends are not the result of aperture effects.

6.4 How environment affects the SF-density relation?

To this point we have examined the environmental dependence on star-formation in galaxies using densities measured by smoothing over the nearest 5–10 galaxies. This has allowed us to describe the effects of the group and cluster environments on the galaxies. It is also possible that galaxies are affected by the presence of individual neighbouring galaxies, for example through disturbance from tidal forces.

In particular, we wish to reexamine for the much larger volume covered by the SDSS dataset the long noted morphological segregation of dwarf galaxies in the local (< 30 Mpc) neighbourhood, whereby dwarf ellipticals are confined to groups, clusters and satellites to massive galaxies, while dwarf irregulars tend to follow the overall large-scale structure without being bound to any of the massive galaxies (Binggeli, Tarenghi & Sandage 1990; Ferguson & Binggeli 1994). In Fig.6.10 we plot the distribution of nearby (distance < 10Mpc) galaxies taken from Karachentsev et al. (2004) in the supergalactic plane X e Y. Blue circles represent galaxies classified as late-type or with no gas emission in HI band, while orange circles represent galaxies classified as early-type and with no gas emission in HI band. The radius of each circle is directly proportional to the galaxy's magnitude up to M_B = -13.5. It appear clear how the dwarf passive galaxies are mostly found near massive systems. Einasto et al. (1974) first noted this segregation when comparing the spatial distribution of dwarf companions to our Galaxy and the nearby massive spirals M 31, M 81, and M 101. He found a striking separation of the regions populated by dE and dIrr galaxies with dEs confined to being close satellites to the primary galaxies, and dIrr found at larger distances. In this analysis we found *no* isolated passively-evolving dwarf galaxy, always finding them gravitationally bound to clusters/groups or as satellites of $> L^\star$ field galaxies, differently from star-forming field dwarfs which appeared randomly distributed throughout the region.

In this context we wish to look at the effects of neighbouring galaxies on the star-formation histories of field galaxies ($\rho < 0.5$), i.e. those not in

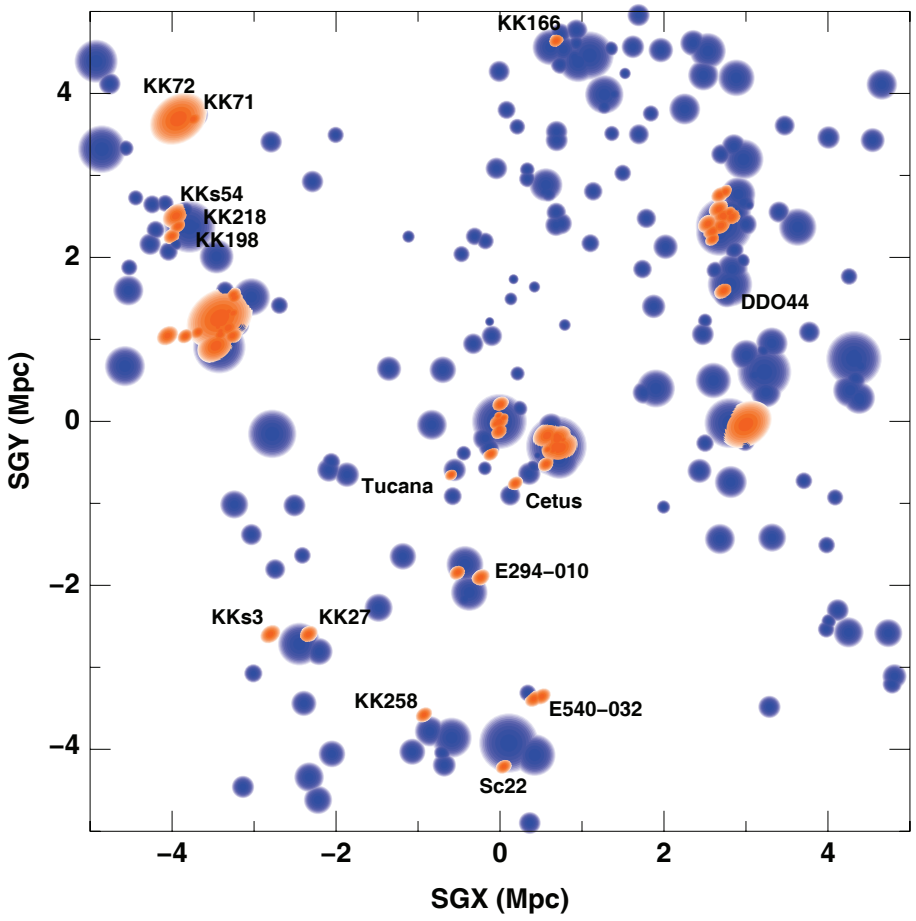

Figure 6.10: Distribution of nearby (distance < 10Mpc) galaxies taken from Karachentsev et al. (2004) in the supergalactic plane X e Y. Blue circles represent galaxies classified as late-type or with no gas emission in HI band, while orange circles represent galaxies classified as early-type and with no gas emission in HI band. The radius of each circle is directly proportional to the galaxy's magnitude up to M_B = -13.5.

groups or clusters for which other processes may well dominate. There are two main physical mechanisms whereby a neighbouring galaxy could affect star-formation in another galaxy, tidal interactions, and ram-pressure stripping caused by the passage of the galaxy through the gaseous halo of its neighbour. In both of these mechanisms, the mass/luminosity of both the *central* galaxy (i.e. that which is being acted on) and the neighbouring galaxy are important for defining the strength of the effect on the *central* galaxy, in particular the greater mass-ratio between the neighbouring galaxy and the central galaxy, the stronger the effect is likely to be. To measure the effect of both the central and neighbouring galaxy masses, we split both the central and neighbouring galaxies into bins of luminosity. It is also important that we take out the effect of the large-scale ($>1\,$Mpc) galaxy density from the equation, as galaxies in higher density regions will naturally have closer neighbours than lower density regions. To measure the effect of the presence of a neighbouring galaxy on the star-formation history of the central galaxy we compare the distances to the nearest neighbour (within a certain luminosity range) for passively-evolving and star-forming central galaxies that have the same mass/luminosity and the same large-scale environment (i.e. their local densities are the same). If the presence of a neighbouring galaxy is important for causing the central galaxy to become passive, we would expect passively-evolving central galaxies to have nearer neighbours (within a certain luminosity range) than star-forming galaxies of the same luminosity and large-scale environment.

In Figure 6.11 the distribution of distances between passively-evolving (EW[Hα]<2Å; red histograms) and star-forming (EW[Hα]>2Å; blue dashed histograms) central galaxies in field regions ($\rho<0.5$) and their nearest neighbours are compared for both different magnitude ranges of central galaxies (in order of increasing luminosity from left to right as indicated) and different magnitude ranges of neighbouring galaxies (in order of increasing luminosity from top to bottom as indicated)

As a consequence of the SF-density relation, even in field regions passively-evolving galaxies will on average be in higher density regions than star-forming galaxies of the same luminosity, and hence on this basis alone would be expected to have closer neighbours on average. To remove this bias, we normalize the density distribution of the star-forming galaxies to that of the passively-evolving galaxies. This is done by splitting the galaxies into ten density bins of equal logarithmic width (0.2 dex) in the range $0.01<\rho<1$ and for each bin j identify a weight $\omega_j = \mathrm{N}^j_{\mathrm{passive}}/\mathrm{N}^j_{\mathrm{SF}}$ where $\mathrm{N}^j_{\mathrm{passive}}$ and $\mathrm{N}^j_{\mathrm{SF}}$ are the total number of passive and star-forming galaxies in that density bin. Each star-forming galaxy belonging to density bin j is then given the corresponding weight ω_j. The resulting weighted population of star-forming

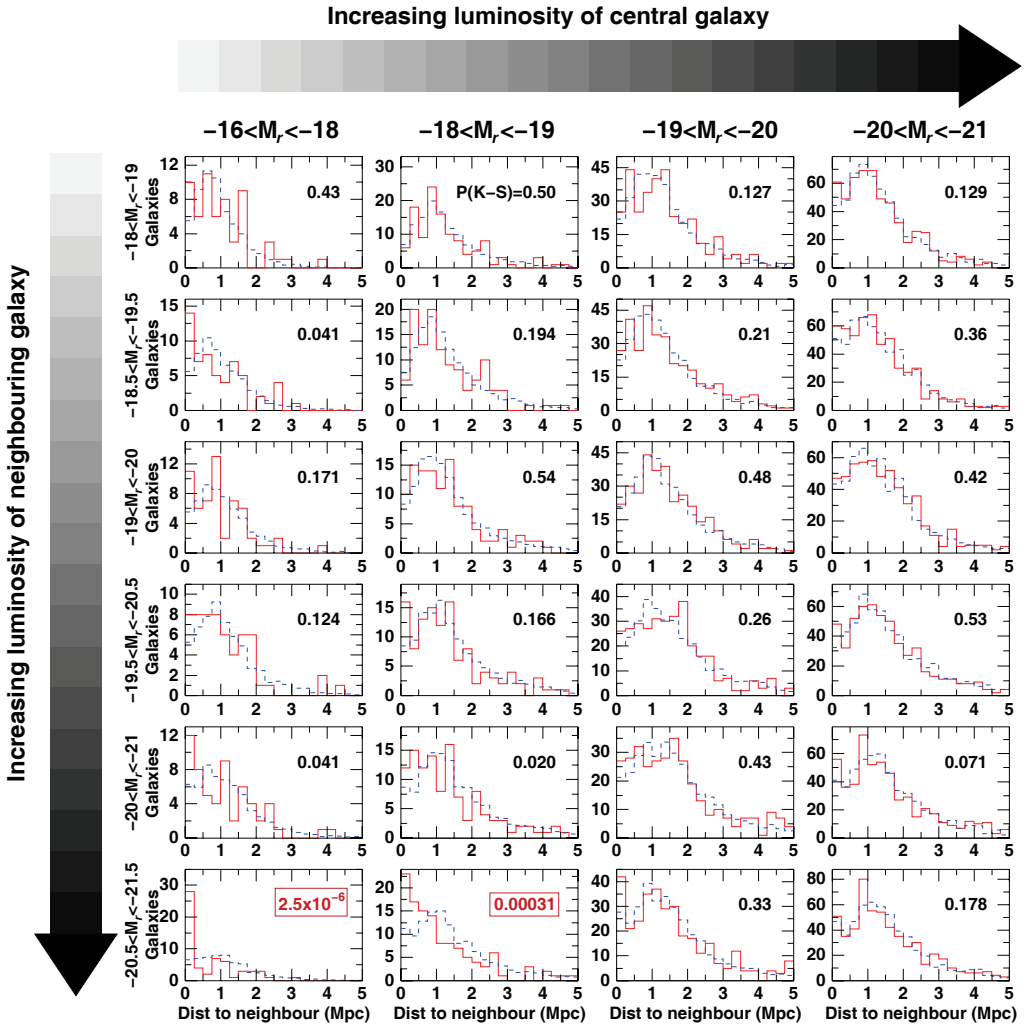

Figure 6.11: The distributions of distances to the nearest neighbouring galaxy within a specific luminosity range (in order of increasing luminosity from top to bottom as indicated) for $\rho < 0.5$ passive (red line) and star-forming (blue dashed line) *central* galaxies also within a specific luminosity range (in order of increasing luminosity from left to right as indicated). The probabilities that the two histograms are taken from the same distribution according to the Kolmogorov-Smirnov test are indicated in the top-right of each panel.

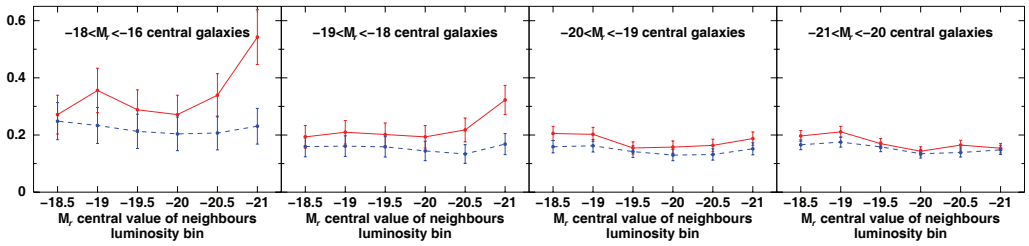

Figure 6.12: The fraction of passive (red lines) and star-forming (blue dashed lines) *central* galaxies which have within 0.5 Mpc one or more galaxies belonging to a fixed range of magnitude. Each panel corresponds to *central* galaxies within a specific magnitude range in order of increasing luminosity from left to right as indicated. The top left panel shows that dwarf passive field galaxies are much more likely to be found in the proximity of massive galaxies than star-forming dwarfs while the giant passive field galaxies show no preference as to their neighbours.

galaxies has the same density distribution as their passive counterparts. The blue-dashed histograms then represent the distribution of distances to the nearest neighbour for the star-forming galaxies where each galaxy i is represented by its corresponding weight ω_i.

For each of the panels in Fig. 6.11 corresponding to a particular luminosity range for central and neighbouring galaxies, we estimate the significance of any differences between the distributions of the distance to the nearest neighbours of passive and star-forming galaxies (the red and blue histograms) using the Kolmogorov-Smirnov test. The results of these are indicated in the top-right of each panel, with significant differences ($P_{KS} < 0.01$) highlighted by red boxes.

Looking at the histograms in the last two columns (corresponding to central galaxies with $M_r < -19$) we see that the distributions of distances to the nearest neighbours of any luminosity range are the same for the passively-evolving and star-forming galaxies. This implies that the star-formation histories of $M_r < -19$ galaxies are not significantly affected by the presence of individual galaxies in their immediate neighbourhoods, and instead it is only the global large-scale environment (as measured here by ρ) to which their SFRs are correlated. Equally if we look at the histograms in the top four rows (corresponding to neighbouring galaxies with $M_r > -20.5$) the distance distribution to the nearest neighbours are the same for passively-evolving and star-forming central galaxies of any luminosity range. Hence star-formation in galaxies (at least for $M_r < -16$) is not significantly affected by the presence

Table 6.3: Candidate isolated passively-evolving dwarfs and possible associated groups. References: (1) Rines & Diaferio (2006), (2) Popesso et al. (2004), (3) White et al. (1999), (4) Mahdavi & Geller (2004).

RA, Dec (J2000)	z	M_r	d_{cl} (Mpc)	Group Name	Refs	N_{gal}	μ_{nu}	σ_z (km/s)	R_{vir} (Mpc)	T_X (keV)	$\log(L_X)$ (erg/s)
14:37:13.70, +02:28:35.9	0.0255	-17.67	2.56	MKW 8	1,2	147	0.0267	492	1.56	3.03	41.98
12:00:26.60, +01:40:07.6	0.0209	-17.32	1.46	MKW 4	1,2	99	0.0199	428	1.25	1.83	41.96
12:00:37.72, +02:08:47.9	0.0201	-17.61	1.41	MKW 4	1,2	99	0.0199	428	1.25	1.83	41.96
15:14:04.35, +03:24:04.9	0.0297	-17.82	0.76			6	0.0292	221	0.52		
09:47:15.48, +37:03:07.1	0.0223	-17.62	1.83	WBL 236	3,4	24	0.0219	324	0.96		41.76

of neighbouring galaxies with $M_r > -20$.

The only luminosity combinations of central and neighbouring galaxies that show any significant difference ($P_{KS} < 0.01$) between the distance distribution to the nearest neighbours of the passive and star-forming central galaxies are the two lower-left panels corresponding to low-luminosity central galaxies ($M_r > -19$) that have bright ($M_r < -20.5$) neighbours. In both these panels we see that passively-evolving dwarf galaxies ($M_r > -19$) are much more likely to have a nearby bright ($M_r < -20.5$) neighbour within ~ 500 kpc than would a star-forming galaxy of the same luminosity and having the same global environment (as measured with ρ). This implies that massive galaxies can influence the star-formation history of neighbouring dwarf galaxies, presumably orbiting as satellites, by causing them to become stop forming stars.

We reillustrate these effects in Figure 6.12 where we plot the fraction of *central* passive (red solid line) and star-forming (blue dashed line) galaxies that have one or more neighbours within 0.5 Mpc belonging to a fixed magnitude range. Each panel corresponds to a different magnitude range of central galaxies as before, while each point corresponds to one of the six magnitude ranges of neighbouring galaxies of Figure 6.11, the central value of which is indicated along the x-axis. The fractions of passive and star-forming giant ($-21 < M_r < -20$) galaxies with a neighbour within 0.5 Mpc are quite similar for every magnitude range of surrounding systems; not only, but the common fractions are quite constant independently of the luminosity of neighbouring galaxies. These observations show that both passive and star-forming massive galaxies have no preferences about their neighbours suggesting a uniform distribution for these systems. Different results are found for dwarf ($-18 < M_r < -16$) field galaxies. In fact, the fractions of passive dwarfs with neighbours within 0.5 Mpc are different from those found for

their star-forming counterparts. The latter show a similar behavior with the field giants having, on average, no preference for neighbours of a particular luminosity. On the contrary the fraction of passive field dwarfs with a close-by galaxy strongly increases with the luminosity of the neighbour, underling that these systems, as was firstly pointed out by Einasto et al. (1974), are not uniformly distributed but are commonly found close to massive galaxies. This trend is also present, even if in a less strong way, for $-19 < M_r < -18$ *central* galaxies and disappears at brighter magnitudes.

These results suggest that the mechanisms transforming giants and dwarfs from star-forming to passive systems are different. The quite uniform spatial distribution of passive field giant galaxies underlines the negligible influence of any environmental interactions in stopping star-formation for these systems, while the frequent presence of nearby massive galaxies to passive field dwarf galaxies is a clear indication of the fundamental impact of massive galaxies on star-formation in nearby dwarf systems.

Out of the 252 passively-evolving dwarf galaxies in the lowest luminosity bin ($-18 < M_r < -16$) 48 are in regions with $\rho < 0.5$. Of these 48, 34 were found to have bright ($M_r < -20$) galaxies within $\sim 500\,\mathrm{kpc}$ and $\sim 500\,\mathrm{km\,s^{-1}}$, 24 of which were within $\sim 200\,\mathrm{kpc}$ and $\sim 200\,\mathrm{km\,s^{-1}}$. No further neighbours are identified if the magnitude limit is extended from $M_r < -20$ to $M_r < -19$. A further nine galaxies were identified as not actually being passively-evolving dwarfs, either having apparent Hα emission not identified by the MPA/JHU pipeline, appearing blue, or having bad photometry which made the galaxy appear much fainter than it actually was.

Only five passively-evolving dwarf galaxies appear to be isolated, being 0.8–1.2 Mpc from the nearest bright galaxy. However, looking a little further out we find that all five appear to lie in the infall regions of galaxy groups at around 1.5–2 virial radii from the group centres, as indicated in Table 6.3. The centres and redshifts of each of the groups were identified as maxima in the luminosity-weighted galaxy density distribution, and the cluster velocity dispersions and virial radii determined as in Girardi et al. (1998) based on the galaxy radial velocities within 2 Mpc and $3\sigma_\nu$ of the cluster centre.

Although the first galaxy lies some 2.5 Mpc from MKW 8, this cluster is part of a larger structure which extends for $\sim$ 7 Mpc around the "isolated" passive dwarf galaxy. It seems reasonable to assume this structure is still in the process of assembly, and hence the dwarf galaxy may have been left behind or thrown out by a previous interaction between the structures. The remaining nearby clusters are rather more isolated and regular, and so it seems less likely that the other four dwarf galaxies were thrown out by cluster interactions. The most likely mechanism for these galaxies to have become passive is that in the past their orbits took them through

their neighbouring group/cluster, whereupon they became passive through ram-pressure stripping and/or tidal interactions. From cosmological N-body simulations Mamon et al. (2004) find that infalling galaxies on radial orbits can bounce out of the clusters, reaching maximum clustercentric distances of between 1 and 2.5 virial radii. The main difficulty is to understand why these galaxies haven't been able to start forming stars again once they are no longer affected by the cluster environment. In particular, while these galaxies may have been completely stripped of gas while in the cluster, outside gas recycling from stellar mass loss should be able to produce enough gas to be detectable (e.g. Jungwiert, Combes & Palous 2001) and subsequently allow star-formation to restart after a few Gyr, although Grebel et al. (2003) suggest that ram-pressure from the passage of the galaxy through the low-density IGN may be sufficient to strip the stellar mass loss as it is recycled. It would be interesting to confirm whether these isolated dwarfs are truly passively-evolving or whether they have any detectable H I.

6.5 The connection with AGN

In recent years observations have shown that at the heart of most if not all massive galaxies is a supermassive black hole (for a review see Ferrarese & Ford 2005), and it has become increasingly clear that the evolution of the galaxy and the central black hole are strongly interdependent. This is manifested most clearly by the tight correlations between the mass of the central supermassive black hole (SMBH) and the global properties of their host galaxies, such as the stellar mass of the bulge component ($M_{BH} = 0.0014 \pm 0.0004\, M_{Bulge}$; Häring & Rix 2004), the stellar velocity dispersion (Gebhardt et al. 2000; Ferrarese & Ford 2005), and the host bulge Sersic index (Graham & Driver 2007). The scatter in the black hole masses around these relations are only of the order 0.3 dex.

Silk & Rees (1998) suggested that these correlations arise naturally through the self-regulated growth of SMBHs through accretion triggered by the merger of gas rich galaxies. Tidal torques produced by the merger channel large amounts of gas onto the central nucleus fuelling a powerful starburst and rapid black hole growth, until feedback from accretion is able to drive quasar winds and expel the remaining gas from the remnant galaxy. Hydrodynamical simulations of gas rich galaxy mergers incorporating star-formation, supernova feedback and black hole growth (Springel, di Matteo & Hernquist 2005a) confirm this picture, reproducing the observed $M_{BH} - \sigma$ relation (di Matteo, Springel & Hernquist 2005). Springel et al. (2005a) show that the presence of the central SMBH has a strong impact on the rem-

nant galaxy, producing passively-evolving spheroidal galaxies (Springel et al. 2005b) consistent with the observed scaling relations (Robertson et al. 2006) and whose gas is heated by the quasar winds forming the observed X-ray emitting halos (Cox et al. 2006), whereas the remnant galaxies in models without SMBHs continued to form stars at a non-negligible rate.

Given the tight correlation between the mass of the central SMBH and that of the host galaxy, we should expect the effects of AGN feedback to be strongly dependent on galaxy mass, being reduced or even negligable for low-mass galaxies. Springel et al. (2005b) find that for merging galaxies with $\sigma = 80\,\mathrm{km\,s^{-1}}$ the effects of black hole growth on the remnant are negligable, the spheroids that form remaining gas rich with ongoing star-formation. Indeed in low-mass galaxies SMBHs may not form at all during mergers. The rapidity of the gas accretion onto the central object depends on the depth of the potential well of the host galaxy, and in low-mass galaxies the accreting gas may have time to fragment and form stars, preventing further dissipation and collapse of the gas (Haehnelt, Natarajan & Rees 1998). Indeed most (50–80%) dwarf galaxies ($\mathrm{M}_B > -18$) appear to host central compact stellar nuclei, regardless of their morphological class (Côté et al. 2006; Rossa et al. 2006), the masses of which scale with the mass of their host galaxy, following the same correlation as that observed for SMBHs (Ferrarese et al. 2006; Wehner & Harris 2006).

In recent years there have been significant advances in the theoretical framework in understanding galaxy evolution, in particular the ability of semi-analytic models to reproduce the global properties observed in the current large scale surveys such as the SDSS. One large problem that the theoreticians have been facing is reproducing the observed break and exponential cut off in the luminosity function at the bright end along with the observation that most massive galaxies are passively-evolving, and have been for many Gyr. These massive galaxies have halos of X-ray emitting hot gas, which without constant energy injection should cool through radiative losses onto the galaxy, fuelling further star-formation (Mathews & Brighenti 2003). However, no evidence of this cooling gas is observed, and AGN feedback has often been put forward as a means of supplying energy to the hot gas, and preventing it from cooling. Croton et al. (2006) have developed semi-analytic models which include AGN feedback to prevent this gas cooling onto massive galaxies, which have been able to successfully reproduce the exponential cut-off in the bright end of the luminosity function and the fact that most massive galaxies are quiescent and dominated by old stars. It is important to note that the feedback considered here is low-level AGN activity from the quasi-continuous accretion from a static atmosphere of hot gas that is in thermal equilibrium with the DM halo.

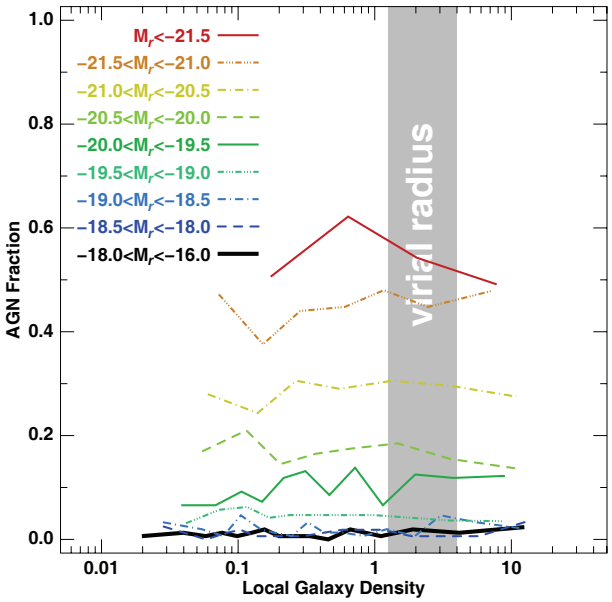

Figure 6.13: The fraction of galaxies classed as AGN from their emission line ratios as a function of local density. Each coloured curve corresponds to a different luminosity bin as indicated. Each density bin contains 150 galaxies.

To examine the possible role of AGN feedback in terminating star-formation in galaxies Fig. 6.13 shows how the AGN fraction depends on both luminosity and environment. Each coloured curve shows the fraction of AGN as a function of local density for a particular luminosity range as indicated. We note that these diagnostics are not sensitive to type 1 AGN with broad-line emission, however these are mostly limited to massive galaxy hosts and at these redshifts they constitute only $<1\%$ of the $M_r < 20$ galaxy population (e.g. Hao et al. 2005; Sorrentino et al. 2006b). For ease of comparison, the colours and curves correspond to the same luminosity ranges as Fig. 6.3.

The fraction of galaxies with an AGN remains constant with local density from the cores of clusters to the rarefied field, for each of the luminosity ranges covered. This is consistent with the result obtained by Miller et al. (2003) for bright ($M_r < -20$) galaxies. Whereas the AGN fraction is independent of density, it varies by more than an order of magnitude with the galaxy's luminosity, from $\sim 50\%$ for the brightest galaxies ($M_r < -21$) to 0–3% by $M_r \sim -18$ (see also Kauffmann et al. 2003c). Hence, the processes that power an AGN must be internal to the galaxy and dependent only on the mass/luminosity of the galaxy, while the galaxy's local environment has little or no effect on its ability to host or power an AGN. Most of the AGN de-

tected here are low-luminosity AGN powered by low-level, quasi-continuous accretion of gas onto a SMBH. High-luminosity ($L[\mathrm{O\,III}] > 10^7 L_\odot$) AGN and quasars are instead preferentially found in the outskirts of clusters or in low-density regions, being relatively absent in cluster cores (Kauffmann et al. 2004; Söchting et al. 2004; Ruderman & Ebeling 2005). These results are consistent with the model for high-luminosity AGN/quasars being triggered by the merging of two gas-rich galaxies, as in the centres of clusters most galaxies have already lost most of their gas.

Martini et al. (2006) find that only $\sim$10% of their X-ray selected AGN in clusters had obvious optical spectroscopic AGN signatures, although in total they found only 5% of $M_R < -20$ cluster members had X-ray emission characteristic of AGN, which is much smaller than the $\sim$30% of $M_r < -20$ galaxies observed here with the optical signatures of AGN. These optically dull AGN are found to have higher inclination angles than those showing optical emission, indicating that extranuclear dust in the host galaxy hides the emission lines of optically dull AGN (Rigby et al. 2006). It should be noted that AGN detection rates are subject to strong aperture biases, because as the physical aperture subtended by the SDSS fibre becomes larger, the nuclear emission from the AGN is increasingly diluted by emission from the surrounding host galaxy. This effect is particularly great for low-luminosity AGN and LINERs where the fraction detected in massive galaxies from their SDSS spectra drops from $\sim$ 60% to $\sim$ 20% with increasing redshift (Kauffmann et al. 2003a; Kewley et al. 2006). For our sample, being at low redshifts the SDSS fibres cover only the nuclear region ($<$ 1kpc) of massive galaxies and so we should not lose a significant fraction of AGN due to dilution of their emission. Another possible bias to the results presented here could be signal-to-noise effects in the classification of AGN. In particular, a 3σ detection of Hα emission is required, yet the median Hα equivalent width of galaxies classed as AGN is just 1.56 Å. This could produce a dependency on the r-band magnitude of the galaxy, as the median uncertainty in EW(Hα) rises from 0.1 Å at $r = 14$ to 0.5 Å by $r = 17.77$. Thus a significant fraction of faint galaxies ($r > 17$) may not be classified as AGN simply due to their low signal-to-noise spectra. However, although this could produce in theory a small bias against detecting AGN in the dwarf galaxies, it should be negligible in comparison to the observed trend with luminosity presented in Fig. 6.13.

The most striking result in Fig. 6.13 is the lack of AGN in dwarf galaxies. As shown in Fig. 6.3 thse galaxies are star-forming and many have strong emission lines due to this star-formation, which could in theory affect the ability to detect any low-luminosity AGN from the BPT diagnostic method. However, as Kauffmann et al. (2003c) show that the presence of even a low-

luminosity AGN with $5 < \log L[\mathrm{OIII}] < 6$ would perturb the emission-line ratios enough to be detected in 93% of dwarf galaxies classifed as star-forming.

Although the biases due to signal-to-noise effects, dust-obscuration, aperture effects, emission from star-forming regions etc are likely to affect the ability to detect AGN in galaxies, the observed trend with luminosity is very strong, and appear broadly consistent with expectations from the tight correlation between the mass of the central SMBH and the host bulge component. At the lowest luminosities, the predicted mass of the central black hole (if there is one at all) is too low to be able to power an AGN detectable in the optical spectrum. With increasing galaxy luminosity, the typical mass of the central SMBH increases (Ferrarese & Ford 2005), becoming increasingly capable of powering an AGN detectable in the optical spectrum, resulting in the AGN fraction increasing with luminosity.

A comparison between Figs. 6.3 and 6.13 finds a remarkable match between the fraction of passive galaxies in low-density environments and the AGN fraction for all of the luminosity bins covered. In these regions, environment-related processes such as galaxy harassment or ram-pressure stripping are not effective, and their star-formation histories are dependent only on mechanisms *internal* to the galaxy, such as their merger history and feedback processes. The strong correlation between the fraction of AGN and passive galaxies in these regions suggests a direct connection, with galaxies becoming passive through AGN feedback, and appears consistent with the current model of the coevolution of AGN and galaxies (e.g. Springel et al. 2005a; Hopkins et al. 2006b,a).

6.6 Comparison with semi-analytic models

To better understand the physical mechanisms that contribute to the observed different environmental trends of galaxies with luminosity, we compare our results with those produced by the semi-analytic models of Croton et al. (2006). These are implemented on top of the Millennium Run N-body simulation, currently the largest dark matter simulation of the concordance ΛCDM cosmology with $\sim 10^{10}$ particles in a periodic box $500h^{-1}$ Mpc on a side, giving a mass resolution of $8.6 \times 10^8 h^{-1}$ Mpc (Springel et al. 2005c). Dark matter halos and subhalos are identified as having 20 or more bound particles, their merging trees constructed, which are subsequently used to populate the halos and subhalos with galaxies according to the prescriptions described in Croton et al. (2006). For each galaxy there are four components: stars, cold gas in the disk, hot gas in the halo, and the central supermassive black hole. The two novel features of this semi-analytic model are: (i)

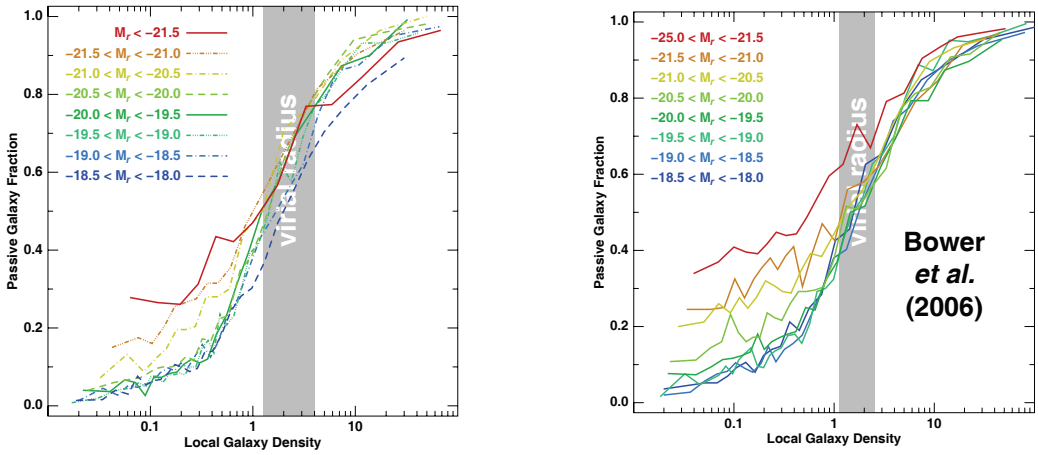

Figure 6.14: The fraction of passively-evolving galaxies as a function of local density in the *Croton et al.* 2006 semi-analytic model. Each coloured curve corresponds to a different luminosity bin as indicated and are analogous to those in Fig. 6.3. Each density bin contains 150 galaxies.

the modeling of gas infall from the halo onto the cold disk, which occurs either through rapid cooling primarily in low-mass galaxies, or cooling from a static halo of hot gas heated by accretion shocks, the dominant process in massive galaxies; and (ii) its inclusion of the growth of black holes, and their subsequent effects on the cold and halo gas in the galaxy. These effects are two-fold, during galaxy mergers a certain fraction of the cold gas is accreted by the black hole, although any resultant energy released such as quasar winds are not modeled, while instead low-level accretion of the hot gas in the halo on the black hole is also described and results in energetic 'radio mode' feedback which can prevent the further cooling of gas from the halo.

As described in the Appendix the resultant galaxy properties are used to create a mock SDSS redshift catalogue, and the local density for each galaxy estimated in the same manner. As in the mock catalogues we do not have information regarding the Hα emission from each galaxy, we instead define galaxies as being passive if they are both red ($u - r > 2.2$) and have a current specific star-formation rate (SFR/$\mathcal{M}$) less than 10% that of the median value of star-forming galaxies ($\sim 10^{-10} h^{-1} \mathrm{M}_{\odot} \mathrm{yr}^{-1} / \mathrm{M}_{\odot}$).

Figure 6.14 (left panel) shows the resultant fraction of passively-evolving galaxies as a function of both local density and luminosity. For comparison in figure is also reported (right panel) the same quantity using the model of Bower et al. (2006): two results are in perfect agreement. Each coloured curve corresponds to a different luminosity bin as indicated, and are analogous to

those for the SDSS dataset shown in Fig. 6.3 allowing a direct comparison.

There are several important discrepancies between the model predictions and the SDSS data, which indicate areas where the models do not accurately describe the physical processes which define whether galaxies are still forming stars or not.

The most notable difference is that the much smaller apparent luminosity dependence in the fractions of passively-evolving galaxies in low-density regions from the models in comparison to those observed in the SDSS data. Whereas the passive galaxy fraction increases from ∼2–8% to ∼ 30% from the lowest to the highest luminosity bins in the models, in the SDSS dataset the increase over the same luminosity range is from 0% to ∼ 50%. As in these low-density regions environmental processes should not be important, the differences must be due to the models treatment of internal feedback processes that truncate and regulate star-formation in galaxies. The discrepancies appear greatest for the most massive galaxies where AGN feedback should be the most important mechanism for truncating star-formation in galaxies, and so this suggests that the prescription for AGN feedback in the models is not efficient enough, the most likely cause of this being the neglect of feedback from quasar winds.

There is also a discrepancy at the low-luminosity end, with fewer passively-evolving dwarf galaxies observed than predicted by the models. While in the SDSS data the passive galaxy fraction continues to fall with luminosity until it reaches zero at $M_r \sim -18$, in the models there appears no luminosity dependence for galaxies fainter than $M_r > -20.5$, in any environment. The C06 model predicts that $6.1 \pm 0.3\%$ of $-18 < M_r < -19$ galaxies in field regions ($\rho < 0.2$) should be passively-evolving, a factor ~ 3 greater than that the $1.9 \pm 0.3\%$ observed in the SDSS dataset. Three-quarters of these galaxies in the C06 model are satellites to $M_r < -20$ galaxies, indicating that this excess most likely related to how the C06 model deals with the evolution of satellite galaxies. In the C06 models, as in most semi-analytic models, when a galaxy becomes a satellite within a more massive halo, it instantly loses the gas from its halo to that of its host, "suffocating the galaxy", and consequently uses up the remainder of its cold gas until it is no longer able to continue forming stars (Larson et al. 1980). This finding of too many passively-evolving dwarf galaxies in low-density environments suggests that the incorporation of "suffocation" into the model is too efficient, terminating star-formation in galaxies too rapidly once they become satellites. This is confirmed by Weinmann et al. (2006b) who split galaxies in the SDSS and C06 catalogues into satellite and central galaxies, and find that in the C06 model catalogues just $\sim 20\%$ $M_r \sim -18$ satellite galaxies are blue, much lower than the $\sim 60\%$ observed in the SDSS data.

Bekki, Couch & Shioya (2001, 2002) performed N-body and hydrodynamical simulations following the effects of the cluster environment on the gaseous halo of an infalling L^* spiral galaxy, and found that for a cluster of mass $\sim 10^{14} \mathrm{M}_{\odot}$ the combination of the cluster tidal field and ram-pressure were able to efficiently strip $\sim 80\%$ of the halo gas over a period of 1–2 Gyr. The stripping should be more rapid for lower mass galaxies. Balogh, Navarro & Morris (2000) elaborated the model of Larson et al. (1980), indicating that the gradual decline of star-formation on the ~ 3 Gyr timescales predicted by suffocation could reproduce the Butcher-Oemler effect and the observed gradual star-formation density relations extending well beyond the cluster virial radius (e.g. Lewis et al. 2002; Treu et al. 2003). By simply assuming the Schmidt-Kennicutt law, Balogh et al. (2000) obtain a relation for the decline in star-formation where no further gas accretion is possible as

$$\mathrm{SFR}(t) = \mathrm{SFR}(0) \left(1 + 0.33 \frac{t}{t_e}\right)^{-3.5} \mathrm{M}_{\odot}\,\mathrm{yr}^{-1}, \tag{6.3}$$

where SFR(0) is the initial star-formation rate, and

$$t_e \approx 2.2 \left[\mathrm{SFR}(0)/\mathrm{M}_{\odot}\,\mathrm{yr}^{-1}\right]^{-0.29} Gyr \tag{6.4}$$

is the characteristic gas consumption time-scale, including the effects of gas recycling. For a typical L^* spiral galaxy with $\mathrm{SFR}(0) \sim 5\,\mathrm{M}_{\odot}\,\mathrm{yr}^{-1}$ we obtain $t_e \sim 1.4$ Gyr, resulting in the galaxy taking ~ 4 Gyr to become passive ($\mathrm{SFR(t)/SFR}(0) \sim 0.1$), a time-scale consistent with the cluster spiral population in $z \sim 0.4$ clusters becoming passive by $z = 0$.

Applying Eq. 6.3 instead to a typical field dwarf galaxy with $M_r \sim -18$ and $\mathrm{SFR}(0) \sim 0.2\,\mathrm{M}_{\odot}\,\mathrm{yr}^{-1}$ we obtain $t_e \sim 3.5$ Gyr, resulting in the galaxy taking ~ 10 Gyr to become passive, consistent with their observed gas depletion time-scales of ~ 20 Gyr (van Zee 2001). Hence, even if deprived of further gas accretion through suffocation, star-formation in dwarf galaxies occurs at a sufficiently low rate that they are unlikely to have consumed all their gas and become passive by the present day if they are acted on only by the mild stripping envisaged in suffocation.

If suffocation alone is unable to terminate star-formation in the dwarf satellites of massive galaxies, then a stronger form of gas stripping is required. Mayer et al. (2001, 2006) show that dwarf spiral galaxies orbiting a Milky Way type galaxy can suffer significant mass loss and have their entire gas content removed or used up in a star-burst, transforming them into passive dwarf ellipticals over a period of ~ 5 Gyr through the combinination of tidal shocks and ram-pressure stripping if their orbits take them within ~ 50 kpc of the primary. Such behaviour is difficult to model within a cosmological

simulation such as that of C06, in particular as the tidal forces acting on the dwarf satellites change rapidly along their orbits, such that the star-formation histories and evolutions (in terms of mass loss) of dwarf satellites could be very strongly affected by even small variations in their orbits (Kravtsov et al. 2004).

Looking at the possible effect of the Millenium simulation neglecting tidal stripping on the satellite population, we find an overabundance of faint satellite galaxies around massive field galaxies in the models in comparison to the SDSS data. In particular for each $M_r < -20$ field galaxy we observe on average 0.125 ± 0.007 $-19 < M_r < -18$ galaxies that lie within 250 kpc and 500 km s^{-1} of it (i.e. that are probable satellites), whereas in the C06 model we find on average 0.195 ± 0.004. A certain fraction of these galaxies will in fact be interlopers, and should be subtracted from this analysis. We estimate the number of interlopers as the number of dwarf ($-19 < M_r < -18$) galaxies found around a dwarf galaxy which has no $M_r < -20$ galaxy within 1 Mpc and 1 000 km s^{-1}, so that neither of the dwarf galaxies are satellites, obtaining a value of 0.083 ± 0.003 per galaxy. This takes into account the natural clustering of dwarf galaxies, independent of the presence of nearby giant galaxies. An alternate estimate for the number of interlopers can be made by assuming interlopers are distributed evenly over the volume covered, and so in this case we would expect 0.019 dwarf galaxies within the volume around each $M_r < -20$ galaxy. Considering the contamination from interlopers to be between these two values, we estimate the excess dwarf satellites in the Millennium simulation to be 65–167%.

6.7 Discussion

Using a volume-limited sample of galaxies from the SDSS DR4 spectroscopic dataset we have examined the star-formation activity of galaxies as a function of both luminosity and environment, the main results of which are summarized in Figure 6.3. In high-density regions the bulk of galaxies are passively-evolving independent of mass. Many processes could contribute to terminating the star-formation in these galaxies, either internal to the galaxy or related to the hostile cluster environment, making it difficult to identify those which are most important. To gain insights into the relative importance of these different mechanisms we instead focus on galaxies in low-density regions for which we can be sure that their star-formation histories have not been influenced by cluster-related processes (thanks to our robust separation of cluster and field populations). Hence the star-formation histories of these galaxies can only be influenced by internal mechanisms such as merging, gas

consumption through star-formation and AGN feedback.

We find that the fraction of passively-evolving galaxies in field regions drops steadily from $\sim 50\%$ at $M_r - 21$ to zero by $M_r \sim -18$. This implies that internal mechanisms are not responsible for the formation of passively-evolving dwarf galaxies, while they become increasingly important with galaxy mass for driving their star-formation histories. This would be consistent with the increasingly early and rapid conversion of gas into stars for more massive galaxies resulting from the Kennicutt-Schmidt law ($\Sigma_{SFR} \propto \Sigma_{gas}^{1.4\pm0.1}$; Kennicutt 1998; Schmidt 1959), which has been shown to hold over several orders of magnitude of gas density, in conjunction with the appearance of a critical gas density below which star-formation does not occur (Martin & Kennicutt 2001). Hydrodynamical simulations of the formation of massive $\sim M^*$ field galaxies show that passively-evolving elliptical galaxies can be produced without recourse to major mergers or feedback mechanisms consuming their gas in a short burst (<2 Gyr) of star-formation at $z>2$ (Chiosi & Cararro 2002; Naab & Burkert 2003). In dwarf galaxies instead star-formation occurs very inefficiently resulting in gas consumption time-scales much longer than the age of the Universe (van Zee 2001) and global star-formation rates that have remained approximately constant since $z \sim 3$ (Panter et al. 2007). These simulations and the observed studies of the global decline of star-formation since $z \sim 1$ through downsizing (Heavens et al. 2004; Noeske et al. 2007a,b) suggest that gas exhaustion through star-formation may play a dominant role in the *global* evolution of star-formation.

This does not appear to be the complete answer, in particular it does not explain the wide variety of star-formation histories seen in field $\sim M^*$ galaxies (Haines et al. 2006b), where completely interspersed mixtures of young and old galaxies (in terms of their stellar populations) are found. This instead suggests that some stochastic processes play a role in determining the star-formation histories of massive galaxies, the most natural being their hierarchical assembly through mergers and the resultant growth of SMBHs and subsequent AGN feedback effects (Hopkins et al. 2006b,a). Moreover we find a close mirroring of the increase in AGN fraction with galaxy luminosity to that observed for the passive galaxies in field regions, suggesting a direct connection between nuclear activity and galaxies becoming passive, reflecting the increasing importance of AGN feedback with galaxy mass for their evolution.

6.7.1 Massive galaxies affected by merging

In the case of massive galaxies ($\mathcal{M} > 10^{10.3} M_\odot$; $M_r < -20$) we confirm the recent results on the environmental dependence of star-formation (Lewis et

al. 2002; Gómez et al. 2003; Tanaka et al. 2004; Rines et al. 2005), finding gradual trends for the fraction of passively-evolving bright galaxies with environment that extend to the lowest densities studied (§ 6.2). Furthermore we find that this correlation with the local density is independent of the presence or absence of *individual* neighbouring galaxies. Rines et al. (2005) find that the fraction of passively-evolving galaxies depends on the local density, and this dependency is the same for galaxies in different types of global environment (within the cluster virial radius, in infall regions, and the field), while Tanaka et al. (2004) find no dependence on system richness for galaxies residing in groups with $\sigma > 200\,\mathrm{km\,s^{-1}}$. In Section 6.3 we also find that the distribution of EW(Hα) of massive galaxies with *current* star-formation shows no dependence on local density in agreement with the results obtained by Balogh et al. (2004a), Tanaka et al. (2004) and Rines et al. (2005). These results together indicate a limited role for mechanisms specific to cluster environments on the termination of star-formation in massive galaxies, in particular excluding mechanisms which result in a gradual decline in the SFR of infalling galaxies. Instead star-formation in massive galaxies is terminated rapidly (on time-scales $<1\,\mathrm{Gyr}$) through processes that depend only marginally on the local density and/or occur at high-redshifts such that ongoing transformations are rare.

This early cessation of star-formation in massive passively-evolving galaxies and the independence of the star-formation histories on the global cluster environment, point towards the evolution of massive galaxies being driven primarily by *internal* mechanisms and their merger history. The environmental trends are then defined by the initial conditions in which galaxies form, whereby massive galaxies are formed earlier preferentially in the highest overdensities in the primordial density field (Maulbetsch et al. 2007), and have a more active merger history (Gottlöber et al. 2001), than those that form in the smoother low-density regions. This implies the environmental trends should be imprinted early on in the massive galaxy population, as is observed with the morphology–density and colour–density relations being already largely in place by $z \sim 1$ (Smith et al. 2005; Cooper et al. 2006), and possibly apparent even at $z > 2$ (Quadri et al. 2007).

This rapid formation of massive galaxies and the early shutdown of star-formation is produced naturally in the monolithic collapse model, where the deep potential wells allow for rapid and efficient conversion of the gas into stars according to the Kennicutt-Schmidt law (Chiosi & Cararro 2002) in a short burst ($<2\,\mathrm{Gyr}$) of star-formation at $z > 2$.

While the monolithic collapse model appears at odds with the hierarchical growth of structures produced in ΛCDM models, Merlin & Chiosi (2006) are able to reproduce the same qualitative star-formation histories for mas-

sive galaxies within a hierarchical cosmological context, most of the merging of substructures occuring early in the galaxy life ($z > 2$). This so-called "revised monolithic" scheme is consistent with the observed rapid evolution and growth of massive galaxies through merging at $z > 1$ (Conselice 2006), and the mild evolution in the number density of massive ($\mathcal{M} > 10^{10.5} \mathrm{M}_{\odot}$) red galaxies to $z \sim 1$ (Bell et al. 2004; Willmer et al. 2006) and beyond (Glazebrook et al. 2004; Cirasuolo et al. 2007; Renzini 2006). Equally the observed bimodality in the colour distribution of galaxies at $z \sim 1.2$ (Bell et al. 2004; Willmer et al. 2006) implies that star-formation must be truncated rapidly and completely in massive galaxies at $z > 1.5$ or even earlier (Kriek et al. 2006). Given the short gas-consumption time-scales of massive galaxies (§1.4.1), to maintain star-formation to the present day would require massive galaxies to continuously accrete of fresh gas from their surroundings. However, massive galaxies in halos of mass $\mathrm{M} > 6 \times 10^{11} \mathrm{M}_{\odot}$ stable virial shocks form which heat infalling gas to the virial temperature, signficantly reducing the accretion rate onto the galaxy, and making the gas vulnerable to feedback effects such as AGN (Dekel & Birnboim 2006). Indeed in many massive galaxies further accretion of gas may be completely shutdown, resulting in the subsequent termination of star-formation without the need for further quenching mechanisms such as mergers or AGN feedback (Birnboim, Dekel & Neistein 2007).

In Section 6.5 we determined the fraction of galaxies with optical AGN signatures as a function of both luminosity and environment. We find the AGN fraction to be independent of local density for galaxies of a given luminosity for $\mathrm{M}_r < -18$. In contrast the AGN fraction is strongly luminosity dependent, increasing from $\sim 0\%$ at $\mathrm{M}_r \sim -18$ to $\sim 50\%$ by $\mathrm{M}_r \sim -21$ in a way that closely mirrors the luminosity-dependence of the passive galaxy fraction in low-density environments. These results suggest that the ability of a galaxy to host an AGN depends only on its mass, as would be expected from the tight $\mathrm{M}_{BH} - \sigma$ relation (Ferrarese & Ford 2005), while the strong correlation between the fractions of galaxies hosting AGN and being passive suggests a direct connection between nuclear activity and a galaxy becoming passive. This appears consistent with the current models of the coevolution of AGN and galaxies (e.g. Springel et al. 2005a; Hopkins et al. 2006b,a), and reflects the increasing importance of AGN feedback with galaxy mass for their evolution, and its increasing efficiency in permanently shutting down star-formation, by expelling gas from the galaxy through quasar winds (di Matteo et al. 2005) and/or preventing further cooling of gas from the surrounding halo (Croton et al. 2006).

It seems impossible for environmental processes to be able to shut off star-formation in massive galaxies at such an early epoch as required: ram-

pressure stripping for example is unlikely to be efficient until later epochs ($z<1$) once the dense cluster ICM has had time to build up, while both galaxy harassment and suffocation take several Gyr to terminate star-formation in galaxies, and simply haven't had time to act. Moreover, even in field regions where these processes are not efficient, massive, passively-evolving galaxies are seen to be in place at $z>1$, with only slight differences are observed in the mean stellar ages and mass-to-light ratios of galaxies in diverse environments (Thomas et al. 2005; Smith et al. 2006; van Dokkum & van der Marel 2007).

Although the formation of passively-evolving early-type galaxies through merging largely took place at $z>1$, there is evidence indicating this process is continuing at lower redshifts. Early-type galaxies that are currently passively-evolving, but with remnant young (1–4 Gyr) stellar populations or E+A spectra indicating <1 Gyr old stars, are preferentially located in low-density environments or poor groups, that is regions where low-velocity interactions should be most frequent (Goto 2005; Nolan, Raychaudhury, & Kabán 2007). The fraction of blue, spiral galaxies in clusters is also observed to drop rapidly from $z\sim0.5$ to $z\sim0$ — the Butcher-Oemler effect — while many spiral galaxies in local clusters show strong evidence of being transformed now by ram-pressure stripping (e.g. Solanes et al. 2001; Koopmann & Kenney 2004; van Gorkom 2004).

As discussed in §1.4.1 the mechanism of suffocation was proposed by Larson et al. (1980) to explain the Butcher-Oemler effect, by stripping the extended gas reservoirs of recently accreted spiral galaxies in clusters at $z\sim0.4$, slowly transforming them by the present day into passively-evolving galaxies by exhausting their remaining gas supplies through star-formation. However, suffocation should not change the morphology or radial profiles of the spiral galaxies, turning them into anemic spirals (van den Bergh 1976) rather than the S0s whose numbers in clusters have increased rapidly since $z\sim0.4$ mirroring the decline of cluster spirals (Dressler et al. 1997).

Instead, studies of spiral galaxies in the Virgo cluster find that a much larger fraction of them have truncated Hα and H I radial profiles (52%) than appear simply anemic (6–13%) with globally reduced star-formation and gas densities (Koopmann & Kenney 2004). Similarly, Vogt et al. (2004) find a significant fraction of spirals with asymmetric Hα profiles and H I rotation curves in nearby rich clusters. It is difficult for suffocation to produce these truncated or asymmetric Hα and H I profiles, and instead it appears more likely that a process such as ram-pressure stripping actively removes the gas from the outside-in, and Boselli et al. (2006) show that ram-pressure stripping is able to reproduce the observed radial profiles. This outside-in removal of the gas should also produce inverted colour gradients in which the inner regions of the galaxy are bluer than the outer regions, as star-formation

is truncated earlier in the periphery than the core of the galaxy, an effect which has been observed for the Virgo spiral NGC 4569 (Boselli et al. 2006).

These truncated spiral galaxies are mostly confined to the inner 1–1.5 Mpc of the Virgo cluster, that is within the virial radius, although there are some well outside the virial radius (Koopmann & Kenney 2004). All of the asymmetric spiral galaxies are located within $1\,h^{-1}$Mpc of the cluster centres with the truncation of the H I and Hα emission preferentially along the leading edge (Vogt et al. 2004). These results are more consistent with the effects of ram-pressure stripping which should affect galaxies only within the cluster cores ($< 0.3\,R_{vir}$), although as the H I deficient spiral galaxies are observed to be on highly-elliptical radial orbits (Solanes et al. 2001), those truncated or asymmetric galaxies at $0.3 < (r/\mathrm{R}_{vir}) < 1.5$ could have recently passed through the cluster core (Mamon et al. 2004).

The few anemic spirals with globally reduced Hα and H I emission are generally found further from the cluster centres than truncated galaxies, half of them are outside the virial radius (Koopmann & Kenney 2004), while Goto et al. (2003) find that passive spirals in the SDSS are generally found in the outskirts of clusters at 1–10 $\mathrm{R_{vir}}$. It could then be that these galaxies are the natural results of suffocation, and may represent an early phase of evolution from spirals to passively-evolving S0s. The finding of significant numbers of truncated spiral galaxies in clusters, implies that the complete removal of gas and transformation into passively-evolving galaxies does not occur rapidly, at least in Virgo-like clusters. This appears inconsistent with our finding of no environmental dependence in the Hα emission of bright star-forming galaxies, as that implies the transformation is either rapid or occurs at high-redshift. One plausible explanation could be due to our measuring the Hα emission from a confined region in the galaxy centre rather than the entire disk, and that star-formation within the truncation radius is relatively unaffected, until the galaxy orbit brings it sufficiently close to the cluster centre that the remaining gas is completely stripped, rapidly terminating star-formation across the galaxy.

6.7.2 Dwarf galaxies affected by environment

In Section 6.2 we showed that the make-up of the dwarf galaxy population varies strongly with environment. Whereas in galaxy groups and clusters the bulk of dwarf galaxies are passively-evolving, as the local density decreases the fraction of passively-evolving dwarfs drops rapidly, reaching zero in the rarefied field. Indeed for the lowest luminosity range covered ($-18 < \mathrm{M}_r < -16$) none of the ~ 600 galaxies in the lowest density quartile are passively-evolving. In Section 6.4 we examined in detail the immediate

environment of those few passively-evolving dwarf galaxies in field regions, finding them very strongly clustered around bright ($M_r < -20.5$) galaxies. Almost without exception those passively-evolving galaxies outside groups and clusters appear to be satellites bound to massive galaxies.

This association of passively-evolving dwarf galaxies as satellites within more massive halos is consistent with the analysis of Zehavi et al. (2005) of the dependence of the galaxy two-point correlation function on luminosity and colour. They find that whereas the overall amplitude of clustering decreases monotonically with magnitude over $-23 < M_r < -18$, the clustering of *red* galaxies on $< 1\,$Mpc scales is strongest for $M_r > -19$. They are able to describe these results using halo occupation distribution (HOD) models in which the faint red galaxies are nearly all satellites in high-mass halos.

These results confirm and significantly extend the long noted morphological segregation of dwarf galaxies in the local ($< 30\,$Mpc) neighbourhood, with dwarf ellipticals confined to groups, clusters and satellites to massive galaxies, while dwarf irregulars tends to follow the overall large-scale structure without being bound to any of the massive galaxies (Einasto et al. 1974; Ferguson & Binggeli 1994). Here dwarf ellipticals (dEs) are generally defined as galaxies with $-18 < M_B < -14$ having smooth, symmetrical surface-brightness profiles implying no spiral structures or star-forming regions, and typically have very low H I mass fractions, and hence we identify these galaxies with our passively-evolving dwarf galaxies, although there are galaxies (e.g. NGC 205 which are classed as dEs but have recent star-formation in their central regions Mateo 1998).

The morphological segregation of dwarf galaxies was first noted by Einasto et al. (1974) who compared the spatial distributions of dwarf companions to our Galaxy and the nearby massive spirals M 31, M 81 and M 101. They found a striking separation of the regions populated by dE and dIrr galaxies with a well defined line of segregation which had a strong luminosity dependence, with more luminous dEs constrained to smaller regions around the primary galaxy. They argued that tidal effects would be insufficient to produce this segregation and that a dense corona of halo gas around massive galaxies is necessary to strip the gas from the satellites as they move through the corona (Gunn & Gott 1972). In the Local Group the only dwarf ellipticals are M 32, NGC 147, NGC 185 and NGC 205, all of which are satellites of M 31, while three of the five dwarf irregulars of comparable brightness (NGC 6822, IC 6822 and WLM) are free-floating within the Local Group potential (e.g. Mateo 1998; van den Bergh 1999). Beyond the Local Group, there are no known isolated dE galaxies within 8 Mpc (Karachentsev et al. 2004).

In a survey covering $900\,\mathrm{deg}^2$ Binggeli, Tarenghi & Sandage (1990) iden-

tify 179 dwarf galaxies, and claim that "*in the field there are virtually no isolated dEs, and that the few dEs outside of gravitationally bound systems are close satellites to massive giants.*" They find just one good candidate for an isolated dE, #179 in their dwarf catalogue. The reported location of this galaxy is covered by the SDSS, but no galaxy is found there, and it appears most likely to correspond to a $z = 0.08$ Sa galaxy 1 arcmin distant.

Dwarf ellipticals (including here dSphs) in contrast are the most numerous galaxy type in clusters, although unlike the field or within groups only a small fraction appear bound to massive galaxies (Ferguson 1992), the rest follow the general cluster potential. However, the ratio of dEs to giants is much greater in clusters than in groups or the field, and so not all cluster dEs can be accounted for by the accretion of "field" dEs (Conselice, Gallagher & Wyse 2001).

This clear segregation of passively-evolving dwarf galaxies places strong constraints on their formation and evolution, in particular as to the physical mechanisms that could cause them to cease forming stars. Most importantly, unlike massive galaxies for which their build-up through mergers appears fundamental in determining their star-formation history, we can rule out merging as a formation mechanism for passively-evolving dwarfs.

Galaxy merging is a stochastic process which occurs independently of the large-scale environment ($> 1\,\mathrm{Mpc}$) of a galaxy (Hopkins et al. 2008). This means that mergers take place in all environments[2], even in voids, as has been observed for interacting pairs (Alonso et al. 2006). This results in merger remnants being ubiquitous, as predicted by Hopkins et al. (2008), and observed in the spatial distribution of post-starburst galaxies (Goto 2005; Hogg et al. 2003) . This is most clearly demonstrated with the presence in all environments of passively-evolving, massive galaxies with old stellar populations, which in field regions make up $> 50\%$ of the total population of massive galaxies, forming an equal interspersed mixture with younger star-forming galaxies (Figs. 3 and 4 from HCPI). Hence dwarf galaxies which have undergone major mergers should also be ubiquitous, as Conselice (2006) shows that they have undergone on average about the same number of major mergers as massive galaxies since $z \sim 3$ (albeit at later epochs), yet in the lowest density quartile we find no passively-evolving galaxies among the ~ 600 $-18 < \mathrm{M}_r < -16$ dwarfs. In addition, mergers cannot explain the observed strong segregation of dwarf galaxies, in particular the presence of a massive galaxy should not affect the merging efficiency of a dwarf galaxy, or the observation that most dwarf star-forming galaxies in clusters are in the process

[2]Except in relaxed, rich clusters where encounter velocities are much higher than the internal velocity dispersions of galaxies, preventing their coalescence (Aarseth & Fall 1980).

of being transformed into passively-evolving galaxies, an environment where mergers are *now* strongly inhibited.

The ineffectiveness of mergers to permanently shut down star-formation in dwarf galaxies can be understood in the context of the current theoretical framework of galaxy evolution. Springel et al. (2005a) show through hydrodynamical simulations of mergers that although both models with and without black holes produce strong starbursts during the mergers followed by a decline in star-formation, in those models without black holes the remnants continue to form stars at a non-negligible rate. Given that the growth of central black holes during galaxy mergers are strongly regulated by the mass of the host galaxy, in low-mass galaxies the resultant black holes (if indeed there is one at all), based on the $M_{BH} - \sigma$ relation (Ferrarese & Ford 2005), are too small to power the quasar winds which would expel the remaining gas and shut down star-formation, as occurs in more massive systems. Indeed for merging galaxies with $\sigma = 80\,\mathrm{km\,s^{-1}}$ Springel et al. (2005b) show that the effects of black hole growth are minimal on star-formation in the remnant galaxy, and the galaxy does not become passive as a result of the merger. Moreover, most dwarf galaxies ($M_B > -18$) appear to host central compact stellar nuclei rather than a central supermassive black hole (Côté et al. 2006), consistent with our observation that the AGN fraction of galaxies falls to close to zero by $M_r \sim -18$ (§6.5). Even if a significant fraction of the available gas in the remnant is used up during the star-burst, the intrinsic low star-formation efficiency of low-mass galaxies and regulatory effects of supernovae feedback, plus the continuous infall and cooling of fresh gas from the halo along filaments (Kereš et al. 2005), ensures that the remaining gas is unlikely to be exhausted. Finally, the quasi-continuous low-level AGN activity that Croton et al. (2006) suggest could inhibit cooling of gas from the diffuse hot gaseous halo of massive galaxies and prevent subsequent star-formation in them, has in contrast little effect against the clumpy nature of the gas infalling along filamentary structures onto the dwarf merger remnants.

In Section 6.3 we find a significant anti-correlation (10σ) between the EW(Hα) of dwarf star-forming galaxies and their local density, producing a systematic reduction of $\sim$30% in the Hα emission in high-density environments with respect to field values. We argue that this implies that the bulk of star-forming dwarf galaxies in groups and clusters are in the process of being slowly transformed into passive galaxies over long time-scales ($> 1\,\mathrm{Gyr}$), and is thus suggestive of suffocation (Balogh et al. 2000).

However, as discussed in § 1.4.1 the long gas consumption time-scales predicted from Eq. 6.3 and observed by van Zee (2001) imply that even if deprived of further gas accretion through suffocation, star-formation in

dwarf galaxies occurs at a sufficiently low rate that they are unlikely to have consumed all their gas by the present day. In low-mass dwarf galaxies ($\mathcal{M} < 10^7 \mathrm{M}_\odot$) as gas collapses and stars form, the resultant feedback from supernovae is able to drive out the remaining gas, temporarily shutting off star-formation, until the gas is able to cool and restart star-formation, resulting in episodic bursts of star-formation every $\sim$300 Myr. In more massive dwarf galaxies, such as those studied here, SN feedback appears too inefficient to power galactic winds that could expel the remaining gas from dwarf galaxies, even during star-bursts (Mac Low & Ferrara 1999; Marcolini et al. 2006). Instead it seems that star-formation in dwarf galaxies appears strongly regulated and rather resilient over long time-scales. This quasi-continuous star-formation in dwarf galaxies seems to have been maintained since early epochs, as the global star-formation rates of galaxies with $\mathcal{M} < 3 \times 10^{10} \mathrm{M}_\odot$ have remained approximately constant since $z \sim 3$ (Heavens et al. 2004; Panter et al. 2007).

A further difficulty for dEs being produced as the result of suffocation is that it does not affect the galaxy structurally, and so we should expect the surface brightness and luminosity to decrease in parallel as the stellar population evolves passively. However, the surface stellar mass densities of passively-evolving dwarf galaxies are 0.5 dex *higher* than their star-forming counterparts of the same stellar mass (Kauffmann et al. 2003b). Hence, if star-formation in dIrr galaxies were to simply be stopped, as in suffocation, the resultant surface densities would be too low in comparison to present-day dEs (Grebel et al. 2003). Equally, the metallicity of dIrrs are too low for their luminosity as compared with dEs, for them to be simply transformed by becoming passive (Grebel et al. 2003), while suffocation provides no means for the rotationally-supported dIrrs to lose their angular momentum to become the dEs where little or no signs of rotation ($< 5\,\mathrm{km\,s^{-1}}$) are seen.

If gas cannot be exhausted through star-formation, expelled by supernovae feedback during star-bursts, or prevented from infalling and cooling through AGN feedback, the end of star-formation and gas removal in dwarf galaxies must come from external mechanisms, such as ram-pressure or tidal interactions (Marcolini et al. 2006).

When galaxies pass through the dense ICM of clusters or the gaseous halos of massive galaxies they feel an effective ram-pressure which, if able to overcome the gravitational attraction between the gas and the disk, is able to effectively strip the gas from the disk (for a review see van Gorkom 2004), according to the Gunn & Gott (1972) condition $\rho_{\mathrm{ICM}} \nu_{gal}^2 > 2\pi G\, \Sigma_\star \Sigma_{gas}$, which has been shown to hold approximately from hydrodynamical simulations (e.g. Marcolini et al. 2003). Hence ram-pressure stripping should be more effective for lower mass, low-surface-brightness galaxies, galaxies on more eccen-

tric orbits, and galaxies in richer environments, such that while for massive galaxies ram-pressure stripping is only effective in the cores of rich clusters, dwarf galaxies can be completely stripped of their gas even in poor groups (Marcolini et al. 2003).

Moore et al. (1996) proposed that cluster spirals could be disrupted by "galaxy harassment", whereby repeated close ($<50\,\mathrm{kpc}$) high-velocity ($>1\,000\,\mathrm{km\,s^{-1}}$) encounters with massive galaxies and the cluster's tidal field cause impulsive gravitational shocks that damage the fragile disks of late-type disks, transforming them over a period of Gyr into spheroids. While $\sim L^*$ spirals are relatively stable to the effects of harassment, suffering little or no mass loss, low surface brightness dwarf spirals with their shallower potentials may suffer significant mass losses (up to 90%) of both their stellar and dark matter components during harassment (Moore et al. 1999), resulting in remnants resembling dwarf ellipticals (Mastropietro et al. 2005).

Dwarf spiral galaxies orbiting as satellites to massive galaxies may also be transformed into passively-evolving dEs through tidal interactions with the primary galaxy and ram-pressure stripping as they pass through its gaseous halo. Mayer et al. (2001) show that dwarf spirals orbiting a Milky Way type galaxy on eccentric orbits taking them within 50 kpc of the primary experience tidal shocks during their pericentre passages, that can cause significant mass loss (mostly of the outer gaseous halo and dark matter, but also of the stellar disk), formation of bar instabilities that channel gas inflows triggering nuclear star-bursts, and loss of angular momentum, resulting in their transformation over a period of $\sim 5\,\mathrm{Gyr}$ an early-type dwarf. Mayer et al. (2006) indicate that while tidal stirring of disky dwarf galaxies can transform them into remnants that resemble dEs after a few orbits, ram-pressure stripping is required to entirely remove their gas component. Kravtsov et al. (2004) show that many dwarf satellites of Milky Way type galaxies have undergone significant mass loss through tidal stripping, and are able to reproduce the observed morphological segregation of dE and dIrr galaxies (Einasto et al. 1974), in which the dEs are those that have suffered significant tidal stripping.

As discussed above star-forming, late-type dwarf galaxies in clusters, groups or bound to massive galaxies can be transformed into dEs through a combination of ram-pressure stripping and tidal interactions. This is supported by the finding of significant populations of dEs in the Virgo cluster having blue central regions caused by recent or ongoing star-formation (Lisker et al. 2006), significant amounts ($>10^7\mathrm{M}_\odot$) of H I gas (Conselice et al. 2003), or clear disk features including spiral arms, bars or significant velocity gradients, with rotational velocities similar to dwarf irregulars of the same luminosity, and anisotropy parameters ($\nu/\sigma_m > 1$) indicating stellar kinemat-

ics dominated by rotation rather than random motions (van Zee, Skillman & Haynes 2004). These populations are found predominately in the cluster outskirts and some have flat distributions of radial velocities, suggesting that they have been recently accreted by the cluster or are on high angular momentum orbits and therefore never go through the cluster core, while normal, non-rotating dEs are concetrated in the cluster core or in high-density clumps (Conselice et al. 2003; van Zee, Skillman & Haynes 2004; Lisker et al. 2007). In a similar H I study, this time of 11 dIrrs in the Virgo cluster, Lee, McCall & Richer (2003) find that five of them are gas deficient by a factor >10 with respect to field dIrrs at comparable oxygen abundances, and this gas deficiency correlates approximately with the X-ray surface brightness of the ICM. These gas-poor dIrrs have typical colours and luminosities of normal field dIrrs, indicating that their star-formation hasn't yet been affected, and suggesting that they have only recently encountered the ICM for the first time. In the Coma cluster Caldwell et al. (1993) and Poggianti et al. (2004) find that whereas bright post-starburst galaxies with k+a spectra are largely absent, there is a significant population of faint galaxies ($M_V > -18.5$) with k+a spectra, which appear associated with substructures in the ICM, the galaxies lying close to the edges of two infalling structures. This strongly suggests that the interaction with the ICM could be responsible for rapidly quenching the star-formation in these galaxies, possibly after a starburst. These observations all point towards the *ongoing* transformation of late-type dwarf galaxies into passively-evolving dwarf ellipticals.

Chapter 7

Robust star-formation indicator: NUV-r vs. b-r colour diagram

In this chapter we combine *Galaxy Evolution Explorer* GALEX near-ultraviolet (NUV) photometry with the volume-limited sample of local galaxies presented in the previous chapter to examine the composition and the environmental dependence of the optical and ultraviolet (UV)-optical colour-magnitude (CM) diagrams[1].

7.1 The make-up of the red sequence

The most widely studied bimodality in galaxy properties is that observed for their colours, that is the clear separation of galaxies into the red sequence and blue cloud populations (e.g. Strateva et al. 2001). This has the advantage that it is easy to measure, particularly at high-redshifts, allowing studies to follow the evolution of the bimodality to $z{\sim}1.2$ and beyond (Bell et al. 2004; Willmer et al. 2006).

A number of studies have followed separately the evolution of the red and blue galaxy luminosity functions to $z > 1$. There is little evolution in the number density of massive ($\mathcal{M}{>}10^{11}$M) red sequence galaxies with only a factor two increase in the stellar mass density from $z{\sim}1$ to the present

[1]The contents of this chapter are published in the article:

- Haines, C. P.; Gargiulo, A.; Merluzzi, P., "The SDSS-GALEX viewpoint of the truncated red sequence in field environments at z 0", 2008, MNRAS, 385, 1201-1210.

day (Bell et al. 2004; Willmer et al. 2006). At lower stellar masses however a much more rapid evolution is observed, with the stellar mass density of $\mathcal{M}<10^{10.3}$ red galaxies dropping by an order of magnitude by $z\sim0.8$ (Bundy et al. 2006). The red sequence thus appears to be built up from the top down, with the most massive galaxies in place first at $z>1$, and the faint end incrementally filled in at lower redshifts.

The epoch and rapidity over which the red sequence is assembled is found to be a function of environment. In cluster environments Tanaka et al. (2005) find no evidence for any significant growth of the red sequence since z=0.83, except for a hint of evolution in the lowest mass bin ($\mathcal{M}<10^{10.5}$M) between z=0.83 and z=0.55. Similarly, de Lucia et al. (2006) find evidence for a deficit of faint ($0.1(L/L^*)0.4$) red sequence galaxies in 18 EDiSCS clusters at $0.4<z<0.8$ with respect to present day clusters. They show that the observations are consistent with a simple model whereby these galaxies are formed as the result of blue galaxies in clusters at z=0.8 having their star-formation suppressed by the hostile cluster environment. In field environments the fraction of galaxies on the red sequence is lower than in clusters at all luminosities and all redshifts to z=0.8 (Tanaka et al. 2005), showing that the colour-density relation is already in place at z=0.8. There is also a deficit of faint red sequence galaxies in field regions, both at $z\sim0.8$ and at the present day, indicating that the assembly of the red sequence is still incomplete in low density environments.

In the following we examine what consequences these observative differences have on the form of the red sequence in the local universe, and its variation from within the high-density environments of clusters and groups, to the lowest density regions of the rarefied field. Throughout we assume a concordance ΛCDM cosmology with Ω_M=0.3, Ω_Λ=0.7 and H_0=70 km s^{-1}Mpc^{-1}.

7.2 The red sequence in optical surveys

It is broadly assumed that red sequence galaxies are passively-evolving galaxies dominated by old stellar populations formed at $z>1$, while blue galaxies are star-forming galaxies, whose optical emission is dominated by young stellar populations. However the optical colours of galaxies do not necessarily fully relate to the underlying star-formation history as just described. In particular galaxies can appear red both because they are passive, but also through high levels of dust extinction produced by star-bursts. A much more reliable measure of recent star-formation in galaxies than their optical colour can be made from their spectra, in particular the level of Hα emission (Kennicutt 1998).

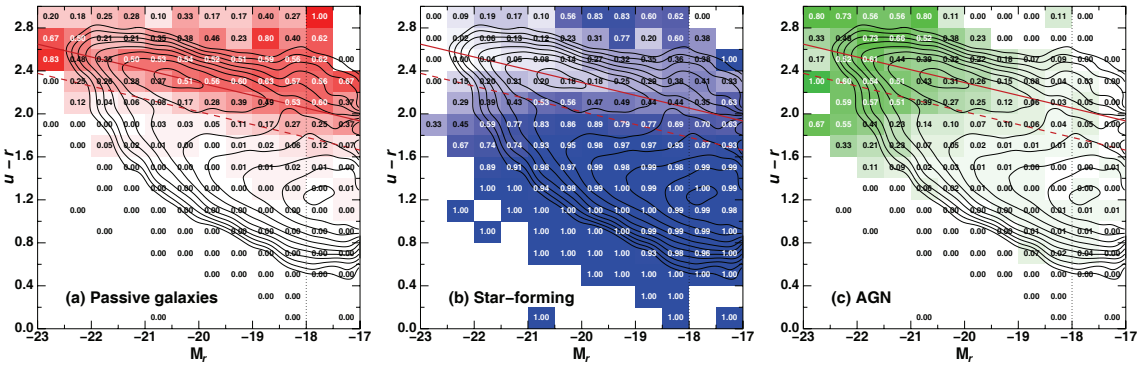

Figure 7.1: The global make-up of the $u{-}r$ / M_r colour-magnitude diagram of galaxies. Contours show the volume-corrected $u{-}r$ / M_r colour-magnitude diagram, and are spaced logarithmically, the spacing between contours indicating a factor $\sqrt{2}$ increase in the galaxy density. Panel (a) shows the global fraction of passively-evolving galaxies in each bin of $u{-}r$ colour and M_r magnitude, with increasingly intense red colours indicating higher passive galaxy fractions in a bin (indicated also by the numeric value). Panels (b) and (c) show the contributions of star-forming galaxies (blue-shaded boxes) and AGN (green-shaded boxes). The solid red line indicates the best-fit C-M relation of Eq. 1, and the dashed line indicates the limit used to separate red sequence and blue cloud galaxies.

In Fig. 7.1 we look at how the $u{-}r$ / M_r colour-magnitude diagram is broken up into (a) passively-evolving, (b) star-forming and (c) AGN components as determined from their spectra. In each panel the black contours indicate the *global* bivariate density distribution of $0.005{<}z{<}0.037$ galaxies in C-M space, where each galaxy is weighted by $1/\mathrm{V}_{max}$ where V_{max} is the maximum volume over which the galaxy could be observed within the survey. For each bin in $u{-}r$ colour and M_r magnitude we calculate the relative contribution of passively-evolving galaxies (EW[Hα]$<$2Å; not AGN), star-forming galaxies (EW[Hα]$>$2Å; not AGN) and AGN, in panels (a-c) respectively. For each bin in the C-M diagram containing at least one galaxy, the box is colour-shaded with increasingly intense red colours indicating higher passive galaxy fractions in that bin. Panels (b) and (c) show the contributions of star-forming galaxies (blue-shaded boxes) and AGN (green-shaded boxes).

The bimodality of galaxy properties in colour-magnitude space is clear, with a population of red ($u{-}r{\sim}2.4$) galaxies forming the red sequence, and the less-luminous "blue cloud" popoulation apparent at $u{-}r{\sim}1.2$. The C-M relation of red sequence galaxies shows the well known slope due to metallicity effects. We apply the method of López-Cruz et al. (2004) to estimate the

slope and width of the C-M relation, using the biweight algorithm (Beers et al. 1990) to estimate the dispersion about the relation (see e.g. Haines et al. 2006a). Panel (a) shows that passively-evolving galaxies are well confined to the red sequence, with virtually no optically-blue ($u{-}r < 1.6$) passive galaxies, and so considering just the passively-evolving galaxies we obtain the best-fitting relation:

$$u - r = 2.291\,(0.004) - 0.1191\,(0.0114) \times (\mathrm{M}_r + 20) \qquad (7.1)$$

(shown by the red solid lines in panels a-c), and a width σ=0.181. We identify red sequence galaxies as those which have colours redder than the black dashed line, which corresponds to a relation $1.5\,\sigma$ bluer than the red sequence, and where equal numbers of passive and star-forming galaxies are observed when averaged over all environments.

In panel (b) we see that virtually all blue galaxies are identified as star-forming from their spectra, and hence to a first approximation the correlation between galaxy colour and the current star-formation rate appears good. However it is also notable that a significant fraction of galaxies with red optical colours ($u{-}r > 2$) are in fact star-forming, particularly at the faint end ($-19{<}\mathrm{M}_r{<}-17$), where 53% of red sequence galaxies (i.e. above the dashed line) are spectroscopically classed as star-forming. Finally in panel (c) we see that AGN are generally red and confined to the most luminous galaxies in the sample where they make up $\sim$50% of the galaxy population, this fraction falling to close to zero by $\mathrm{M}_r{\sim}-18$ as shown in chapter 6.

Hence, while passive galaxies are red, *red galaxies are not necessarily passive.* In particular, Davoodi et al. (2006) find that 17% of red sequence galaxies are dusty, star-forming galaxies (identified by their high $24\,\mu$m/$3.6\,\mu$m flux ratios and Hα emission), while Wolf et al. (2005) find that dusty, star-forming galaxies make up more than one-third of the red sequence population, finding them preferentially in the outskirts of clusters. Given that the relative fractions of passively-evolving/red and star-forming/blue galaxies of a given luminosity are strongly dependent on local environment, particularly at the faint end (Balogh et al. 2004a; Baldry et al. 2006; Haines et al. 2007), the contamination of the red sequence by star-forming galaxies is also likely to be strongly dependent on environment.

In Table 7.1 we examine how the fraction of red sequence galaxies (i.e. above the red dashed lines in Fig. 7.1) which are spectroscopically classed as star-forming varies with both environment and luminosity. Globally, we find that 31% of red sequence galaxies (with $\mathrm{M}_r{<}-17$) are star-forming, similar to that found by Wolf et al. (2005), but larger than the 17% obtained by Davoodi et al. (2006). This difference is most likely due to their sample being

Table 7.1: Fraction of red sequence galaxies classified as star-forming as a function of both environment and luminosity

Magnitude range	Gals	Global fraction	Field ($\rho < 0.5$)	Cluster ($\rho > 1.0$)
all	6189	31.4±1.1%	37.2±2.2%	24.6±1.5%
$M_r<-20$	3068	18.1±1.1%	21.0±2.1%	14.0±0.4%
$-19<M_r<-17$	1579	51.7±3.1%	73.0±7.8%	35.4±3.5%

biased towards more luminous galaxies than ours, and indeed we find just 18% of $M_r<-20$ galaxies to be star-forming. We find that the contamination of dusty star-forming galaxies is much greater in field regions than in clusters, and in all environments the contamination is greater at faint magnitudes. We note that most galaxies which are above the red sequence ($u-r\sim2.8$) are in fact star-forming, their red colours simply due to dust extinction.

The most notable value in Table 7.1 is that for $-19<M_r<-17$ red sequence galaxies in field regions, where we find 73±8% to be classed as star-forming. This has important consequences for interpreting many of the recent studies for the build-up of the red sequence, both in the local universe, and at high redshifts. For example, Baldry et al. (2006) show that in low-density regions the fraction of galaxies belonging to the red sequence is strongly dependent on stellar mass, dropping from ∼80% at $\log \mathcal{M}\sim11.4$ to ∼5% at $\log \mathcal{M}\sim9.0$. In chapter 6, we find that the fraction of passively-evolving galaxies drops to precisely zero by $M_r\sim-18$ or $\log \mathcal{M}\sim9.2$. Similarly, Tanaka et al. (2005) determine the luminosity function of red sequence galaxies in field regions, obtaining a Schechter function with a very shallow faint-end slope ($\alpha=-0.14$), but which appears to flatten out at the faintest magnitudes ($-19<M_V<-17.5$) due to a residual population of faint red sequence galaxies. Our results indicate that around three-quarters of this residual faint red sequence population in field regions are in fact star-forming galaxies. Hence if a more robust colour selection could be applied to separate passive and star-forming galaxies, this residual faint red population would largely disappear in field regions (if not entirely[2]).

[2]In chapter 6, we find all the few passively-evolving dwarf galaxies in field regions to be satellites to massive galaxies

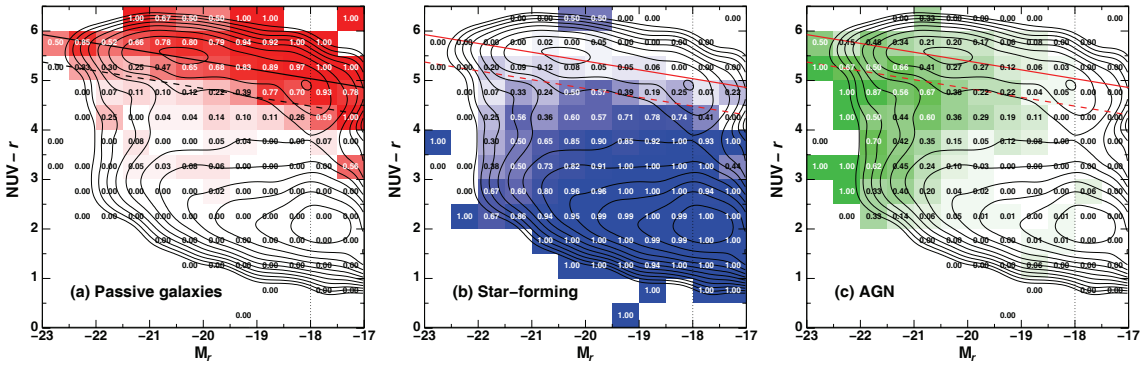

Figure 7.2: The global make-up of the NUV$-r$ / M_r colour-magnitude diagram of galaxies. Contours show the volume-corrected NUV$-r$ / M_r colour-magnitude diagram, and are spaced logarithmically, the spacing between contours indicating a factor $\sqrt{2}$ increase in the galaxy density. Panel (a) shows the global fraction of passively-evolving galaxies in each bin of NUV$-r$ colour and M_r magnitude, with increasingly intense red colours indicating higher passive galaxy fractions in a bin. Panels (b) and (c) show respectively the contributions of star-forming galaxies (blue-shaded boxes) and AGN (green-shaded boxes). The solid red line indicates the best-fit colour-magnitude relation of Eq. 2, and the dashed line indicates the limit used to separate red sequence and blue cloud galaxies.

7.3 The GALEX-SDSS view of the red sequence at $z\sim0$

The UV photometry from *GALEX* provides a global measure of star-formation that is an order of magnitude more sensitive than optical photometry (e.g. $u-r$) alone to low levels of recent star-formation[3] overlaid on otherwise old stellar populations (e.g. Martin et al. 2005, 2007; Kauffmann et al. 2006). Similarly, the NUV$-r$ colour is shown to correlate tightly with the birthrate parameter b (the ratio of the current to past-averaged star-formation rates; Salim et al. 2005) and the age-sensitive spectral indices d4000 and Hδ (Martin et al. 2007), implying that the star-formation history of a galaxy can be constrained from its NUV$-r$ colour alone. Moreover Salim et al. (2005) show that the combined FUV and NUV photometry can be used to obtain reliable measures of dust-corrected SFRs for star-forming galaxies to an accuracy of 0.2 dex.

To resolve the limitations inherent in separating passively-evolving and star-forming galaxies from just their $u-r$ colours, we take advantage of the available *GALEX* UV data. Fig. 7.2 shows the global make-up of the NUV$-r$ / M$_r$ colour-magnitude diagram, breaking it up into its (a) passive-evolving, (b) star-forming and (c) AGN components, analogously to Fig. 7.1. The bimodality of galaxy properties in colour-magnitude space is again apparent, with a robust separation of red and blue galaxies about a colour NUV$-r\sim4$ (see also Wyder et al. 2007) that appears much cleaner than for the optical counterpart.

Passive galaxies (panel a) are well confined to the red sequence, with few showing blue UV-optical colours (NUV$-r < 4$). We estimate the zero-point, slope and dispersion of the red sequence as before using those galaxies classified as passively-evolving, obtaining the C-M relation:

$$\mathrm{NUV} - r = 5.393\,(0.013) - 0.1782\,(0.0223) \times (\mathrm{M}_r + 20) \qquad (7.2)$$

(shown by the black solid line in panel a) and a dispersion of $\sigma_{\mathrm{NUV}-r} = 0.370\pm0.007$, consistent the 0.3–0.5 mag obtained by Wyder et al. (2007). As before we identify red sequence galaxies as those which are less than $1.5\,\sigma$ bluer than the C-M relation, i.e. that lie above the dashed line.

In panel (b) we see that virtually all blue galaxies with NUV$-r<4$ are spectroscopically star-forming (except at the very bright end where AGN begin to dominate as shown in panel c). Unlike the optical colour-magnitude diagram where a significant fraction of red galaxies were also classified as

[3] where 1% of the galaxy's mass in stars form in the last Gyr

Table 7.2: Fraction of NUV$-r$ selected red sequence galaxies classified as star-forming as a function of environment and luminosity

Magnitude range	Gals	Global fraction	Field (ρ<0.5)	Cluster (ρ>1.0)
all	796	8.5±1.3%	10.6±4.2%	5.8±1.3%
$M_r<-20$	358	6.1±1.6%	3.3±2.7%	5.0±1.9%
$-19<M_r<-17$	245	10.2±2.7%	31±24%	5.0±2.0%

star-forming, we see few star-forming galaxies with NUV$-r > 5$. Indeed, globally we find that just 8% of galaxies belonging to the NUV-optical red sequence are classified as star-forming as opposed to 31% of galaxies from the optical red sequence. In Table 7.2 we report the corresponding fractions of star-forming galaxies among the NUV-optical red sequence population as a function of both magnitude and environment. In all cases the contamination of the NUV-optical red sequence by star-forming galaxies is significantly less (by typically a factor 3–5) than for the optically selected red sequence galaxies, being 10% for all subsamples except for the faint, field galaxy population where 30% appear to be star-forming. However we note that this last result is based on just four star-forming galaxies out of thirteen $-19<M_r<-17$ red sequence galaxies. We thus argue that the position of a galaxy in the NUV$-r$ / M_r colour-magnitude diagram can be used as a robust classifier of its recent star-formation history, efficiently separating passively-evolving and star-forming galaxies.

In panel (c) we show that AGN dominate the bright end of the colour-magnitude diagram, and typically have NUV$-r$ colours that are intermediate between the red sequence and blue cloud, lying in the so-called "green valley". Indeed this preponderance of AGN in the transition zone between the red sequence and blue cloud has been proposed as evidence for galaxies becoming passive as the result of AGN feedback (e.g. Kauffmann et al. 2006; Martin et al. 2007). The concept that these intermediate objects in the "green valley" represent a third population that is distinct both from the red and blue sequences is confirmed by Wyder et al. (2007) who were unable to fit the overall NUV$-r$ colour distribution of galaxies by double Gaussians in the same way as Baldry et al. (2004) were able to using their $u-r$ colours, due to excess galaxies with intermediate NUV$-r$ colours.

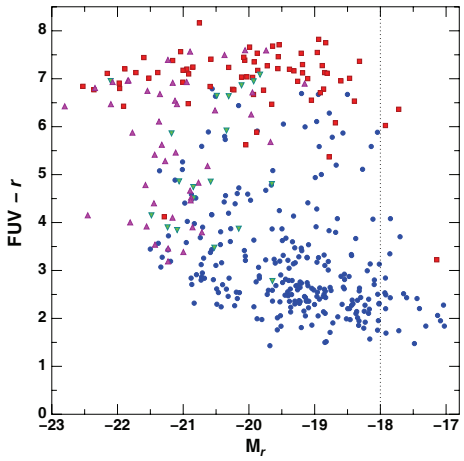

Figure 7.3: The FUV$-r$ / M$_r$ colour-magnitude diagram of galaxies. Red squares and blue circles indicate passive (EW[Hα]<2Å) and star-forming (EW[Hα]>2Å) galaxies, while green and magenta triangles indicate AGN with EW(Hα)>2Å and EW(Hα)<2Å respectively.

7.3.1 Comparison to FUV and MIR indicators

The FUV is yet more sensitive to recent star-formation than the NUV, and traces star-formation on time-scales of $\sim10^8$ years, while the NUV does the same but for time-scales five to ten times longer. However, galaxies are $\sim$1 mag fainter in the FUV than the NUV, and so a significant number of SDSS galaxies are not detected in the MIS FUV imaging. Hence we consider only the deeper DIS images, and in Fig. 7.3 we show the FUV$-r$ / M$_r$ colour-magnitude diagram for z<0.05 SDSS galaxies with DIS FUV imaging. We separate galaxies into star-forming (EW[Hα]>2Å; shown as blue circles) and passively-evolving (EW[Hα]<2Å; red squares) galaxies. Galaxies with optical AGN signatures are indicated by green triangles (for those with EW[Hα]>2Å) or magenta triangles (EW[Hα]<2Å).

As for the NUV we see a robust separation of passive and star-forming galaxies, with the red sequence dominated by passive galaxies at FUV$-r\sim7$ and the blue cloud of star-forming galaxies at FUV$-r\sim3$. Even in the FUV however, we see some galaxies spectroscopically classified as star-forming with red FUV-optical colours, although they are found only on the lower edge of the red sequence with FUV$-r\sim6$. The separation is only marginally better than that based on the NUV$-r$ colour.

In Fig. 7.4 we compare the observed NUV$-r$ colour with the ratio of 24μm to 3.6μm IR luminosities obtained by the SWIRE IR survey (Lonsdale et al. 2003), matching the z<0.05 SDSS galaxies with the public SWIRE

IRAC+24μm band-merged catalogues for the Lockman, ELAIS-N1 and ELAIS-N2 fields. The 24μm luminosity is known to be a well-calibrated indicator of the SFR (Calzetti et al. 2007), while the 3.6μm flux can be used to trace the stellar mass distribution of galaxies almost independently of dust obscuration effects. Hence the 24μm to 3.6μm flux ratio can be considered as a good measure of the specific SFR of a galaxy, and Davoodi et al. (2006) use $\log(L_{24}/L_{3.6})=-0.7$ to separate star-forming and passive galaxies. We see that the NUV$-r$ colour and $F_{24}/F_{3.6}$ ratio are strongly correlated, and both are directly related to the spectroscopic classification based on the galaxy's nebular emission: star-forming galaxies have high $F_{24}/F_{3.6}$ ratios and blue NUV$-r$ colours, while passive galaxies have exclusively low $F_{24}/F_{3.6}$ ratios and red NUV$-r$ colours. Most importantly, we see that of the galaxies on the NUV-optical red sequence, only those spectroscopically classified as star-forming or AGN have high $F_{24}/F_{3.6}$ ratios, the 24μm emission in the case of the latter produced by dust heated by the AGN rather than star-formation. There is no evidence for a population of galaxies with ongoing star-formation that is so completely obscured so as to not show any Hα emission or UV flux, and so we can gain a robust classification of galaxies into passive and star-forming by a combination of SDSS spectra and NUV photometry.

7.3.2 Environmental trends of the NUV$-r$ C-M relation

In Figure 7.5 we compare the NUV$-r$ / M_r colour-magnitude diagrams of galaxies in field ($\rho<0.5$; left panel) and cluster ($\rho>1.0$; right panel) environments. In chapter 6 we found that the few passively-evolving dwarf galaxies in field regions ($\rho<0.5$) were always satellites to massive galaxies ($M_r<-20$), and that throughout the SDSS DR4 there were no passively-evolving dwarf galaxies $2\,R_{vir}$ from a massive halo, whether that be a cluster, group or massive galaxy. Hence to confirm this result we remove the $\sim$10% of field galaxies that are found within a projected distance of 400 kpc and a radial velocity within 300 km s^{-1} of a $M_r<-20$ galaxy. Our resultant field galaxy sample thus excludes galaxies which are satellites within massive halos, however it may include galaxies which have had a fly-by encounter with a massive galaxy in the recent past. The NUV-optical red sequence should then represent only those galaxies which have become passive through internal processes such as merging, AGN feedback and gas exhaustion through star-formation.

In cluster regions ($\rho>1$; right panel) there is a clear NUV-optical red sequence dominated by passively-evolving galaxies that extends to at least the completeness limit of the survey ($M_r=-18$). There appears to be a break

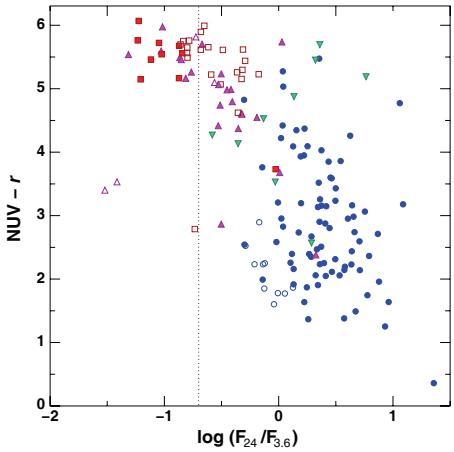

Figure 7.4: NUV$-r$ colour against the ratio of 24μm to 3.6μm luminosity. Solid symbols are as in Fig. 7.3. Open symbols indicate galaxies not detected in 24μm at the 450μJy SWIRE limit. The dotted line indicates the MIR cut used to separate star-forming and passive galaxies in Davoodi et al. (2006).

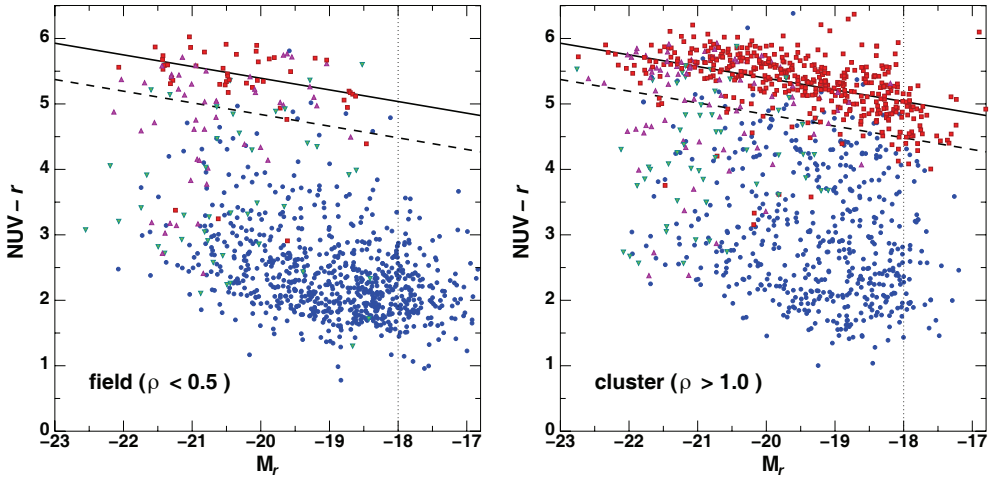

Figure 7.5: The NUV$-r$ / M$_r$ colour-magnitude diagram of galaxies in the lowest (ρ<0.5) and highest (ρ>1.0) density environments. Red squares and blue circles indicate passive (EW[Hα]<2Å) and star-forming (EW[Hα]>2Å) galaxies, while green and magenta triangles indicate AGN with EW(Hα)>2Å and EW(Hα)<2Å respectively. The dotted line indicates the completeness limit of the volume covered, while the solid and dashed lines are as in Fig. 7.2.

in the red sequence at $M_r\sim-20.5$, with massive red sequence galaxies having similar colours (NUV$-r\sim$5.7) while fainter galaxies become increasingly blue. Similar trends have been seen by Boselli & Gavazzi (2006) who find the dichotomy between giant and dwarf red sequence galaxies to be even stronger when using the FUV-optical or FUV-NIR colours. Wyder et al. (2007) in contrast find no evidence of a break in the NUV-optical red sequence, fitting it instead by a straight line for $-23.5<M_{r,0.1}<-18$. Fitting separate C-M relations to bright ($M_r<-20$) and faint ($-21<M_r<-18$) passively-evolving galaxies we obtain slopes of -0.043 ± 0.052 and -0.222 ± 0.039 respectively, and hence the break appears significant. Considering now a C-M relation with break at $M_r=-20.5$ the overall dispersion is reduced slightly to $\sigma_{\rm NUV-}r=0.345\pm0.007$, with no significant difference between bright and faint magnitudes.

At all luminosities we see an extended tail of galaxies with bluer colours, being mostly AGN at the bright-end and star-forming galaxies at fainter magnitudes. Although many of these galaxies have NUV$-r\sim$2 corresponding to the peak of the blue cloud distribution seen in Fig. 7.2, a significant fraction are found with transitional colours being in the "green valley" with NUV$-r\sim$4–5. We see no obvious separation between the red sequence and the blue cloud populations in cluster environments.

In the field however, the dominant feature of the colour-magnitude diagram becomes the blue cloud population at NUV$-r\sim$2, made up almost entirely of star-forming galaxies, except at the very bright tip (M_rM^*) where AGN take over. The red sequence is now sparsely populated at all magnitudes and appears truncated below $M_r\sim-18.5$.

7.3.3 The red and blue galaxy luminosity functions

In Fig. 7.6 we plot the red and blue galaxy luminosity functions (as red and blue symbols respectively) in both field and cluster environments, based on the galaxies shown in Fig. 7.5, where the dashed line is used to separate the red and blue galaxy populations. We correct for incompleteness at faint magnitudes by weighting each galaxy by $1/V_{max}$. For each luminosity function we determine the best-fitting single Schechter (1976) function based on a maximum-likelihood analysis, shown by the black curves. The resultant best-fit parameters are presented in Table 7.3, where the reported errors represent the 68.3% confidence limits in α and M^*.

We see little sign of variations in the luminosity function of blue galaxies from field to cluster environments, with marginal evidence for an increase in the luminosity of M^* from field to cluster environments, but no difference in the faint-end slope. In contrast the luminosity function of the red sequence

populations in field and cluster environments are inconsistent at $>3\,\sigma$ level. In particular, the red sequence luminosity function in field regions peaks at $M_r{\sim}-20.5$ and drops rapidly at magnitudes fainter than $M_r{\sim}-18.5$, with no red galaxies at $M_r{>}-18$. This decline results in a very shallow faint-end slope $\alpha{=}+0.484{\pm}0.365$, and we are also able to fit the red sequence field galaxy population equally well by a single Gaussian function with $\sigma{=}0.684{\pm}0.088$ and $M^*_r{=}-20.23{\pm}0.16$ as shown by the dashed curve in Fig 7.6.

7.4 Discussion

We have examined the make-up and environmental dependencies of the optical and UV-optical colour-magnitude diagrams, combining *GALEX* UV photometry with a volume-limited ($0.005{<}z{<}0.037$) subset of SDSS DR4 galaxies (from chapter 6) to produce a sample of 4 065 galaxies with both NUV photometry and SDSS DR4 spectroscopy.

About 30% of red sequence galaxies in the optical C-M diagram show signs of ongoing star-formation from their spectra having EW(Hα)>2Å. This contamination is greatest at faint magnitudes ($M_r{>}-19$) and in field regions where as many as three-quarters of red sequence galaxies are star-forming. This has important consequences for understanding the build-up of the red and blue sequences being interpreted as the hierarchical assembly of star-forming and passively-evolving galaxies, as the colour of the galaxy cannot be always reliably related to its star-formation history. Instead a significant fraction (and in some cases the majority) of galaxies on the red sequence have star-formation histories more in common with the blue cloud population and appear red simply due to dust, the presence of which is directly related to them having active ongoing star-formation.

The effect of the contamination of the faint end of the red sequence by dusty star-forming galaxies is likely to become increasingly important at higher redshifts, where the global star-formation rates (Noeske et al. 2007a; Zheng et al. 2007), and hence the effects of dust extinction are that much higher. This produces a significant overestimation of the amount of stellar mass already in the red sequence at a given epoch, particularly at low masses, and an overestimation of the look-back time by which the stellar mass is assembled in passively-evolving galaxies. Similarly, the global amounts of stellar mass and star-formation in the blue sequence of star-forming galaxies will be underestimated. These effects could bias the interpretation of studies looking at the evolution of the optically-defined red and blue sequences with redshift in terms of the hierarchical assembly and conversion of accreted gas into stars in passive and star-forming galaxies (e.g. Bell et al. 2004), the result

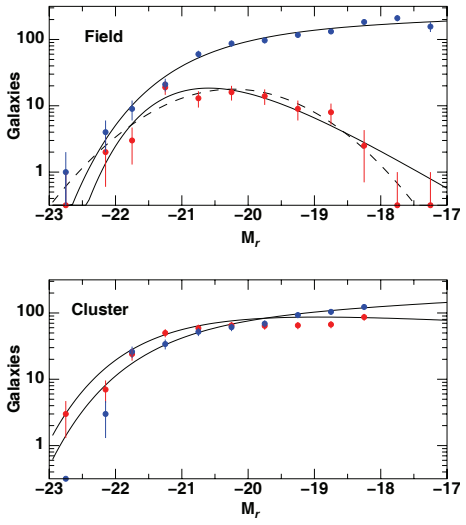

Figure 7.6: The red and blue galaxy luminosity functions for cluster and field environments. The best-fit single Schechter functions are indicated by black curves. For the red sequence galaxies in field regions the best fitting single Gaussian function is also shown by the dashed black curve.

of which could be the over-estimation of the importance of dry mergers to create the present day population of passively-evolving galaxies.

Instead the NUV$-r$ colour allows a much more robust separation of passively-evolving and star-forming galaxies, with a clear red sequence of passively-evolving galaxies at NUV$-r5$ and a well separated blue sequence of star-forming galaxies at NUV$-r<4$. We find that globally only 8% of UV-selected red sequence galaxies are star-forming, i.e. one quarter of the contamination seen in the optical red sequence. By comparing the NUV$-r$ colour with both FUV and *Spitzer* 24μm photometry we confirm this robust separation, finding no evidence for a population of galaxies with star-formation that is so heavily obscured so as to not show any Hα emission or UV flux. We thus indicate that through a combination of SDSS spectra and NUV photometry we can gain a robust classification of galaxies into passive and star-forming. This allows the build-up of the UV-selected red sequence with redshift and environment to be directly interpreted in terms of the assembly of stellar mass in passively-evolving galaxies (Arnouts et al. 2007; Martin et al. 2007).

In cluster and group environments the UV-selected red sequence is fully in place to at least $M_r=-18$. In sharp contrast in isolated field regions (where the majority of galaxies are found) the number density of UV-optical red sequence galaxies declines rapidly at magnitudes fainter than $M_r\sim-18.5$ with

Table 7.3: Best-fitting luminosity functions

LF params	α	M*	ψ
Field regions (ρ<0.5, >400 kpc from M$_r$<20.0 galaxy)			
red	+0.484±0.365	−20.16±0.26	49.3
blue	−1.078±0.071	−20.71±0.19	163.2
Cluster regions (ρ>1.0)			
red	−0.884±0.122	−21.28±0.25	135.9
blue	−1.126±0.121	−21.25±0.28	110.3

no galaxies seen fainter than M$_r\sim-18$. This confirms the findings of Paper II that no passively-evolving dwarf galaxies are found more than two virial radii from a massive halo, whether that be a group, cluster or massive galaxy. Hence in these regions the build-up of the red sequence of passively-evolving galaxies is incomplete, forming from the top down and being largely absent at M$_r-18.5$. Only *internal* processes such as merging, supernovae and AGN feedback mechanisms, and gas exhaustion due to star-formation can be responsible for completely stopping star-formation in these galaxies, and hence cannot be effective in low-mass galaxies (for a discussion see Haines et al. 2007) as otherwise passively-evolving dwarf galaxies would be ubiquitous. Instead the passively-evolving dwarf galaxies that dominate (in terms of numbers) groups and clusters and make up the faint-end of the cluster red sequence must have had their star-formation quenched through processes directly related to their environment such as ram-pressure stripping or tidal shocks.

Arnouts et al. (2007) have followed the build-up with redshift of the passive and star-forming galaxy populations as selected from their rest-frame NUV$-r$ colour. They are able to obtain a similarly robust separation of rest-frame UV-selected red and blue sequence galaxies to at least $z\sim1.2$ and probably as early as $z=2$. They find that the stellar mass density of red sequence galaxies has increased by a factor two since $z\sim1.2$, and that this increase can be accounted for entirely by the shutdown of star-formation in active galaxies without requiring additional growth through dry mergers, in agreement with the results of Bell et al. (2007) who derive the global star-formation contribution of blue and red galaxy populations from ultraviolet and *Spitzer* 24 μm luminosities.

These results support the downsizing paradigm whereby the red sequence

is built-up from the top down, being already largely in place at the bright end by $z\sim1$ (Bell et al. 2004; Willmer et al. 2006), and the faint end filled in at later epochs in clusters and groups through environment-related processes such as ram-pressure stripping or galaxy harassment. This filling in of the faint end appears to occur mainly at $z<1$, and occurs earlier in the richest clusters. Tanaka et al. (2007) find few faint red galaxies in four clumps belonging to a large-scale structure at $z\sim1.2$ suggesting that the red sequence is truncated within groups at $M^*+1.5$, whereas by combining several rich clusters at $z\sim1.2$ Strazzullo et al. (2006) find the red sequence to be fitted by a Schechter function with $\alpha=-0.85$ to at least $M^*+2.5$. de Lucia et al. (2006) find an increase of a factor two in the dwarf-to-giant ratio of red sequence galaxies from $z\sim0.8$ to $z\sim0.4$, while Stott et al. (2007) find evidence for a further doubling of the dwarf-to-giant ratio since $z\sim0.5$.

At all epochs to $z\sim0.8$ Tanaka et al. (2005) find a deficit of faint ($M_V > M_V^*+1$) red sequence galaxies in field regions, with respect to cluster and group environments, although their deficits are not as dramatic as presented here due to the use of photometric redshifts and statistical subtraction methods to define the field sample, as well as the use of rest-frame $U-V$ colour-magnitude diagrams to define the red sequence population. To obtain clearer results for the field dwarf galaxy population at these redshifts would require a large-scale spectroscopic survey of galaxies to $\sim M^*+3$ in order to define both the redshifts and environments of each galaxy, something that is within reach of present surveys (e.g. DEEP2, VVDS), at least to $z\sim0.4$.

Conclusions

This thesis addresses a fundamental open issue of the extragalactic astronomy: how, when, and where galaxies evolve. To this aim we investigate galaxy properties as a function of both luminosity and environment. In particular, we wish to distinguish between mechanisms that are internal to the galaxy, such as merging, AGN feedback, or gas consumption through star-formation, and those related to the direct interaction of the galaxy with its surroundings including ram-pressure stripping and galaxy harassment.

For this analysis we use the Shapley Optical Survey (SOS: Mercurio et al. 2006; Haines et al. 2006a) complemented with medium resolution spectroscopy (Smith et al. 2007) for a subsample of galaxies, and NYU-VAGC low-redshift galaxy catalogues (Blanton et al. 2005c) taken from the SDSS DR4 spectroscopic dataset complemented with NUV and FUV photometry from GALEX archive (Haines, Gargiulo & Merluzzi 2008).

The SOS covers a 2 $\deg^2$ region of the Shapley supercluster core at $z = 0.05$ in two bands (B and R). The galaxy sample is complete to B=22.5 ($>M_\star+6$, N_{gal}=16588), and R=22.0 ($>M_\star+7$, N_{gal}=28008). The complementary spectroscopic sample consists of 541 R<18 galaxies down to $\sigma_0 \sim 50\,\mathrm{km\,s^{-1}}$. Furthermore, from the SDSS NYU-VAGC catalogue, we select a sample of 27753 galaxies in the redshift range $0.005 < z < 0.037$ that is $>90\%$ complete to $M_r = -18.0$ and for which photometry and spectroscopy are available. GALEX NUV imaging provides photometry for 4065 galaxies (403 at FUV wavelengths, and 156 at in the MIR) for the latter sample.

The key feature of these samples is their coverage of environments spanning a wide range of density and dynamical states (from cluster cores to the field), and luminosities/masses (from giant to dwarf galaxies). This allows us to investigate the different physical mechanisms that drive the star-formation in giant and dwarf galaxies.

The main results of this work are the following.

- The global properties of dwarf galaxies in the Shapley supercluster change significantly from the cluster cores to the virial radius, both in terms of the luminosity function, and the mean galaxy colours, which

indicates that these galaxies are being transformed by processes directly related to the supercluster environment. As galaxy mergers should be infrequent in any of the environments covered by the SOS, the finding of such large changes in the mean galaxy colour or fraction of faint blue galaxies within the SOS, indicates that some process other than merging must be responsible. The analysis of the luminosity function suggests that galaxy harassment is important for shaping the galaxy luminosity function at magnitudes fainter than $\sim M^* + 1$, and additional evidence in favour of faint galaxies being transformed by ram-pressure stripping and undergoing starbursts triggered by shocks in the ICM produced by cluster mergers are found studying the colour distribution. These results indicate that the effect of environment on faint ($M^* + 1$) galaxies is quite different from that observed for bright galaxies (Gómez et al. 2003; Lewis et al. 2002). While bright galaxies appear to be transformed by processes that can take place well outside the virial radius, that is galaxy merging or suffocation, we find in this analysis that many faint galaxies are affected directly by their interaction with the supercluster environment, although we cannot rule out that the faint galaxies are also transformed outside the virial radius, beyond the limits of our survey.

- The observed clear trend between the FP residuals and age and α/Fe, with those galaxies with effective radii smaller than predicted by the FP to have stellar populations systematically older and with higher abundances than average, is fully consistent with the predictions of Hopkins et al. (2008). They make specific predictions for the effects of varying the dissipational fraction on the remnant spheroids of a given mass, showing that ellipticals formed through mergers with higher dissipation fractions should be more α-enriched. As merger remants involving more dissipation are expected to be more compact, we should expect both mean stellar age and [α/Fe] to anti-correlate with the residuals in the r_e direction, as we find. These observed significant anti-correlations strongly support the merger hypothesis for the formation of elliptical galaxies, and imply a fundamental connection between the structures and stellar populations of early-type galaxies.

- Using star-formation indicators, we find that massive galaxies ($\mathcal{M} > 10^{10.5}\mathrm{M}_\odot$; $\mathrm{M}_r < -20$) show only gradual trends of star-formation with environment, the fraction of passively-evolving galaxies increasing gradually with local density from $\sim$ 50% to $\sim$ 70% in high-density regions, the trend extending to the lowest density regions studied, well

beyond the effects of cluster-related processes. For these galaxies only the large-scale galaxy density appears important for defining their star-formation history, and not their immediate neighbours or even whether it is within a cluster or group, implying that cluster-related mechanisms are not important. The star-formation histories of massive galaxies appear to be predefined by the initial conditions in which they form, whereby in high-density regions they are likely to form earlier and have more active merger histories than those in low-density regions, resulting in the observed gradual SF-density relations. In contrast, the star-formation histories of dwarf galaxies ($\mathcal{M} \sim 10^{9.2} \mathrm{M}_{\odot}$, $\mathrm{M}_r \sim -18$) are strongly dependent on their local environment, the fraction of passively-evolving galaxies dropping from $\sim$70% in dense environments, to $\sim$0% in the rarefied field. Indeed for the lowest luminosity range covered ($-18 < M_r < -16$) none of the $\sim$600 galaxies in the lowest density quartile are passively-evolving. The few passively-evolving dwarfs in field regions are strongly clustered around bright ($> L^*$) galaxies, and throughout the SDSS sample we find no passively-evolving dwarf galaxies more than $\sim$2 virial radii from a massive halo, whether that be a cluster, group or massive galaxy. This limit of around 2–2.5 virial radii corresponds to the maximum distance from a cluster or massive galaxy that a galaxy can rebound to having been previously subhalos within massive halos (Mamon et al. 2004; Diemand et al. 2007), and so it seems reasonable to believe that all passively-evolving dwarf galaxies are or have been satellites within a massive DM halo. Our finding that passively-evolving dwarf galaxies are only found within cluster, groups or as satellites to massive galaxies indicates that internal processes or merging are not responsible for terminating star-formation in these galaxies. Instead the evolution of dwarf galaxies is primarily driven by the mass of their host halo, probably through the combined effects of tidal forces and ram-pressure stripping. We find a significant anti-correlation (10σ) between the EW(Hα) of dwarf ($-19 < \mathrm{M}_r < -18$) star-forming galaxies and local density, producing a a systematic reduction of $\sim$30% in the Hα emission in high-density regions with respect to field values. We argue that this implies that the bulk of star-forming dwarf galaxies in groups and clusters are currently in the process of being slowly transformed into passive galaxies. The transformation of dwarf galaxies solely through environmental processes results in the wide variety of star-formation histories observed in the local dwarf galaxy population (Mateo 1998). Examining the fraction of passively-evolving galaxies as a function of both luminosity and local environment, we find that in high-density regions $\sim$ 70% of

galaxies are passively-evolving independent of luminosity. In the rarefied field, where environmental related processes are unlikely to be effective, however the fraction of passively-evolving galaxies is a strong function of luminosity, dropping from 50% for $M_r < -21$ to zero by $M_r = -18$. This strong luminosity dependence of the fraction of passive galaxies in field regions reflects with the systematic trend with increasing galaxy mass for star-formation histories to be driven by internal mechanisms as opposed to environmental processes.

- In cluster and group environments the UV-selected red sequence is fully in place to at least $M_r = -18$. In sharp contrast in isolated field regions (where the majority of galaxies are found) the number density of UV-optical red sequence galaxies declines rapidly at magnitudes fainter than $M_r \sim -18.5$ with no galaxies seen fainter than $M_r \sim -18$. Hence, in these regions the build-up of the red sequence of passively-evolving galaxies is incomplete, forming from the top down and being largely absent at $M_r - 18.5$. Only *internal* processes such as merging, supernovae and AGN feedback mechanisms, and gas exhaustion due to star-formation can be responsible for completely stopping star-formation in these galaxies, and hence cannot be effective in low-mass galaxies as otherwise passively-evolving dwarf galaxies would be ubiquitous. Instead the passively-evolving dwarf galaxies that dominate (in terms of numbers) groups and clusters and make up the faint-end of the cluster red sequence must have had their star-formation quenched through processes directly related to their environment such as ram-pressure stripping or tidal shocks.

  These results support the downsizing paradigm whereby the red sequence is built-up from the top down, being already largely in place at the bright end by $z \sim 1$ (Bell et al. 2004; Willmer et al. 2006), and the faint end filled in at later epochs in clusters and groups through environment-related processes such as ram-pressure stripping or galaxy harassment. This filling in of the faint end appears to occur mainly at $z < 1$, and occurs earlier in the richest clusters.

The observed bimodality of galaxy properties unequivocally supports a different evolutionary scenario for dwarf and giant galaxies, and in particular, the observed transition from environmentally to internally-driven star-formation histories is likely due to a combination of factors:

- the increasing efficiency and rapidity with which gas is converted into stars for more massive galaxies, resulting in gas-consumption timescales for massive galaxies that are much shorter than the Hubble time;

- the mode for the accretion and cooling of fresh gas onto the galaxy from its surroundings. When galaxy halos reach a mass $\sim 10^{12} M_{\odot}$ expanding shocks heat infalling gas to the virial temperature of the halo, producing a stable atmosphere of hot, diffuse gas which is vulnerable to feedback effects that can prevent the gas from cooling onto the galaxy (Kereš et al. 2005; Dekel & Birnboim 2006);

- AGN feedback in the form of quasar winds which can expel the remaining gas from a galaxy and/or the quasi-continuous low-level AGN activity that prevents cooling of the diffuse atmosphere of hot gas in massive galaxies. The observed paralleled increasing fractions of AGN and passive field galaxies with luminosity supports the importance of AGN feedback in shutting down star-formation in galaxies, a process which should become increasingly efficient with galaxy mass as the result of the tight $M_{BH} - \sigma$ relation;

- the increased susceptibility of low-mass galaxies to disruption by environmental effects such as tidal shocks and ram-pressure stripping due to their shallow potential wells.

The combined effect of these processes is to produce the observed bimodality in the global properties of galaxies about a characteristic mass of $\sim 3 \times 10^{10} M_{\odot}$ (Kauffmann et al. 2003a), although given that several models that treat each of these processes in diverse ways are qualitatively able to reproduce this bimodality (e.g. Menci et al. 2005; Bower et al. 2006; Croton et al. 2006; Cattaneo et al. 2006; Dekel & Birnboim 2006), it will be difficult to quantify the relative importance of the mechanisms for driving the star-formation histories of galaxies.

Future Work

The work presented in this thesis has attempted to answer many complex and related open questions related to galaxy evolution, in particular examining the origin of the bimodality of galaxy properties and how galaxies are transformed from star-forming disks to passively-evolving spheroids. Although, hopefully we have been successful in answering some questions (at least partially), in particular showing that different physical mechanisms drive the evolution of giant and dwarf galaxies, and being able to quantify the relative importance of internal and environmental processes, there remain many unanswered questions. These partial successes have however given us inspiration and new ideas to approach these remaining issues, and address some of the limitations of the datasets used in this thesis.

Perhaps the main unresolved problem related to this thesis project is *which* physical processes are behind the transformation of gas-rich star-forming galaxies, which have been observed to be accreted by clusters at $z \sim 0.5$–1, into the passive ellipticals and S0s which dominate present day clusters. Despite huge efforts over the last thirty years, it has proved remarkably difficult to witness these transformations directly, and identify the mechanisms which reshape and quench the star-formation in infalling spirals. As many of these previous studies have done, this thesis has been largely based on optical photometry and fibre-based spectroscopy, which as discussed in the introduction has its limitations, in particular the effect of dust obscuration.

Many of the proposed physical mechanisms behind the transformation of galaxies in cluster environments induce heavily obscured star-bursts, effectively hiding the crucial stages of the transformation from optical observations with dust. The recent availability of mid-infrared (MIR) imaging from the *Spitzer space telescope*, uniquely sensitive to this obscured star-formation allows new progress to be made. Other mechanisms such as suffocation may act over such long time-scales that no clear transformation signature appears in the optical spectra alone. This can be addresed by combining both optical spectroscopy and UV imaging which are both sensitive in diverse ways to intermediate age ($10^8 - 10^9$yr) stars, and have shown that such a slowly-

quenched population exists.

A second issue related to the fibre-based spectroscopy used in this thesis, both from the AAOmega spectroscopy used for the fundmental plane study, and the SDSS spectroscopy, is that the fibres only cover the central regions of the galaxies, effectively missing a significant fraction of the light, which can lead to aperture biases as discussed in the thesis. Moreover, the spectroscopic data does not contain any spatial information, such as how the star-formation may be spread over the galaxy, or whether there are age- or metallicity-gradients, or provide any kinematical information such as rotation curves, or decoupled cores.

In order to ascertain which physical mechanism transforms galaxies in cluster environments needs much, if not all, of the above information, above and beyond the datasets used within this thesis. This has inspired us to embark on a long-term project aimed at distinguishing between the various proposed physical mechanisms behind galaxy transformations in dense environments, in the uniquely dynamically-active region of the Shapley supercluster core, for which we already had in hand a significant amount of high-quality data. Over the last year we have successfully obtained complementary multi-wavelength data for this region, along with further AAOmega spectroscopy, and ultimately EU funding to undertake a long-term programme with the state-of-the-art integral-field spectrograph WiFeS (Wide Field Spectrograph at 2.3m telescope of the Australian National University) of $\sim$ 100-200 supercluster members. ACCESS (A Complete CEnsus of Star-formation and nuclear activity in the Shapley supercluster; P.I. Dr. P. Merluzzi) is a 4-year research programme funded by an International Research Staff Exchange Scheme (IRSES) within the European Commission's Seventh Framework Programme. The institutes participating in ACCESS are: (i) Istituto Nazionale di Astrofisica – Osservatorio Astronomico di Capodimonte, Naples; (ii) University of Durham, UK; (iii) University of Birmingham, UK; and (iv) the Australian National University. Below are briefly described the new datasets which will form the basis of this research programme:

AAOmega spectroscopy In May 2007, a further $\sim$500 spectra were obtained by Dr. R. J. Smith at AAOmega, which should be comparable to those used in the fundamental plane study of this thesis. These spectra were selected from the SOS according to having $R < 18.0$, and should ensure a homogeneous sample of supercluster members over the entire SOS region, that is around 80% complete to $R = 18.0$.

***R*-band surface photometry** Surface photometry has now been derived in all the SOS R-band images (both mosaics and individual exposures)

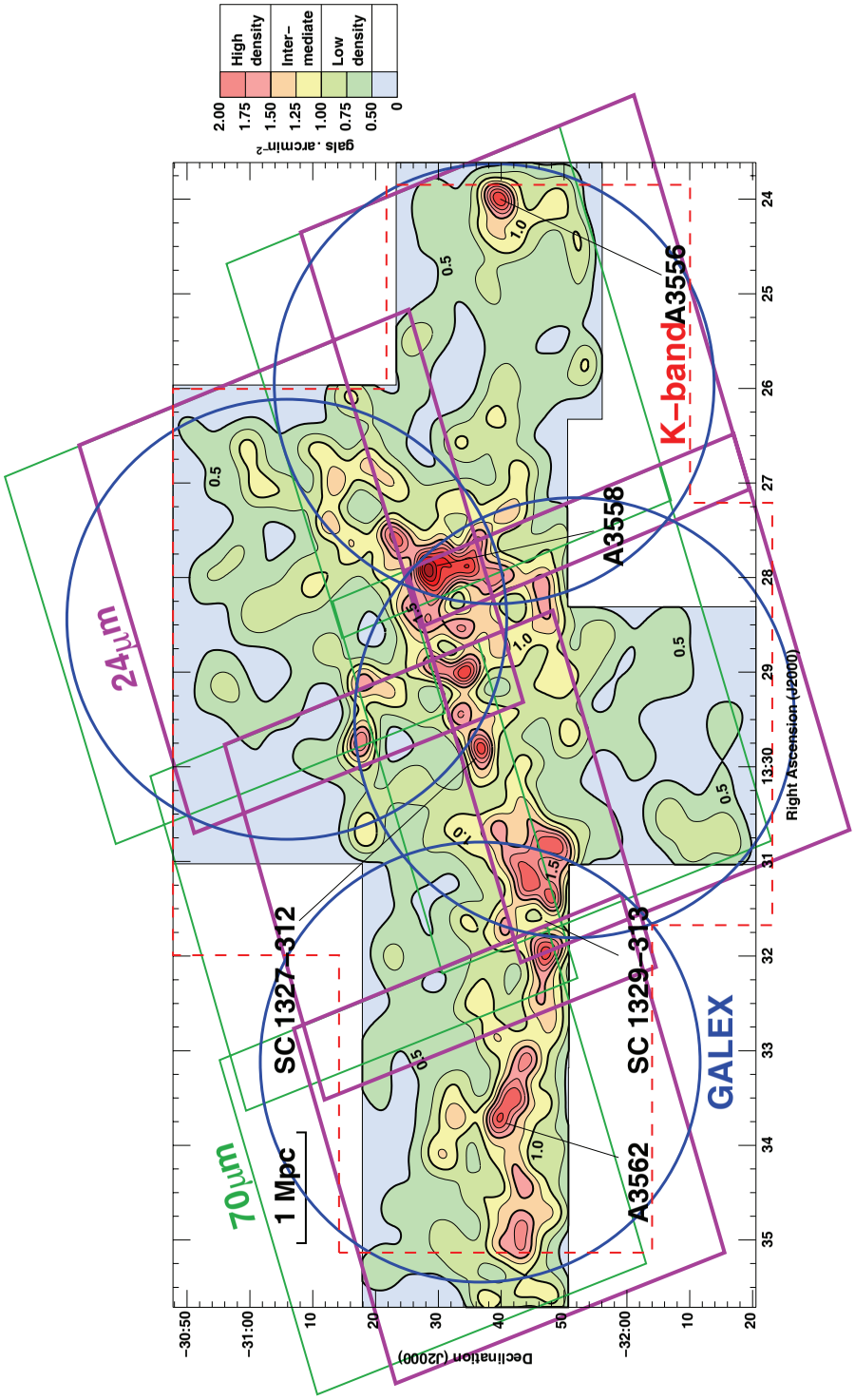

Figure 7.7: Map of the SOS region showing the areas covered by the new multi-wavelegth datasets: K-band imaging from UKIRT/WFCAM (red dashed lines); NUV/FUV imaging from *GALEX* (blue circles); 24μm and 70μm MIPS photometry from Spitzer (magenta and green boxes).

providing structural parameters (and errors) to essentially all $R < 18$ galaxies over the $2\,\mathrm{deg}^2$ SOS region.

K-band imaging In April 2007, K-band imaging was obtained for the whole SOS region using the Wide Field infrared Camera (WFCAM) instrument on the 4m United Kingdom Infra-Red Telescope (UKIRT) in Hawaii. A total of five tiles (each made of four interleaved exposures) were observed, with exposure times of 300 s, resulting in images $\sim$80% complete to $K = 18.0$, and a pixel scale of 0.4 arcsec. K-band structural parameters have also been obtained using 2DPHOT.

UV imaging We obtained NUV and FUV imaging of the whole SOS region through a successful Cycle 4 *GALEX* proposal (P.I. R. J. Smith). Four 70 arcmin diameter fields were observed simultanaeously in the NUV and FUV wavebands in May 2008, with exposure times of 1000-1500s, and reaching magnitude limits of $m_{AB} \sim 23$.

MIR imaging We also obtained MIR photometry (24, 70 and 160μm) of the whole SOS region through a successful 14.8 hr Cycle 5 *Spitzer* proposal (P.I. C. Haines). Five overlapping fields were observed in August 2008 with MIPS in scanning mode, reaching a 5σ sensitivity of $\sim 460\mu$Jy at 24μm, corresponding to a bolometric infrared luminosity of $\sim 5\times10^8 L_\odot$ or a star-formation rate of just $0.038\,\mathrm{M}_\odot$/yr at the supercluster redshift.

WiFeS IFU spectroscopy The main aim of ACCESS is to undertake a long-term survey programme ($>$ 70 nights) with the state-of-the-art integral-field spectrograph WiFeS on the Australian National University 2.3m telescope. This instrument allows the obtaining of spatially-resolved spectroscopy over a $38''\times25''$ field with $1''\times1''$ resolution elements, covering the full optical wavelength range (3200–9500Å) at medium resolution. With exposure times of 4–8 hours per galaxy, we expect to be able to obtain high-quality spatially-resolved spectroscopy out to r_e of $\sim$100–200 members of the Shapley supercluster to $R < 18$. These datacubes will allow us to map in detail the kinematics, and the star-formation density (both current and recent past), dust stellar ages and metallicity.

Figure 7.7 shows a map of the original Shapley Optical Survey region, with the coverage of the recently acquired multi-wavelength datasets superposed.

The scientific goals of ACCESS are:

a) Searching for the ram pressure effects Ram pressure from the passage of the galaxy through the dense ICM can effectively remove the

cold gas supply and thus rapidly terminate ongoing star-formation, either by stripping the gas directly (Abadi et al. 1999), or by inducing a starburst in which all of the gas is consumed (Fujita & Nagashima 1999). Gas is stripped incrementally from the outside-in, resulting in inverted colour and age gradients in the galaxies, and truncated Hα emission profiles. The most dramatic ICM-galaxy interactions should occur when two clusters merge, as shock fronts created in the ICM may trigger starbursts in galaxies over large scales (Roettiger, Burns & Loken 1996). Importantly, in terms of their environmental effects, these mechanisms all require a dense ICM, and so their evolutionary effects on massive galaxies are limited to the cores of clusters, but extend to poorer environments for dwarf galaxies which are easier to strip. To address this topic (i) optical-NIR internal colour gradients and (ii) age gradients and Hα emission profiles will be derived for the super-cluster galaxy population and their distribution will be analysed as a function of galaxy mass (either stellar or dynamic) and environment. There is already much existing X-ray data (from ROSAT, ASCA, XMM-Newton and Chandra) in this region, allowing us to infer the local ICM density for each galaxy.

b) Probing galaxy merging Galaxy mergers represent an efficient mechanism to generate angular momentum loss in the gas of galaxies and the subsequent fuelling of significant star formation or nuclear activity, and may be the only means of powering the more extreme ultra-luminous infrared galaxy (ULIRG) and quasar populations. Simulations demonstrate the efficiency of mergers in transforming star-forming spirals into passively-evolving spheroids, producing both the required morphogical evolution, and through the effect of AGN feedback permanently shutting down star-formation. However, galaxy mergers cannot occur when the encounter velocities between galaxies are much greater than the internal velocity dispersion of galaxies (Aarseth & Fall 1980). Thus mergers are frequent in small groups, but rare in rich clusters (Ghigna et al. 1998), seemingly making Shapley an unlikely environment for merging to occur. However, as groups fall into the super-cluster, the merging frequency is thought to be temporarily boosted (Moss 2006) such that in dynamically active clusters merging is in fact rather common, and may be behind the apparent correlation between the frequency of cluster LIRGs and the dynamical status of the clusters. The WiFeS and complementary UV-FIR data will be crucial to identifying both ongoing mergers and merger remnants by detecting the imprints of the interactions on the kinematics and morphology of the remnant and

triggered obscured nuclear starbursts. By producing a systematic census of merger remnants in the Shapley super-cluster, we will be able to: (i) follow the long-term transformational effects of merging on the remnants, (ii) quantify where and how frequently mergers occur, and (iii) quantify how much merging induced starbursts contribute to the global cluster star-formation rate.

c) Probing galaxy harassment Galaxy harassment is the process whereby repeated close (<50 kpc), high-velocity (>1000 km s^{-1}) encounters with massive galaxies and the cluster's tidal field cause impulsive gravitational shocks that damage the fragile disk of late-type spirals (Moore et al. 1996), transforming them over a period of several Gyr. Galactic harassment is effective throughout a cluster, including beyond the virial radius, but its effects should be greater for those clusters with higher velocity dispersions. Such interactions may trigger nuclear starbursts and will also leave imprints on the kinematics including dynamically decoupled cores and tidal tails. The internal kinematics will be studied for a sample of super-cluster galaxies selected to span a wide range of mass and spectral type and located in different environments. The Spitzer and WiFeS data will be crucial to catch the interacting galaxies in the act, before they have moved too far apart to be identified as interacting.

d) Probing galaxy suffocation When a galaxy falls into a more massive halo, the diffuse gas in its halo is lost to the ICM. This prevents further cooling and replenishment of the cold gas supply leading to "suffocating" of the galaxy (Blanton et al. 2000; Diaferio et al. 2001) as star-formation declines slowly and the remaining cold gas is used up (Larson et al. 1980). In this process the kinematics, structural parameters or internal colour gradients should be relatively unaffected, and we would not expect to find a large obscured starburst population. Internal kinematics and structural parameters for a sample of super-cluster galaxies will be correlated with their star-formation indicators as well as with the diffuse gas distribution.

e) Statistical census of obscured star-formation in local cluster galaxies To date there is not a large mid-IR based study of star-formation in local galaxy clusters, extending to IR luminosities typical of normal star-forming dwarf galaxies ($L_{IR}sim5 \times 10^8 L_\odot$), previous studies concentrating on luminous infrared galaxies (LIRGs, $L_{IR} > 10^{11} L_\odot$) that represent the extreme starburst population, and contribute $\leq$10% of the global star-formation rate in the local Universe (Le Floch et al.

2005). Star-formation in clusters is instead likely to be dominated by either infalling spiral galaxies whose star-formation has not yet been quenched, or low-mass galaxies undergoing starbursts triggered by their interaction with the cluster environment. By measuring the SFRs of each galaxy, and identifying both normal spiral and interacting galaxies (e.g. using the asymmetry parameter, Conselice 2003), we will measure the fraction of star-formation in cluster galaxies (combining the Shapley super-cluster data with those of the previously observed clusters) that has been triggered by environmental processes, and also see how this fraction varies with galaxy mass. The quantity, nature (LIR/M) and location of the infrared population provide crucial discriminatory signatures as to the processes behind their star-formation and the transformation of galaxies in dense environments (see Zhang 2008). For example mergers will result in the global cluster star-formation rate being dominated by a small population of ULIRGs, while suffocation models predict no cluster ULIRGs and few LIRGs, all of which would be massive spirals yet to have been quenched.

f) Correlate obscured star formation with hierarchical cluster assembly
We will investigate in detail how obscured star-formation relates to the dynamical status of the clusters, correlating the global MIR-based SFRs with the level of substructure in the clusters. To this aim the Shapley data will be complemented by existing sets of data for four other nearby rich clusters: Coma, Abell 1367, Hercules (using Spitzer) and Virgo (IRAS), but will be unique in sampling such a dense dynamically active region. Within each cluster we will also correlate the positions of starburst galaxies with the position of infalling galaxy groups identified from the redshift and X-ray data.

g) Compare mid-IR, optical, radio and UV star-formation indicators
These data will in particular allow us to explore the relationship between obscured and unobscured star-formation in galaxies, and its variation with both galaxy mass and environment. This goal can be achieved by comparing global SFRs from GALEX, Spitzer, WiFeS and VLA. These comparisons will be vital for calibrating and interpreting existing and future large-scale surveys of star formation in the local universe based on just one or more of the above measures such as those obtained from the fibre-based spectroscopy of the Sloan Digital Sky Survey.

i) Investigating the fundamental plane of low mass early-type galaxies
Finally, we plan to extend the study of the fundamental plane detained

in this thesis, firstly by taking adavantage of the recently completed surface phototometry survey of all $R < 18$ galaxies in the SOS region, in conjunction with the new AAOmega spectroscopy, in order to increase the sample size by a factor 3–4. This will allow us to measure the effects of environment on the fundamental plane, as well as measure the relative distances to each of the clusters in the supercluster core, to constrain the geometry of the supercluster core. WiFeS data will be precious to really understand the origin of the tilt of the fundamental plane, by probing how the velocity dispersions and rotation velocities depends on the aperture, and the role of stellar populations in driving the tilt.

Bibliography

Aarseth S. J., Fall S. M., 1980, ApJ, 236, 43

Abadi et al., 1999, MNRAS, 308, 947

Abazajian K. et al., 2005, ApJ, 625, 613

Abell G. O., Corwin H. G. Jr., Olowin R. P., 1989, ApJS, 70, 1

Adelman-McCarthy J. K. et al., 2006, ApJS, 163, 38

Alonso S. M., Lambas D. G., Tissera P., Coldwell G., 2006, MNRAS, 367, 1029

Arnouts S., de Lapparent V., Mathez G. et al., 1997, A&AS, 124, 163

Arnouts S. et al. 2007, A&A, 476, 137

Avila-Reese V., 2006, preprint, astro-ph/0605212

Babu G. J., Singh K., 1983, Ann. Stat., 11, 999

Baldry I. K., Glazebrook K., Brinkmann J., Ivezić Ž, Lupton R. H., Nichol R. C., Szalay A. S., 2004, ApJ, 600, 681

Baldry I. K., Balogh M. L., Bower R. G., Glazebrook K., Nichol R. C., Bamford S. P., Budavari T., 2006, MNRAS, 373, 469 (BB06)

Baldwin J. A., Phillips M. M., Terlevich R., 1981, PASP, 93, 5

Balogh M. L. et al., 1997, ApJ, 488, L75

Balogh M. L., Morris S. L., Yee H. K. C., Carlberg R. G., Ellingson E., 1999, ApJ, 527, 54

Balogh M. L., Navarro J. F., Morris S. L., 2000, ApJ, 540, 113

Balogh M. L. & Morris S. L., 2001, ApJ, preprint, astro-ph/0007111

Balogh M. L. et al., 2004a, MNRAS, 348, 1355 (B04)

Balogh M. L., Baldry I. K., Nichol R., Miller C., Bower R., Glazebrook K., 2004b, ApJL, 615, 101 (BB04)

Bardelli S., Zucca E., Malizia A. et al., 1996, A&A, 305, 435

Bardelli S., Pisani A., Ramella M., Zucca E., Zamorani G., 1998, MNRAS, 300, 589

Bardelli S., Zucca E., Zamorani G., Vettolani G., Scaramella R., 1998, MNRAS, 296, 599

Bardelli S., Zucca E., Zamorani G., Moscardini L., Scaramella R., 2000, MNRAS, 312, 540

Bardelli S., Zucca E., Baldi A., 2001, MNRAS, 320, 387

Barnes J. E., 1988, ApJ, 331, 699.

Barnes J. E. & Hernquist L., 1991, ApJ, 370, L5

Barnes J. E. & Hernquist L., 1992, ARA&A, 40, 705

Beers T.C., Flynn K., Gebhardt K., 1990, AJ, 100, 32

Barnes J. E. & Hernquist L., 1996, ApJ, 471, 115

Bekki K., Couch W. J., Shioya Y., 2001, PASJ, 53, 395

Bekki K., Couch W. J., Shioya Y., 2002, ApJ, 577, 651

Bell E. F., de Jong R., 2001, ApJ, 550, 212

Bell E. F. et al., 2004, ApJ, 608, 752

Bell E. F., Phleps S., Somerville R. S., Wolf C., Borch A., Meisenheimer K., 2006, ApJ, 652, 270

Bell E. F. et al., 2007, ApJ, 663, 834

Bender R., Burstein D., Faber S. M., 1992, ApJ, 399, 462

Benson et al., 2003, AJ, 125, 1866

Bernardi M., et al., 2003, AJ, 125, 1866

Bernstein G. M., Nichol R. C., Tyson J. A., Ulmer M. P., Wittman D., 1995, AJ, 110, 1507

Bertin E., Arnouts S., 1996, A&AS, 331, 439

Bertin G., Ciotti L., Del Principe M., 2002, A&A, 386, 149

Bharadwaj S., Sahni V., Sathyaprakash B. S., Shandarin S. F., Yess C., 2000, ApJ, 528, 21

Binggeli B., Tarenghi M., Sandage A., 1990, A&A, 228, 42

Binney & Tremaine, 1998, in *Galactic Astronomy*, Princeton Univeristy Press

Birnboim Y., Dekel A., Neistein E., 2007, MNRAS, 380, 339

Biviano A., Durret F., Gerbal D. et al., 1995, A&A, 297, 610

Blanton M., Cen R., Ostriker J.P., Strauss M.A., Tegmark M., 2000, ApJ, 531, 1

Blanton M. R. et al., 2001, AJ, 121, 2358

Blanton M. R. et al., 2003b, AJ, 125, 2276

Blanton M. R. et al., 2003a, ApJ, 594, 186

Blanton M. R. et al., 2003c, AJ, 125, 2348

Blanton M. R. et al., 2005a, ApJ, 629, 143

Blanton M. R. et al., 2005b, ApJ, 631, 208

Blanton M. R. et al., 2005c, AJ, 129, 2562

Blanton M. R. et al., 2006, ApJ, 645, 977

Blanton M. R., Berlind A. A., 2007, ApJ, 664, 791

Bond J.R. et al., 1984, in *Formation and Evolution of Galaxies and Large Structure in the Universe*, ed. J. Audouze & J. Tran Than.

Boselli A. & Gavazzi G., 2006, PASP, 118, 517

Boselli A. et al., 2006, ApJ, 651, 811

Bournaud F. et al, 2005, A&A, 437, 69

Bower R. G., Lucey J. R., Ellis R. S., 1992, MNRAS, 254, 589

Bower R. G. et al., 2006, MNRAS, 370, 645

Brinchmann J., Charlot S., White S. D. M., Tremonti C., Kauffmann G., Heckman T., Brinkmann J., 2004, MNRAS, 351, 1151

Bruzual A. G., 1983, ApJ, 273, 105

Bruzual A. G. & Charlot S., 2003, MNRAS, 344, 1000

Bundy K. et al., 2006, ApJ, 651, 120

Caldwell N., Rose J. A., Sharples R. M., Ellis R. S., Bower R. G., 1993, AJ, 106, 473

Calzetti D. et al. 2007, ApJ, 666, 870

Caon N., Capaccioli M., D'Onofrio M., 1993, MNRAS, 265, 1013

Cappellari M. et al., 2006, MNRAS, 366, 1126

Cardelli J. A., Clayton G. C., Mathis J. S., 1989, ApJ, 345, 245

Cattaneo A., Dekel A., Devriendt J., Guideroni B., Blaizot J., 2006, MNRAS, 370, 1651

Charlot S., Fall S. M., 2000, ApJ, 539, 718

Chiosi C., Carraro G., 2002, MNRAS, 335, 335

Christlein D., Zabludoff A. I., 2005, ApJ, 616, 192

Cirasuolo M. et al., 2007, MNRAS, 380, 585

Cole et al., 2001, MNRAS, 326, 255

Conroy C., Gunn J. E. & White M., 2008, arXiV:0809.4261

Conselice C. J., Gallagher J. S. III, Wyse R. F. G., 2001, ApJ, 559, 791

Conselice C. J., O'Neill K., Gallagher J. S. III, Wyse R. F. G., 2003, ApJ, 591, 167

Conselice C. J., 2006, ApJ, 638, 686

Cooper M. C. et al., 2006, MNRAS, 370, 198

Côté P. et al., 2006, ApJS, 165, 57

Couch W. J. et al., 1994, ApJ, 430, 121.

Couch W. J. et al., 2001, ApJ, 549, 820.

Cox T. J., Di Matteo T., Hernquist L., Hopkins P. F., Robertson B., Springel V., 2006, ApJ, 643, 692

Croton D. J. et al., 2006, MNRAS, 368, 11

Davoodi P. et al., 2006, MNRAS, 371, 1113

de Block W., van der Hulst J. & Bothun G. D., 1995, MNRAS, 274, 235.

De Filippis E., Schindler S., Erben T., 2005, A&A, 444, 387

de Freitas Pacheco J. A., Michard R. & Mohayaee R., 2003, preprint, astro-ph/0301248

Dekel A. & Silk J., 1986, ApJ, 303, 39

Dekel, A., & Woo, J. 2003, MNRAS, 344, 1131

Dekel A. & Birnboim Y., 2006, MNRAS, 368, 2

de Lapparent V., 2003, A&A, 408, 845

de Lapparent V., Galaz G., Bardelli S., Arnouts S., 2003, A&A, 404, 831

de Lucia G., Springel V., White S. D. M., Croton D., Kauffmann G., 2006, MNRAS, 366, 499

de Propris R., Liske J., Driver S. P., Allen P. D., Cross N. J. G., 2005, AJ, 130, 1516

De Rijcke S., Dejonghe H., Zeilinger W. W., Hau, G. K. T., 2001, ApJ, 559, 21

Desroches L. et al., 2007, MNRAS, 377, 402

de Vaucouleurs, G., 1948, Ann. Astrophys., 11, 247, Discovery of the $R^{1/4}$ law.

de Vaucouleurs G., 1961, ApJS, 5, 233

Diaferio A., Kauffmann G., Balogh M.L., White S,D.M., Schade D., Ellingson E., 2001, MNRAS, 232, 999

Diemand J., Kuhlen M., Madau P., 2007, ApJ, 667, 859

di Matteo T., Springel V., Hernquist L., 2005, Nature, 433, 604

Djorgovski S., Davis M., 1987, ApJ, 313, 59

D'Onofrio M. et al., 2008, ApJ, 685, 875

Dressler A., 1980, ApJ, 236, 772

Dressler A., Thompson I. B., Shectman S. A., 1985, ApJ, 288, 481

Dressler A. et al., 1997, ApJ, 490, 577

Dressler A. et al., 1999, ApJS, 122, 51

Drinkwater M. J., Parker Q. A., Proust D., Slezak E., Quintana H., 2004, PASA, 21, 89

Driver S. P. et al., 2006, MNRAS, 368, 414

Eggen O. J., Lynden-Bell D., Sandage A.R., 1962, ApJ, 136, 748

Einasto J., Saar E., Kaasik A., Chernin A. D., 1974, Nature, 252, 111

Eisenstein D.J., Hogg D.W., Fukugita M., et al., 2003, ApJ, 585, 694

Faber S.M., Willmer C.N.A., Wolf C., et al., 2007, ApJ, 665, 265

Ferguson H. C., 1992, MNRAS, 255, 389

Ferguson H. C., Binggeli B., 1994, A&ARv, 6, 67

Ferrarese L., Merrit, 2000, ApJ, 539, 9

Ferrarese L., Ford, H., 2005, Space Science Reviews, 116, 523

Ferrarese L. et al., 2006, ApJS, 164, 334

Finoguenov A., Henriksen M. J., Briel U. G., de Plaa J., Kaastra J. S., 2004, ApJ, 611, 811

Forbes et al., 1998, ApJ, 508, 43

Fujita Y., Nagashima M., 1999, ApJ, 516, 619

Fukugita M., Shimasaku K., Ichikawa T. A. W., 1995, PASP, 107, 945F

Garilli B., Maccagni D., Andreon S., 1999, A&A, 342, 408

Gebhardt K., et al., 2000, ApJL, 539, 13

Gerhard O., Kronawitter A., Saglia R. P., Bender R. 2001, AJ, 121, 1936

Ghigna S., Moore B., Governato F., Lake G., Quinn T., Stadel J., 1998, MNRAS, 300, 146

Girardi M., Giuricin G., Mardirossian F., Mezzetti M., Boschin W., 1998, ApJ, 505, 74

Glazebrook K., et al., 2004, Nature, 430, 181

Gómez P. L., Nichol R. C., Miller C. J., et al., 2003, ApJ, 584, 210

Goto T. et al., 2003, PASJ, 55, 757

Goto T., 2005, MNRAS, 357, 937

Gottlöber S., Klypin A., Kravtsov A. V., 2001, ApJ, 546, 223

Graham A. W., Guzmán R., 2003, AJ, 125, 2936

Graham A. W., Jerjen H., Guzman R., 2003, AJ, 126, 1787

Graham A. W., Driver S., 2007, ApJ, 655, 77

Gray M. E., Wolf C., Meisenheimer K., Taylor A., Dye S., Borch A., Kleinheinrich M. 2004, MNRAS, 357, L73

Grebel E. K., Gallagher J. S., Harbeck D., 2003, AJ, 125, 1926

Gregg M., 1992, ApJ, 384, 43

Greggio L & Renzini A., 1983, A.A, 118, 217.

Gunn J. E., Gott J. R., 1972, ApJ, 176, 1

Haehnelt M. G., Natarajan P., Rees M. J., 1998, MNRAS, 300, 817

Haines C. P., Campusano L. E., Clowes R. G., 2004a, A&A, 421, 157

Haines C. P., Mercurio A., Merluzzi P., La Barbera F., Massarotti M., Busarello G., Girardi M., 2004b, A&A, 425, 783

Haines C. P., Merluzzi P., Mercurio A., Gargiulo A., Krusanova N., Busarello G., La Barbera F., Capaccioli M., 2006a, MNRAS, 371, 55

Haines C. P., La Barbera F., Mercurio A., Merluzzi P., Busarello G., 2006b, ApJL, 647, 21

Haines C. P., Gargiulo A., La Barbera F., Mercurio A., Merluzzi P., Busarello G., 2007, MNRAS, 381, 7

Hambly N. C., MacGilivray H. T., Read M. A., 2001, MNRAS, 326, 1279

Hao L. et al., 2005, AJ, 129, 1783

Häring N., Rix H.-W., 2004, ApJL, 604, 89

Heavens A., Panter B., Jimenez R., Dunlop J., 2004, Nature, 428, 625

Hernquist L., 1989, Nature, 340, 687

Hernquist L., 1992, ApJ, 400, 460

Hernquist L., 1993, ApJ, 409, 548

Hernquist L. & Mihos J. C., 1995, ApJ, 448, 41

Hogg D. W. et al., 2003, ApJ, 585, L5

Hopkins A. M., et al., 2003, ApJ, 599, 971

Hopkins P. F., Hernquist L., Cox T. J., Di Matteo T., Robertson B., Springel V., 2006b, ApJS, 163, 1

Hopkins P. F., Hernquist L., Cox T. J., Robertson B., Springel V., 2006a, ApJS, 163, 50

Hopkins P. F. et al., 2008, ApJS, 175,356-389.

Hopkins P. F. et al., 2008, ApJS, 175, 390-422.

Huang et al., 2005, ApJ, 584, 230

Hubble E. P., 1926, ApJ, 64, 321

Hubble E. P., Humason M. L., 1931, ApJ, 71, 43

Hubble E. P., 1936, The Realm of the Nebulae. Yale University Press, New Haven

Hyde J. B. & Bernardi M., 2008, preprint, astro-ph 081049924

Jesseit R. et al., 20076, MNRAS, 376, 997.

Jogee S., 2006, in *Physics of Active Galactic Nuclei on All Scales*, ed. Alloin D., Johnson R.,Lire P., 143.

Jørgensen I., Franx M., 1994, ApJ, 433, 553

Jørgensen I., Franx M., Kjægaard P., 1995, MNRAS, 276, 1341

Jørgensen I., Franx M., Kjægaard P., 1996, MNRAS, 280, 167 (JFK96)

Jungwiert B., Combes F., Palous J., 2001, A&A, 376, 85

Kang X., Jing Y. P., Mo H. J., Börner, 2005, ApJ, 631, 21

Kapferer W., et al., 2007, A&A 466, 813

Karachentsev I. D., Karachentseva V. E., Huchtmeier W. K., Makarov D. I., 2004, AJ, 127, 2031

Karachentsev I. D., 2005, AJ, 129, 178

Katz & Gunn, 1991, ApJ, 377, 365

Kauffmann G., White S. D. M., Guideroni B., 1993, MNRAS, 264, 201

Kauffmann G. et al., 2003a, MNRAS, 341, 33 (K03)

Kauffmann G. et al., 2003b, MNRAS, 341, 54

Kauffmann G. et al., 2003c, MNRAS, 346, 1055

Kauffmann G. et al., 2004, MNRAS, 353, 713

Kauffmann G., 2004, ApJ, 611, L89

Kauffmann G. et al., 2006, MNRAS, 367, 1408

Kauffmann G. et al., 2007, ApJS, 173, 357

Kelson D. D., Illingworth G. D., van Dokkum P. G., Franx M., 2000, ApJ, 531, 184

Kennicutt R. C. Jr., 1998, ARA&A, 36, 189

Kereš D., Katz N., Weinberg D. H., Davé R., 2005, MNRAS, 363, 2

Kewley L. J., Dopita M. A., Sutherland R. S., Heisler C. A., Trevena J., 2001, ApJ, 556, 121

Kewley L. J., Jansen R. A., Geller M. J., 2005, PASP, 117, 227

Kewley L. J., Groves B., Kauffmann G., Heckman T., 2006, MNRAS, 372, 961

Kochanek et al., 2001, ApJ, 560, 566

Kodama et al., 1998, A&A, 334, 99

Kodama T., Bower R.G., 2001, MNRAS, 321, 18

Koopmann R. A., Kenney J. D. P., 2004, ApJ, 613, 851

Kormendy J., 1976, ApJ, 218, 333

Kravtsov A. V. et al., 2004, ApJ, 609, 35

Kriek M. et al., 2006, ApJL, 649, 71

Kron R. G., 1980, ApJS, 43, 305

Kroupa P., 2001, MNRAS, 322, 231

Kull A., Böhringer H., 1999, A&A, 341, 23

Kuntschner H. et al., 2006, MNRAS, 369, 497

La Barbera F., de Carvalho R. R., Kohl-Moreira J. L., Gal R. R., Soares-Santos M., Capaccioli M., Santos R., Sant'Anna N., 2008a, PASP, 120, 681

La Barbera F., Busarello G., Merluzzi P., de la Rosa I., Coppola G., Haines C. P., 2008b, astro-ph/0807.3829

Lacey C., Cole S., 1993, MNRAS, 262, 627

Lake & Katz, 1998, ApJ, 495, 152L

Landolt A. U., 1992, AJ, 104, 340

Larson R. B., 1975, MNRAS, 173, 671

Larson R. B., Tinsley B. M., Caldwell C. N., 1980, MNRAS, 237, 692

Lee H., McCall M. L., Richer M. G., 2003, AJ, 125, 2975

Lee H. et al., 2006, ApJ, 647, 970.

Lemson G., Kauffmann G., 1999, 302, 111

Lequeux J. et al., 1979, A&A, 80, 155

Lewis I. et al., 2002, MNRAS, 334, 673

Lisker T., Glatt K., Westera P., Grebel E. K., 2006, AJ, 132, 2432

Lisker T., Grebel E. K., Binggeli B., Glatt K., 2007, ApJ, 660, 1186

Longmore A. et al., 1982, MNRAS, 200, 325

Lonsdale C. J. et al., 2003, PASP, 115, 897

López-Cruz O., Barkhouse, W.A., Yee H.K.C., 2004, ApJ, 614, 679

Mac Low M.-M., Ferrara A., 1999, ApJ, 513, 142

Madgwick D. S., Lahav O., Baldry I. K., et al., 2002, MNRAS, 333, 133

Mahdavi A., Geller M. J., 2004, ApJ, 607, 202

Mamon G. A., Sanchis T., Salvador-Solé E., Solanes J. M., 2004, A&A, 414, 445

Mandelbaum R. et al., 2006, MNRAS, 368, 715

Maraston C., 2005, MNRAS, 362, 799

Marcolini A., Brighenti F., D'Ercole A., 2003, MNRAS, 345, 1329

Marcolini A., D'Ercole A., Brighenti F., Recchi S., 2006, MNRAS, 371, 643

Martin C. L., Kennicutt R. C., 2001, ApJ, 555, 301

Martin D. C., Fanson J., Schiminovich D. et al., 2005, ApJL, 619, 1

Martin D. C. et al., 2007, ApJS, 173, 342

Martini P., Kelson D. D., Kim E., Mulchaey J. S., Athey A. A., 2006, ApJ, 644, 116

Mastropietro C., Moore B., Mayer L., Debattista V. P., Piffaretti R., Stadel J. 2005, MNRAS, 364, 607

Mateo M., 1998, ARA&A, 36, 435

Mateus A., Sodré L., Cid Fernandes R., Stasińska G., Schoenell W., Gomes J. M., 2006, MNRAS, 370, 721

Mateus A., Sodré L., Cid Fernandes R., Stasińska G., 2007, MNRAS, 374, 1457

Mathews W. G., Brighenti F., 2003, ARA&A, 41, 191

Matković A. Guzmán R., 2005, MNRAS, 362, 289

Matteucci F., 1996, *Fundamentals of Cosmic Physics*, Vol. 17, pp. 283-396

Maulbetsch C., Avila-Reese V., Colin P., Gottlöber S., Khalatyan A., Steinmetz M., 2007, ApJ, 654, 53

Mayer L., Governato F., Colpi M., Moore B., Quinn T., Wadsley J., Stadel J., Lake G., 2001, ApJ, 559, 754

Mayer L., Mastropietro C., Wadsley J., Stadel J., Moore B., 2006, MNRAS, 369, 1021

McGaugh S.S., Schombert J. M. & Bothun G. D., 1994, MNRAS, 267, 129

McGaugh S.S. & de Block W. J. G., 1997, ApJ, 481, 689

Melnick J., Quintana H., 1981, A&AS, 44, 87

Menci N., Fontana A., Giallongo E., Salimbeni S., 2005, ApJ, 632, 49

Mercurio A., Massarotti M., Merluzzi P., et al., 2003, A&A, 408, 57

Mercurio A., Merluzzi P., Haines C. P., Gargiulo A., Krusanova N., La Barbera F., Busarello G., Capaccioli M., Covone G., 2006, MNRAS, 368, 109

Merlin E., Chiosi C., 2006, A&A, 457, 437

Metcalfe N., Godwin J. G., Spenser S. D, 1987, MNRAS, 225, 581

Metcalfe N., Godwin J. G., Peach J. V., 1994, MNRAS, 267, 431 (MGP94)

Mihos J. C. & Hernquist L. 1994, ApJ, 431, L9

Mihos J. C., Hernquist L., 1996, ApJ, 464, 641

Mihos J. C., 2004, in *Clusters of Galaxies: Probes of Cosmological Structure and Galaxy Evolution*, Cambridge University Press, edited by J.S. Mulchaey, A. Dressler, and A. Oemler, p. 278

Miller C. J. et al., 2003, ApJ, 597, 142

Miller N. A., 2005, AJ, 130, 2541

Molinari E., Chincarini G., Moretti A., De Grandi S., 1998, A&A, 338, 874

Moore B., Katz N., Lake G., Dressler A., Oemler A. Jr., 1996, Nature, 379, 613

Moore B., Lake G., Katz N., 1998, ApJ, 495, 139

Moore B., Lake G., Quinn T., Stadel J., 1999, MNRAS, 364, 465

Morgan W. W., 1958, PASP, 70, 415

Morrissey P., Schiminovich D., Barlow T. A. et al. 2005, ApJL, 619, 7

Moustakas J., Kennicutt R. C. Jr., Tremonti, C. A., 2006, ApJ, 642, 775

Naab T. & Burkert A. 2003, ApJ, 597, 893

Naab T., Jesseit R., Burkert A. 2006a, MNRAS, 372, 839

Naab T., Khochfar S., Burkert A. 2006b, ApJ, 636, L81

Naab T. & Trujillo I. 2006, MNRAS, 369, 265

Nelan J. E., Smith R. J., Hudson M. J., Wegner G. A., Lucey J. R., Moore S. A. W., Quinney S. J., Suntzeef N. B., 2005, ApJ, 632, 137

Nigoche-Netro A. et al., 2008, preprint, asrto-ph 08051142

Noeske K. G. et al., 2007a, ApJ, 660, L43

Noeske K. G. et al., 2007b, ApJ, 660, L47

Nolan L. A., Raychaudhury S., Kabán A., 2007, MNRAS, 375, 381

Oemler A., 1974, ApJ, 194, 1

Osterbrock D. E., 1960, ApJ, 132, 325

Panter B., Jimenez R., Heavens A. F., Charlot S., 2007, MNRAS, 378, 1550

Panuzzo P. et al., 2007, ApJ, 656, 206

Pilyugin L. S. & Ferrini F., 2000, A&A, 354, 874

Pisani A., 1993, MNRAS, 265, 706

Pisani A., 1996, MNRAS, 278, 697

Poggianti B. M. & Wu H., 2000, ApJ, 525, 157

Poggianti B. M., Bridges T. J., Komiyama Y., Yagi M., Carter D., Mobasher B., Okamura S., Kashikawa N., 2004, ApJ, 601, 197

Poggianti B., von der Linden, A., de Lucia, G., et al. 2006, ApJ, 642, 188

Popesso P., Böhringer H., Brinkmann J., Voges W., York D. G., 2004, A&A, 423, 449

Popesso P., Biviano A., Böhringer H., Romaniello M., 2006, A&A, 445, 29

Proctor R. N. & Sansom A. E., 2002, MNRAS, 333, 517

Quadri R. et al., 2007, ApJ, 654, 138

Quintana H., Carrasco H., Reisenegger A., 2000, AJ, 120, 511

Rawle T. D. et al., 2008, MNRAS, 389, 1891

Raychaudhury S., 1989, Nature, 342, 251

Reda F. et al., 2005, MNRAS, 360, 693

Reisenegger A., Quintana H., Carrasco H., Maze, J. 2000, AJ, 120, 523

Renzini A., 2006, ARA&A, 44, 141

Rigby J. R., Rieke G. H., Donley J. L., Alonso-Herrero A., Pérez-González P. G., 2006, ApJ, 645, 11

Rines K., Geller M. J., Kurtz M. J., Diaferio A., 2005, AJ, 130, 1482 (R05)

Rines K., Diaferio A., 2006, AJ, 132, 1275

Robertson B., Cox T. J., Hernquist L., Franx M., Hopkins P. F., Martini P., Springel V., 2006, ApJ, 641, 21

Roediger E., Hensler G., 2005, A&A, 433, 875

Roettiger K., Burns J. O., Loken C., 1996, ApJ, 673, 451

Rossa J. et al., 2006, AJ, 132, 1074

Ruderman J. T., Ebeling H., 2005, ApJL, 623, 81

Salim G. et al., 2005, ApJ, 619, L39

Sánchez-Blázquez P. et al., 2006, MNRAS, 371, 703

Sanders D. B. & Mirabel I. F., 1996, ARA&A, 34, 749

Scannapieco C., Tissera P. B., White S. D. M., Springel V., 2006, MNRAS, 371, 1125

Shapley H., 1930, Bull. Harvard Obs., 874, 9

Shapley A. E. et al., 2005, ApJ, 635, 1006

Schechter P., 1976, ApJ, 203, 297

Schlegel D. J., Finkbeiner D. P., Davis M., 1998, ApJ, 500, 525

Schmidt M., 1959, ApJ, 129, 243

Schweizer F. & Seitzer P., 1992, AJ, 104, 1039

Schweizer F., 1992, in *Physics of Nearby Galaxy: Nature or Nurture?*, ed. Thuan T. X., Balkowski C. & Tran Thanh van J., 283

Schweizer F., 1996, AJ, 111, 109

Schweizer F., 1998, in *Galaxy: Interactions and Induced Star Formation*, ed. R. C. Kennicutt Jr., Schweizer F., Barnes J. E., Friedli D., Martinet L., Pfenniger D., 105

Sersic, J. L., 1968, *Atlas de Galaxies Australes*, Generalized $R^{1/4}$ law.

Shimasaku K. et al., 2001, AJ, 122, 1238

Silk J., Rees M., 1998, A&A, 334, L1

Silverman B. W., 1986, Density Estimation for Statistics and Data Analysis. Chapman and Hall, London

Smail I. et al., 1999, ApJ, 525, 609

Smith R. J., et al., 2004, AJ, 128, 1558

Smith G. P., Treu T., Ellis R. S., Moran S. M., Dressler A. 2005, ApJ, 620, 78

Smith R. J., Hudson M. J., Lucey J. R., Nelan J. E., Wegner G. A., 2006, MNRAS, 369, 1419

Smith R. J., Lucey J. R., Hudson M. J., 2007a, MNRAS, 381, 1035 (SLH)

Söchting I. K., Clowes R. G., Campusano L. E., 2004, MNRAS, 1241, 1254

Solanes J. M., Manrique A., García-Gómez C., González-Casado G., Giovanelli R., Haynes M. P., 2001, ApJ, 548, 97

Sorrentino G., Antonuccio-Delogu V., Rifatto A., 2006a, A&A, 460, 673

Sorrentino G., Radovich M., Rifatto A., 2006b, A&A, 451, 809

Spayberry et al., 1995, AJ, 109, 558

Springel V., White S.D. M., Tormen G., Kauffmann G., 2001, MNRAS, 328, 726

Springel V., di Matteo T., Hernquist L., 2005a, MNRAS, 361, 776

Springel V., di Matteo T., Hernquist L., 2005b, ApJL, 620, 79

Springel V. et al., 2005c, Nat, 435, 629

Stoughton C. et al., 2002, AJ, 123, 485

Stott J. P., Smail I., Edge A. C., Ebeling H., Smith G. P., Kneib J.-P., Pimbblet K. A., 2007, ApJ, 661, 95

Strateva I. et al., 2001, AJ, 122, 1861

Strauss M. A. et al., 2002, AJ, 124, 1810

Strazzulo et al. et al. 2006, A&A, 450, 909

Struble M. F. & Rood H. J., 1999, ApJS, 125, 35

Struck C., 2005, preprint (astro-ph/0511335)

Tanaka M., Goto T., Okamura S., Shimasaku K., Brinkmann, J., 2004, AJ, 128, 2677 (T04)

Tanaka M. et al., 2005, MNRAS, 362, 268

Tanaka M. et al. 2007, MNRAS, 377, 1206

Tassis K., Kravtsov A., V., Gnedin N. Y., 2008, ApJ, 672, 888

Thomas D., Maraston C., Bender R., 2003, MNRAS, 339, 897

Thomas D., Maraston C., Bender R., Mendes de Oliveira C., 2005, ApJ, 621, 673

Thomas J., Saglia R. P., Bender R., Thomas D., Gebhardt K., Magorrian J., Corsini E. M., Wegner G., 2005, MNRAS, 360, 1355

Thomas T., Katgert P., 2006, A&A, 446, 31

Tinsley B. M., 1980, *Fund Cosmic Phys.*, 5, 287

Toomre A., Toomre J., 1972, ApJ, 178, 623

Toomre A., 1977, in Tinsley B. M., Larson R. B., eds, Evolution of Galaxies and Stellar Populations. Yale Univ. Obs., New Haven, p. 401

Tremonti C. A. et al., 2004, ApJ, 613, 898

Treu T., Ellis R. S., Kneib J.-P., Dressler A., Smail I., Czoske O., Oemler A., Natarajan P., 2003, ApJ, 591, 53

Trujillo I., Burkert A., Bell E. F., 2004, ApJL, 600, 39

Tully et al., 1982, ApJL, 257, 527

Vandame B., 2004, PhD thesis

van den Bergh S., 1976, ApJ, 206, 883

van den Bergh S., 1999, A&A Review, 9, 273

van Dokkum & Stanford, 2003, ApJ, 585, 78

van Dokkum P., van der Marel R. P., 2007, ApJ, 655, 30

van Gorkom J., 2004, in eds. Mulchaey J. S., Dressler A., Oemler A., Clusters of Galaxies: Probes of Cosmological Structure and Galaxy Evolution. Cambridge University Press, New York, p. 306

van Zee L., 2001, AJ, 121, 2003

van Zee L., Skillman E. D., Haynes M. P., 2004, AJ, 128, 121

Venturi T., Bardelli S., Morganti R., Hunstead R. W., 2000, MNRAS, 314, 594

Venturi T., Bardelli S., Dallacasa D., et al., 2003, A&A, 402,913

Vogt N., Haynes M. P., Giovanelli R., Herter T., 2004, AJ, 127, 3300

Vollmer B., Cayatte V., Balkowski C., Duschl W. J., 2001, ApJ, 561, 708

Wainer H. & Thissen D., 1976, Psychometrika, 41, 9

Wehner E. H., Harris W. E., 2006, ApJL, 644, 17

Weinmann S. M., van den Bosch F. C., Yang X., Mo H. J., 2006a, MNRAS, 366, 2

Weinmann S. M., van den Bosch F. C., Yang X., Mo H. J., Croton D. J., Moore B., 2006b, MNRAS, 372, 1161

White S. D. M., Rees M. R., 1978, MNRAS, 183, 341

White R. A., Bliton M., Bhavsar S. P., Bornmann P., Burns J. O., Ledlow M. J., Loken C., 1999, AJ, 118, 2014

Whitmore B. C. & Gilmore D. M., 1991, ApJ, 367, 64

Woo J., Corteau S. & Dekel A., 2008, MNRAS, 390, 1453

Worthey G. & Ottaviani D. L., 1997, ApJS, 111, 377

Wyder T. et al., 2007, ApJS, 173, 293

Willmer C. N. A., Faber S. M., Koo D. C. et al., 2006, 647, 853

Wittman B.M., Tyson J.A., Dell'Antonio I.P. et al., 2002, SPIE, 4836, 73

Wolf C., Meisenheimer K., Kleinheinrich M., et al., 2004, A&A, 421, 913

Wolf C., Gray M. E., Meisenheimer K., 2005, A&A, 443, 435

Yagi, M., Kashikawa, N., Sekiguchi, M., et al., 2002, AJ, 123, 87

Yan R., Madgwick D. S. & White M., 2003, ApJ, 598, 848

Yang X., Mo H. J., van den Bosch F. C., Jing Y. P., 2005, MNRAS, 356, 1293

Yi, S. K., Yoon, S.-J., Kaviraj, S., et al. 2005, ApJL, 619, 111

Younger et al., 2008, ApJ, 686, 815

York D. G. et al., 2000, AJ, 120, 1579

Young C. K., Currie M. J., 1994, MNRAS, 268, L11

Zaritsky D., Gonzalez A. H., Zabludoff A. I., 2006, ApJ, 638, 725

Zehavi I. et al., 2005, ApJ, 630, 1

Zheng X. Z., et al. 2007, ApJL, 661, 41

Acknowledgements

I warmly thank Graham Smith, Trevor Ponman, and Raychaudhury Somak and at Birmingham University for the kind hospitality and the stimulating scientific discussions during my months spent in England; Russell Smith and John Lucey for the spectroscopic dataset which allowed me the study of the fundamental plane of Shapley Supercluster, for the suggestions on the FP analysis and for the warm welcome during my visit at Durham University; my correlators Klaus Meisenheimer and Giuseppe Longo for the scientific guide during my PhD experience. To interact with all of you has deeply enriched not only my PhD experience, providing me with precious information and hints for my research, but above all, my personal growth.

Special thanks are for Chris Haines for all the many things you taught me and for believing in my ability to carry out this work: sincerely thank!

I wish to thank Paola Merluzzi and Gianni Busarello for giving me the opportunity to carry out the research presented in this thesis and to have been a present guide and a constant example during all these years.

Amata Mercurio and Francesco La Barbera...thanks, thanks and thanks for being always there to help me and to answer my questions...every time I came to the Observatory I always found in you much more than two colleague...two friends.

Thanks to ALL my friends here in the Observatory: Crescenzo, Roberto, Ida, Eugenio, Massimo, Alessandra...thank to be me friends!

Geppina...simply thank to be in the exactly way you are!

Finally, thank to all my family...large, noisy...united...you are and always will be my real support.

We thank the Deep Lens Survey and NOAO, who provided the galaxy counts used to derive the LFs.

Funding for the SDSS and SDSS-II has been provided by the Alfred P. Sloan Foundation, the Participating Institutions, the National Science Foundation, the U.S. Department of Energy, the National Aeronautics and Space Administration, the Japanese Monbukagakusho, the Max Planck Society, and the Higher Education Funding Council for England. The SDSS Web Site is http://www.sdss.org/.

The SDSS is managed by the Astrophysical Research Consortium for the Participating Institutions. The Participating Institutions are the American Museum of Natural History, Astrophysical Institute Potsdam, University of Basel, University of Cambridge, Case Western Reserve University, University of Chicago, Drexel University, Fermilab, the Institute for Advanced Study, the Japan Participation Group, Johns Hopkins University, the Joint Institute for Nuclear Astrophysics, the Kavli Institute for Particle Astrophysics and Cosmology, the Korean Scientist Group, the Chinese Academy of Sciences (LAMOST), Los Alamos National Laboratory, the Max-Planck-Institute for Astronomy (MPIA), the Max-Planck-Institute for Astrophysics (MPA), New Mexico State University, Ohio State University, University of Pittsburgh, University of Portsmouth, Princeton University, the United States Naval Observatory, and the University of Washington.

This research has made use of the NASA/IPAC Extragalactic Database (NED) which is operated by the Jet Propulsion Laboratory, California Institute of Technology, under contract with the National Aeronautics and Space Administration.

The Millennium Run simulation used in this paper was carried out by the Virgo Supercomputing Consortium at the Computing Centre of the Max-Planck Society in Garching. The semi-analytic galaxy catalogue is publicly available at http://www.mpa-garching.mpg.de/galform/agnpaper

GALEX (*Galaxy Evolution Explorer*) is a NASA Small Explorer, launched in April 2003. We gratefully acknowledge NASA's support for the construction, operation, and science analysis for the GALEX mission, developed in cooperation with the Centre National d'Etudes Spatiales of France and the Korean Ministry of Science and Technology.